THE DEVELOPMENT AND EVALUATION OF HEAD PROBES FOR OPTICAL IMAGING OF THE INFANT HEAD

GILBERTO BRANCO

DEPARTMENT OF MEDICAL PHYSICS & BIOENGINEERING
UNIVERSITY COLLEGE LONDON (UCL)

SUPERVISORS
PROF. JEREMY C. HEBDEN
PROF. DAVID T. DELPY

THESIS SUBMITTED FOR THE DEGREE OF DOCTOR OF PHILOSOPHY (PH.D.)
AT THE UNIVERSITY OF LONDON

JANUARY 2007

ABSTRACT

The objective of this thesis was to develop and evaluate optical imaging probes for mapping oxygenation and haemodynamic changes in the newborn infant brain. Two imaging approaches are being developed at University College London (UCL): optical topography (surface mapping of the cortex) and optical tomography (volume imaging). Both have the potential to provide information about the function of the normal brain and about a variety of neurophysiological abnormalities. Both techniques require an array of optical fibres/fibre bundles to be held in contact with the head, for periods of time from tens of seconds to an hour or more. The design of suitable probes must ensure the comfort and safety of the subject, and provide measurements minimally sensitive to external sources of light and patient motion.

A series of prototype adaptable helmets were developed for optical tomography of the premature infant brain using the UCL 32-channel time-resolved system. They were required to attach 32 optical fibre bundles over the infant scalp, and were designed to accommodate infants with a variety of head shapes and sizes, aged between 24-weeks gestational age and term. Continual improvements to the helmet design were introduced following the evaluation of each prototype on infants in the hospital. Data were acquired to generate images revealing the concentration and oxygenation of blood in the brain, and the response of the brain to sensory stimulation. This part of the project also involved designing and testing new methods of acquiring calibration data using reference phantoms.

The second focus of the project was the development of probes for use with the UCL frequency-multiplexed near-infrared topography system. This is being used to image functional activation in the infant cortex. A series of probes were developed and experiments were conducted to evaluate their sensitivity to patient motion and to compression of the probe. The probes have been used for a variety of functional activation studies.

ACKNOWLEDGEMENTS

I would like to express my gratitude to my supervisors, Prof. Jeremy Hebden and Prof. David Delpy, for their encouragment and guidance throughout my Ph.D. I am great indebted to Prof. Jeremy Hebden, who gave special attention and support to my work. Much appreciation is also given to Dr. Alan Cottenden and Dr. Adam Gibson for their advice and suggestions.

I would like to thank all my colleagues in the Biomedical Optics Research Laboratory with whom I spent a pleasant time, especially Roberto Carlos Aguilera, Teresa Correia, Caroline Reid, Peck Hui Koh, Dr. Terence Leung, Dr. Julian Henty, Dr. Jan Laufer, Dr. Louise Enfield, Dr. Anna Blasi, and Dr. Yasuyo Minagawa-Kawai. Additionally, much appreciation is given to the scientific and friendly environment provided during the Journal Club and BORL meetings.

I would also like to thank the staff from the department mechanical workshop, especially Mr. Bill Raven, Mr. Stewart Morrison, and Mr. Denzil Booth, who taught me the basic operation and features of several instruments and mechanical tools.

I am very grateful to CAPES Foundation and the Federal Technological University of Parana (UTFPR) for supporting my studies at University College London. I am also indebted to my colleagues at the Electronics Department at UTFPR, who carried on with my duties during the period when I was on leave.

Most of all, I would like to thank my parents Ivan Branco (in memory) and Glacy Nascimento Branco, who gave me the inspiration to pursue my objectives, and my in-laws who always had a word of comfort.

In particular, I would like to thank my beloved wife Camila, who devoted her energy and love, supporting and encouraging me during this chapter of our lives. I dedicate this thesis to Camila with all my love.

LIST OF ACRONYMS

ADF Acquisition definition file

AH Adaptable helmet

CBF Cerebral blood flow [ml/100g/min]

CBV Cerebral blood volume [ml/100g]

CFD Constant fraction discriminator

CMH Custom made helmet

CSF cerebrospinal fluid

CT Computed tomography

CW Continuous wave

DP differential pathlength

DPF Differential pathlength factor

EEG Electroencephalograph

EIT Electrical impedance tomography

FEM Finite element method

FMRI Functional MRI

HIE Hypoxic ischaemic encephalopathy

IVH Intraventricular haemorrhage

MBLL Modified Beer-Lambert Law

MCP-PMT Micro-channel plate photomultiplier tube

MONSTIR Multi-channel optoelectronic near-infrared system for time-resolved image reconstruction

MEG Magnetoencephalography

MRI Magnetic resonance imaging

NIRS Near-infrared spectroscopy

OFC Occipitofrontal circumference

PDE Partial differential equation

PET Positron emission tomography

PMDF Photon measurement density function

PMT Photomultiplier tube

PTA Picosecond time analyser

RTE Radiative transport equation

SNR Signal-to-noise relation

SPECT Single photon emission computed tomography

TCSPC Time correlated single photon counting

TOAST Temporal optical absorption and scattering tomography

TPSF Temporal point spread function

UCL University College London

CONTENTS

TABLE OF FIGURES

2 Basic Anatomy and Physiology of the Human Brain

3 Technique for Brain Imaging

4 Optical Imaging at UCL

5 Performance of the Optical Tomography Head Probes

6 Performance of the Optical Topography Head Probes

TABLE OF TABLES

2 Basic Anatomy and Physiology of the Human Brain

3 Technique for Brain Imaging

5 Performance of the Optical Tomography Head Probes

Chapter 1

Introduction

1.1 Motivation

Brain imaging systems have traditionally been used to identify and delineate the morphology of abnormalities. More recently functional imaging methods have become popular which take advantage of the fact that regional blood flow and haemoglobin oxygen saturation changes occur in response to neural and electrical activation such as that caused by movement, sensing or thinking. However, efforts to use techniques such as Single Photon Emission Computed Tomography (SPECT), Positron Emission Tomography (PET) and functional Magnetic Resonance Imaging (fMRI) routinely in critically ill patients have proven difficult. Although successful in many cases, and potentially of use in the future to direct therapeutic interventions and provide prognostic information, these modalities are not feasible in many situations due to the problems and hazards of moving patients, especially newborn infants, from the intensive care unit, and the hazards of ionising radiation for SPECT and PET. Thus, a continuous functional imaging method suitable for use at the bedside could be really beneficial (Meek, 2002), (Hintz *et al*, 2001), (Isobe *et al*, 2001).

Optical imaging is a developing field that has the potential to provide considerable insights into the mechanisms of damage in the neonatal brain as well as into the functional development of both the normal and abnormal brain.

The vulnerability of infants (particularly if they are undergoing intensive care) and the inability of them to actively co-operate with the evoked studies (i.e. they will not remain motionless or perform tasks on request) represent a unique challenge, which also can potentially be addressed by optical imaging.

Optical techniques can be used on extremely fragile infants, because firstly, the radiation used is non-ionizing, and therefore patients can be exposed repeatedly without the harm associated with an accumulated dose, such as X-rays. Secondly, optical methods offer the potential to differentiate between soft tissues (e.g. grey and white matter), due to their different absorption or

scattering properties at NIR wavelengths (650 – 1000 nm). Thirdly, the specific absorption of natural chromophores (such as haemoglobin) allows functional information to be obtained (Hebden *et al*, 1997). In addition, its use rarely presents ethical dilemmas, and sedation of the subjects is not generally necessary (Meek, 2002).

New methods of imaging the oxygenation and haemodynamics of the newborn infant brain are being developed based on near-infrared light. The imaging techniques known as optical topography and optical tomography have the potential to provide information about the function of the normal brain, and about a variety of cerebral pathologies. The former provides a distinction between tissues based on their optical properties obtained from measurements of reflected light and is more appropriate to surface mapping of the cortex. The latter provides volume images using measurements of transmitted light (Hebden, 2003). Both exploit the differences between the absorption spectra of oxy-haemoglobin and deoxy-haemoglobin at near infrared wavelengths, and offer a means of monitoring brain oxygenation safely in an intensive care environment without interference with the normal handling of the infant.

1.2 The UCL Systems

A 32-channel time-resolved system has been developed at UCL (1996) for 3D optical imaging of the newborn infant brain (Schmidt *et al*, 2000). Picosecond pulses from a dual-wavelength fibre laser are delivered to the head surface via single optical fibers integrated within larger fibre bundles which transport the transmitted light to photon-counting detectors. Acquiring measurements therefore requires coupling up to 32 fibre bundles to the scalp of the infant. For the initial studies performed with the system, this was achieved using helmets custom-made for each infant. However, customised helmets are time-consuming to construct (6-10 hours), and have been designed for specific babies. Therefore an adjustable helmet has been developed to overcome such limitations.

The UCL optical topography system currently consists of 16 laser diode sources (eight at 785 nm and eight at 850 nm) and eight avalanche photodiode detectors. Each source is modulated at a different frequency in parallel, and the detected signals are demultiplexed in software in real-time using a Fourier transform. This novel approach provides flexibility in the positioning of the sources and detectors, and different arrangements can be accommodated with only minor adjustments to the control software. Probes have been developed for studies of cortical activation in newborn infants (Blasi *et al*, 2006), (Branco *et al*, 2006), (Everdell *et al*, 2005).

1.3 The Objectives

Tomographic and Topographic imaging approaches require an array of optical fibres/fibre bundles to be held in contact with the infant head, for periods of time from a few tens of seconds for some functional studies to an hour or more for repeated tomography measurements. The design of suitable probes must ensure the comfort and safety of the infant, and provide measurements which are minimally sensitive to head movement and the presence of hair beneath the probe. Probes must also exclude ambient light, and prevent light leaking between source and detector fibers around the surface of head.

The principal objectives of this research are to:

I. Design, construct, and evaluate the performance of head probes for performing optical tomography and topography of the newborn brain using the two UCL systems;
II. Develop practical means of acquiring both functional and static images of the infant brain and corresponding measurements;
III. Investigate the main causes of data error and develop means of minimising them.

1.4 Structure of this Thesis

This thesis presents a brief description of existing brain imaging modalities: the new methods of imaging the oxygenation and haemodynamics of the

newborn infant brain and their potential for providing valuable functional and physiological information and the main objectives of this research project.

Chapter 2 describes the basic anatomy and surrounding structures, and the main absorbers of NIR light in the human brain. The modelling of light propagation through these structures also is covered. The final section in this chapter describes birth injuries and a brief introduction to the use of near infrared spectroscopy as a potential tool to continuously monitor cerebral functions in the infant brain.

Chapter 3 briefly emphasizes the physical principles and intrinsic limitations of methodologies of brain imaging before proceeding to a discussion of optical imaging techniques, known as optical topography (surface mapping of the cerebral cortex) and optical tomography (volume imaging), and their associated instrumentation.

Chapter 4 focuses on the UCL systems with a brief description of the principal elements/components of each instrument and the usual data treatment and image reconstruction process.

Chapter 5 describes the development, manufacture & performance of helmets developed for optical tomographic imaging of the infant brain. It also presents results on a range of infants at rest, during functional stimulation (auditory and language stimuli).

Chapter 6 describes the development, manufacture & performance of probes developed for optical topographic imaging of the cortical regions of infant brain at rest and during functional stimulation.

Chapter 7 presents a discussion of the results acquired using both probes developed for this project, and concludes this thesis with suggestions for future work.

Chapter 2

Fundamentals of Tissue Optics

2.1 Introduction

The application of lasers and other optical technology to problems in biomedicine is a rapidly growing field. These applications can be classified as either therapeutic or diagnostic. In therapeutic applications, the transformation of light energy into chemical, thermal or mechanical energy, via light absorption, can cause a direct and selective cell death (Niemz, 1999). In this project the fluence rates are chosen to be sufficiently small, thus these effects can be ignored. The light-tissue interactions in the diagnostic approach must by contrast be non-destructive and the main goal is to study the physiology or pathology of the tissue. There are a variety of potential optical methods to evaluate the light-tissue interactions, such as diffuse reflection spectroscopy and time resolved transmittance among others.

The fundamental optical characteristics that are exploited for diagnostic information are absorption and scattering (elastic and inelastic) in the wavelength region of 600 – 1000nm (near-infrared, NIR range) where tissue scattering predominates over absorption. This research project concerns the use of sources in the near-infrared range only.

2.2 Optical properties

Photon propagation in biological tissue is characterised by the basic optical properties of absorption, scattering, and refractive index. These properties govern the numbers of photons that are transmitted between points on the surface of tissue.

2.2.1 Refractive Index

The simplest of the optical properties of tissues is the refractive index n, which determines the speed of light in the medium. Changes in the refractive index, either continuous or abrupt (at boundaries), give rise to scattering, refraction and reflection. Refraction usually occurs when light is incident at the boundary between two media of different indices of refraction (Figure 2.1),

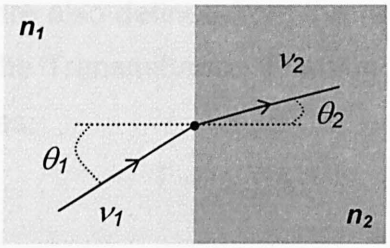

Figure 2.1 Refraction of light between two media with different refractive index (n_1<n_2).

and is governing by Snell's law. It states that:

$$v_1.sin(\theta_1) = v_2.sin(\theta_2) \quad [2.1]$$

where θ_1 is the angle of incidence, θ_2 is the angle of refraction (to the normal of the interface), and v_1 and v_2 are the speeds of light in the media, and are related to the refractive index of each media ($n = c_{vacuum}/v$). Since tissues are heterogeneous in composition, one may need to know the refractive indices for the various tissue constituents or an averaged value for the tissue as a whole. The overall refractive index is considered to be around 1.4 for most tissue types (Delpy *et al*, 1988).

2.2.2 Absorption

The transmitted light intensity $I_{(d)}$ across a homogeneous and non-scattering medium of thickness d, which is illuminated by a collimated beam of light of intensity I_0 at the wavelength λ will be given by:

$$I_{(d)} = I_0.e^{(-\mu_a.d)} \quad [2.2]$$

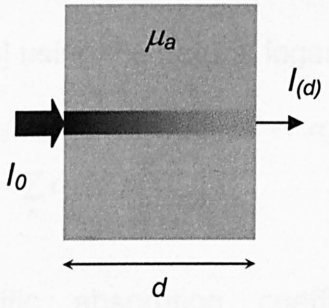

Figure 2.2 Attenuation of light through a non-scattering medium.

where μ_a is the absorption coefficient of medium [mm^{-1}] for a given wavelength λ, and it represents a probability per unit length of a photon being absorbed.

Other parameters are also defined from the ratio of the transmitted to incident intensity, such as the Transmittance *T*, which is usually what a spectroscopic instrument measures:

$$T = I_{(d)} / I_0 \qquad [2.3]$$

and Absorbance *A* (representing the loss in light intensity), which is usually measured in units of optical density (OD), and is given by equation [2.4].

$$A = log_{10}\left(1/T\right) = log_{10}\left(I_0/I_{(d)}\right) = k.d \qquad [2.4]$$

An equivalent absorbance relationship was developed by Beer in 1852 (equation [2.5]). It states that for an absorbing compound dissolved in a non-absorbing medium, the attenuation is proportional to the concentration of the compound in the solution *([C],* [molar]), the specific extinction coefficient of the compound (ε, [molar^{-1}.mm^{-1}]) and distance between the points where the light enters and leaves the solution (the optical pathlength *d*).

$$A = \varepsilon.[C].d = k.d = log_{10}\left(I_0/I_{(d)}\right) \qquad [2.5]$$

The equation [2.5] can be extended if the solution contains several different absorbing compounds, considering the contributions of each compound (for instance, components of blood like oxy and deoxy- haemoglobin, water, etc):

$$A(\lambda) = \varepsilon_1(\lambda).[C_1].d + \varepsilon_2(\lambda).[C_2].d + ...\varepsilon_n(\lambda).[C_n].d = \qquad [2.6]$$
$$= \sum_n \varepsilon_n(\lambda).[C_n].d$$

Rewriting the equation [2.6] using the natural logarithm base yields:

$$log_e\left(I_{(d)}/I_0\right) = \alpha_1(\lambda).[C_1].d + \alpha_2(\lambda).[C_2].d + ...\alpha_n(\lambda).[C_n].d \qquad [2.7]$$
$$= \sum_n \alpha_n(\lambda).[C_n].d$$

where α is the specific absorption coefficient of the compound ([molar^{-1}.mm^{-1}]). This differs from the specific extinction coefficient (ε) by a scaling factor equal to $log_e(10)$.

2.2.3 Scattering

Scattering is a physical process by which light interacts with matter to change its direction, so if the medium is scattering, the path taken by the photons are no longer direct (see section 2.6.1). Light scattering in tissue depends upon many variables including the size of the scattering particle, the wavelength of the light and the variation of the refractive indices of the various tissue components, such as cell membranes and organelles.

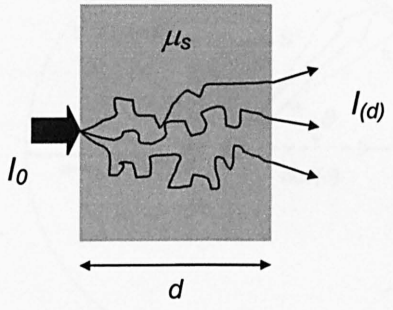

Figure 2.3 Attenuation of light through a scattering medium.

Elastic scattering (i.e. no loss of energy) can still give rise to attenuation of a light beam by deflecting photons from their initial path. In the same manner as for absorption, the final non-scattered intensity component of light $I_{(d)}$, transmitted through a medium of thickness d when illuminated by a source of intensity I_0 is described by:

$$I_{(d)} = I_0.e^{(-\mu_s.d)} \qquad [2.8]$$

where μ_s is the scattering coefficient of the medium [mm^{-1}] for a given wavelength λ, and represents a probability per unit of length of a photon being scattered.

2.2.4 Anisotropy and the Coefficient of Anisotropy *g*

The practical effect of scattering and absorption by a particle upon a parallel beam of light propagating in one given direction is that the beam intensity in this direction is reduced. Light which is absorbed is dissipated as thermal energy, and light which is scattered keeps its intensity but travels in another direction (Cope, 1991). Therefore, it is convenient to describe the angular

distribution of scattered light by defining an angular probability function of a photon to be scattered by an angle θ. If all scatter directions are equally probable, the scattering is isotropic. Otherwise, anisotropic scattering occurs. In elastic scattering, when a photon is scattered from its original direction ($\boldsymbol{s}$) by a particle, it emerges in a new direction ($\boldsymbol{s'}$), as shown in Figure 2.4. The angular probability of this change in direction is given by the phase function $p(\boldsymbol{s},\boldsymbol{s'})$ over its domain (solid angle Ω of 4π *steradians*).

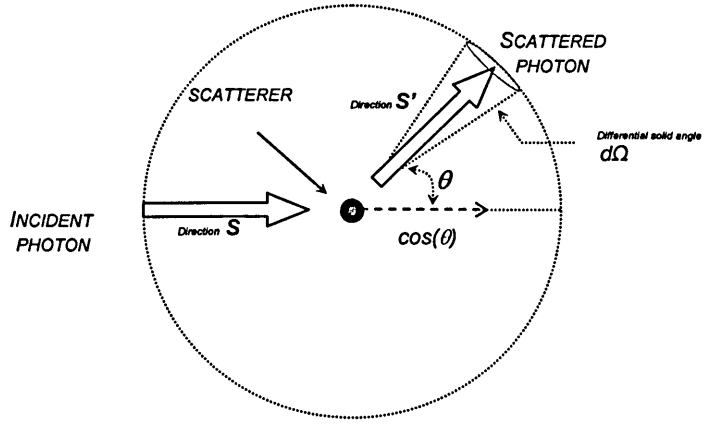

Figure 2.4 Elastic scattering event, based on (Vo-Dinh, 2003) (p2-7).

For a random medium that is isotropic in terms of its physical properties (refractive index, density), it can be assumed that this probability is independent of direction $\boldsymbol{s}$ and only depends on the angle between the incident and scattered directions θ. Thus, the phase function can be expressed as a function of the scalar product of the unit vectors in the initial and final directions, which is equal to the cosine of the scattering angle θ:

$$\boldsymbol{p(s,s')} = \boldsymbol{p(s.s')} = \boldsymbol{p}(cos(\theta)) \qquad [2.9]$$

A measure of the anisotropy of scattering is given by the coefficient of anisotropy g, which represents the average value of the cosine of the scattering angle. This can be expressed as:

$$g = \int_{-1}^{1} cos(\theta).p(cos(\theta)).d(cos(\theta)) \qquad [2.10]$$

The value of g approaching 1, 0, and -1 describe extremely forward, isotropic, and highly backward scattering respectively, and in biological tissue, g lies in the range $0.69 \leq g \leq 0.99$ (Cheong *et al*, 1990).

It is also convenient to express the characteristic scatter of tissue in terms of the transport scatter coefficient (μ_s'), which represents the effective equivalent number of isotropic scatters per unit of length, usually [mm^{-1}], and is used in the diffusion theory of light propagation in random media. Thus,

$$\mu_s' = \mu_s.(1-g) \qquad [2.11]$$

Finally, the total transport attenuation coefficient (μ_{total}) can be found:

$$\mu_{total\_transport} = \mu_s' + \mu_a = \mu_s.(1-g) + \mu_a \qquad [2.12]$$

2.3 Absorption characteristics of the main chromophores in tissue

The tissue compounds which absorb light in the spectral region of interest are known as chromophores. Each chromophore has its own particular absorption spectrum which describes the level of absorption at each wavelength. In the near-infrared range (NIR), known as *the absorption window* or *therapeutic window*, the major absorbing components in the soft tissues are water, oxyhaemoglobin and deoxyhaemoglobin. There are also minor contributions from other tissue chromophores, such as melanin, lipids, etc. The absorption spectra of some common chromophores are shown in figure 2.5.

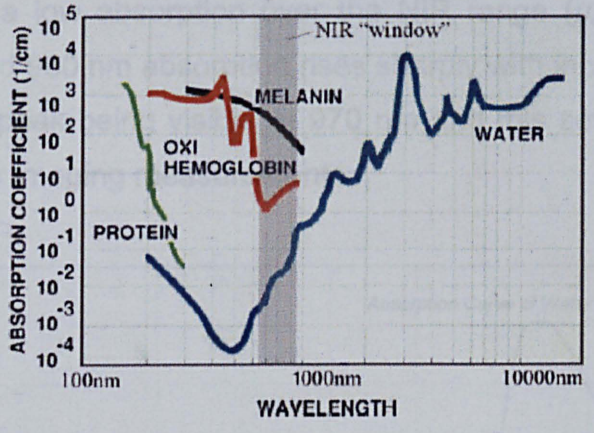

Figure 2.5 The absorption spectra for the main chromophores found within tissue.

At the shorter wavelength end, the window is bound by the absorption of haemoglobin (in both its oxygenated and deoxygenated forms). At the IR end of the window, penetration of light is limited by the absorption properties of water. Within the therapeutic window, scattering is dominant over absorption, and the propagation of light becomes diffuse (Niemz, 1999), (Elwell, 1995).

The concentration of water and melanin remains virtually constant with time (static absorbers). On the other hand, the concentrations of dynamic absorbers, such as oxygenated and deoxygenated haemoglobin (related with blood oxygenation), and cytochrome oxidase (an enzyme in the oxidative metabolic pathway that provides an indicator of tissue oxygenation and cell metabolism), provide clinically useful physiological information. However, the concentration of cytochrome oxidase in tissue is inferior when compared with haemoglobin (at least one order of magnitude below that of haemoglobin) (Elwell, 1995), (Cope and Delpy, 1988).

2.3.1 Water

The average water content of the neonatal brain is 90% (Cope, 1991) and in adult brain is about 80% of its weight (Woodard and White, 1986). Because of its high concentration in most biological tissue, water is considered to be one of the most important chromophores in tissue spectroscopy measurements. Nevertheless, for the purposes of most clinical measurements the water concentration in tissue can be thought of as constant, and as such water acts as a fixed constant absorber (Elwell, 1995). From figure 2.6, it can be seen that water has a low absorption over the NIR range (μ_a = 0.0022 mm^{-1} at 800 nm). Beyond 900 nm absorption rises sharply with increasing wavelength, with a spectral peak being visible at 970 nm and this sets an upper limit for spectroscopic or imaging measurements.

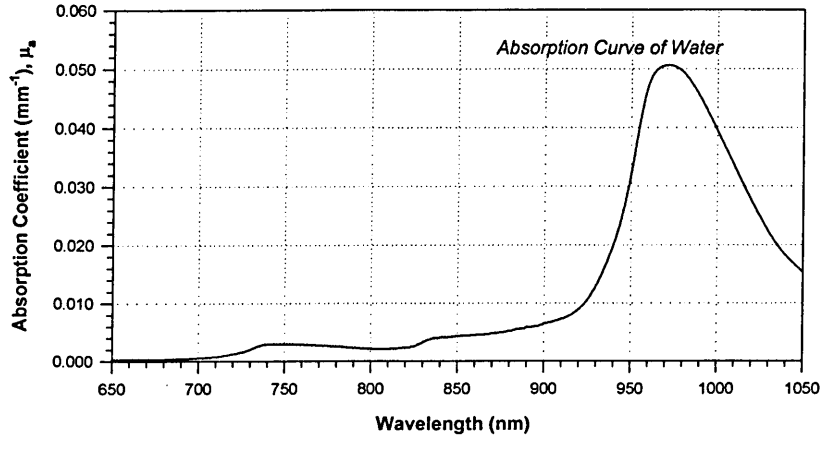

Figure 2.6 The Absorption spectrum for pure water at 37°C over the wavelength range from 650 –1050 nm (Matcher *et al,* 1993).

2.3.2 Lipids (fat)

The absorption spectrum of lipids is similar to that of water. However, its overall contribution to absorption is relatively small due to the low content of fat in the brain (about 5% of the total net weight of a newborn infant's brain) (Cope, 1991). The lipids are considered a fixed constant absorber with concentration normally unchanging during clinical measurements and so the measurements of changes in attenuation are not affected (Elwell, 1995). Figure 2.7 shows the absorption spectrum of pure pork fat between 650 nm and 1000 nm, which is thought to be similar to that of human lipids in muscle tissue (Conway *et al,* 1984).

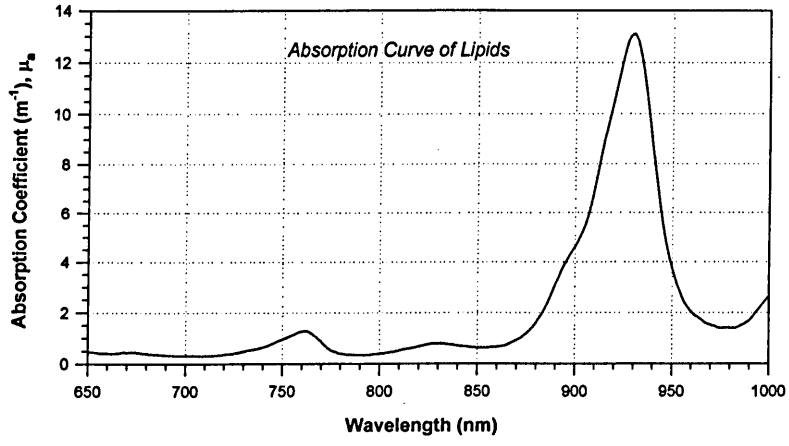

Figure 2.7 Spectrum of pork fat in the NIR from 650 to 1000 nm (van Veen *et al*, 2000).

2.3.3 Haemoglobin

The average composition by volume of blood is: 54% of plasma, 45% of red blood cells and 1% of white blood cells and platelets in the normal adult (Marieb and Hoehn, 2006). Haemoglobin molecules, which can be found within the red blood cells, carry 97% of the oxygen in the blood, while 3% is dissolved in the plasma. Each haemoglobin molecule consists of the four *haem* groups (iron atom at the centre of its structure, which has certain paramagnetic properties, see section 3.6) bound to the protein *globin* (figure 2.8) (Martini *et al*, 1998). Haemoglobin has an important role in the transport and delivering of oxygen from the lungs to tissues (oxyhaemoglobin), and carrying carbon dioxide from the tissue (deoxyhaemoglobin) back to the lungs.

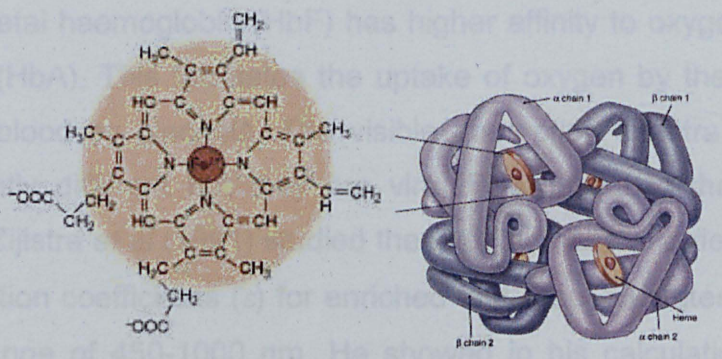

Figure 2.8 The structure of Haemoglobin, which consists of four globular protein subunits (α and β chains), and each subunit contains a single molecule of *haem*, a porphyrins ring surrounding a single ion of iron, (Martini *et al*, 1998) (p630).

The amount of haemoglobin in the blood determines how much oxygen the red blood cells are capable of carrying to other cells. The normal ranges for haemoglobin concentrations are (which change according age and sex) 14 to 20 grams per decilitre in infants, 13 to 18 g/dL in adult males, and 12 to 16 g/dL in adult females (Marieb and Hoehn, 2006). Haemoglobin molecules (Hb) in the red blood cells are responsible for almost all of the absorption of light by blood. However, the absorption spectrum of haemoglobin (figure 2.9) changes when oxygenation/de-oxygenation occurs. Oxygenated haemoglobin is a strong absorber up to 600 nm (sets a lower limit for spectroscopic or imaging measurements); then its absorption drops off very sharply and remains low. The absorption of deoxygenated haemoglobin, however, does not drop sharply; it stays relatively high, although it decreases with increasing wavelengths. The two absorption spectra cross around 800 nm (the isosbestic point, $\alpha_{HbO2} = \alpha_{Hb}$).

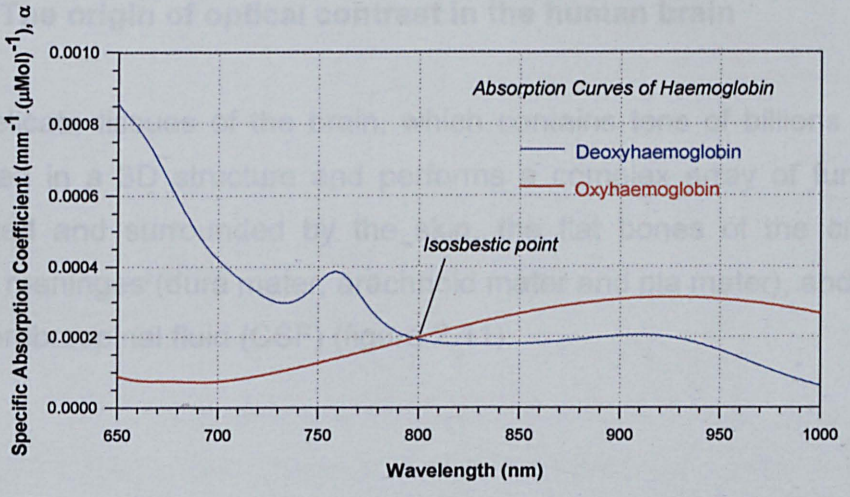

Figure 2.9 Specific absorption coefficients (α) of the states of haemoglobin (Cope, 1991).

In addition, foetal haemoglobin (HbF) has higher affinity to oxygen than adult haemoglobin (HbA). This facilitates the uptake of oxygen by the foetus from the mother's blood by placenta. The visible absorption spectra of HbF and HbA are slightly different but they are virtually identical in the NIR range (figure 2.10). Zijlstra *et al* (1991) studied these differences and determined the specific extinction coefficients (ε) for enriched and reduced states of HbF and HbA in the range of 450-1000 nm. He showed in his calculations of blood oxygen saturation (SO_2) that a method based on 2 wavelengths, such as pulse oximetry (660/940 nm), can result in an underestimation of SO_2 if HbF instead of HbA is being measured. However, the studies of Wickramasinghe *et al* (1993) have shown that adult Hb can be assumed for infants without introducing a significant error.

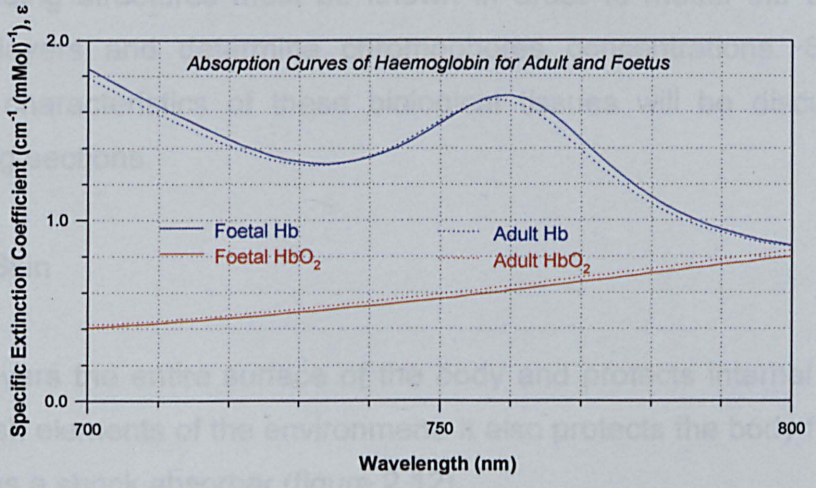

Figure 2.10 Spectra of adult and foetal absorption curve (Zijlstra *et al*, 1991).

2.4 The origin of optical contrast in the human brain

The delicate tissues of the brain, which contains tens of billions of neurons arranged in a 3D structure and performs a complex array of functions, are protected and surrounded by the skin, the flat bones of the cranium, the cranial meninges (dura mater, arachnoid mater and pia mater), and the watery fluid cerebrospinal fluid (CSF) (figure 2.11).

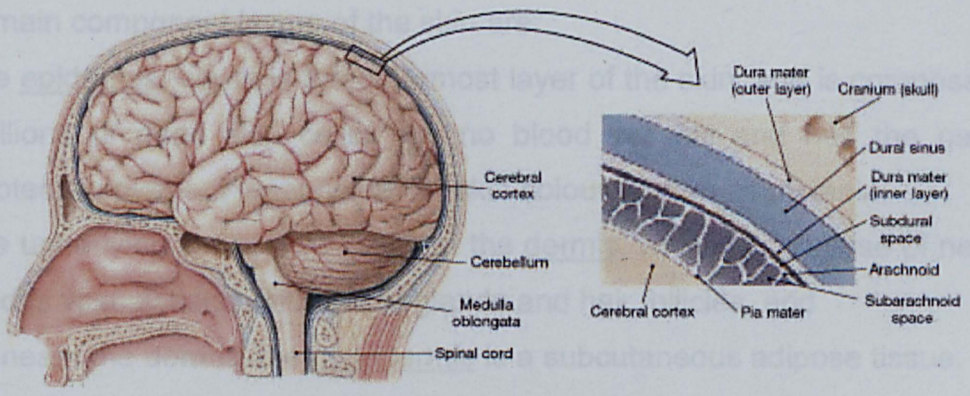

Figure 2.11 Human brain and surrounding structures (Martini *et al*, 1998) (p441).

In applications involving NIR spectroscopy of the brain, light must pass through the skull and surface tissues layers before entering and exiting the brain. Firbank *et al* (1993) stated the optical properties of these tissues and surrounding structures must be known in order to model the effects of the tissue layers and determine chromophores concentrations. Some of the optical characteristics of these biological tissues will be discussed in the following sections.

2.4.1 Skin

Skin covers the entire surface of the body and protects internal organs from the harsh elements of the environment. It also protects the body from injury by acting as a shock absorber (figure 2.12).

Figure 2.12 Skin and underlying subcutaneous tissue (Martini *et al*, 1998) (p199).

The main component layers of the skin are:

- the epidermis, which is the outermost layer of the skin, and is composed of millions of dead skin cells, has no blood vessels and has the natural protective pigment responsible for skin colour, known as melanin;
- the underlying connective tissue of the dermis, which is compose of nerves and is vascularised, with sweat glands and hair follicles, and
- beneath the dermis, the hypodermis is a subcutaneous adipose tissue.

Due to melanin in the epidermis layer, light is highly absorbed, as shown in table 2.1, and especially in the ultraviolet region (Elwell, 1995). Simpson *et al* (1998) concluded that transmission of light through the skin will be highly dependent on the pigmentation of the skin.

Table 2.1 Optical coefficients of human dermis, (Simpson *et al*, 1998).

SKIN LAYER		μ_a [mm^{-1}]	μ_s'[mm^{-1}]
DERMIS + EPIDERMIS	CAUCASIAN	0.033 ± 0.009	2.73 ± 0.54
HYPODERMIS	CAUCASIAN	0.013 ± 0.005	1.26 ± 0.34
DERMIS + EPIDERMIS	NEGROID	0.241 ± 0.153	3.21 ± 2.04

MEASUREMENTS REALIZED EX VIVO AT 663 nm.

It is noticeable from the values shown in table 2.1 that the attenuation of light by the skin is strongly dominated by scattering. Simpson *et al* (1998) also concluded that for both dermis and epidermis the transport scattering coefficient decreases monotonically, with increasing wavelength (i.e. a general decrease of scatter due to the size of the particle in comparison with the wavelength).

2.4.2 Bones & Skull

The skull grows and expands in proportion to the growth of the brain. At (term) birth, the majority of the bones of the skull are ossified (i.e. the bones have developed from dense connective tissue and cartilage). The areas where the bones join together are called sutures, and where they have not come together is covered by areas of fibrous connective tissue known as fontanelles (figure 2.13).

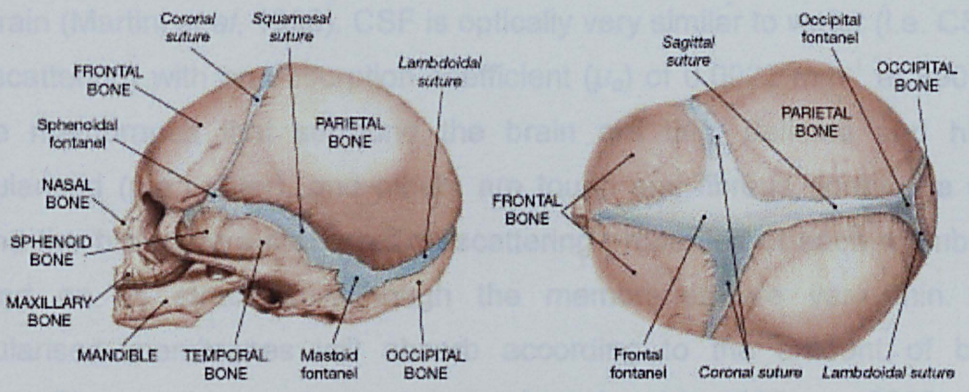

Figure 2.13 The skull of a term neonate, extracted from (Martini *et al*, 1998) (p211).

These connections are quite flexible enabling distortion without damage to the skull, and ease the passage of the infant through the birth canal. Damage could occur if pressure is applied to the head. In addition, the skull is a smooth bone, made up of two thin layers of compact bone (responsible for the skeleton's strength) compressing an irregular layer of spongy bone (made up of a network of tiny strands of bone called trabeculae), which contains red bone marrow (diploë) (figure 2.14).

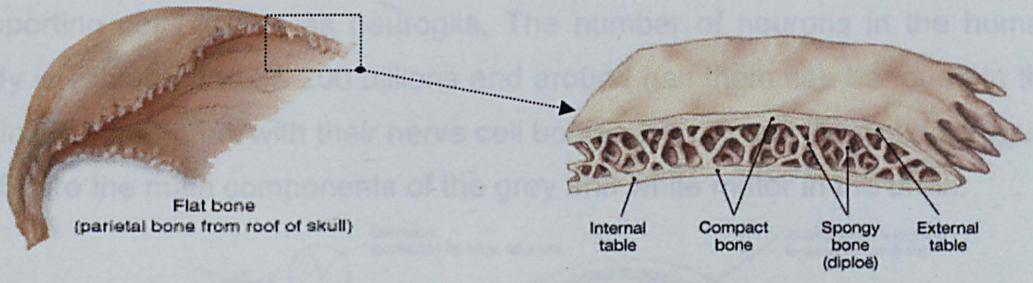

Figure 2.14 Cross section of flat bone of skull (Martini *et al*, 1998) (p170).

Firbank *et al* (1993) have studied the optical properties of adult skull in the wavelength range 650 to 950 nm, obtaining values of μ_a = 0.04 to 0.05 mm^{-1} and μ_s' = 2.7 to 1.3 mm^{-1}. The average value of g varied from 0.925 to 0.945. The presence of a small quantity of blood in bone has little effect on the overall absorption by the bone (Elwell, 1995).

2.4.3 Cerebrospinal fluid and membranes

Cerebrospinal fluid (CSF) and membranes surround the brain and much of the spinal cord. CSF circulates through the cerebral ventricles (internal structures in the brain, formed by four chambers), supporting, cushioning and sustaining

the brain (Martini *et al*, 1998). CSF is optically very similar to water (i.e. CSF is non-scattering) with an absorption coefficient (μ_a) of 0.0022 mm^{-1} at 800 nm. Some membranes that surround the brain are thin, delicate and highly vascularised (pia matter), and others are tough and fibrous, forming a sack around the brain (dura matter). The scattering properties of each membrane depend on its structure, although the membranes are very thin. The vascularised membranes will absorb according to the amount of blood present. The membranes themselves are low absorbing (Hillman, 2002). Very few models of light propagation in the adult and neonatal heads take into account the presence of CSF fluid and the surrounding membranes.

2.4.4 Characteristics of the human brain

2.4.4.1 Neurons and Cerebral cortex

Nerve tissue in the brain has two cell types: neurones (or nerve cells) and supporting cells knows as neuroglia. The number of neurons in the human body is estimated to be 200 billions and around half them can be found in the brain. The neurones with their nerve cell bodies (soma) and their axons (figure 2.15) are the main components of the grey and white mater in the brain.

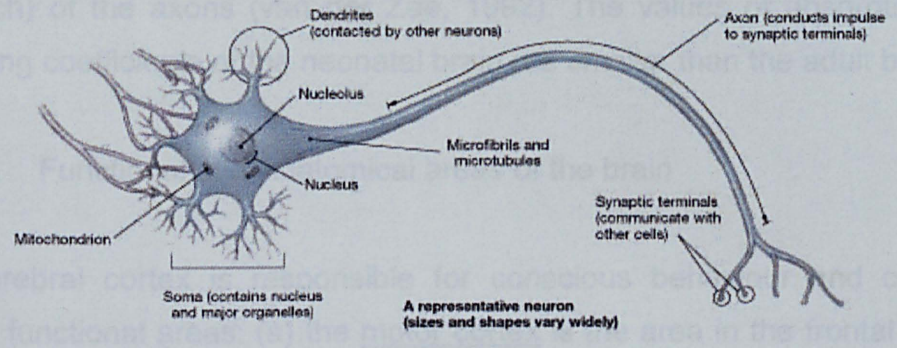

Figure 2.15 A neurone or nerve cell, extracted from (Martini *et al*, 1998) (p134).

The cerebral cortex constitutes a superficial layer of grey matter (high proportion of nerve cell bodies) and internally the white matter which is responsible for communication between axons. The white matter appears white because of the multiple layers formed by the myelin sheaths around the axons, which are the origin of the high, inhomogeneous and anisotropic scattering properties of brain (figure 2.16).

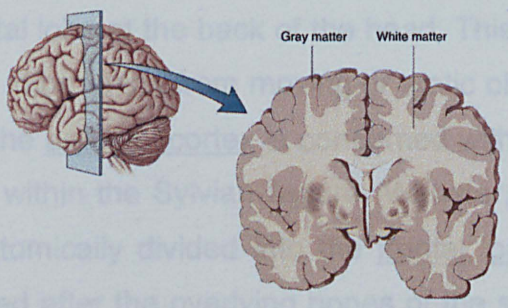

Figure 2.16 Representation of cross section of the adult brain, showing the grey and white matter.

Extracted from Rolfe (2000) and van der Zee (1992), table 2.2 shows values of optical properties of brain tissue for the adult and neonatal brain.

Table 2.2 Optical coefficients of human dermis, (Simpson *et al*, 1998).

PARAMETER	BRAIN TISSUE	ADULT BRAIN	NEONATAL BRAIN [40 WEEK GESTATION]
g	WHITE MATTER	0.957*	0.982*
	GREY MATTER	0.82*	0.978*
μ_a [mm^{-1}]	WHITE MATTER	0.0032 – 0.01	0.037 – 0.048
	GREY MATTER	0.032 – 0.038	0.033 – 0.05
μ_s'[mm^{-1}]	WHITE MATTER	9.26 – 7.78	1.2 – 0.85
	GREY MATTER	2.64 – 2	0.62 – 0.43

* VALUES AVERAGED OVER THE WAVELENGTH RANGE MEASUREMENTS REALIZED FROM [650 – 900 nm]

A comparison between values of the optical properties shows that white matter is more scattering than grey matter ($\mu_s'_{WHITE\ MATTER} >> \mu_s'_{GREY\ MATTER}$) for both adult and neonatal brain, due to the high refractive index of the myelin (lipid-rich) of the axons (van der Zee, 1992). The values of absorption and scattering coefficients of the neonatal brain are smaller than the adult brain.

2.4.4.2 Functional and Anatomical areas of the brain

The cerebral cortex is responsible for conscious behaviour and contains various functional areas: (a) the motor cortex is the area in the frontal lobe in charge of movement and the area on each side of the brain is in charge of the contralateral side of the body. Consequently activation of the right side of the body produces a response on the left side of the brain and vice-versa. The size of the area involved in the task depends on its complexity: the more complex the task, the bigger the area involved; (b) the somatosensory cortex is the region concerned with processing tactile and proprioceptive (position sense) information; (c) the visual cortex is in charge of processing visual data,

and lies in the occipital lobe at the back of the head. This is highly specialized for processing visual information from moving or static objects and for pattern recognition; and (d) the auditory cortex is concerned with the hearing and lies in the temporal lobe within the Sylvian fissure (Webster, 1992). The cerebral cortex is further anatomically divided into the frontal, parietal, occipital, and temporal lobes, named after the overlying bones of the skull and as shown in figure 2.17.

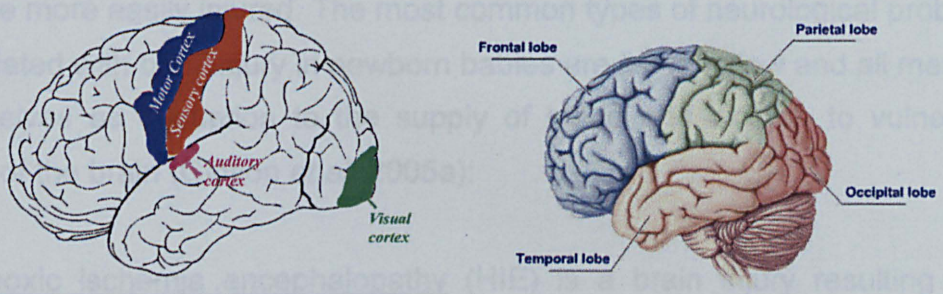

Figure 2.17 Representation of the functional regions where are located the motor, somatosensory, primary visual and auditory cortices (Webster, 1992) (p197), and the anatomically division of the brain (Marieb and Hoehn, 2006).

2.4.5 Summary

In the composition of biological tissue, static absorbers like water (and CSF), melanin, and lipids, have fixed concentrations, and their contributions to the overall attenuation are low within the therapeutic window. Although the CSF layer is non-scattering its presence has been shown to affect light propagation in the head (Okada and Delpy, 2003), (Okada *et al*, 1997), and it is sometimes considered together with its surrounding membranes in light propagation models (Fukui *et al*, 2003). However, the principal interaction of interest occurs when light strikes a blood vessel. The light is absorbed by the dynamic absorbers: oxyhaemoglobin (HbO_2) and deoxyhaemoglobin (Hb). Changes in the intensity of the incoming light can be converted into changes in concentrations of oxyhaemoglobin and deoxyhaemoglobin, which can be used to provide information on blood oxygenation status. Also, indirect information can be gained from the different optical properties of the tissues, which are the basis of several potential clinical applications, such as cerebral imaging modality for mapping oxygenation and haemodynamics in the brain of newborn infants or cortical functional activity in adults, (Hebden, 2003).

2.5 Optical monitoring of the brain injury in infants

2.5.1 Brain Injury during birth

Occasionally during the birth process, the baby may suffer a physical injury that is simply the result of being born. This is sometimes called birth trauma or birth injury. Premature babies (< 37 weeks of gestation) are more fragile and may be more easily injured. The most common types of neurological problems associated with birth injury in newborn babies are listed below and all manifest themselves as disruption to the supply of blood and oxygen to vulnerable areas of the brain (Gibson *et al*, 2005a):

I. Hypoxic ischemia encephalopathy (HIE) is a brain injury resulting from (perinatal) asphyxia, and is one of the most commonly recognized causes of severe, long-term neurological deficits in children, due to impaired CBF (Shalak and Perlman, 2004). When the infant newborn brain is subject to the asphyxia, its circulation becomes vasodilated with an increase of cerebral blood volume (CBV) (Meek, 2002), (Meek *et al*, 1999 a), (Wyatt, 1993).

II. Periventricular leukomalacia (PVL) is the damage and softening of the white matter around the ventricles (with subsequent cyst formation) due to an incomplete state of development of the vascular supply and impairment in regulation of cerebral blood flow (CBF) (Volpe, 2001). Studies in preterm infants during the first 3 days of their life demonstrated an increased risk of development of both IVH and PVL due to a low level of CBF (normal response to extrauterine life) (Meek, 2002), (Meek *et al*, 1999 a).

III. Intraventricular haemorrhage (IVH) is a bleeding inside or around the ventricles due to damage of capillaries occurring during periods of fluctuation in blood pressure, which are common during birth (Gibson *et al*, 2005a), (Whitelaw, 2001). The amount of bleeding varies and it is often described in four grades: grades I (bleeding occurs just in a small area of the ventricles) and II (bleeding also occurs inside the ventricles) are most common, and grades III (ventricles are enlarged by the blood) and IV (bleeding into the brain tissues around the ventricles) are the most serious and may result in long-term brain injury to the baby (figure 2.18).

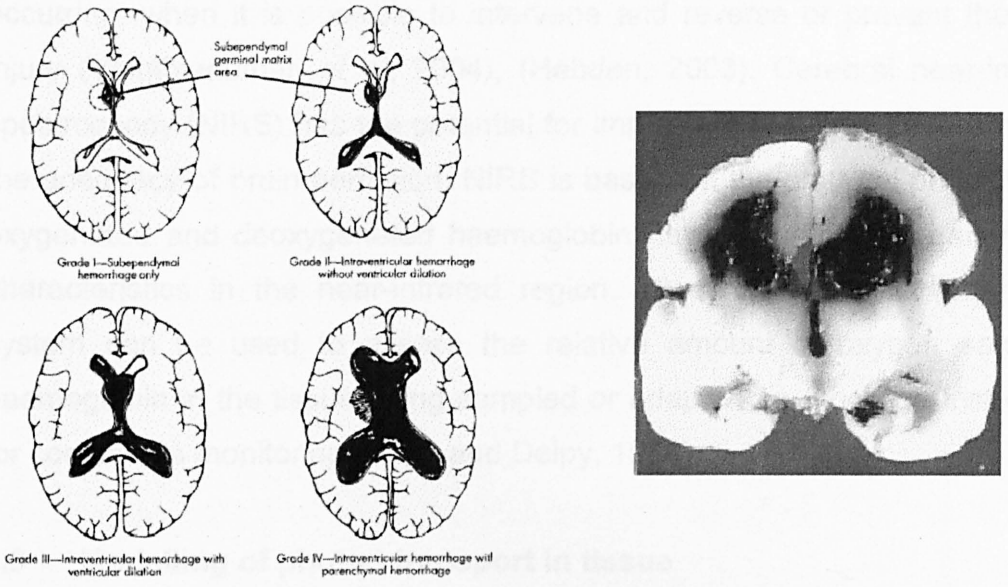

Figure 2.18 LEFT: Periventricular - intraventricular haemorrhage grades. Extracted from (Merestein *et al*, 1998) (p599), and RIGHT: Massive intraventricular haemorrhage, without distension of the ventricles (Whitelaw, 2001).

2.5.2 Monitoring brain injury

Currently, birth injuries have been diagnosed clinically by cranial ultrasound (US- which gives only anatomical information), computerised tomography (CT- rarely used on newborns because of the ionizing radiation and limited due to high water content in the preterm infant brain (Halliday *et al*, 1998)), and MRI (which is often not appropriate due to the fragile state of the infant and the reluctance to transport the infant out of an intensive care unit) (Gibson *et al*, 2005a). Other techniques such as electroencephalography (EEG), magnetoencephalography (MEG), PET, and fMRI can be used to non-invasively investigate cerebral function. Although these techniques are widely used clinically, the instruments are expensive (with the exception of EEG), require specially trained technical staff to operate, and patients have to be moved from their controlled environment and taken to specially constructed rooms where the investigation is carried out. In the case of PET, patients have to be injected with radioisotopes, which is not appropriate for multiple repeated studies. All of these factors make these imaging methods unsuitable for imaging cerebral function in babies in real time, especially if they are being cared for in an intensive care unit. It is desirable to have a clinical test that would allow detection of potential brain injury before it occurs or as it is

occurring, when it is possible to intervene and reverse or prevent the brain injury (Vainthianathan *et al*, 2004), (Hebden, 2003). Cerebral near-infrared spectroscopy (NIRS) has the potential for immediate real-time assessment of the adequacy of brain perfusion. NIRS is based on the physical principle that oxygenated and deoxygenated haemoglobin have different light-transmitting characteristics in the near-infrared region. Thus, a light-emitting/detecting system can be used to assess the relative amount of oxygen saturated haemoglobin in the tissue being sampled or adapted as a cotside instrument for continuous monitoring (Cope and Delpy, 1988).

2.6 Modelling of photon transport in tissue

An understanding of the propagation of light in tissue enables optical techniques, such as NIR spectroscopy to yield quantitative information about tissue oxygenation and haemodynamics, and NIR imaging to produce surface maps of the cortex activation or volume images of spatial/temporal changes in *[HbO_2]*, *[Hb]* and *[total Hb]* in the infant brain.

2.6.1 Modified Beer-Lambert Law (MBLL)

Scattering causes light to travel extra distance in tissue, increasing the probability of photon absorption. The differential pathlength *DP*, the real optical pathlength, can be obtained from the differential pathlength factor *DPF*, given by:

$$DP = DPF.d \qquad [2.13]$$

where the geometrical distance between the source and detector is *d*. The differential pathlength factor or scaling factor will depend on the number of scattering events that occur. The *DPF* will in practise be a function of the scattering coefficient (it will increase with increasing μ_s), the anisotropy *g*, the absorption coefficient (it will decrease with increasing μ_a), and the geometry of the medium. It must be included in the Beer-Lambert law to describe attenuation in a scattering medium (Matcher *et al*, 1993). The *DPF* can be considered approximately constant for a given tissue, since the measured

difference in attenuation is small compared with the large constant background attenuation in tissue (Elwell, 1995). It is also necessary to introduce an additive term *G* due to the scattering losses. Thus,

$$I_{(d)} = I_0.e^{(-\mu_a.DPF.d+G)} \quad [2.14]$$

This is known as the modified Beer-Lambert Law. *G* is dependent on the measurement geometry and the scattering coefficient of the tissue under study and is largely unknown. Consequently, spectroscopic measurements generally assume that *G* is constant during the measurement period and attempt to quantify changes in the absorption instead of absolute values:

$$\Delta A_{21} = A_2 - A_1 = log_e\left(I_1/I_2\right) = DPF.d.\Delta\mu_{21} = \quad [2.15]$$
$$A_2 - A_1 = DPF.d.\alpha(\lambda).\Delta[C]_{21}$$

The differences in attenuation measured between two oxygenation states is given by ΔA_{21} corresponding to an absorption change of $\Delta\mu_{a21}$. The *DPF* can be measured by two methods: intensity modulated optical spectroscopy (see section 3.10.2) or time of flight (see section 3.10.3). According to Duncan *et al* (1995), the values of the differential pathlength factor are 4.99 (± 9%) for infant head and 6.26 (± 14.1%) for adult head at 807 nm.

2.6.1.1 Determination of the blood oxygenation status with NIR light

The parameter which establishes the degree of the oxygenation of blood is the oxygen saturation (SO_2) and it is calculated using the absolute values of concentration and is given by:

$$SO_2[\%] = \frac{[HbO_2]}{[HbO_2]+[Hb]}.100 \quad [2.16]$$

Considering the contribution of oxy and deoxy-haemoglobin (equation [2.7]), it is possible to determine the absorption coefficient of blood at two different λ's as follows:

$$\mu_{\lambda 1} = \alpha_{HbO_2}(\lambda_1).[HbO_2] + \alpha_{Hb}(\lambda_1).[Hb] \quad [2.17]$$

$$\mu_{\lambda 2} = \alpha_{HbO_2}(\lambda_2).[HbO_2] + \alpha_{Hb}(\lambda_2).[Hb] \quad [2.18]$$

By solving the simultaneous equations [2.16], [2.17] and [2.18], it is possible to obtain the oxygen saturation as shown in equation [2.19].

$$SO_2[\%] = \frac{\alpha_{Hb}(\lambda_1).\mu_{\lambda_2} - \alpha_{Hb}(\lambda_2).\mu_{\lambda_1}}{\alpha_{Hb}(\lambda_1).\mu_{\lambda_2} - \alpha_{Hb}(\lambda_2).\mu_{\lambda_1} + \alpha_{HbO_2}(\lambda_2).\mu_{\lambda 1} - \alpha_{HbO_2}(\lambda_1).\mu_{\lambda_2}}.100 \quad [2.19]$$

Figure 2.9 provides the values of α_{HbO2}, α_{Hb} for any two wavelengths in the NIR range, so by measuring the $\mu_{\lambda 1}$ and $\mu_{\lambda 2}$, the oxygen saturation can be determined by using equation [2.19]. SO_2 is directly related to the supply of blood and usage by the tissue, and indicates its functional activity. For instance, non-invasive measurement of SO_2 is a common bedside procedure in hospitals. It is performed continuously, safely and instantaneously by pulse oximeters. The measurements are typically made on fingers and/or ear lobes. A two-wavelength method is used to quantify changes in light attenuation during the systolic phase of blood flow in tissue, which are converted to levels of oxygen blood saturation. For more details about pulse oximetry see Mendelson (1992).

2.6.1.2 Determination of the chromophores concentrations

Because the two forms of haemoglobin have different absorption spectra in the NIR range, it is possible to measure the relative concentration of oxyhaemoglobin ($[HbO_2]$) and deoxyhaemoglobin ($[Hb]$) using measurements at two wavelengths (λ_1,λ_2) of the differences in attenuation or absorption ($\Delta A(\lambda_1),\Delta A(\lambda_2)$). If just the contribution of two chromophores is considered, the equations [2.7] and [2.15] can be written as follows:

$$\Delta A(\lambda_1) = DPF(\lambda_1).d.\left(\alpha_{HbO_2}(\lambda_1).\Delta[HbO_2] + \alpha_{Hb}(\lambda_1).\Delta[Hb]\right) \quad [2.20]$$

$$\Delta A(\lambda_2) = DPF(\lambda_2).d.\left(\alpha_{HbO_2}(\lambda_2).\Delta[HbO_2] + \alpha_{Hb}(\lambda_2).\Delta[Hb]\right) \quad [2.21]$$

In order to determine the changes in concentrations of the two states of oxygenation, the equations [2.22] and [2.23] are rearranged. These values can describe how well the blood is oxygenated.

$$\Delta[HbO_2] = \frac{\alpha_{HbO_2}(\lambda_2).\frac{\Delta A(\lambda_1)}{DPF(\lambda_1)} - \alpha_{HbO_2}(\lambda_1).\frac{\Delta A(\lambda_2)}{DPF(\lambda_2)}}{(\alpha_{Hb}(\lambda_1).\alpha_{HbO_2}(\lambda_2) - \alpha_{Hb}(\lambda_2).\alpha_{HbO_2}(\lambda_1)).d} \quad [2.22]$$

$$\Delta[Hb] = \frac{\alpha_{Hb}(\lambda_1).\frac{\Delta A(\lambda_2)}{DPF(\lambda_2)} - \alpha_{Hb}(\lambda_2).\frac{\Delta A(\lambda_1)}{DPF(\lambda_1)}}{(\alpha_{Hb}(\lambda_1).\alpha_{HbO_2}(\lambda_2) - \alpha_{Hb}(\lambda_2).\alpha_{HbO_2}(\lambda_1)).d} \quad [2.23]$$

2.6.2 The Radiative Transfer Equation (RTE)

In the RTE approach light is treated as composed of distinct particles (photons) propagating through a medium. The model is restricted to interactions between light particles themselves and is derived by considering changes in energy flow due to incoming, outgoing, absorbed and emitted photons within an infinitesimal volume *dV* in the medium (energy balance). The model considers a small packet of light energy defined by its position *r*, direction of propagation $\hat{s}$, over a time interval *dt*, and with propagation speed *c* (figure 2.19).

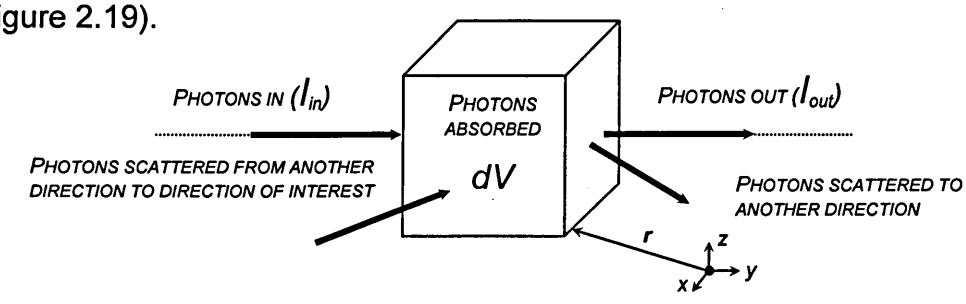

Figure 2.19 Model for RTE

The change in energy radiance $I(r,t,\hat{s})$ is equal to the loss in energy due to absorption and scattering out of $\hat{s}$, plus the gains in energy from light scattered into the $\hat{s}$-directed packet from other directions and from any local source of the light at *r*. This energy balance is represented by the individual terms in the RTE:

$$\frac{1}{c}\frac{\partial I(r,t,\hat{s})}{\partial t} + \hat{s} \bullet \nabla I(r,t,\hat{s}) = \quad [2.24]$$
$$= -[(\mu_a + \mu_s').I(r,t,\hat{s})] + \mu_s' \int_{4\pi} p(\hat{s},\hat{s}').I(r,t,\hat{s}').d^2\hat{s}' + q(r,t,\hat{s})$$

Each term in equation [2.24] represents in time domain:

$\frac{1}{c}\frac{\partial I(r,t,\hat{s})}{\partial t} + \hat{s} \bullet \nabla I(r,t,\hat{s})$	The difference between the number of photons entering the volume and the number of photons leaving it per unit time	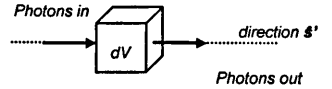
$(\mu_a + \mu_s').I(r,t,\hat{s})$	The attenuation given to light due to absorption and scattering	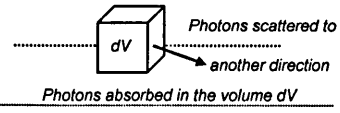
$\mu_s' \int_{4\pi} p(\hat{s},\hat{s}').I(r,t,\hat{s}').d^2\hat{s}'$	The increase in the light due to scatter from all directions to final direction $\hat{s}'$	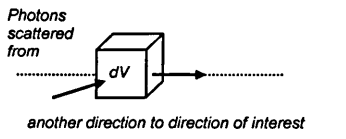
$q(r,t,\hat{s})$	Local sources [W/m^3/sr] (for instance, fluorescence)	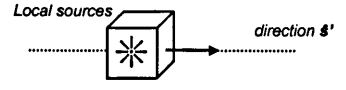

Two important parameters are $\Phi(r,t)$ which represents photon density or diffuse photon fluence (inside the element), and $J(r,t)$ which is the photon flux or current (at its boundary). The latter is a measurable parameter and allows equation [2.24] to be solved for μ_s' and μ_a, respectively (Kaltenbach and Kaschke, 1993).

$$\Phi(r,t) = \int_{4\pi} I(r,t,\hat{s}').d\hat{s}' \qquad [2.25]$$

$$J(r,t) = \int_{4\pi} \hat{s}.I(r,t,\hat{s}').d\hat{s}' \qquad [2.26]$$

Exact solutions for the RTE exist for simple cases such as isotropic scattering in simple geometries. A more in-depth treatment of the subject is given in the review papers by (Arridge and Hebden, 1997) and (Patterson *et al*, 1991).

2.6.2.1 The diffusion approximation to the RTE

Three variables in the RTE depend on direction $\hat{s}$: the radiance $I(r,t,\hat{s})$, the phase function $p(\hat{s},\hat{s}')$ and the source term $q(r,t,\hat{s})$. If these are expanded into spherical harmonics, an infinite series of equations which approximate to the RTE is obtained. The P_N approximation is obtained by taking the first N spherical harmonics, of which the simplest is the time-dependent P_1 approximation. If the following assumptions are made: (a) scatter is the dominant interaction: $\mu_s' >> \mu_a$, (b) phase function $p(\hat{s},\hat{s}')$ is independent of the

absolute angle, (c) photon flux $J(r,t)$ changes slowly $dJ(r,t)/dt = 0$ and (d) all sources are isotropic, the result is the time-dependent **Diffusion equation**:

$$\frac{1}{c}\frac{\partial \Phi(r,t)}{\partial t} - \nabla \bullet \kappa(r)\nabla\Phi(r,t) + \mu_a(r)\Phi(r,t) = q(r,t) \qquad [2.27]$$

where:

$$J(r,t) = -\kappa(r)\nabla\Phi(r,t) \qquad (1^{st}\text{ Fick's Law}) \qquad [2.28]$$

$\kappa(r)$ is the diffusion coefficient defined as:

$$\kappa(r) = \frac{1}{3.[\mu_a(r) + \mu_s'(r)]} \qquad [2.29]$$

The diffusion equation [2.27] has been widely used to model light transport in tissue, although it is necessary to assume that light propagates diffusively (which is generally the case in bulk tissue), and the source and detector are separated in space and time, to ensure that the light is diffuse when it reaches the detector. By contrast, these assumptions generally do not hold near the source, near the surface and internal boundaries and in anisotropic tissues, and in regions of either high absorption or low scatter (voids regions, such as the ventricles and CSF). For these cases, higher order approximations to the RTE may be required (Gibson *et al*, 2005a), and models which incorporate void regions within a diffusing model (Riley *et al*, 2000).

2.6.2.1.1 Green's functions

A general method for solving partial differential equations (PDE) such as the diffusion equation is the application of Green's functions, where the source term $q(r,t)$ consists of an infinitely short pulse or δ-function (any other source can be obtained by convolution (Arridge *et al*, 1992)). An example of analytical solution was developed by Patterson *et al* (1989) for a homogeneous slab where boundaries are described using the so-called method of images. This yields time-resolved reflectance and transmittance equations, and least-squared fitting to experimental data allows the optical coefficients to be determined. For instance, during the determination of the optical properties of a liquid slab of intralipid solution (mixture used for reference phantoms, see section 5.2.2.2), a rectangular transparent receptacle is filled with the

homogenous solution (nominal properties of the mixture are $\mu_s' = 1\ mm^{-1}$, $\mu_a = 0.01\ mm^{-1}$). A connector for a light source is attached on one of the faces, and another for a detector is attached on the opposite face. Both connectors are at the same height and located in the middle of each face. A representation of the experiment is shown in figure 2.20. A short pulse from a laser source (see section 4.2.1) is applied and the time-resolved transmitted intensity across the solution is detected (50 mm of thickness). The values of the absorption and scattering coefficients are obtained from the temporal distribution of transmitted light due by fitting with the corresponding Green function (figure 2.20). For more details see (Patterson *et al*, 1989).

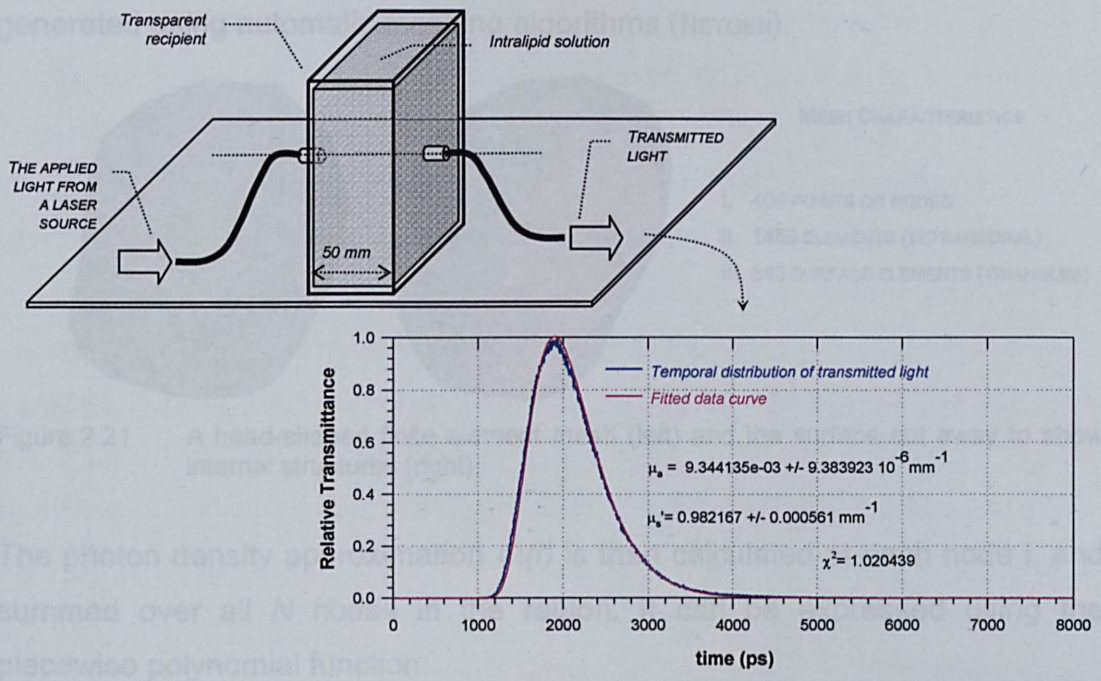

Figure 2.20 TOP: A measured transmittance signal and the correspondent fitted curve, BOTTOM: A measured transmittance signal and the correspondent fitted curve.

Other analytical solutions for simple geometries, such as spheres and cylinders, as well as the frequency domain equivalents of the equations, are given in (Arridge *et al*, 1992). For more complex geometries, the solutions are solved numerically.

2.6.2.1.2 Finite element method (FEM)

The finite element method can be applied in order to solve numerically the partial differential equations (such as diffusion equation) for arbitrary and

complex geometries. Arridge *et al* (1993) stated that FEM can be applied anywhere where a differential equation formulation is available for the transport model. The method involves dividing a region of interest (or domain) into a finite number of volume or area elements. The boundary of one element consists of discrete points called nodes (or connecting points). Surface domains may be subdivided into triangles and volumes may be subdivided into tetrahedral (polyhedrons) shapes. Each element has its individual set of optical properties (μ_a and μ_s'). The shape and distribution of the elements is ideally defined by automatic meshing algorithms (e.g. NETGEN developed by Schöberl, (1997)). Figure 2.21 shows a finite element (volume) mesh generated using automatic meshing algorithms (NETGEN).

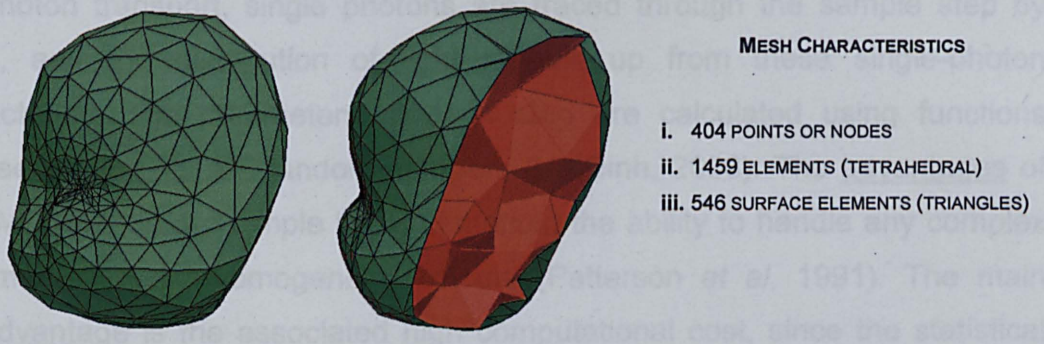

Figure 2.21 A head-shaped finite element mesh (left) and the surface cut away to show internal structures (right).

The photon density approximation $\Phi_i(t)$ is then calculated at each node i, and summed over all N nodes in the region. It can be expressed using the piecewise polynomial function:

$$\Phi^h(r,t) = \sum_i^N \Phi_i(t) u_i(r) \qquad [2.30]$$

The h superscript denotes the iterative process that is calculated at the nodes and which provides an approximate solution for photon density $\Phi(t)$. The $u_i(r)$ is a basis function and it describes the way that the function $\Phi_i(t)$ is allowed to vary over an element (between nodes). Its simplest form is to be a constant, although a variety of basis functions can be used (Arridge and Schweiger, 1993). The advantages of this method are its computational speed, the high flexibility (as for the Monte Carlo method) when applied to complex geometries and it can model photon density and flux everywhere. The

disadvantages are that there is no means of deriving individual photon histories and it is subject to the same limitations as the diffusion equation (Arridge *et al*, 1993).

2.6.2.2 The Monte Carlo Method

Many problems of practical interest often involve a range of light sources, multiple tissues types, and complex geometries. Analytical solutions for realistic scenarios are complicated, even when possible. These more realistic cases are instead solved with numerical techniques. For RTE problems, the most widely used approach is the Monte Carlo (MC) method. In this approach to photon transport, single photons are traced through the sample step by step, and the distribution of light is built up from these single-photon trajectories. The parameters of each step are calculated using functions whose arguments are random numbers (Vo-Dinh, 2003). The advantages of the MC method are simple implementation, the ability to handle any complex geometries and inhomogeneous media (Patterson *et al*, 1991). The main disadvantage is the associated high computational cost, since the statistical accuracy of results is proportional to [number of traced photons]^{½}. As the numbers of photons in the simulation grows toward infinity, the MC prediction for the light distribution approaches an exact solution of the RTE (Niemz, 1999). A MC simulation of absorption and scattering has 5 main steps: source photon generation, pathway generation, absorption, elimination, and detection.

2.6.3 Optical image reconstruction

Optical image reconstruction involves deducing the internal distribution of μ_a and μ_s' that correspond to a set of measurements recorded. The process applied to optical tomography involves the solution of the forward and the inverse problems. The forward problem is to predict the distribution of light y in the object under examination. This uses a model of photon migration in the object to generate a sensitivity matrix J (or forward operator) which relates the

distribution of light on the boundary of the object with its internal properties x, as shown in equation [2.31].

$$y = J.x \qquad [2.31]$$

The forward problem can generate model data for comparison with experimental data or to test reconstruction techniques. The distribution of light y can be determined with previous knowledge of the geometry of the object, the location of the sources and detectors, and background parameters. In a similar way, in the inverse problem an image (2D or 3D) of the internal properties of the object can be recovered from the distribution of measurements on the boundary y by inverting the forward operator J, as shown in equation [2.32].

$$x = J^{-1}.y \qquad [2.32]$$

However, this inversion is ill posed (the solution may not be unique) and is generally highly underdetermined (the number of unknowns exceeds the amount of data), and does not yield to straightforward analytical methods (Arridge and Hebden, 1997). Image reconstruction methods can be categorised as either linear and or non-linear.

2.6.3.1 Linear reconstruction

The linear reconstruction method is the simplest way to recover an optical image. This involves considering changes in the optical properties $\Delta x = (x\text{-}x_0)$, and corresponding changes in the measured data $\Delta y = (y\text{-}y_0)$. By expanding equation in terms of the Taylor series yields:

$$y = y_0 + F'(x_0)(x - x_0) + F''(x - x_0)^2 + \ldots \qquad [2.33]$$

where F', F'' ... are the first derivative, second derivative and so on. In the case of difference imaging, which is usually employed (see section 4.2.7.5), the changes in the optical properties Δx are small, and equation [2.33] can be linearized, yielding:

$$\Delta y = J.\Delta x \qquad [2.34]$$

As described earlier, the image reconstruction consists of the product of the inversion of the forward operator J and the change in measurements or difference between two states (Δy):

$$\Delta x = J^{-1}.\Delta y \qquad [2.35]$$

There are several techniques to invert a matrix; one of the most common is the Tikhonov regularisation of the Moore-Penrose generalised inverse method:

$$\Delta x = J^{T}(J.J^{T} + \lambda.I)^{-1}.\Delta y \qquad [2.36]$$

where the parameter of regularisation λ is typically ~0.01 and I is the identity matrix. An advantage of linear reconstruction is that it does not require a good forward model for good results to be achieved, although this method can only reconstruct small changes in the optical properties, otherwise the reconstruction will probably fail, especially if the reference phantom has optical properties that are not close to those of the tissue analized. For more details see (Gibson *et al*, 2005a) and (Gibson *et al*, 2005b).

2.6.3.2 Non-linear reconstruction

Non-linear reconstruction is a method where the difference between the values calculated by a forward model and the experimental data is used to update the sensitivity matrix J of the model and to minimise this difference between the estimated and the measured data. The *image reconstruction package* developed at UCL, known as TOAST (Temporal Optical Absorption and Scattering Tomography) is a software for image reconstruction in diffuse optical tomography, which involves:

- a forward solver, a finite element model (FEM) to simulate the light transport in tissue (scattering medium), which has the flexibility to handle complex geometries (essential for imaging a real infant's brain); and
- an iterative inverse solver, a non-linear reconstruction algorithm which compares the measured TPSF data and the data generated by the FEM model (forward solver), acting iteratively on the trial solution. Once the

difference is below a set limit, the generated model is considered a good approximation with the true tissue optical properties.

A more detailed description of the method of reconstruction and the main theoretical principles involved in TOAST are given elsewhere (Arridge, 1999), (Arridge, 1993).

Chapter 3

Techniques for Brain Imaging

3.1 Introduction

Modern imaging methods provide the opportunity for non-invasive *in vivo* study of human organs and can provide measurements of local neuronal activity of the living human brain. These imaging modalities can be divided into two global categories (Fantini *et al*, 2001):

- Functional imaging represents a range of measurement techniques in which the aim is to extract quantitative information about physiological function from image-based data. Although high-resolution images are desirable, the emphasis is on the extraction of physiological parameters rather than the visual interpretation of the images. Functional modalities include SPECT and PET (known as nuclear medicine imaging modalities), and fMRI. EEG, MEG, Electrical Impedance Tomography (EIT) can also be named as a functional imaging technique.
- Structural imaging represents a range of measurement techniques which can display anatomical information. These modalities include X-ray, CT, MRI, and US.

3.2 Electroencephalography (EEG)

Electroencephalography is a non-invasive technique that detects electrical impulses in the brain due to neuronal activity using electrodes placed on the patient's scalp (EEG cap). The recording of conventional EEG traces represents changes in electrical activity in the order of tens of milliseconds, and are used to monitor responsiveness, coma and brain death; locate areas of damage following head injury; and investigate epilepsy (Teplan, 2002), although it is usually necessary for a trained neurologist to perform the analysis (Law et al, 1991). The spatial resolution of the EEG techniques is limited due to layers of CSF, skull, and scalp between the electrodes and the current source in the brain. Consequently, the electrical potential distribution on the scalp is blurred and it is difficult to determine the location of regions of electrically activity. To enhance the electrical source location, various

techniques are performed: (i) to increase the numbers of channels, (ii) to apply a second derivative of the scalp potential (surface Laplacian) for emphasizing the differences in the topography potential, and (iii) to apply a finite element head model containing prior anatomical information derived from MRI, which is used to reduce the distortion of the EEG signals (due to the tissues head layers). This provides a numerical estimate of the electrical potentials near the cortex surface (Srinivasan, 1999), (Gevins, 1998). This is known as high resolution EEG, and it has been used as a tool in the study of cortical activation during external stimulation and cognitive studies. Figure 3.1 illustrates the topographic mapping obtained from somatosensory cortex activation and the enhancement obtained when the numbers of channels is increased (Gevins, 1998).

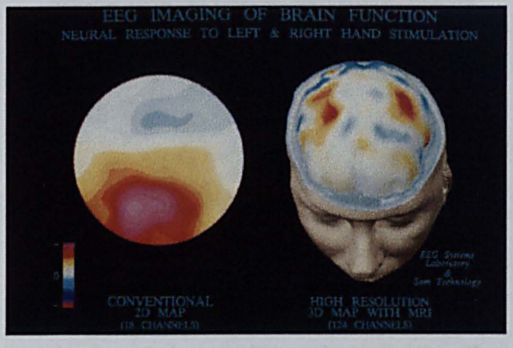

Figure 3.1 Activation mapping of left middle and right index fingers (adult) using 18 channels (nose at the top) and 124 channels and deblurring (Gevins, 1998).

3.3 Magnetoencephalography (MEG)

Magnetoencephalography is a non-invasive technique that records magnetic flux changes over the surface of the head (~10^{-15} Tesla) from synaptic discharge tangential currents due to the activity of neurons. MEG measurements are carried out in magnetically shielded rooms, using sensitive super-conducting quantum interference devices (SQUIDS) to detect these tiny magnetic fields. The MEG sensor consists of a flux transformer coupled to a SQUID, which considerably amplifies the weak extra cranial magnetic field and converts it into a voltage. During studies, the subject sits or lies with their head inside a sensor helmet. The whole head device has 64 – 304 sensors (Paetau, 2002). Because the sensors are placed over the head, but not

necessary touching it, the technique may be used on people with open head injuries (Fenwick, 1987). MEG provides a sub-millisecond temporal resolution with a spatial resolution of a few millimetres. Its drawback is that it gives no anatomical information and the head has to be kept immobile with respect to the helmet, preventing long-term recording. Most MEG studies have been conducted on adult subjects, but some MEG data already exists on children, especially those undergoing presurgical evaluation for epilepsy surgery (Paetau, 2002). Some MEG systems are adapted for use on neonates and studies have been performed evaluating simultaneous MEG and EEG recording (figure 3.2). MEG data shares the basic features and frequency content of EEG, with predominant activity in the slow frequency delta band (frequency < 3.5 Hz) (Haddad *et al*, 2006).

Figure 3.2 The newborn's head is positioned close to the detection coils of the magnetometer. The concave surface of the array (151 channels) is curved to fit the shape of maternal abdomen to optimize recording of (fetal) magnetic signals. Extracted from (Haddad *et al*, 2006).

3.4 Electrical Impedance Tomography (EIT)

EIT is a non-invasive technique, where images of the conductivity (σ) of the body can be reconstructed from voltage measurements made on the surface. In this modality, a series of electrodes are attached to the body and each measurement is made by applying an electrical current with one electrode-pair while using another pair to sample the voltage distribution. The current is applied consecutively through different pairs and the corresponding voltages are measured by all remaining pairs (figure 3.3). The reconstruction process is performed by an algorithm which relates the measured voltages to the conductivity within the sampled region (i.e. by solving an inverse problem).

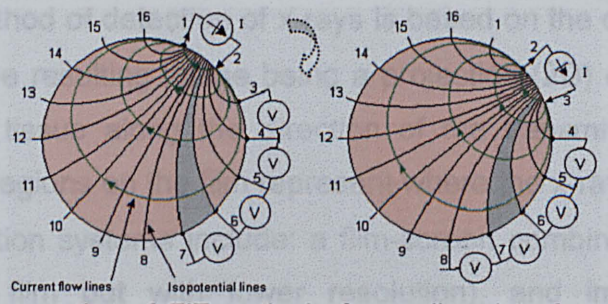

Figure 3.3 Representation of EIT method of recording data for a cylindrical volume conductor with 16 equally spaced electrodes (Neighbouring Method), LEFT: the first 4 voltage measurements for the set of 13 measurements are shown, and RIGHT: another set of 13 measurements is obtained by changing the current feeding electrodes. Extracted from (Malmivuo and Plonsey, 1995).

Recently, the application of EIT to functional imaging of brain was reported (Gibson, 2000), including evoked response to visual, motor and somatosensory tasks (Tidswell *et al*, 2001).

3.5 X-ray and Computed Tomography (CT)

X-rays are ionizing electromagnetic radiation with wavelengths in the range from 0.01 to 100 nm (~10 keV to 150 keV) (Vo-Dinh, 2003). As illustrated in figure 3.4 the x-ray photons from the source that pass straight through the patient carry the main information, and the radiographic image is formed by the interaction of these photons with the detector. The scattered photons carry little useful information and most can be captured by a scatter grid, reducing the background signal that degrades the contrast (Webb, 2000). The radiography projection is a 2D x-ray shadow image of the 3D anatomy of the patient, and each element of this image represents a sum of the linear attenuation along the x-ray's path.

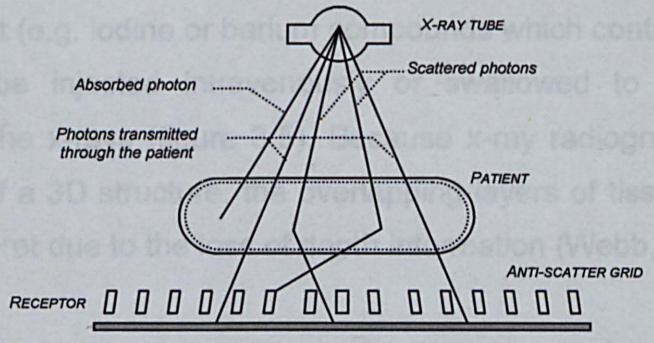

Figure 3.4 Schematic representation of the radiographic imaging chain, reproduced from (Webb, 2000) (p21).

The common method of detection of x-rays is based on the direct exposure of x-ray film, with the resulting image being a projection (2D) of the attenuating properties of all tissue along the direction of the transmitted rays (Webb, 2003). The dark regions on the film represent where the x-rays were detected. Alternative detection systems include: a film-screen combination (faster than direct exposure film but with lower resolution), and image intensifiers. Recently, digital radiography systems have been developed which offer the potential to improve image quality using optoelectronic detectors (charged coupled device – CCD) and flat panel displays (Yaffe and Rowlands, 1996). Further details are given in (Vo-Dinh, 2003), (Webb, 2003), (Webb, 2000).

The attenuation of x-rays in biological tissue increases with the linear attenuation coefficient (dependent on the atomic number of the tissue and is generally inversely proportional to the x-ray energy) and with its thickness. Thus, thicker parts of the body or bone (high concentration of calcium) will produce a higher attenuation, and will need higher energy x-rays (up to 150 keV) to produce an image and a higher radiation dose to the tissues. Soft tissues (as in the breast, muscle and fat) have low atomic numbers and can be imaged with lower energy x-rays (15 to 25 keV). To observe good contrast between different types of soft tissue it is important to use lower energy x-rays since higher energy will pass straight through. In general, in x-ray diagnostic imaging it is important to have a good tissue contrast while keeping radiation dose as low as possible (Vo-Dinh, 2003) and (Webb, 2000). A major application of x-rays is to image broken bones (dense tissues). However, to increase image contrast between blood vessels and the surrounding tissues, a contrast agent (e.g. iodine or barium compounds which contains high atomic number) can be injected intravenously or swallowed to emphasize the attenuation of the x-rays (figure 3.5). Because x-ray radiography provides a 2D projection of a 3D structure, the overlapping layers of tissue can often be difficult to interpret due to the loss of depth information (Webb, 2000).

Figure 3.5 Cerebral angiogram showing an aneurysm of a cerebral artery. Extracted from (Suetens, 2001) (p34).

CT enables the acquisition of 2D x-ray images of thin tissue slices through the body. This is achieved by rotating a source around the patient (360°), and measuring the intensity of transmitted rays from different angles. A series of projections of an object enables a cross-sectional image to be generated (figure 3.6) and multiple images from adjacent slices allow a 3D image to be reconstructed.

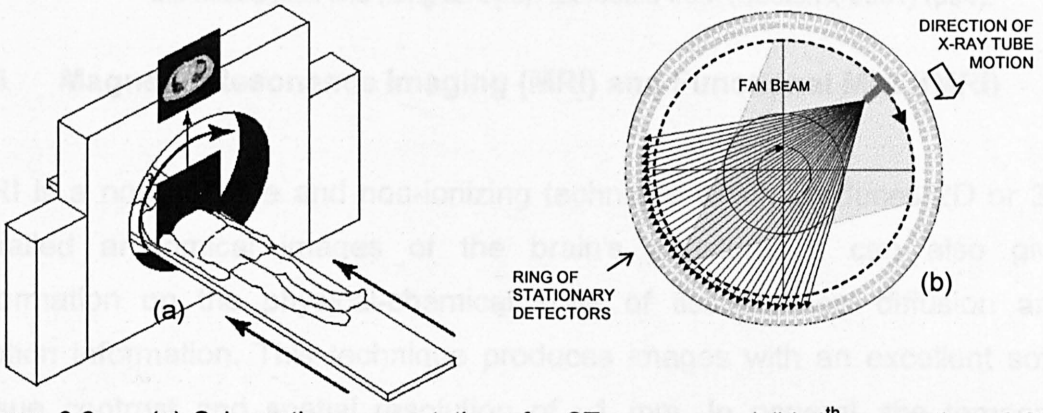

Figure 3.6 (a) Schematic representation of a CT scanner and (b) 4th generation of CT scanner with a rotating x-ray source and a continuous stationary ring of detectors. Extracted from (Suetens, 2001) (p37).

Improvements in CT technology have reduced the overall radiation dosage, decreased the scanning time and allowed the imaging of whole organs or the whole body in 5 to 20 seconds with 0.5 to 1 mm slice thickness (Kalender, 2006). Multiples slices can be acquired to cover a larger volume of the patient using a spiral/helical CT. This employs a spiral trajectory of the x-ray beams by the simultaneous translation of the patient bed and the rotation of the x-ray source and detectors (Webb, 2003). Recovery of the distribution of attenuation within the subject involves using a suitable reconstruction algorithm, such as filtered back-projection (Webb, 2003).

A major medical application of CT images is as a diagnostic tool for investigating skull fractures and underlying brain damage, such as intracranial haemorrhage (figure 3.7). For the case of neonatal brain, the examination requires moving the infant from a controlled environment to the CT scanner (Rennie, 2005). In addition, CT is less useful for premature infants due to the high water content in the brain (Halliday *et al*, 1998).

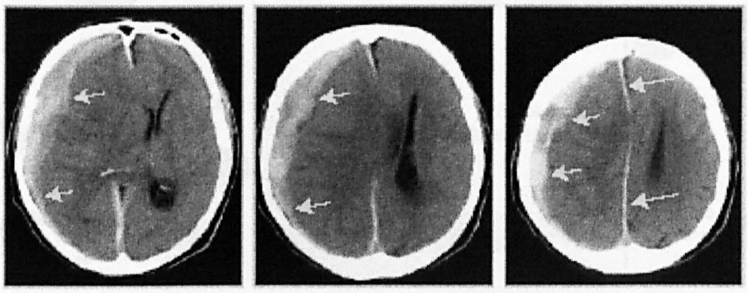

Figure 3.7 Subsequent CT slices through the brain show a subdural haemorrhage as a hyper dense region along the inner skull wall (short arrows). The blood causes an increased pressure on the brain structures with a displacement of the midsagittal line (long arrows). Extracted from (Suetens, 2001) (p54).

3.6 Magnetic Resonance Imaging (MRI) and Functional MRI (fMRI)

MRI is a non-invasive and non-ionizing technique which produces 2D or 3D detailed anatomical images of the brain's structure. It can also give information on the physical-chemical state of tissues, flow diffusion and motion information. This technique produces images with an excellent soft-tissue contrast and spatial resolution of ~1 mm. In general, the temporal resolution is lower for than US or CT, and the scan is very susceptible to patient motion. The patient is placed inside a strong and constant magnetic field (1.5 Tesla). The magnetic field interacts with atomic nuclei of the biological tissue (and with hydrogen nuclei in particular because of the human body is composed primarily of water). Because of the intrinsic properties of atomic nuclei with spin, a magnetic moment (μ) is generated along the spin axis (figure 3.8 (a)) (Webb, 2003). The natural condition of these magnetic fields is no fixed orientation (random), which gives no global magnetic field (figure 3.8 (b)). The nuclei subjected to an external magnetic field (B_o) adopt specific states allowed by quantum mechanics known as spin-up (lower

energy) or spin-down (higher energy). This interaction also results in the precession of nuclear magnetic moment with angular frequency ω_o (figure 3.8 (c)) (Webb, 2003).

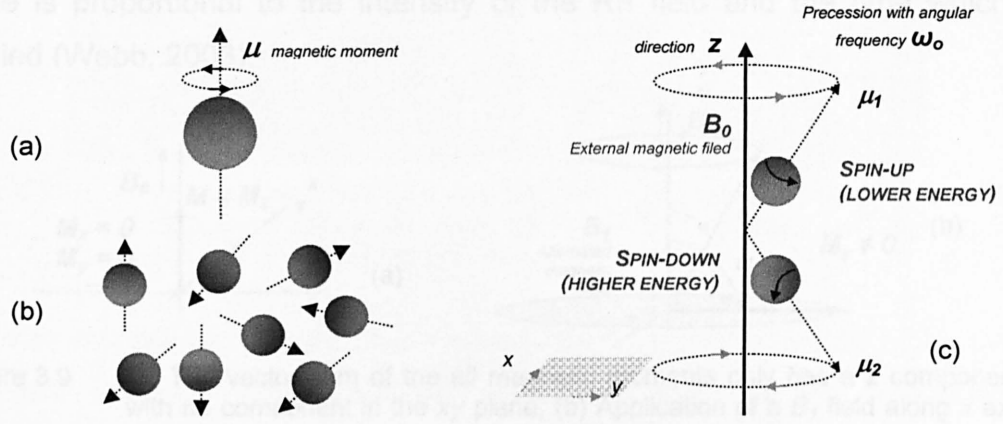

Figure 3.8 (a) Spinning nuclei possesses a magnetic moment, acting like a small magnet, (b) In the absence of an external, magnetic field, the orientations of the magnetic moments are random and (c) Interaction between magnetic moment and the external magnetic field, based on (Webb, 2003) (p159-160).

The proportionality between the angular frequency of precession (ω_o) and B_o is given by equation [3.1], where γ is the gyromagnetic ratio. For hydrogen nucleus (single proton), $\gamma/(2\pi)$ is 42.57 MHz.Tesla^{-1}.

$$\omega_o = \gamma . B_o \qquad [3.1]$$

The precession frequency is known as the Larmor frequency. From figure 3.8 (c), the longitudinal components of the magnetic moment μ_{1z} and μ_{2z} are equal but opposite. The transverse components average to zero at any instant in any large sample. Although in the sample, slightly more spins occupy the lower-energy spin-up state than the higher-energy spin-down state (e.g. in 1 cm^3 of water at 1.0 T there are about 10^{15} excess spins in the lower level – (Vo Dinh, 2003) – according to the Boltzmann distribution). Thus, a net magnetisation (***M***) is created and aligned to the external field (figure 3.9 (a)). Without B_o and at room temperature, net magnetization is null (Webb, 2000). In order to create M_x and M_y components, it is necessary to flip the net magnetisation from the *z* axis into the *xy* plane (figure 3.9 (a)). This can be achieved using an external coil to apply a short varying magnetic field (B_1)

with resonance frequency ω_o, perpendicular to the constant field. The effect of applying the B_1 along x axis is to create a component of net magnetization M_y (figure 3.9 (b)), and α is the angle in which the $\boldsymbol{M}$ is rotated due to B_1. This angle is proportional to the intensity of the RF field and the time which is applied (Webb, 2003).

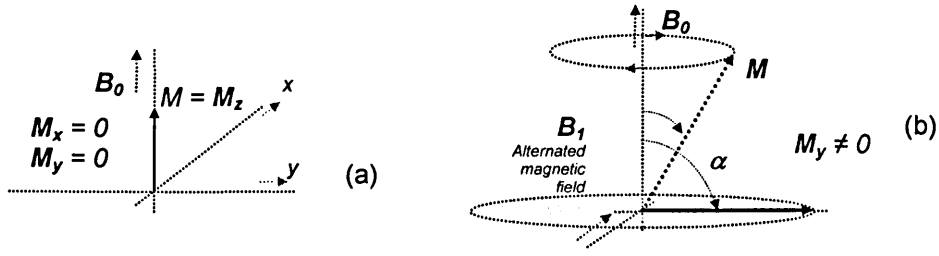

Figure 3.9 (a) The vector sum of the all magnetic moments only has a *z* component, with no component in the *xy* plane, (b) Application of a B_1 field along *x* axis rotates the resulting magnetic moment toward the *y* axis, based on (Webb, 2003) (p166-167).

A coil placed near the sample will detect the varying transverse component of $\boldsymbol{M}$ as a current oscillating at the Larmor frequency. MRI measures the rates of two relaxation processes characterized by time constants T_1 and T_2. When the B_1 is turned off, the nuclei return to the equilibrium state (M_z), emitting energy at the same frequency as was previously absorbed. The decay rate is related to the type and molecular environment of the nucleus, and the spins in the higher state will return to the lower state giving energy to the surrounding tissue (lattice). This process ends when the original magnetization M_z is reached at rate given by T_1 (or spin-lattice) relaxation. The second relaxation process involves the loss of phase coherence, and is known as T_2 (or spin-spin) relaxation. The T_1 and T_2 time constants depend on whether the protons are contained within fat, cerebrospinal fluid, white matter, etc. In practice, the decay of the transverse magnetization is characterised by T_2^* relaxation time which is shorter than T_2 due to additional factors such as field inhomogeneities (Webb, 2003). Most clinical MRI acquisition procedures acquire a set of slices through the anatomical region under study by applying a selective radiofrequency (RF) pulse simultaneously with one of the x, y or z magnetic field gradients (produced by mutually orthogonal set of gradient coils) (figure 3.10) (Webb, 2003).

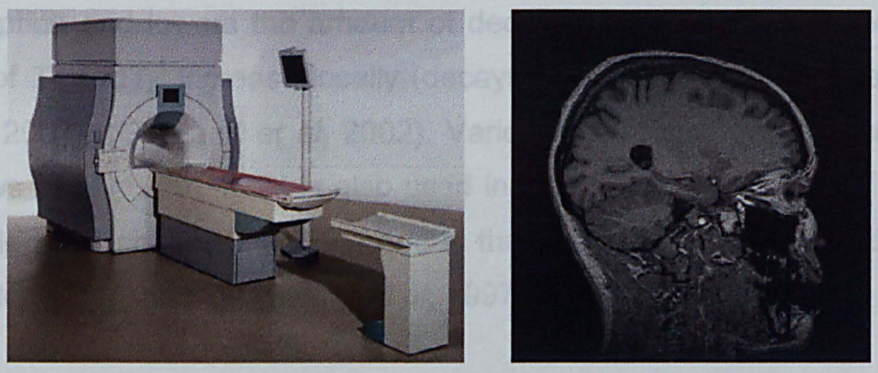

Figure 3.10 LEFT: A conventional MRI scanner, RIGHT: Sagittal view, showing excellent soft-tissue contrast between grey and white matter and high spatial resolution. Extracted from (Suetens, 2001) (p80).

The advantages of MRI include: no use of ionization radiation; high spatial resolution and high contrast between soft tissues; the possibility of performing repeated scans; the ability to acquire sectional views in any direction; the scanner has no moving parts. There are some disadvantages, such as the necessity for the patient to remain still, and for this reason it might be necessary to sedate infants. For their own safety, people with pacemakers or with metal parts in their body must not be scanned. Some patients also suffer claustrophobia during prolonged studies (Mazziota, 2000). MRI is commonly used to assess haemorrhage, hypoxia/ischaemia and maturation of the neonatal brain (Rennie, 2005). MRI is a technique which is used to evaluate brain structure (as CT), and it can also demonstrate the progress of myelination in the developing brain because of the changes in free water content (Halliday *et al*, 1998).

Functional MRI (fMRI) is a technique that measures changes in cerebral blood flow and oxygen level which reflect localized changes in brain activity induced by sensory, motor, or cognitive tasks. It explores a phenomenon known as the BOLD effect (blood oxygen level dependent) to identify areas of the brain that are involved in performing specific tasks, by evaluating the differences in signal intensity between task periods and relaxation periods The local indicator of functional activation is given by deoxy-haemoglobin (due to its paramagnetic properties). When brain activity occurs it causes more blood flow to the active area, which over compensates for the increased oxygen

consumption and lowers the amount of deoxy-haemoglobin. As a result, the values of T_2 and T_2^* increase locally (decays at a slower rate) in these areas (Webb, 2003), (Gowland *et al*, 2002). Various applications are described by Matthews *et al* (1999). fMRI is also used in presurgical evaluation of patients with epilepsy (Bookheimer, 1996) and in the study of the regions of the brain associated with language (Binder *et al*, 1997).

3.7 Positron Emission Tomography (PET) and Single Photon Emission Computed Tomography (SPECT)

PET is a nuclear medicine imaging modality that provides information about the regional cerebral blood flow and tissue metabolism by detecting how quickly tissues absorb or eliminate radioactive isotopes. A radioactive gas or an injection of a biological molecule (glucose) tagged with isotopes is administered to the patient, and it accumulates in areas of the body for which the molecule has an affinity. For instance, glucose labelled with ^{11}C (half-life, 20 min), or labelled with ^{18}F (half-life, 1.8 h), accumulates in the regions of the brain where it is used as the primary source of energy (Webster, 1992). An increase of neural activity in the brain leads to an increase in metabolic demand for oxygen and glucose, and consequently an increase in CBF. Therefore, the region receives a greater concentration of the radioactive tracer, which emits positrons, which interact with the electrons of the tissue cells, producing two high energy gamma rays (emitted in opposite directions) that are detected by the solid-state detectors surrounding the patient. The location of the detectors and the line along the annihilation defines where it has occurred inside the body (figure 3.11).

The image reconstruction is based on iterative algorithms or filtered back-projection methods. However, before reconstruction, the data must be compensated for attenuation effects (Webb, 2003). The major problem with PET is its cost and the short half-life of most positron emitting isotopes, which require an on-site cyclotron (used to produce the radioisotopes).

Nevertheless, PET is used in research studies, such as epilepsy (Volder, 2002), and for the diagnosis and staging of cancer (Ollinger and Fessler, 1997)

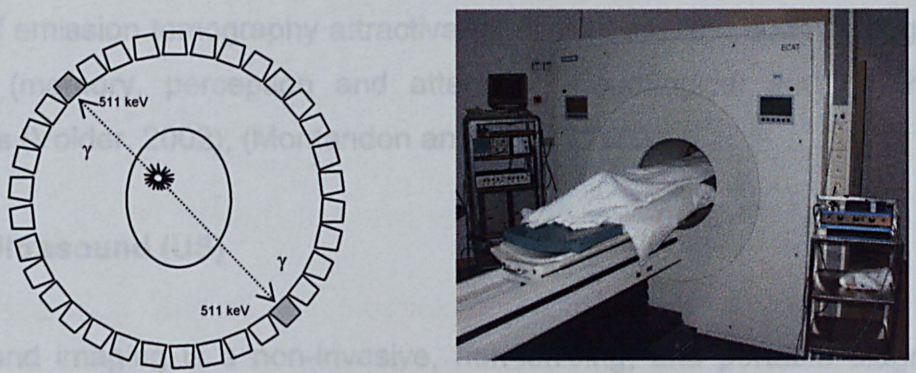

Figure 3.11 LEFT: Schematic representation of positron-electron annihilation and detection. Both particles are converted into a pair of photons of 511 keV each one travelling in opposite directions (two γ-rays). RIGHT: View of a commercial PET scanner (Suetens, 2001) (p115 and 121).

SPECT is also a nuclear medicine imaging tool which produces 2D or 3D images by tracing an intravenous radioactive substance. SPECT, as with PET, acquires information on the concentration of radio nuclides introduced to the patient's body. However, the isotopes used are gamma ray emitters and hence only single photons are detected. SPECT imaging involves the rotation of a photon detector array around the body to acquire data from multiple angles (figure 3.12), from which the position and concentration of radionuclide distribution is determined. Because the emission sources are inside the body cavity, mathematical reconstruction algorithms are used. A spatial resolution of 8 – 9 mm is normally achieved (Webb, 2003).

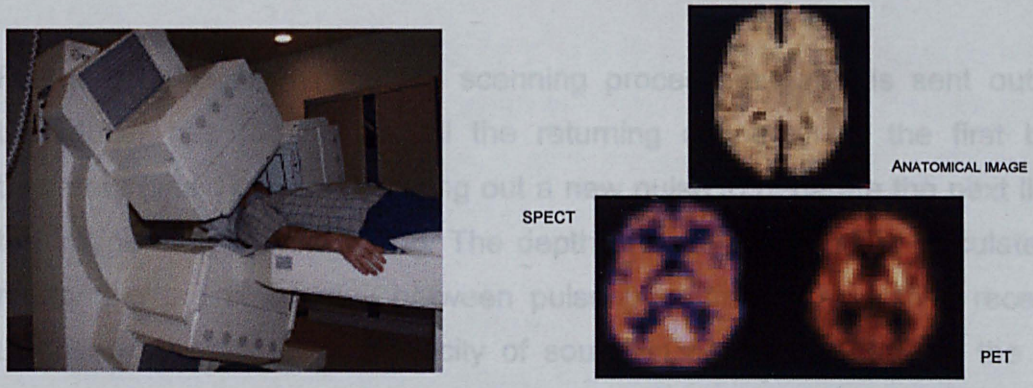

Figure 3.12 LEFT: SPECT scanner with 3 detector heads, (Suetens, 2001) (p120). RIGHT: Comparison among anatomical image and nuclear imaging methods (Montandon and Zaidi, 2002).

Although SPECT imaging resolution is not quite as good as that of PET (5 – 8 mm), the availability of SPECT radio pharmaceuticals (for the brain), and the practical and economic aspects of SPECT instrumentation make this mode of emission tomography attractive for clinical studies, such as cognitive studies (memory, perception and attention), neurological and psychiatric diseases (Volder, 2002), (Montandon and Zaidi, 2002).

3.8 Ultrasound (US)

Ultrasound imaging is a non-invasive, non-ionising, and portable diagnostic modality which has extensive use in the clinical environment. Sound waves (~1 to 10 MHz, with 1-3 MHz used for imaging deep-lying structures and 5-10 MHz for imaging regions closer to the body surface) are emitted from a transmitter-receiver (piezoelectric crystal) placed on the skin over the area to be scanned. The waves strike internal organs and are partly reflected back to the receiver, and are partly transmitted. The intensity of the reflection depends on the mismatch in acoustic impedance of the two tissues, and it in turn is expressed as a function of the tissue density and compressibility. The more rigid the tissue, the greater the value is the impedance of tissue. If the mismatch in impedance is large between adjacent tissues, more ultrasound is reflected. This can greatly attenuate the transmitted beam and makes imaging of structures behind bone difficult. US is also used to measure blood flow in vessels via a Doppler shift in the backscattered frequency from blood cells.

Figure 3.13 illustrates the US scanning process: a pulse is sent out, the transducer has to wait for all the returning echoes from the first beam trajectory (line 1), before sending out a new pulse to generate the next line in the image (line 2), and so on. The depth of the boundaries is calculated by measuring the time delay between pulse transmission and echo reception using an estimate of the velocity of sound in tissue. Because of the finite speed of sound the depth of the image and its width (number of lines) limit the maximum frame rate (Webb, 2003).

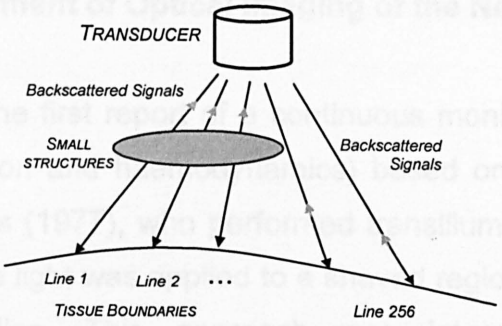

Figure 3.13 The principles of US imaging reproduced from (Webb, 2003) (p108).

US scanning is utilized for diagnosis and prognosis of intraventricular haemorrhage (figure 3.14), periventricular leukomalacia, and hydrocephalus. The brain is accessed through the anterior or posterior fontanelle or through the (relatively) thin parietal bones (figure 2.13).

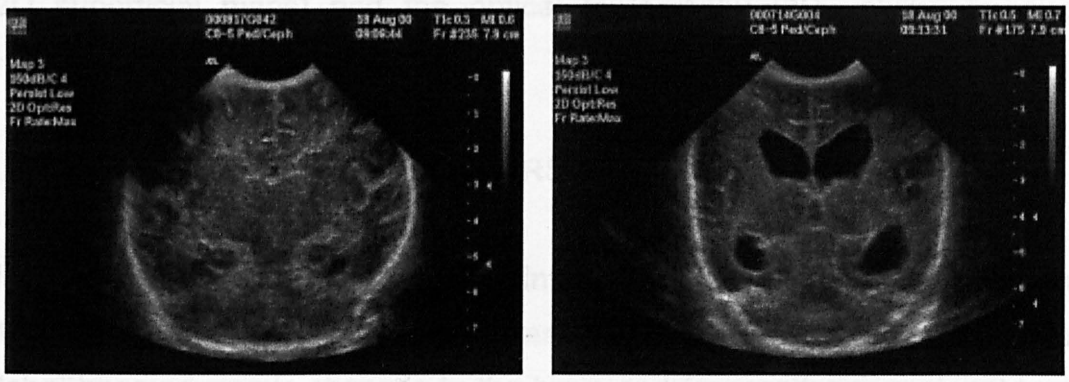

Figure 3.14 LEFT: Slice selection in coronal view showing normal cranial ultrasound, with the skull appearing as dense white echoes (Halliday et al, 1998) (p373). RIGHT: Fluid filled cerebral cavities on both sides as a result of an intraventricular haemorrhage, (Suetens, 2001) (p106).

Advantages of ultrasound scanning are: it is portable, it involves no ionizing radiation, it is relatively inexpensive, it involves minimal preparation, it provides an instantaneous image, patient motion is not critical, and the probe can be easily moved to select different scanning planes.

Some disadvantages are associated with poor visualizing of areas of the brain (subdural and subarachnoid spaces), bones are obstacles for imaging, non-skilled operators may misinterpret findings, and it is a structural imaging modality with no information on tissue functions (Halliday *et al*, 1998).

3.9 The Development of Optical Imaging of the Neonatal Head

In the late 1970s, the first report of a continuous monitoring of physiological changes (oxygenation and haemodynamics) based on visible and NIR light was made by Jöbsis (1977), who performed transillumination measurements on a cat's head. The light was applied to a shaved region of the temples using optical fibre bundles. This approach was later called near-infrared spectroscopy (NIRS). It has been used to study cerebral haemodynamics, regional blood volume, regional CBF and regional haemoglobin oxygen saturation (rSO_2) of human cortex (Meek, 2002), (Fantini *et al*, 2001), (Benaron *et al*, 2000) and (Elwell, 1995). Recently, it also has been extended into the development of imaging methods which give information on spatial localization. Two distinct approaches are being pursued: optical topography (2D superficial maps) and the optical tomography (3D volume imaging) (Hebden, 2003).

3.9.1 Near Infrared Spectroscopy (NIRS)

Near infrared spectroscopy is a non-invasive technique used for monitoring blood oxygenation and its kinetics. It has been used in research for measuring global haemodynamic changes in the brain and for monitoring regional brain activation during stimulation. This technique utilises the optical properties of the natural chromophores (haemoglobin and cytochrome aa_3). It can measure changes in the concentrations of oxygenated ($[HbO_2]$) and deoxygenated haemoglobin ([Hb]), and can monitor change in cerebral blood volume (CBV) with high temporal resolution and using compact instrumentation. The biomedical applications of NIRS are based on the fact that safe doses of NIR light can pass through large thicknesses (several centimetres) of skin, bone, and soft tissue, and especially of the neonatal infant brain (smaller head diameter and the bones are less mineralised than adults). Light propagating between two points on the tissue surface is highly scattered, with a mean optical pathlength which is much larger than the geometrical source-detector

separation and which is wavelength dependent (due to μ_a, μ_s', g, see section 2.6.1). As a consequence, straightforward measurements of transmitted or reflected intensity can only give *relative values* of brain properties that are highly non-localized.

Figure 3.15 shows a light source and a detector element separated at some distance from each other. It is possible to detect the transmitted light at two or more wavelengths, allowing the assessment of changes in $[HbO_2]$ and $[Hb]$ (see section 2.6.1.2).

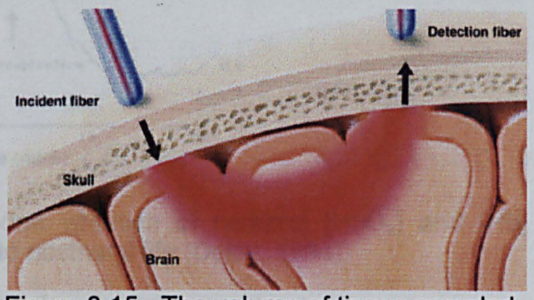

Figure 3.15 The volume of tissue sampled by an NIR measurement.

Increasing the number of wavelengths enables measurements of changes in cytochrome aa_3 (a 4-wavelength system is described in Cope and Delpy, (1988)). A schematic representation of a single channel NIRS measurement on a baby's head is illustrated in figure 3.16.

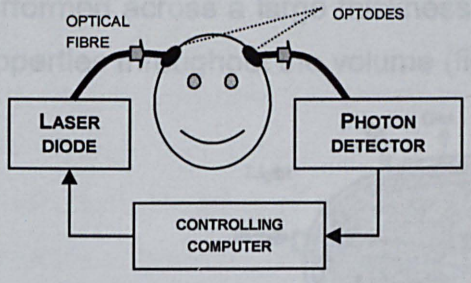

Figure 3.16 LEFT: schematic of the experimental set up for NIRS measurements across the head, from (Elwell, 1995). RIGHT: A baby with optodes positioned over the head (Delpy *et al*, 1988).

NIRS has evolved into a valuable research tool for studying infant cerebral haemodynamics and metabolism, evoked response to visual, olfactory, auditory stimulation, and to monitor the human foetal brain during labour (Hebden, 2003). Figure 3.17 shows a recording made during the final stages of a normal delivery, showing the rapid and large change in blood oxygenation that occurs once the baby is born and takes its first breath of air (Delpy, 1994).

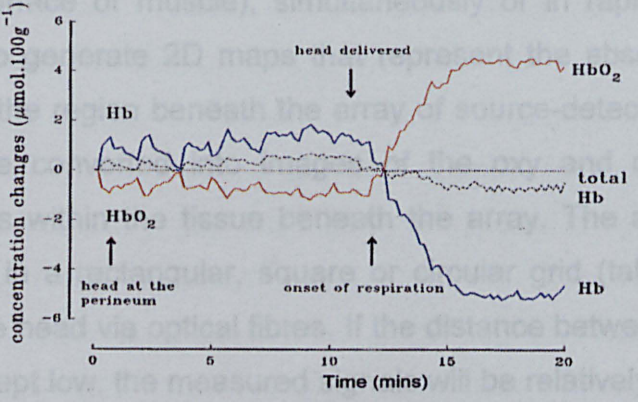

Figure 3.17 Recorded signals of the temporal variation of cerebral [HbO_2] and [Hb] during the transition from foetal to postnatal life (Delpy, 1994).

While NIRS provides only global measurements, localisation, to enable mapping of brain function, (i.e. imaging) can be achieved by increasing the number of sources and detector on the surface of the tissue. Two distinct imaging approaches have been explored: Optical Topography is an imaging technique which acquires a number of reflectance measurements on the skin to probe the optical properties of regions just below the surface; and Optical Tomography is an imaging technique where transmittance measurements are performed across a large thickness of tissue in order to determine the optical properties throughout the volume (figure 3.18).

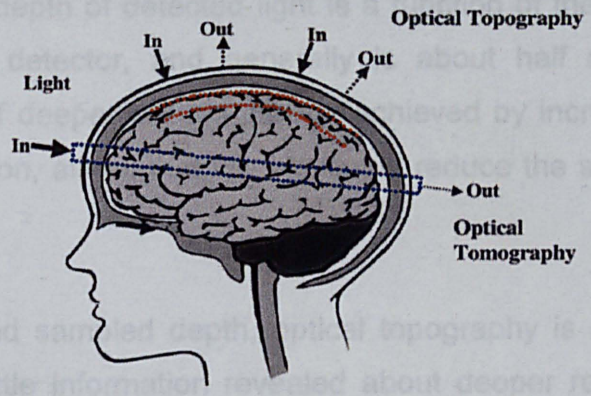

Figure 3.18 Concept of optical topography and tomography (Koizumi *et al*, 2003).

3.9.2 Optical Topography

This is a method for acquiring multiple reflectance measurements at small source-detector separations (a few centimetres) over a large area of tissue

(e.g. head surface or muscle), simultaneously or in rapid succession. The objective is to generate 2D maps that represent the absorption and scatter properties of the region beneath the array of source-detector pairs. Normally, the maps are converted into images of the oxy and deoxy-haemoglobin concentrations within the tissue beneath the array. The arrangement of the pairs can be in a rectangular, square or circular grid (table 3.1), which are coupled to the head via optical fibres. If the distance between the sources and detectors is kept low, the measured signals will be relatively high enabling fast acquisitions between successive pairs (of the order of 100 ms), (Hebden, 2003).

Table 3.1 Different arrays of sources and detectors for optical topography.

PROBE CONFIGURATION	SOURCES	DETECTOR	MEASUREMENT COMBINATION
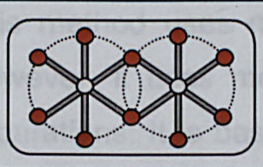	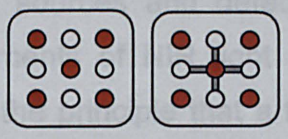	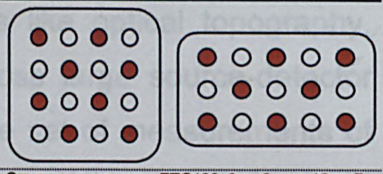	
GEOMETRICAL ARRANGEMENT OF THE 16 SOURCES AND 2 DETECTORS USED BY (FRANCESCHINI *ET AL*, 2000) IN AN INVESTIGATION OF MAPPING OF THE ARTERIAL PULSATION AT REST AND THE SPATIALLY-RESOLVED HAEMODYNAMICS ON THE PRIMARY MOTOR CORTEX DURING CONTRALATERAL HAND TAPPING.	GEOMETRICAL ARRANGEMENT OF THE 20 SOURCES AND 8 DETECTORS (TWO SURFACE CONFIGURATION) IS USED WITH THE ETG100 OPTICAL TOPOGRAPHY SYSTEM OF HITACHI MEDICAL CORP AND IS ABLE TO ASSESS LEFT-RIGHT BRAIN DOMINANCE IN MOTOR, AUDITORY AND LANGUAGE BRAIN FUNCTIONS (KAWAGUCHI *ET AL*, 2001)		OTHER ARRAYS FROM ETG100: 6 BY 8 AND 16 BY 7, THE FORMER TO STUDY THE VISUAL CORTEX, AND FOR FINE MEASUREMENTS OF AREAS ON ONE SIDE OF THE BRAIN; AND THE LATER FOR SIMULTANEOUS MEASUREMENTS OF BROCA'S AREA AND WERNICKE'S AREA, WHICH ARE IMPORTANT IN LANGUAGE FUNCTION RESEARCH (KAWAGUCHI *ET AL*, 2001).

The penetration depth of detected light is a function of the distance between the source and detector, and generally is about half of this separation. Measurements of deeper tissues can be achieved by increasing the source-detector separation, although it will inevitably reduce the signal-to-noise ratio (SNR).

Due to the limited sampled depth, optical topography is a cortical mapping technique with little information revealed about deeper regions of the brain (e.g. detection of intraventricular haemorrhages) (Hebden, 2003). Therefore, it is appropriate for applications which involve investigating cortical brain function, such as the regions associated with brain cognition, and sensory activation (Meek, 2002), or examining superficial tissues, like forearm muscles (Vaithianathan *et al*, 2004), (Hamaoka *et al*, 2000).

The process of data acquisition can be performed in two distinct ways: serial acquisition, which can be slow due to the illumination of one source at a time while detecting using all detectors, and frequency modulated parallel acquisition which has all sources activated at once. Each source is modulated at a different frequency and then can be separated by Fourier transform (Everdell *et al*, 2005), (Everdell *et al*, 2004), (Franceschini *et al*, 2003) or by using lock-in amplifiers (Koizumi *et al*, 2003), (Yamashita *et al*, 2001), (Yamashita *et al*, 1999). Simple image reconstruction methods are employed to display changes occurring in areas where activation occurred.

3.9.3 Optical Tomography

This method uses multiple sources and detectors like optical topography. However, it uses measurements of NIR light across large source-detector separations. It is based on the principle that a finite set of measurements of transmitted light between pairs of points on the surface of the object of interest is sufficient to reconstruct a 2D slice or a 3D representation of the object's internal scattering and absorbing properties. It is appropriate for measurements of changes deep below the surface. Figure 3.19 shows possible geometries (optode positions) for tomography measurements of the baby's head (Hebden, 2003).

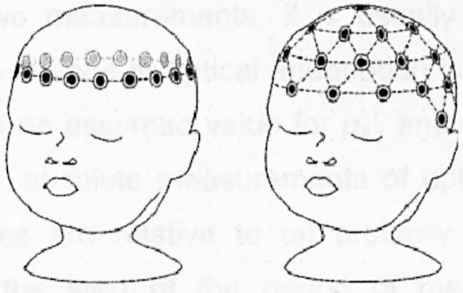

Figure 3.19 Potential arrays of sources-detectors for transverse (LEFT) and full (RIGHT) 3D imaging of infant head. Extracted from (Hebden, 2003).

Tissue in general is highly scattering, especially in the NIR therapeutic window. The emerging transmitted signal is weak. Hence it is necessary to integrate the detected signal over several seconds or more. Although, this makes an optical tomography system unsuitable for fast haemodynamic

analysis (e.g. cortical activations studies), it can be potentially used for long-term infant monitoring in the neonatal intensive care unit (Hebden *et al*, 2002), (Hebden *et al*, 1997).

3.10 Experimental Techniques and Optical Instrument Types

The main aim of optical imaging is to reconstruct a spatial map of μ_a, μ_s', or both from measurements of diffusely reflected or transmitted light. With such maps at multiple wavelengths other biological characteristics, like maps of blood volume or oxygen concentration, can be generated. The main categories of measurements that have been used are continuous wave measurements (or steady-state domain), frequency domain, and time domain. The different systems will be described in the following sections.

3.10.1 Continuous Wave Instruments (CW)

The simplest optical imaging system uses light sources which emit light continuously at a constant intensity, or modulated at low frequency (a few kHz). A CW system records only the amplitude decay of the incident light, which alone is insufficient to distinguish between changes in absorption and scatter (Arridge and Lionheart, 1998). However, when imaging changes in properties between two measurements, it is usually assumed that scatter remains constant. The change in optical attenuation is then used to estimate the change in μ_a given an assumed value for μ_s', and maps of activation can be obtained. However, absolute measurements of optical properties are not possible and all values are relative to an arbitrary background, which is usually the state at the start of the period of measurements. The CW instrument records data at two or more wavelengths (depending on the number of chromophores), and then uses the changes in intensity to calculate the changes in chromophore concentrations. The study of haemodynamic changes in the cortex is a common application. The advantages of this instrument include its low cost, simplicity, and high sampling rate (which can

be at up to 100 Hz). The drawbacks of CW instruments are that the differential pathlength must be determined separately, and the difficulty to separate absorption and scattering (Arridge and Lionheart, 1998). The measurements of light intensity are more susceptible to the optical properties of tissues at or immediately below the surface than to the properties of localized regions deeper within the tissue, due to the banana-shaped volume of tissue over which the measurement is sensitive (known as the photon measurement density function or PMDF), which is narrow near the source and detector and very broad in the middle (figure 3.20) (Gibson *et al*, 2005a), (Arridge, 1995).

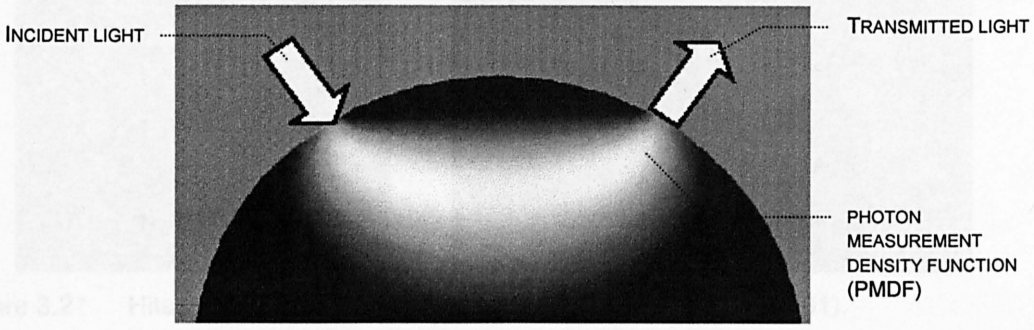

Figure 3.20 Boundary of the banana-shaped sensitivity region.

The detected intensity is thus highly dependent on surface coupling, being affected by slight movements or changes in the applied pressure of optical fibres in contact with the skin. Also, hairs can attenuate the intensity measurements. Attempts to reduce these problems are being implemented using a (linear) reconstruction model which assumes coupling coefficients as additional unknowns in the reconstruction problem and recording differences in intensity, acquired over a period short enough so that the unknown coupling can be assumed to have remained constant (Boas *et al*, 2001).

The first commercial optical topography system is the Hitachi ETG-100 which is a 24-channel (24 source-detector pair) measurement system (figure 3.21). The instrument consists of 16 laser diodes (8 at 780 nm and 8 at 830 nm) and 8 avalanche photodiode (APD) detectors. Each laser source is intensity modulated at a different frequency, and the output from each detector is applied to an array of 48 lock-in amplifiers. This approach enables the discrimination of different frequencies in the detected signal, and allows all the

sources to be illuminated simultaneously, so an image can be produced quickly (Yamashita *et al*, 1999). This equipment has been evaluated in several studies (Koizumi *et al*, 2003), (Yamashita *et al*, 2001), (Isobe *et al*, 2001) (Kawaguchi *et al*, 2001), (Taga *et al*, 2000), (Yamashita *et al*, 1999). The most recent Hitachi system is the ETG 7000 with 120 channels and 40 pairs of laser diodes and 40 APD detectors, and it is able to image the entire adult cortex.

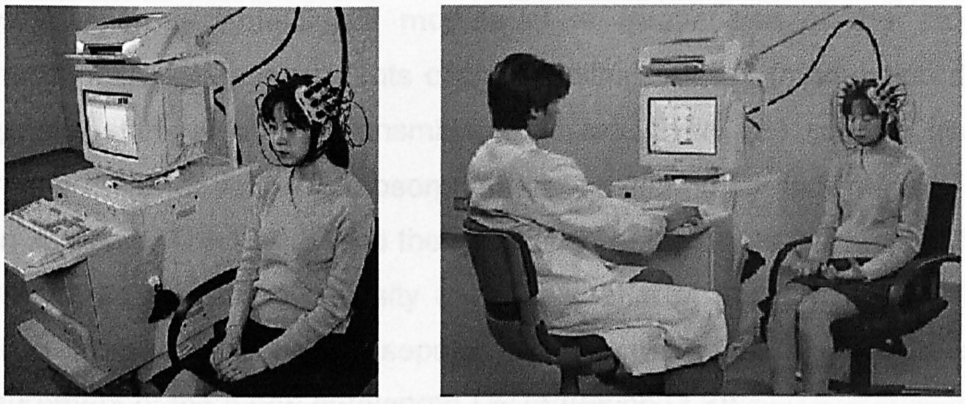

Figure 3.21 Hitachi ETG 100 24-channel system (Kawaguchi *et al*, 2001).

Similar systems have been employed to image the cortex of newborn babies. Hintz *et al* (2001) have studied motor activation in response to passive movement of the arms in premature babies, using a system consisting of 18 laser diode sources and 16 photodiode detectors. Franceschini *et al* (2003) have investigated the motor cortex activation in adults using a system based on 16 laser diode sources and 16 photodiode detectors, and utilizes an infinite impulse response filter (a digital filter, Oppenheim and Schafer (1989)), instead of Fourier transforms, to obtain the individual source signals. At UCL, Vaithianathan *et al* (2004) have built a system with a flexible pad, to be applied to an infant's head, and Everdell *et al* (2004) have developed a new approach, which involves using software to demultiplex the multiple source signals. The system has been evaluated in several studies (Blasi *et al*, 2006), (Branco *et al*, 2006), (Everdell *et al*, 2004). For more details see section 4.3. Bluestone *et al* (2001) have reported measurements on the human forehead with a dynamic near-infrared optical tomography (DYNOT) system, a commercial CW instrument developed by Schmitz *et al* (2002) to perform

tomographic imaging. This system employs frequency encoded multi-wavelength DC illumination, a time-multiplexed source, and parallel multi-channel detection with fast gain switching.

3.10.2 Frequency Domain Instruments (FD)

In frequency domain systems (figure 3.22) the light source shines with an intensity which is sinusoidally modulated at frequencies of the order of hundreds of MHz. Measurements of the amplitude decay (modulation depth) and phase shift (ϕ) of the transmitted/reflected signal (I) can be used to determine mean of values of absorption and scattering coefficients within the region sampled. The scatter and the absorption of the tissue will have different effects on the measured intensity and phase-shift of the transmitted signal, enabling their effects to be separated. The phase shift gives a direct measurement of the mean pathlength *DP* (equation [3.2]).

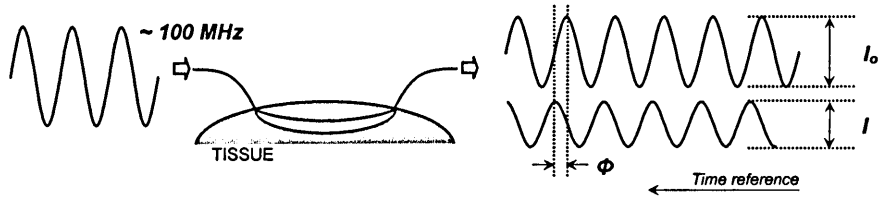

Figure 3.22 The parameters which are measured by a FD systems: the decrease in intensity and the phase change, based on (Hillman, 2002) (p32).

$$DP = \frac{\phi.c}{2\pi.f.n} \qquad [3.2]$$

where ϕ is the phase shift measured in radians [rad], f is the frequency modulation [Hz], n is the refractive index and c is the speed of light in a vacuum. The frequency chosen is related with the spatial resolution: greater spatial resolution is observed at higher modulation frequencies, although above 200 MHz the linear relationship between the average optical pathlength and the phase shift no longer applies (Delpy and Cope, 1997). Frequencies around 100 MHz generally are adequate for this technique (Hebden *et al*, 1997). The sources are typically laser diodes (1- 100 mW) and optical fibres are used to deliver light from the diode to the tissue and to collect the

transmitted/reflected light. The detectors used include photomultiplier tubes (PMTs), and avalanche photodiodes (Hielscher *et al*, 2002).

FD systems currently used for brain imaging studies includes that developed by Franceschini *et al* (2000). This is a two wavelength (758 and 830 nm) frequency modulated (110 MHz) system, with 16 intensity modulated sources (8 per each wavelength) and 2 photomultiplier tube detectors. It has been used for non-invasive optical imaging of the healthy adult brain with temporal resolution of 160 ms. They report the arterial pulsation and motor activation in the cerebral cortex and quantify temporal changes in cerebral oxy and deoxy-haemoglobin concentration. Toronov *et al* (2001) describe a similar system used on adults to record data during motor activity (using a sequence of stimulation by finger motion and rest) simultaneously with fMRI imaging system. Meanwhile, Zhao *et al* (2005) have developed a multi-wavelength frequency domain system to investigate *in vivo* the optical properties of the neonatal brain.

3.10.3 Time Domain Instruments (TD)

Time domain instruments (or time resolved instruments) apply a very short light pulse (of order of picoseconds) that is broadened considerably after travelling through several centimetres of soft tissue such that it extends over nanoseconds. The measurement of the times of flight of photons travelling between a source and a detector provides a temporal distribution known as the **T**emporal **P**oint **S**pread **F**unction – TPSF (figure 3.23).

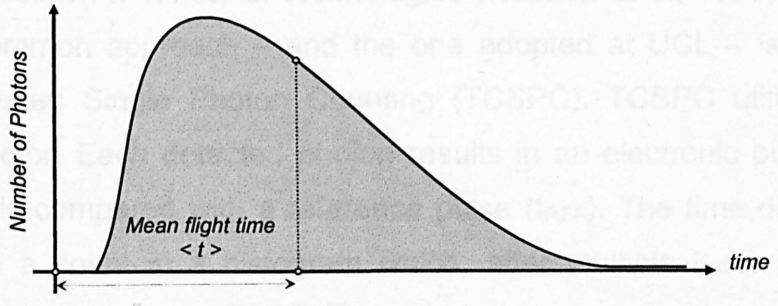

Figure 3.23 TPSF in domain time representing the tissue's impulse response function

This statistical distribution contains information about the scattering and absorbing characteristics of the tissue sampled. For instance, a higher scattering medium will broaden an input pulse due to the increase in the average path taken by the photon, and a higher absorption medium will narrow an input pulse because a longer path is more likely to be attenuated. The mean flight time (< *t* >) of the distribution is correlated with the differential pathlength factor (*DPF*) by equation [3.3], where *n* is the refractive index, *c* is the speed of light in a vacuum, and d is the source-detector separation.

$$DPF = \frac{DP}{d} \approx \frac{c}{d.n}\langle t \rangle \qquad [3.3]$$

The slope of the TPSF at large flight times can yield information about the absorption coefficient; the higher the absorption, the higher the slope (Hielscher *et al*, 2002). By comparing the shape of the temporal curves with analytical expressions derived from solutions to the diffusion approximation, the coefficients can be determined using fitting procedures (Patterson *et al*, 1989). TD systems provide various datatypes, which can be extracted from a TPSF, such as the mean flight time, variance or integrated intensity (the total number of photons in the measured TPSF and is equivalent to a CW measurement). FD data can be obtained from the Fourier transform of a TPSF at any frequency (or at all frequencies simultaneously), which is an advantage over FD systems. The main disadvantages of TD systems are their cost and complexity compared with CW and FD. However, they are potentially capable of providing more useful information when imaging the internal regions of the brain. Various time-domain instruments have been developed for optical imaging, based on a variety of technologies (Hebden *et al*, 1997). However, the most common approach – and the one adopted at UCL – is known as Time Correlated Single Photon Counting (TCSPC). TCSPC utilises a fast photon detector. Each detected photon results in an electronic pulse whose arrival time is compared with a reference pulse (t_{REF}). The time difference is recorded as a count in a histogram which, after multiple laser repetitions, develops gradually into the TPSF. To avoid "pile-up" errors, the probability of detecting two photons per reference pulse must be negligible (typically <

0.01%). The advantages of this system compared to other time resolved methods are a very high dynamic range and excellent temporal linearity (provided the maximum photon count rate is not exceeded) (Delpy and Cope, 1997). Systems typically employ PMT or MCP-PMT detectors, which have the advantage of a large collection area. The drawback of TCSPC is a comparatively low temporal resolution (typically of the order of tens to hundreds of picoseconds) whereas a streak camera, for example, has a resolution of < 10 ps (Delpy *et al*, 1988). The first optical tomography of the infant brain was attempted successfully by the group of Dr. Benaron at Stanford University, who developed an imaging system based on the measurement of photon time-of flight between points on the circumference of the infant head (Benaron *et al*, 2000). Thirty-four pairs of sources and detectors fibres (with the end with small right-angle prism) were attached to the head using a flexible headband (figure 3.24) (Hintz *et al*, 1998), and were used to obtain 2D tomographic slice images of anatomical disorders and functional activation. A time between 2 to 6 hours was necessary for the scanning process, which it was dependent on the head size and the number of wavelengths used (Benaron *et al*, 2000).

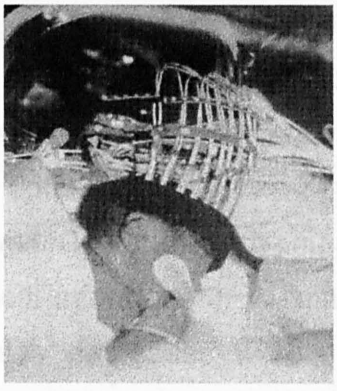

Figure 3.24 Flexible headband used in clinical studies (Hintz *et al*, 1998).

A 64-channel TCSPC based time-resolved instrument that employs specially developed low power picosecond diode lasers and fast PMT detectors is described by (Oda *et al*, 1997). A 32-channel near-infrared system developed at UCL for 3D optical imaging of the neonatal infant brain has been developed by Schmidt et al (2000). For more details see section 4.2.

3.11 Comparison of Current Neuroimaging Methods

Optical imaging offers advantages over both MEG and fMRI, both of which involve the use of large, heavy, expensive instruments, and a dedicated building to eliminate effects of external magnetic fields. Yet both systems require that the subject remains motionless during measurements, otherwise spatial resolution could be severely compromised. Patient motion is a particular issue for infants, and it is nearly impossible to make any sort of measurements without pharmacologic intervention. However, such intervention can also affect normal neural functions, making evaluation and study of voluntary response impracticable.

Optical Imaging can be physically compact, lightweight, and fully portable. Normally optical imaging systems employ flexible fibre optics and small movement of the subject can be tolerated. An important feature of this technique not shared by fMRI and MEG is the capability to rapidly and simultaneously measure changes in local cerebral blood volume (CBV), and oxy and deoxyhaemoglobin concentrations. PET can measure the cerebral metabolic rate of glucose consumption, cerebral metabolic rate of oxygen consumption and cerebral blood flow. PET also utilizes inhalation or injection of radioactive agents so cannot be used for continuous monitoring. Contrast agents are not required for optical imaging, like X-ray and CT. Optical imaging offers functional imaging, which is a major advantage when compared with US (which gives only anatomical information). A limitation of Optical Imaging is the spatial resolution, which decreases with increasing depth below the surface. However, this is a consequence of the nature of scattered light. Thus, optical imaging cannot replace either MRI or CT for obtaining deep tissue structural information. However, optical methods may serve as an adjunct tool for such modalities since they are generally compatible with simultaneous MRI or CT imaging, and also offer several advantages related with safety, cost, sensitivity to functional changes and use at the bedside (Gibson *et al*, 2005a).

Chapter 4

Optical Imaging at UCL

4.1 Introduction

In this chapter, the two imaging systems developed for clinical testing at UCL will be explained. First, the instrumentation designed for 3D optical tomography known as the **M**ulti-Channel **O**ptoelectronic **N**ear-Infrared **S**ystem for **T**ime-resolved **I**mage **R**econstruction (MONSTIR) will briefly described. This will include a description of the acquisition protocol and the processing and treatment of experimental TPSF data (datatypes). Second, the recently built frequency multiplexed near infrared topography system, for imaging functional activation in the brain.

4.2 MONSTIR

MONSTIR was designed as a continuous bedside monitor for obtaining optical images of premature babies' brains, which are at an increased risk of suffering permanent brain damage due to dysfunction in cerebral oxygenation (hypoxic-ischemia), leading to severe neurodevelopmental disorders (section 2.5). The system provides temporal measurements of photons transmitted diffusively through the tissue enabling the reconstruction of internal distributions of absorption and scattering properties. The MONSTIR system is illustrated in figure 4.1.

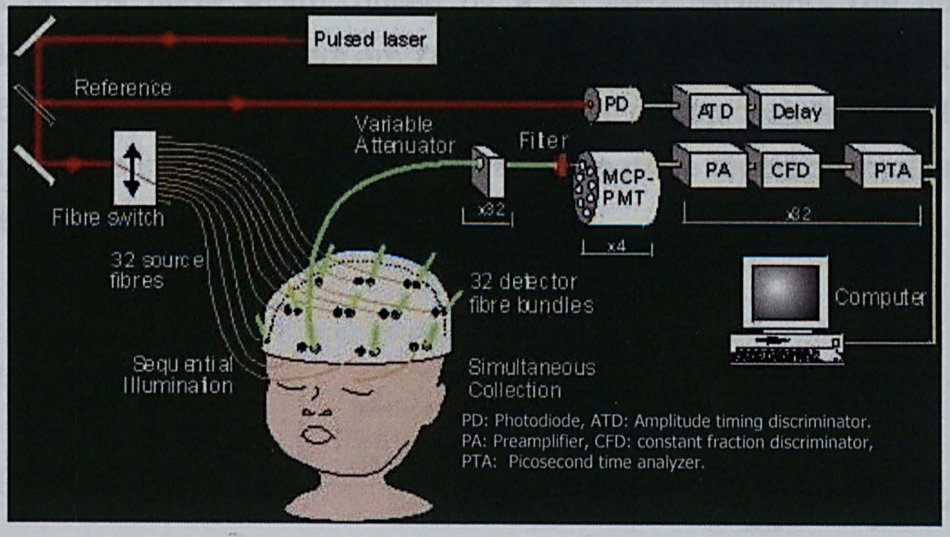

Figure 4.1 LEFT: MONSTIR at cotside, RIGHT: A schematic representation of the 32-channel time resolved imaging system.

This system is based on 32 independent Time Correlated Single Photon Counting (TCSPC) channels which measure the times of flight of photons travelling through the tissue under study. For each detector a histogram of the times of flights for all the detected photons is generated in the form of a TPSF.

NIR pulses from a dual wavelength fibre laser are coupled successively (by a fibre switch) into 32 fibres that *sequentially* deliver them over the surface of the tissue. Meanwhile the transmitted light is detected *simultaneously* by 32 fibre bundles, which surround the source fibre. The detector bundles are coupled to very sensitive optical detectors (four 8-channel microchannel-plate photomultiplier tubes, MCP-PMTs) via variable optical attenuators, which ensure that the detected flux does not exceed the maximum photon count rate (~2.5×10^5 photon/seconds). Electronic pulses are generated each time a photon is detected. The measurement of the delay between these pulses and the reference pulse allows histograms of photons flight times (TPSFs) to be built up (Schmidt *et al*, 2000), (Schmidt, 1999). The principal elements/components of MONSTIR are described in the following sections.

4.2.1 Laser Source

MONSTIR has a custom-built laser source containing two picoseconds fibre lasers (< 2ps pulse width), driven by a 40 MHz oscillator. The nominal wavelengths of the two lasers are 780 and 815 nm with nominal power output of ~55 mW per wavelength. Each laser is pulsed continuously at 40 MHz and the pulses are interlaced to produce an effective pulse repetition frequency of 80MHz (figure 4.2).

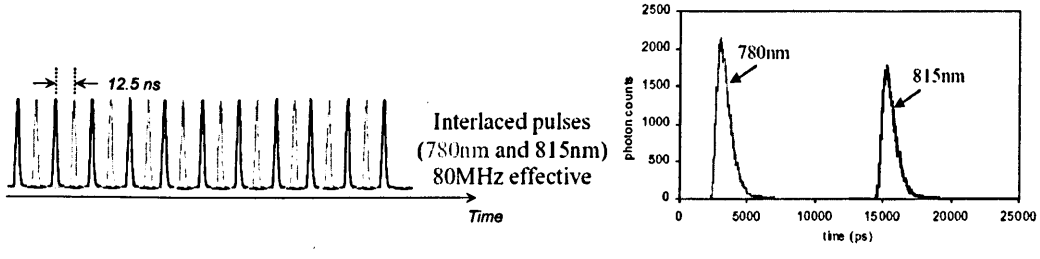

Figure 4.2 Pulsing of the fibre laser source.

4.2.2 Optical Fibres

A fast fibre switch (controlled by software) couples the output of the laser to one of 32 source fibres integrated along the central axis of each detector fibre bundle. Each bundle is sheathed in a protective plastic cover (figure 4.3).

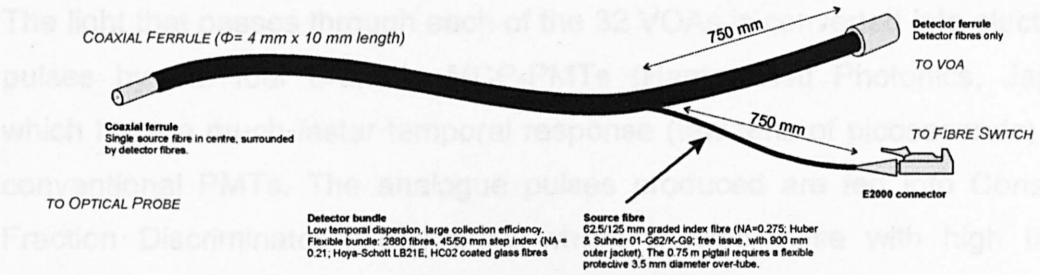

Figure 4.3 Schematic diagram of the coaxial fibre bundles.

These bundles are attached to the optical probes using connectors constructed from black, NIR absorbing plastic. More details about the optode connectors and the infant optical probes are given in chapters 5 and 6.

4.2.3 Variable Optical Attenuators (VOAs)

VOAs are custom-built electronic devices which limit the amount of light reaching each MCP-PMT channel to ensure that it does not saturate or damage the detectors. Each VOA is based on a rotating disc containing a series of pinholes of different diameter. They also ensure that the flux of photons is kept sufficiently small to prevent detection of multiple photons during each cycle (single photon counting limit: ~2.5×10^5 counts per second), and reduce the incidence of cross-talk between physically adjacent channels of the detector which may become significant if the corresponding count rates are very different. The VOAs are controlled via software, with settings pre-defined for each source position according to a so-called Acquisition Definition File (ADF). The ADF for an imaging experiment can be estimated or optimised empirically via an automated process that finds the VOA position corresponding to a predefined maximum count rate. During the performance of an infant head study, the VOA positions are determined immediately prior to data acquisition. An additional function of the VOAs is to provide a zero

transmission to protect the very sensitive MCP-PMTs from room light when an acquisition is not in progress.

4.2.4 Detectors and Electronics Processing

The light that passes through each of the 32 VOAs is converted into electronic pulses by the four 8-anode MCP-PMTs (Hamamatsu Photonics, Japan), which have a much faster temporal response (few tens of picoseconds) than conventional PMTs. The analogue pulses produced are fed into Constant-Fraction Discriminator (CFD) units where a logic pulse with high timing accuracy is produced. With this generated pulse and a reference pulse from the laser, the Picosecond Time Analysers (PTAs) calculate the arrival times of individual photons. The measured photon flight times are automatically recorded and stored in histograms (TPSFs) by the PTA. These data are transferred to the control PC following illumination at each source position (Schmidt, 1999). Later, the available measured TPSFs are mathematically processed prior to the image reconstruction.

4.2.5 MONSTIR Image Data Acquisition Software (MIDAS)

MIDAS is a computer program developed to: (i) control the hardware and data read-out of the MONSTIR system, (ii) perform the data acquisition by the use of the ADF file (which define the VOA settings, the exposure time and the order in which individual sources will be illuminated), (iii) read out the TPSF data from the PTAs, storing it in a binary file along with header information about the measurement, and (iv) monitor the flow of water used to remove heat from the Peltiers Cooler units which house the MCP-PMTs to reduce thermal noise.

4.2.6 MONSTIR Hardware Improvements

The initial MONSTIR prototype (figure 4.1) was completed in 2001 and used for the first time to perform 3D optical imaging of infants. However, some improvements to the MONSTIR system are currently being implemented. The

most important is new PC-based fast-timing electronics (Becker & Hick L, Germany). A router multiplexes the signals from all channels on each MCP-PMT to one of four timing units. Double-buffering of storage memory allows data to be acquired continuously without a delay to upload data. A new laser monitoring unit has been installed which continuously measures the laser output at both wavelengths and thus enables any variation in output to be calibrated. An alternative design of VOA is being introduced shortly, based on photographic film, allowing an increase in attenuation range from 2.2 to 4.2 optical densities (Jennions *et al*, 2006).

4.2.7 Processing & Treatment of data

This section involves a briefly description of the processing and treatment of experimental TPSF data (datatypes), which will be used for the software package for image reconstruction TOAST (**T**emporal **O**ptical **A**bsorption and **S**cattering **T**omography).

4.2.7.1 Calibration Measurements

In order to produce reliable datatypes, compensations must be made for the temporal response of the system. An Absolute Calibration measurement is required in order to determine the absolute *temporal* characteristics of each detector channel. This calibration involves an implicit assumption that the measurement of the time of arrival of the back-reflected light from the surface of the object is a good approximation for the temporal distribution measured if the source and detector were held in contact. Thus, the absolute calibration measurements (which produces two files: AbsCal_w_1.tps and AbsCal_w_2.tps) are obtained by illuminating each source in turn and measuring the light reflected at the surface of the object using the corresponding detector. A detailed discussion is given in (Hebden *et al*, 2003). A Source Calibration is also necessary to compensate for the *different lengths* of the source fibres. This procedure uses a calibration tool which consists of a clear resin cylinder with a small scattering target embedded and attached to an optical fibre and located in the centre of the cylinder. The source calibration (which also produces two

files: SrcCal_w_1.tps and SrcCal_w_2.tps) involves illuminating the target using each source fibre in turn, with a single detector coupled to the target. Fortunately the properties of the source fibres do not change significantly and this procedure needs to be performed just occasionally. These measurements enable the absolute temporal offsets to be obtained for all source-detector combinations (Schmidt *et al*, 2000). Thus, the calibrated TPSF for source *i* and detector *j* ($C_{i,j}$) can then be determined from the measured TPSF $M_{i,j}$ as follows:

$$C_{i,j} = (M_{i,j} * S_j) \otimes (A_j * S_i) \qquad [4.1]$$

where S_j represents a source calibration measurement for source ***j*** and detector ***x*** and A_j represents an absolute calibration measurement for source ***j*** and detector ***j*** coupled together, * represents a convolution operation and ⊗ represents a deconvolution operation.

4.2.7.2 Optode Positions

The optode positions on the helmet are measured (following each infant imaging experiment) using a 3D digitizer arm (Microscribe 3D, Immersion Corp., USA - figure 4.4). After acquiring a set of measurements defining the reference axes for the frame and the *zero reference*, each optode position is recorded (average of three measurements) using a sensitive probe, which gives the spatial coordinates. A few more positions are taken of the contours of the helmet itself to generate the mesh for the FEM, which will be used in the forward solver.

Figure 4.4 Digitizer arm recording the spatial coordinates of the plastic connectors.

4.2.7.3 Surface & Volume Mesh

The approach used to generate a volume mesh for image reconstruction is to warp a generic infant head shaped surface (previously generated, processed and stored as a triangulated surface mesh with 1437 nodes and 2872 elements) to conform to the measured optodes positions (figure 4.5) using MATLAB™ (the generic surface is translated, rotated, stretched linearly and the nearest node on the generic surface to each measured point is identified) and Visualization Toolkit (the warp process generates a new surface which passes through the measured points - VTK, Kitware, Inc., USA).

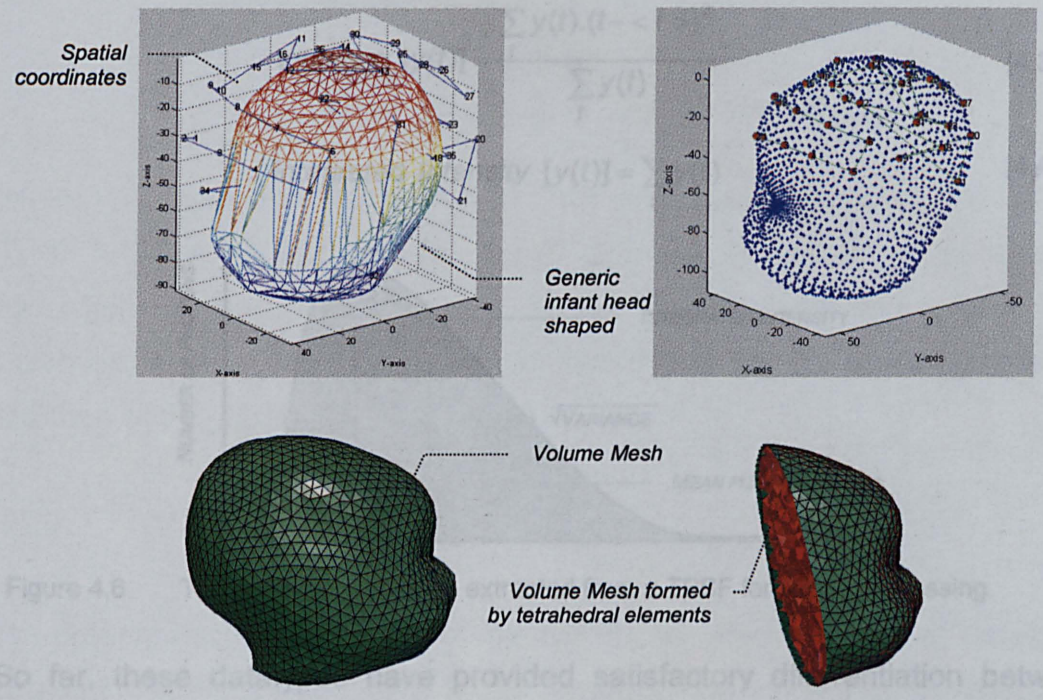

Figure 4.5 Surface and Volume meshes generated for modelling (Gibson *et al*, 2003a).

4.2.7.4 Datatypes from TPSFs and QM file

The full set of data from a single scan can consist of up to 1024 TPSFs for each wavelength ($s_1\_w_1$.tps ... $s_{32}\_w_1$.tps and $s_1\_w_2$.tps ... $s_{32}\_w_2$.tps). However, these data are a full temporal profile of the broadened laser pulse which was modified by the optical properties of the biological tissue. In order to significantly reduce memory requirements and computing time in the image reconstruction process, various specific characteristics are extracted from the

TPSFs (in the form of integral transforms), which are known as datatypes. The ideal TPSF is illustrated in figure 4.6 and the following equations ([4.2] to [4.4]) represent the datatypes commonly extracted from TPSFs for image reconstruction: the mean flight time, variance about the mean (or *central* variance), and integrated intensity (area under the curve). These datatypes are defined in terms of *y(t)* which is the discrete data (sampled every 5 ps) acquired by MONSTIR (Hillman, 2002).

$$< t >= \text{Mean flight time } [y(t)] = \frac{\sum_t y(t).t}{\sum_t y(t)} \quad [4.2]$$

$$\text{Variance } [y(t)] = \frac{\sum_t y(t).(t - < t >)^2}{\sum_t y(t)} \quad [4.3]$$

$$\text{Integrated Intensity } [y(t)] = \sum_t y(t) \quad [4.4]$$

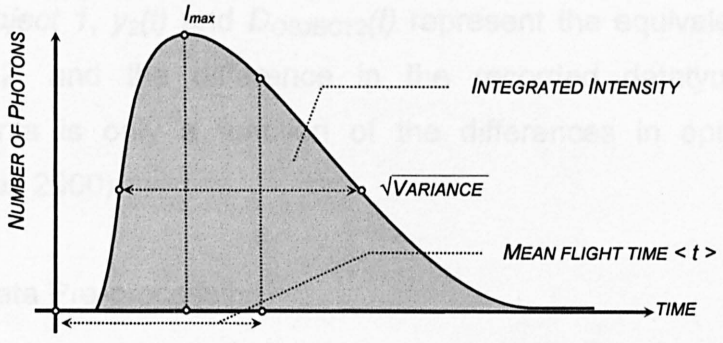

Figure 4.6 The common datatypes extracted from a TPSF for image processing.

So far, these datatypes have provided satisfactory differentiation between absorption and scatter, while being robust to the intrinsic noise present in the raw TPSFs (Hillman *et al*, 2000). The software used to generate the datatypes is known as MONSTIX, which also generates the QM file (Q = SOURCE, M = MEASUREMENT) that defines the location of sources and detectors on the surface of the object of study and also defines which detectors are active for each source.

4.2.7.5 Difference Imaging

Difference Imaging is a self-calibrating imaging technique and involves reconstruction of the difference between the properties of the object and a

reference medium (phantom), or differences in the object under different conditions (e.g. evoked response). This technique is less sensitive to the implicit errors in the measurements of the connector positions and additional calibration measurements are unnecessary (Hebden *et al*, 2003). It will also tend to cancel any instability due to the MONSTIR system which affects both the data acquired on the object and the reference with the same source and detector positions. Thus, it can be shown that relations between transformed convolved functions for meantime and intensity are:

$$Meantime\ [y_1(t)] - Meantime\ [y_2(t)] = \ldots \quad [4.5]$$
$$\cdots Meantime\ [D_{OBJECT1}(t)] - Meantime\ [D_{OBJECT2}(t)]$$

$$\log\left((Intensity\ [y_1(t)]\right) - \log\left((Intensity\ [y_2(t)]\right) = \ldots \quad [4.6]$$
$$\cdots \log\left((Intensity\ [D_{OBJECT1}(t)]\right) - \log\left((Intensity\ [D_{OBJECT2}(t)]\right)$$

where $y_1(t)$ represents the measured TPSF and $D_{OBJECT1}(t)$ represents the true TPSF for *object 1*, $y_2(t)$ and $D_{OBJECT2}(t)$ represent the equivalent parameters for *object 2*, and the difference in the recorded datatypes from both measurements is only a function of the differences in optical properties (Hillman *et al*, 2000).

4.2.7.6 Data Pre-processing

Pre-processing of the data is necessary to eliminate some datatypes contaminated by unacceptable levels of noise, which would otherwise cause artefacts in the reconstructed image. The first pre-processing step involves viewing the TPSF recorded for each source-detector combination (across the infant head) and reference phantom for the same source-detector pair, simultaneously (a programme was developed for this purpose VIEWTPSFS.m / **MATLAB™**), and rejecting those contaminated by noise. The common causes of noise are as follows:

(a) Pre-peaks, if light passes directly between adjacent optodes due to poor optode contact, the TPSF exhibits a large pre-peak (figure 4.7).

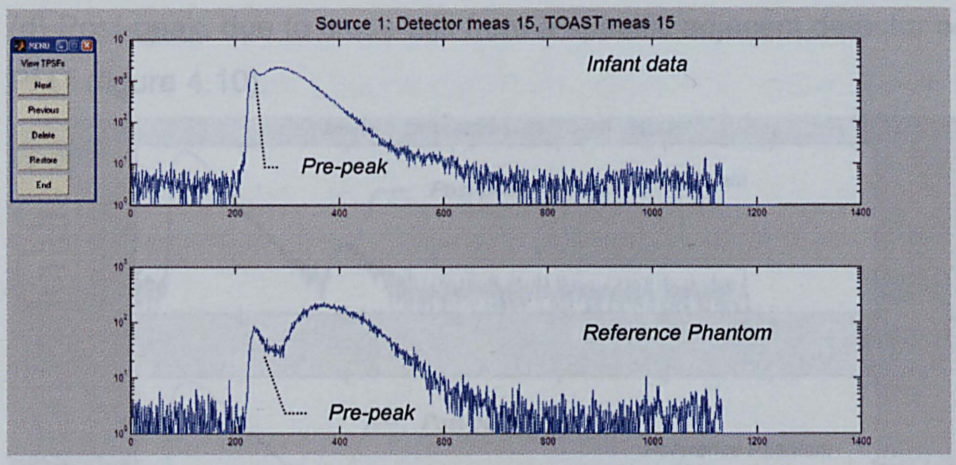

Figure 4.7 Both TPSFs are contaminated due to pour coupling between optode-infant head or -reference phantom, and in both cases are manifested as a large pre-peak. This source-detector pair is normally **rejected**.

(b)DC offset, this can be caused by (i) detected room light (due to poor optode contact) and (ii) excessive detector cross-talk (figure 4.8).

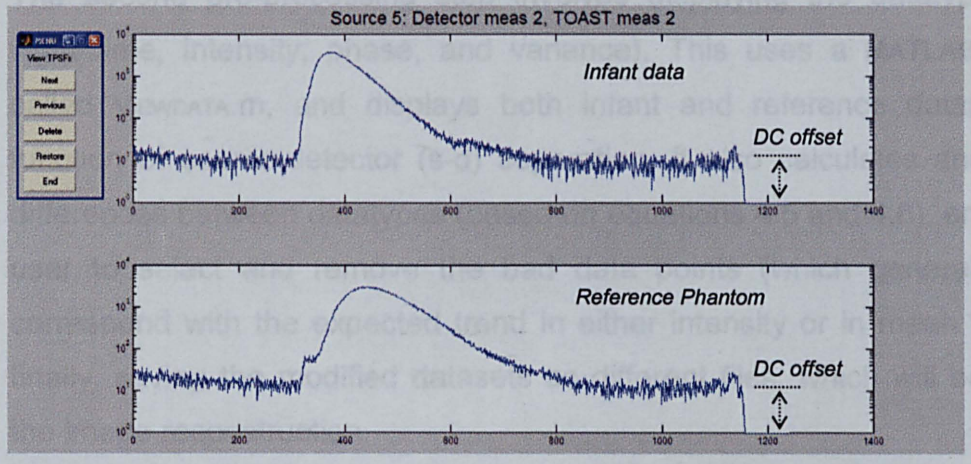

Figure 4.8 Both TPSFs are contaminated and the DC level which is probably from external light and the cross talk between neighbouring detector channels. This source-detector pair is normally **rejected**.

(c) Absence of signal in one or both measurements (figure 4.9).

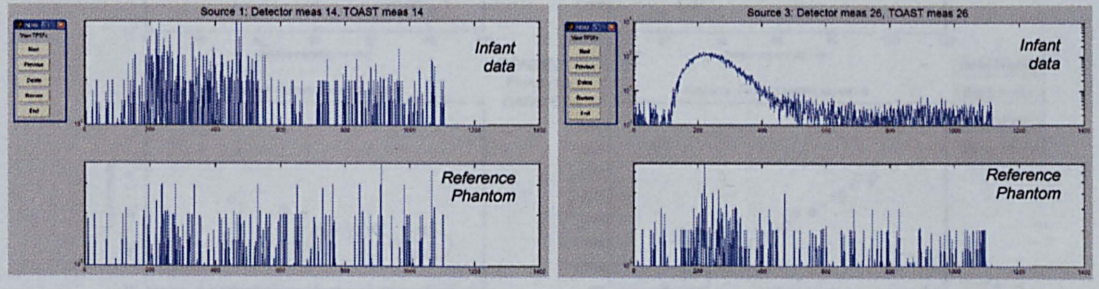

Figure 4.9 LEFT: No source signal. This source-detector pair is **rejected** and RIGHT: Reasonable coupling between source-surface of the infant head and very poor coupling between source-reference, which is probably of occurring due to the non-conformity of the surface of the phantom with the connector. This source-detector pair is **rejected**.

(d) Post-peak, due to cross-talk from a specific adjacent detector on the MCP-PMT (figure 4.10).

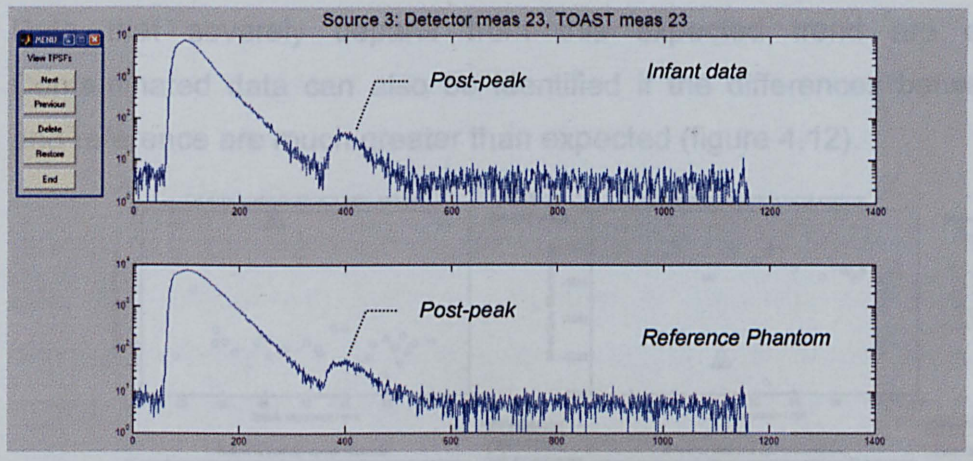

Figure 4.10 Cross talk due to between neighbouring detectors channels from one single MCP unit. This source-detector pair is normally **rejected**.

The second pre-processing step involves displaying the datatypes (mean flight time, intensity, phase, and variance). This uses a **MATLAB™** routine called VIEWDATA.m, and displays both infant and reference datasets as a function of source-detector (s-d) separation. It also calculates and displays differences between datatypes (based on equations 4.5 and 4.6), enabling the user to select and remove the bad data points (which generally do not correspond with the expected trend in either intensity or in mean time) and, finally, saving the modified datasets as different files, which will be used for the image reconstruction.

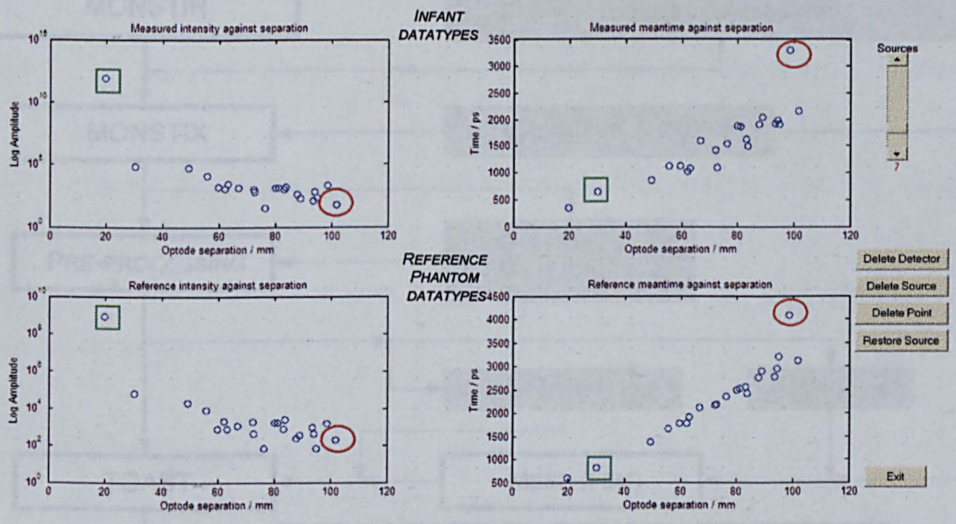

Figure 4.11 Deletion of "bad points" in intensity (□) and in mean time (○).

For instance, mean-time is expected to increase with the increasing separation, and the (natural logarithm of) intensity is expected to decrease. Data that severely departs from this expected trend are eliminated. Contaminated data can also be identified if the differences between object and reference are much greater than expected (figure 4.12).

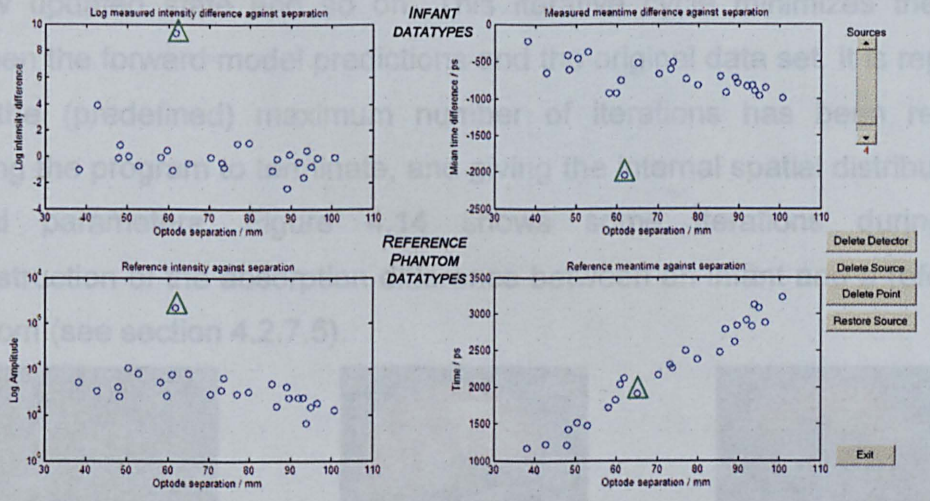

Figure 4.12 Deletion of "bad points" in difference between mean time data and reference mean time data (△).

The edited data are saved in new files, along with a new QM file. These files and the volume mesh are then used with TOAST to generate difference images. An illustration of this process is shown in figure 4.13.

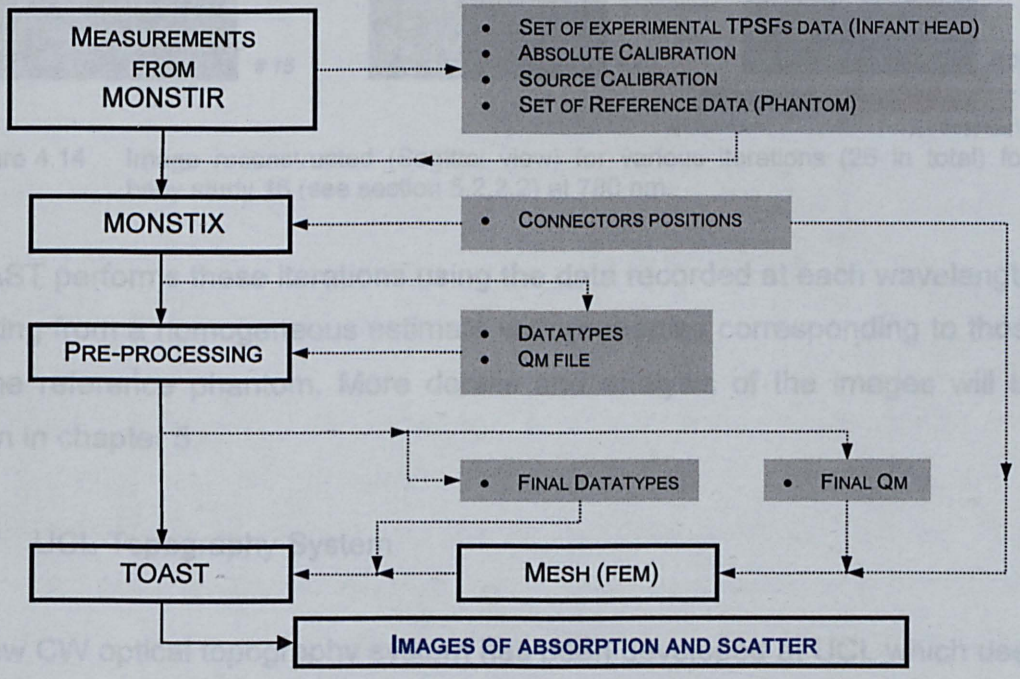

Figure 4.13 Data processing steps for 3D optical tomography.

The reconstruction method used by TOAST is a non-linear process, where the first prediction of the forward model (data_simulated$_1$) is compared with the measurements (data_real). The difference is used to update the forward solver and a second prediction is produced (data_simulated$_2$). This distribution is fed back into the forward solver to calculate a new error, giving a new updated state and so on. This iterative cycle minimizes the error between the forward model predictions and the original data set. It is repeated until the (predefined) maximum number of iterations has been reached causing the program to terminate, and giving the internal spatial distribution of optical parameters. Figure 4.14 shows some iterations during the reconstruction of the absorption difference between an infant and a reference phantom (see section 4.2.7.5).

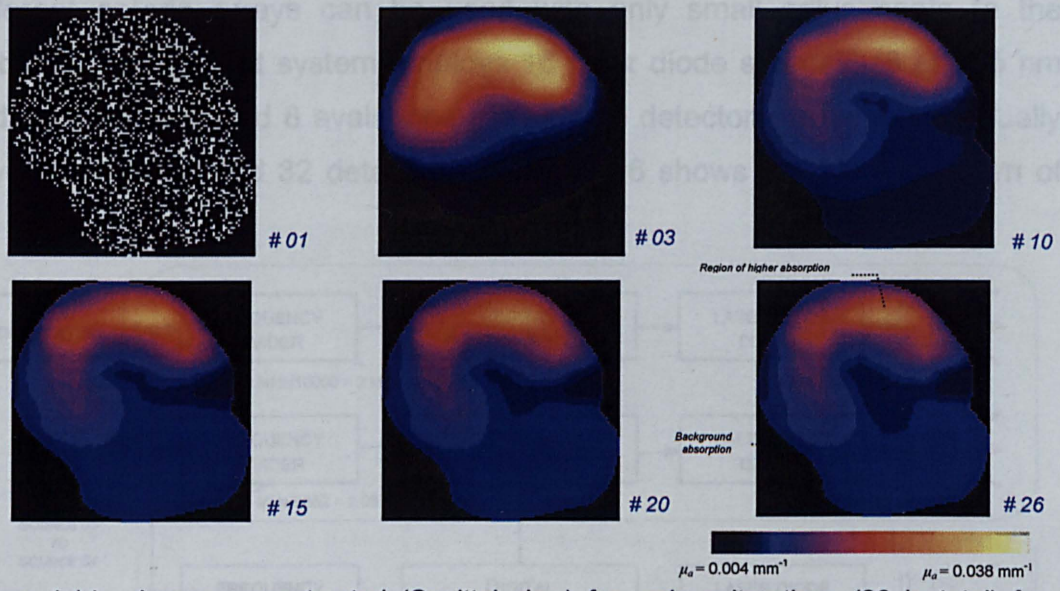

Figure 4.14 Image reconstructed (Sagittal view) for various iterations (26 in total) for baby study 16 (see section 5.2.2.2) at 780 nm.

TOAST performs these iterations using the data recorded at each wavelength, starting from a homogeneous estimate with properties corresponding to those of the reference phantom. More details and analysis of the images will be given in chapter 5.

4.3 UCL Topography System

A new CW optical topography system has been developed at UCL which uses software to demultiplex multiple source signals which are modulated at

different frequencies in parallel (figure 4.15) (Everdell *et al*, 2005). This novel approach increases the flexibility in the positioning of sources and detectors compared to other systems that require multiple lock-in amplifiers (e.g. Hitachi ETG 100 optical tomography system described by Yamashita *et al* (1999)).

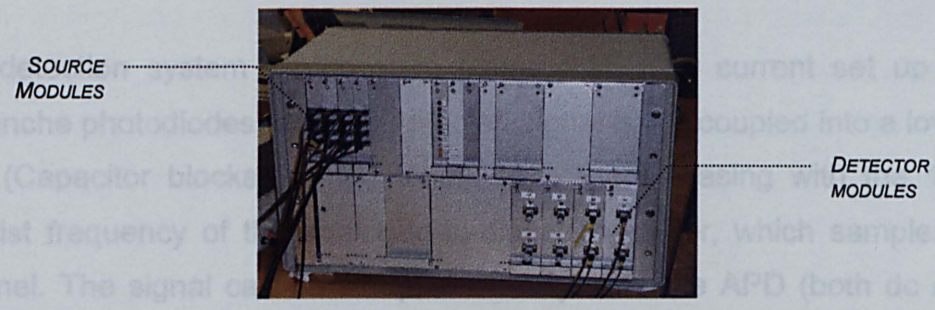

Figure 4.15 UCL topography system with 16 laser sources and 8 photodiode detectors.

Different optode arrays can be used with only small adjustments to the software. The current system employs 16 laser diode sources, (8 at 785 nm and 8 at 850 nm) and 8 avalanche photodiode detectors, but may eventually have 64 sources and 32 detectors. Figure 4.16 shows the block diagram of the laser source.

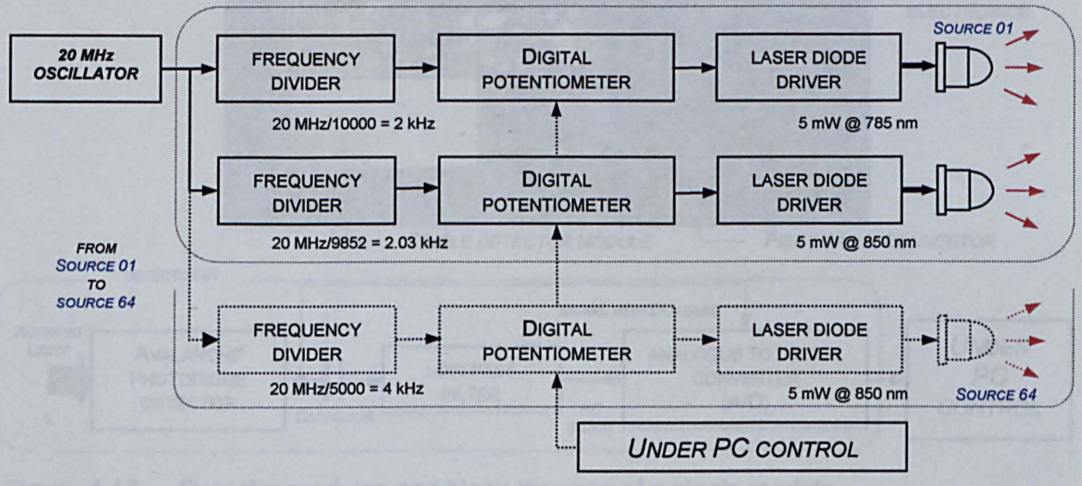

Figure 4.16 Block diagram of laser sources.

To reduce the frequency drift between the different sources, a single 20 MHz quartz crystal oscillator provides all the frequencies to encode the square waves that are used to modulate the emitted light intensity from the diode lasers. A frequency divider reduces the original frequency to tens of kHz and to a unique frequency value, for each laser source. The square waves modulate the 16 laser diode sources, driven by frequencies ranging from 2 to

4 kHz. The frequencies are kept within one octave to prevent any possible interference from harmonics. Changes in light intensity of the sources are realized by a software-controlled digital potentiometer, with a mean power emitted per laser diode of ~2 mW.

The detection system is shown in figure 4.17. The current set up has 8 avalanche photodiodes, and the detected signal is AC coupled into a low-pass filter (Capacitor blocks the DC level), to prevent aliasing with the 10 kHz Nyquist frequency of the analogue-to-digital converter, which samples each channel. The signal can be sampled directly from the APD (both dc and ac components) or from the output of the low-pass filter (just an ac component). To separate the measurement signal from the different sources, a Fast Fourier Transform is applied. This new approach reduces the cost of increasing the number of channels which is usually achieved by introducing further lock-in amplifiers. A spatial map can be made with signal from the sampled tissue (Everdell *et al*, 2005), (Everdell *et al*, 2004).

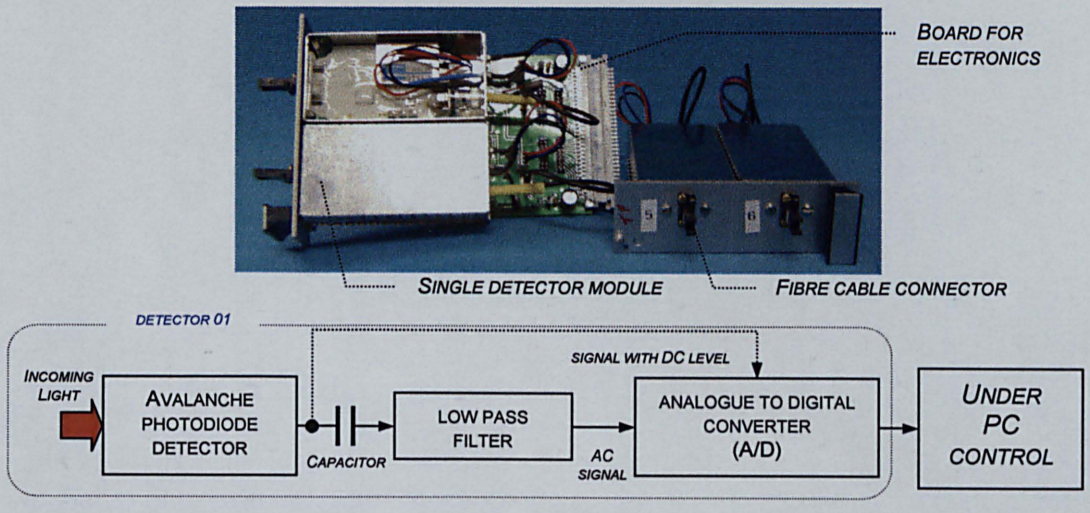

Figure 4.17 Detector modules and block diagram of a single module.

The system is designed to produce images at 10 frames per second with a maximum of 32 detectors. However, the reduction of the number of detectors can increase the image rate (e.g. 40 frames/s with 8 detectors or even faster), which may enable imaging of fast physiological events, such as fast neuronal response in the brain (Francheschini and Boas, 2004).

A linear reconstruction algorithm is used for the UCL topography system to recover differences in absorption occurring near the surface and has been used to produce maps of cortical activation due to passive motor stimuli. This linear technique is more appropriate when reference data are available, which closely match the data of interest. Ideal data are those acquired before and during a change (e.g. due to cortical activation by stimuli), and provides a superior image quality when compared with non-linear reconstruction (Gibson *et al*, 2005b). More details and analysis of the imaging process will be given in chapter 6.

Chapter 5

Performance of the Optical Tomography Head Probes

5.1 Introduction

The ability to acquire optical imaging measurements from the heads of newborn infants has been limited by the lack of appropriate probes which can be (safely) attached to the head. In this section, new designs of probes for tomography are introduced and their performance is evaluated. The broad objective is to design a device to hold an array of optodes against a baby's head so that useful data can be measured reliably, easily and safety. The criteria for evaluation of the probes include the comfort and safety of the probes, the quality of the recorded data, the sensitivity to (head) movement and ambient light, and the effectiveness of coupling to the head (prevention of light leaking between source and detector bundles fibres around the surface of head). Initially, the design, characteristics and manufacture of the custom-made helmets will be presented, and their evaluation based on the quality of data and image reconstructions acquired for clinical measurements. Thereafter the development of adaptable helmets (prototypes I, II and III) will be presented including the results of clinical measurements performed so far and a comparison between the prototypes and custom-made helmets.

5.2 Analysis of the custom-made helmets (CMHs)

5.2.1 First custom-made helmet prototype

The first prototype of fibre holder was a custom-made helmet, which was manufactured by directly moulding a rigid thermoplastic™ (which becomes flexible when it is warmed - WFR/Aquaplast Co. Wyckoff, NJ) using a cardboard template. The template was generated by taking transverse, coronal and sagittal digital photographs of the infant's head. The photographs were processed and scaled to real size, and the final cardboard template also included a 10 mm margin for the insulating foam. The template was used to make a suitable base for the back of the head and a T-shaped component which was attached to the forehead. The two parts had 32 plastic connectors. Each plastic connector (known as *monstode*) was made of black NIR absorbing plastic and used to hold the source fibres and the detector bundles

at a distance of ~10 mm from the tissue surface (the first measurements employed separated source and detector fibres, although these later become integrated). A plastic base with 3 pillars was made to anchor the helmet and to help support the weight of the fibre bundles (figure 5.1).

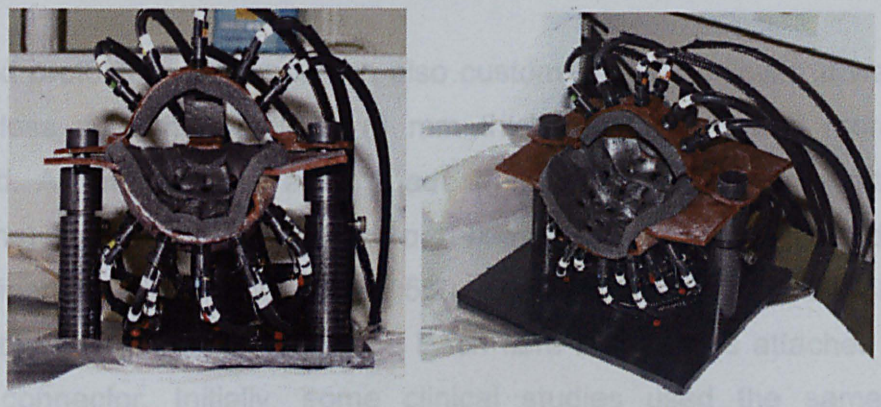

Figure 5.1 The first fibre holder. Extracted from (Hillman, 2002) (p278).

The very first clinical study using a custom-made helmet (CMH) was performed on a healthy baby, 30 week gestation age. During the clinical study, the infant was held in the *imaging cot* for a total of 2.5 h and showed no signs of discomfort or even marks (i.e. red spots) on the skin surface of the head after data acquisition. This clinical study allowed evaluation of the effectiveness of calibration techniques. Preliminary 2D image reconstructions of oxygen saturation and blood volume were generated from 10 source-detector locations confined to a single ring around the head. However, the first CMH showed some limitations, such as:

- a prolonged period of the manufacture, which took ~48 hours to mould the parts into a like-head surface and to attach the 32 plastic connectors to the parts;
- light leakage from the T-shape part of the forehead;
- some detectors at the base of the neck were obscured by the foam lining;
- the attachment of the optical bundles was time consuming due to the number screws used to hold them in place;
- the T-shaped component gave only limited coverage of the top of the infant's head, and
- a higher density of illuminating points over the back of the head (22 bundles or 67% of the total).

More details about this prototype and the plastic connector are given in (Hillman, 2002).

5.2.2 Second custom-made helmet prototype

The next prototype of helmet was also custom-made. However, it was made with a less rigid thermoplastic (3 mm thickness), which was more easily moulded. A template was again made from photographs (three orthogonal directions) and used to make a two-part helmet. The two parts were designed to be joined, forming a shell (figure 5.2). The interior surface of the shell was lined with soft NIR absorbing foam. Each fibre bundle was attached using a plastic connector. Initially, some clinical studies used the same plastic connectors used for the first helmet. However, a new design of connector was manufactured to accommodate the new integrated fibre bundles (shown in figure 4.3).

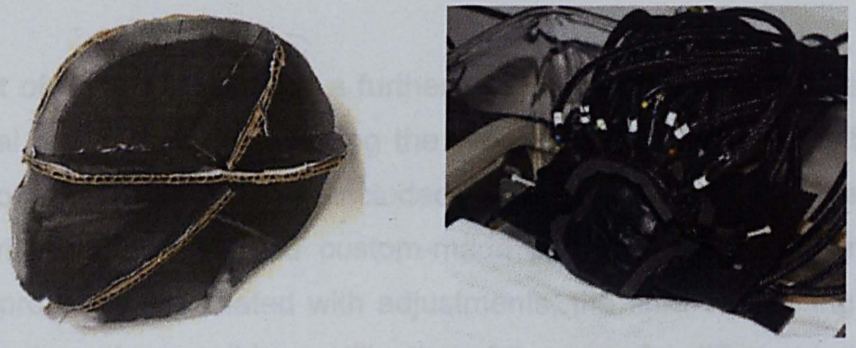

Figure 5.2 (a) A cardboard representation of the infant's head, and (b) the custom-made helmet attached with the fibre bundles from MONSTIR.

Several clinical studies were performed using this helmet including those described in Hebden *et al* (2002), which reported the first 3D images of the newborn infant brain using transmitted light, and Hebden *et al* (2004), which described 3D optical tomography of induced haemodynamic and blood oxygenation changes within the brain of a ventilated newborn infant. Table 5.1, extracted from Austin *et al*, (2006), summarizes the series of 14 clinical studies that successfully acquired full sets if imaging data using 14 distinct customised helmets.

Table 5.1 Details of 14 babies scanned with MONSTIR using Custom-made helmets.

BABY DETAILS					
BABY STUDY #	BIRTH AGE [WEEKS^{+DAYS}]	AGE AT STUDY [DAYS]	CORRECTED AGE [WEEKS^{+DAYS}]	CLINICAL CONDITION	COMMENTS
1	30^{+0}	12	31^{+5}	PRETERM BILATERAL IVH LEFT>RIGHT	IMAGE RECONSTRUCTED (HEBDEN *ET AL*, 2002)
2	39^{+0}	46	45^{+4}	HEALTHY TERM	INSUFFICIENT LIGHT ACROSS THE HEAD
3	37^{+0}	3	37^{+3}	SEVERE BIRTH ASPHYXIA	VOLUME AND OXYGENATION DIFFERENCE IMAGING (HEBDEN *ET AL*, 2004)
4	25^{+5}	42	31^{+5}	RIGHT HPI	ON CPAP, DID NOT TOLERATE HELMET
5	32^{+6}	27	36^{+5}	PRETERM	ABANDONED DUE TO MOVEMENT
6	28^{+5}	38	34^{+1}	PRETERM BILATERAL IVH	POOR OPTODE CONTACT
7	28^{+5}	40	34^{+3}	PRETERM	IMAGE RECONSTRUCTED
8	32^{+1}	28	36^{+1}	PRETERM TWIN, LOW HB COUNT	IMAGE RECONSTRUCTED
9	32^{+1}	28	36^{+1}	PRETERM TWIN	POOR OPTODE CONTACT
10	29^{+0}	39	34^{+4}	PRETERM TWIN	IMAGE RECONSTRUCTED
11	29^{+0}	39	34^{+4}	PRETERM TWIN, LEFT IVH	IMAGE RECONSTRUCTED
12	26^{+1}	92	39^{+2}	PRETERM	POOR OPTODE CONTACT
13	32^{+1}	25	35^{+5}	PRETERM	IMAGE RECONSTRUCTED
14	32^{+1}	25	35^{+5}	PRETERM	IMAGE RECONSTRUCTED
IVH: INTRAVENTRICULAR HAEMORRHAGE				HPI: HAEMORRHAGIC PARENCHYMAL INFARCT	
CPAP: CONTINUOUS POSITIVE AIRWAY PRESSURE				HB: HAEMOGLOBIN	

5.2.2.1 Manufacture of the CMHs

As a part of this Ph.D. project, a further five customised helmets were made for clinical measurements following the procedure previously described. The design of these prototypes included modifications to the mechanical characteristics of the second custom-made prototype. These attempted to address problems associated with adjustments, the time consuming process of manufacture, the possible re-utilisation of the parts for different babies, and the quality of the data for image reconstruction. Figure 5.3 shows the parts of one of these latter CMHs.

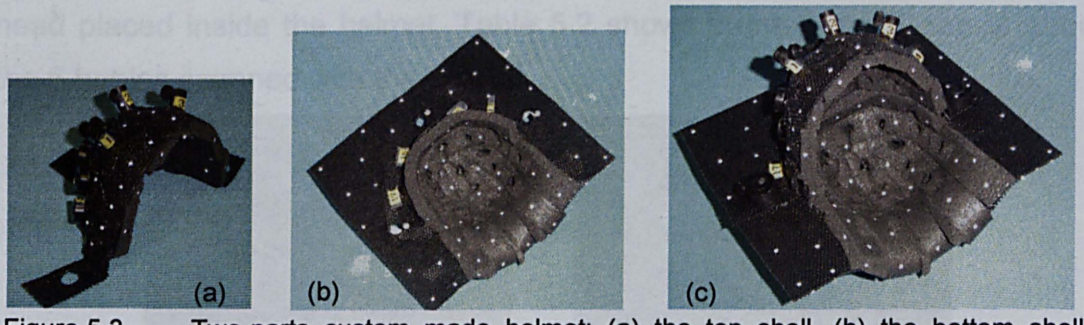

Figure 5.3 Two-parts custom made helmet: (a) the top shell, (b) the bottom shell (note a circular ring) and (c) the final helmet

After the manufacture of each customised helmet (~ 6 to 10 h per helmet) and a few days before the clinical study, one or more fitting-checks were made to

evaluate the quality of the fit and the coupling of the plastic connectors to the baby's head (time required ~15 minutes). Figure 5.4 shows a baby during an initial check of a custom-made helmet, assisted by a nurse.

Figure 5.4 Baby performing a fitting-check of the custom-made helmet.

In comparison with the first helmet described in section 5.2.1, later prototypes had:

- a more uniform distribution of the 32 optodes over the surface of the head;
- more flexibility in the helmet design provided by the new plastic connectors, and
- a more rapid attachment of the integrated fibre bundles.

5.2.2.2 Clinical measurements and Performance of CMHs

All the babies were preterm and each study began immediately following a feed (when the infant would most probably sleep). The helmets were cleaned and sterilized beforehand, and parental consent was obtained to perform the experiments. Figure 5.5 shows a baby comfortably settled in the cot with the head placed inside the helmet. Table 5.2 shows some general details about the 5 babies scanned with the CMHs.

Figure 5.5 Baby settled inside the cot with the custom-made helmet during a clinical study.

Table 5.2 Details of 5 babies scanned with MONSTIR using CMHs.

BABY DETAILS					
BABY STUDY #	BIRTH AGE [WEEKS^{+DAYS}]	AGE AT STUDY [DAYS]	CORRECTED AGE [WEEKS^{+DAYS}]	OFC* [cm]	CLINICAL CONDITION
15	26^{+1}	92	36^{+1}	32	PRETERM HEALTHY
16	32^{+1}	25	35^{+5}	34	PRETERM HEALTHY
17	32^{+1}	25	35^{+5}	34	PRETERM HEALTHY
18	28^{+0}	48	34^{+6}	35	PRETERM HEALTHY
19	31^{+1}	35	36^{+1}	29.3	PRETERM HEALTHY

*OCCIPITOFRONTAL CIRCUMFERENCE (OFC). FOR THE CORRECTED AGE ABOVE THE EXPECTED RANGE OF OFC IS ~30 TO 35 CM (SEE FIGURE 5.9).

The studies were performed at the cotside with the fibre bundles attached on the helmet. The typical sequence employed for static imaging is summarised in table 5.3.

Table 5.3 Data recording with MONSTIR system and using Custom-made helmets.

GENERAL SEQUENCE		
	SEQUENCE	COMMENTS
1	ADF DATA ACQUISITION	AUTOMATED PROCESS FOR OPTIMIUM POSITIONS OF THE VOAS (~ 20 MIN).
2	DATA IMAGE ACQUISITION	STATIC IMAGE ACQUISITION (~ 12 MIN PER DATASET).
3	CALIBRATION DATA ACQUISITION	ABSCAL#_W_1.tps & ABSCAL#_W_2.tps.
4	REFERENCE DATA ACQUISITION	FIT OF THE REFERENCE BALLOON INSIDE THE HELMET, FILLING IT WITH INTRALIPID SOLUTION (~ 20 MIN) & ACQUISITION (~ 12 MIN).
5	CONNECTOR POSITIONS	MEASUREMENTS MADE WITH DIGITISER ARM FOR FEM MODEL (~ 15 MIN).

Data are composed of a set of TPSFs from which various datatypes are extracted (section 4.2.7.4). For image reconstruction less sensitive to inaccuracies in the optode position measurements, a difference imaging method is performed (section 4.2.7.5). Initially this involved acquiring a set of TPSFs from a homogeneous reference phantom (a white rubber balloon – figure 5.6) filled with a scattering fluid (mixture of 10% Intralipid^{TM}, water-soluble NIR dye, and distilled water) and with overall optical properties of μ_s' = 1 mm^{-1} and μ_a = 0.01 mm^{-1}. These values are chosen to be within the range of the properties of grey and white matter of neonatal brain tissue (van der Zee 1992). The balloon is attached via plastic tubing to a reservoir containing the scattering fluid, with valves and a 60 ml syringe in the circuit to facilitate filling and emptying of the balloon. A validation of this technique has been performed using appropriate phantom experiments (Yusof *et al*, 2003). The disadvantage of this approach is the tendency of the near-spherical balloon not to deform sufficiently to make contact with all the optodes in the helmet, which results in a loss of data. Later, the optode positions are measured with a digitiser arm. A more detailed sequence is given in section 5.3.2.1.

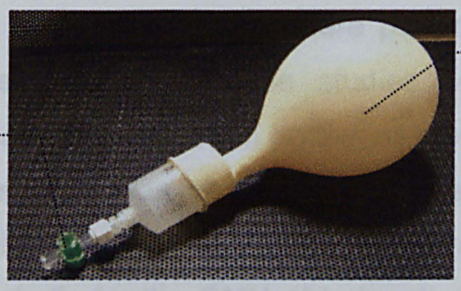

Figure 5.6 The homogeneous reference phantom.

The quality of the data acquired using a customised helmet is dependent on the coupling between the surface of the baby's head and the optical optodes attached to the helmet. Poor coupling can contaminate the data with ambient light and/or light leakage between sources and detectors around the surface of the head. Thus, the quality of the data provided by the helmets may be evaluated quantitatively by considering the percentage of *un-rejected data*, which is determined from the final QM file (sections 4.2.7.4 and 4.2.7.6), and from the original ADF (section 4.2.3). The table 5.4 shows the values of this percentage for each customised helmet used with the respective babies and the final average performance.

Table 5.4 Evaluation of custom-made helmets.

PERFORMANCE OF THE CUSTOM MADE HELMETS					
BABY STUDY	15	16	17	18	19
THE TOTAL NUMBER OF CHANNELS	1024	1024	1024	992	992
CLOSED CHANNELS ("0") – ADF	73	96	46	86	136
ACTIVE CHANNELS (AC)	951	928	978	906	856
QM FILE (UN-REJECTED DATA – URD)	272	480	721	454	456
REJECTED DATA (= AC - URD)	679	448	257	452	400
PERFORMANCE OF EACH HELMET (= (URD/AC).100%)	**28.6%**	**51.7%**	**73.7%**	**50.1%**	**46.7%**
AVERAGE PERFORMANCE	**50.2 ±16.1%** (55.6 ± 12.3% WITHOUT BABY STUDY 15)[1]				
[1] AVERAGE PERFOMANCE DESCONSIDERING THE SMALLEST PERFORMANCE OF THE STUDIES					

The performance of the customised helmet for baby study 15 shows a significantly higher rate of rejected data (the lowest performance of the five studies), which is due to excessive contamination of the data by ambient light and light leakage. In an attempt to reduce further contamination in following studies, the procedures for moulding the shells, attaching the plastic connector and fitting were reviewed to improve the conformity of the shells with the babies' heads.

The subsequent baby studies 16 and 17 were performed on the same day (twins with the same OFC). For these studies two top sections were manufactured to be used with a common bottom section. Although, the helmet performance of both studies was above 50% of useful data (including the highest performance of the five studies), it was highly varied. A particular large non-conformity of the shells for the CMH of baby study 16 was noted. Thus, the two parts of the helmet (top and bottom sections) should be custom made for each baby and re-utilization of parts was avoided for the next two studies. Both performances were slightly near 50% of useful data (the performance of each helmet was 50.1% (baby study 18) and 46.7% (baby study 19)). Some head movement and discomfort (crying) was noticed during baby study 19, which is a likely cause of reduced performance of the customised helmet during the experiment. Images were successfully reconstructed from four of the five studies. Just one experiment (baby study 15 - table 5.2) failed to provide sufficient data. For instance, figure 5.7 shows coronal, transverse and sagittal views across the 3D images of baby study 17 and represents the distribution of absorption at 780 and 815 nm respectively.

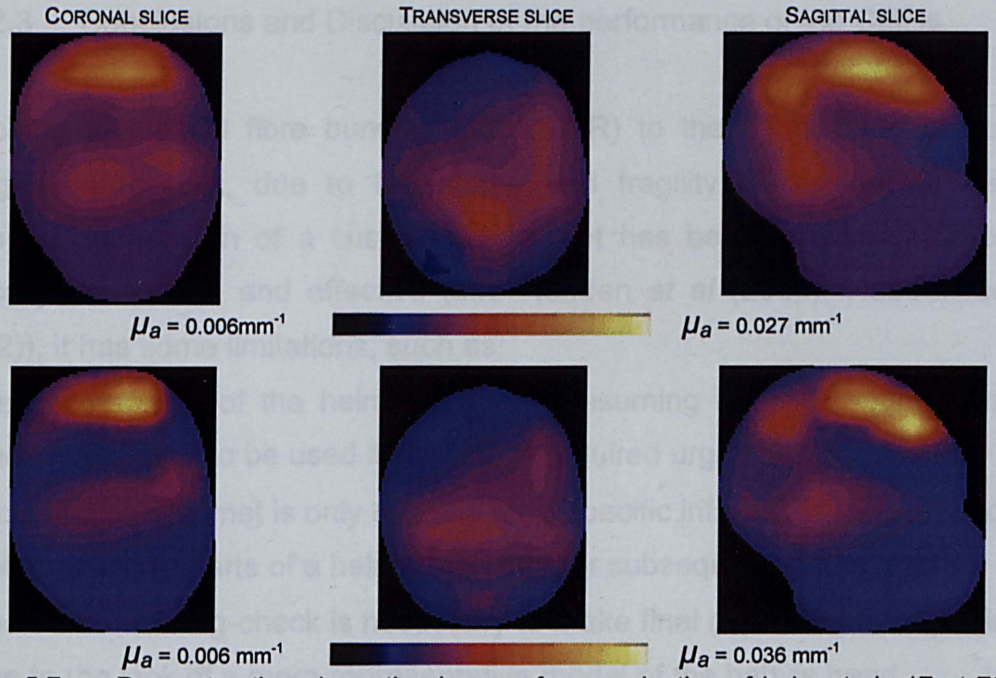

Figure 5.7 Reconstruction absorption images from evaluation of baby study 17 at 780 (top) and 815 nm (bottom).

The coronal and transverse slices are centred on the expected locations of the cerebral ventricles. The coronal slices exhibit a horizontal band of reduced

absorption across the image, which is probably due to light pathway through the CSF-filled regions, via Sylvian fissures as illustrated in figure 5.8. The current inability of TOAST to model non-scattering regions contributes towards this feature. Until more sophisticated reconstruction techniques can be employed (Riley *et al*, 2000), this and other possible object-dependent artefacts must be taken into account when attempting to interpret optical tomography images of the newborn infant brain.

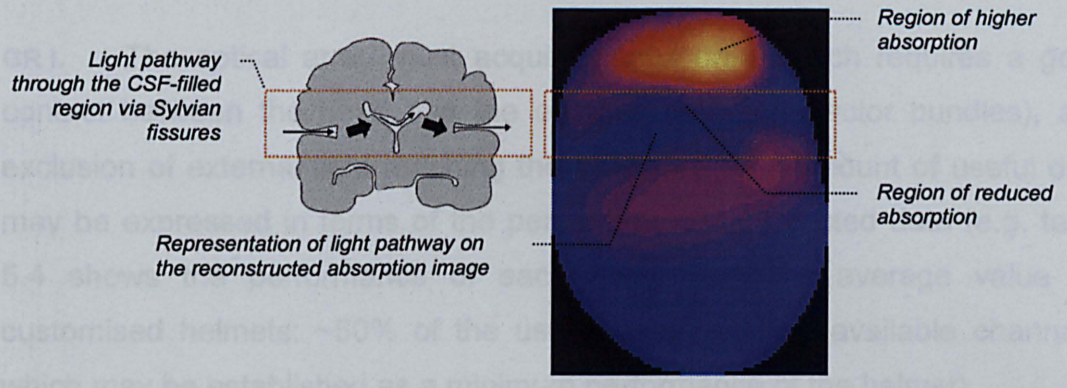

Figure 5.8 LEFT: a path which light can take across the brain, via the CSF-filled Sylvian fissures and the central ventricular system with a minimum scatter. RIGHT: A Coronal slice shows a region of low absorption and minimal scattering.

5.2.2.3 Conclusions and Discussion of the performance of the CMHs

Attaching 32 optical fibre bundles (MONSTIR) to the infant head is not a straightforward task, due to the shape and fragility of the baby's head. Although, the design of a customised helmet has been proven to be both clinically acceptable and effective (see Hebden *et al* (2004), Hebden *et al* (2002)), it has some limitations, such as:

- the construction of the helmet is time consuming (6 – 10 hours), which does not allow it to be used if imaging is required urgently;
- a customised helmet is only suitable for a specific infant (it is recommended not to re-utilize parts of a helmet for another subsequent study), and
- one or more fitting-check is necessary to make final adjustments, especially due to the lack of a more representative model of the baby's head.

Therefore, an adjustable or adaptable helmet is required to accommodate a large range of head shapes and sizes, and to overcome the limitations of the custom-made helmets.

5.2.2.4 General Recommendations (GR)

The design of a device to hold an optical array against an infant baby's head can be specified in terms of essential and desirable requirements, which help to gather useful and reliable data easily and safely. Based on experiences with the custom-made helmets, these requirements can be specified as follows:

GR I. The optical array must acquire useful data, which requires a good contact between the head and the optodes (source/detector bundles), and exclusion of external light reaching the detectors. The amount of useful data may be expressed in terms of the percentage of un-rejected data (e.g. table 5.4 shows the performance of each helmet and its average value for customised helmets: ~50% of the useful data from the available channels, which may be established as a minimum performance of the helmet).

GR II. The probe must have a rigid geometry to allow accurate and stable measurement/determination of the locations of the fibre bundles. The method of difference imaging relies on identical optode positions for infant and reference measurements. This improves the accuracy of reconstructions by removing systematic errors and eliminates the effect of coupling coefficients on the intensity measurements.

GR III. The probe must be portable and accommodate a baby's head safely, and be quickly and easily removed for emergency nursing care.

1. The portability of the probe is desirable to enable MONSTIR to be used at the cotside in intensity care. Figures 5.1 and 5.2 show helmets, which are portable and can be easily accommodated inside cots.
2. It is desirable to easily and safely attach and de-attach the fibres bundles from the connectors of the helmet, without specialized skills or tools.
3. It must be possible to access to the baby quickly for emergency nursing care, with parts of the helmet easily and safely removed from the rest of the frame.

4. The surfaces in contact with the baby must be covered with protective soft foam and must not cause pressure marks on the infant's head.
5. Protective or supporting parts of the helmet must not exert excessive pressure on the infant's head.
6. The natural cavities (ears, nose and eyes) must be completely shielded from the incident NIR-light, especially the eyes.
7. It is desirable that the whole structure of the helmet is compatible with other medical apparatus (e.g. nasal tubes, feeding lines).

GR IV. The optical array must provide an adequate yet safe exposure of the skin to each source fibre (the profile of the light emerging from the current source fibre is Gaussian).

1. It is desirable that the angle between the beam and skin surface is 90 degrees.
2. The optical connector must maintain the ends of the fibres at a distance of ~10 mm above the scalp, illuminating a circular area of 6 mm diameter (see figure 5.10).

GR V. The probe must support the weights of the baby's head and the attached fibre bundles without collapsing. If we make the reasonable assumption that the weight of an infant head is no greater than 25% of the total weight, it is possible to estimate the minimum weight which the probe must support. Figure 5.9 gives the maximum weight of 4.5 kg at full-term, and consequently a weight of the baby's head is ~1.13 kg. The total weight of the 32 fibre bundle is ~0.8 kg. Thus, the minimum weight which the probe must support is ~2 kg.

GR VI. The optical array needs to be adaptable to a large range of sizes and shapes of babies heads, providing maximum possible coverage of the scalp for 3D image reconstruction of the brain. The overall head shape is closely related to the bony structures of the skull and the shape of the underlying brain. Any alterations of the head shape can be the result of unusual brain growth or effects of illnesses (see section 2.5). A common and practical method of evaluation of the skull size and shape is to use the chart of head

circumference versus (gestational) age (figure 5.9). This chart is used to give an estimated range of head size that the optical probe should accommodate. Thus, the gestational age range from 24 to 40 weeks gives a range of head diameter of ~6 to 11.2 cm (or ~22 to 35.2 cm of head circumference or occipitofrontal circumference, OFC).

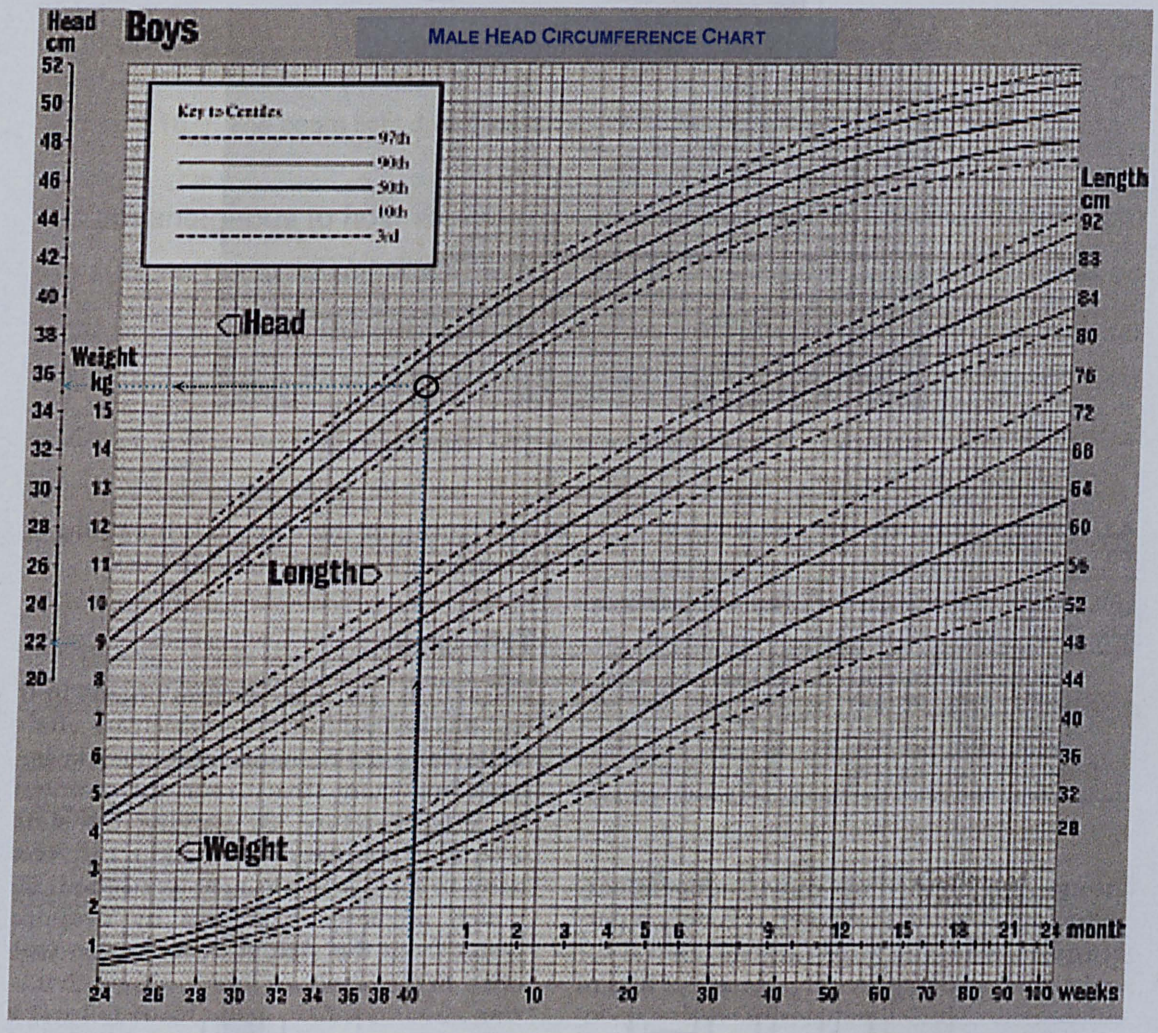

Figure 5.9 Male head circumference chart (sizes for girls are fractionally smaller). Extracted from (Johnston, 1998) (p45).

5.3 Adaptable Helmets (AHs)

5.3.1 Adaptable helmet prototype I

The first prototype of the AH was developed using the same sort of flexible thermoplastic used for the custom-made helmets, and a new plastic connector was designed to allow radial translation of the fibre bundles. The dimensions

of the connector and its open aperture are largely dictated by the divergence of the source beam, as shown in figure 5.10.

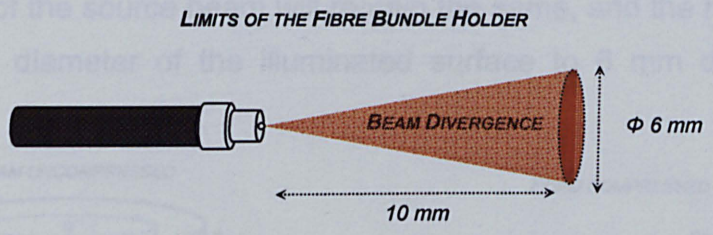

Figure 5.10 The beam light divergence.

It is advantageous to hold each source-detector optode at some distance from the surface because: (a) illuminating a larger area allows a higher power to be used before exceeding safety limits for skin irradiance (Maximum Permissible Exposure, MPE ~ 2 mW/mm^2 – (Schmidt, 1999)), (b) the larger area also reduces the influence of small head movement, the presence/movement of hairs (small scale irregularities at the head surface), which brings benefits to the reconstruction algorithm (see section 4.2.7.5), and (c) the connectors provide extra protection to the tip of the bundle and reduce the risk of it being damaged. Thus the connector design holds the optode at a distance of approximately 15 mm from the surface of the uncompressed foam, providing an illumination area of the diameter 6 mm. Figure 5.11 shows the final design of the fibre bundle connector.

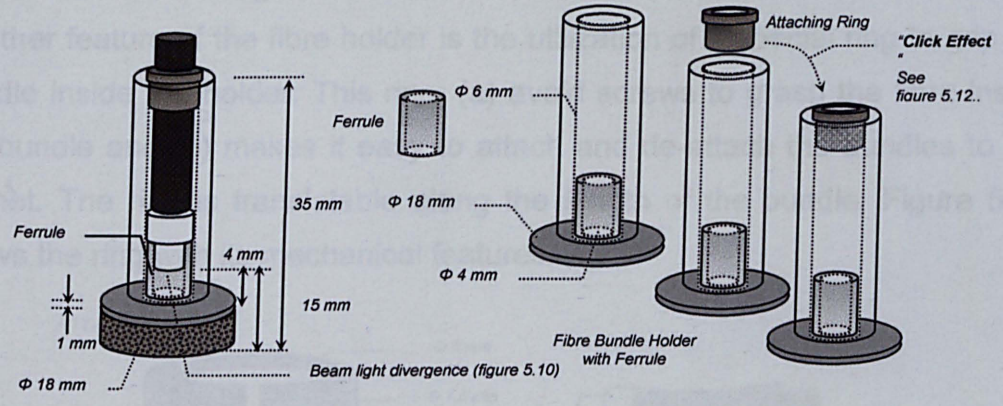

Figure 5.11 The Fibre Bundle Holder with ferrule and attaching ring.

When the fibre cable holder is used in phantom studies and clinical measurements, the flange's foam is (carefully) compressed against the infant head (or phantom), changing its thickness and consequently the distance of

the ferrule from the surface. The design of the holder takes into account that the thickness of the foam will be altered by a few millimetres. However, the divergence of the source beam will remain the same, and the hole in the foam restricts the diameter of the illuminated surface to 6 mm diameter (figure 5.12).

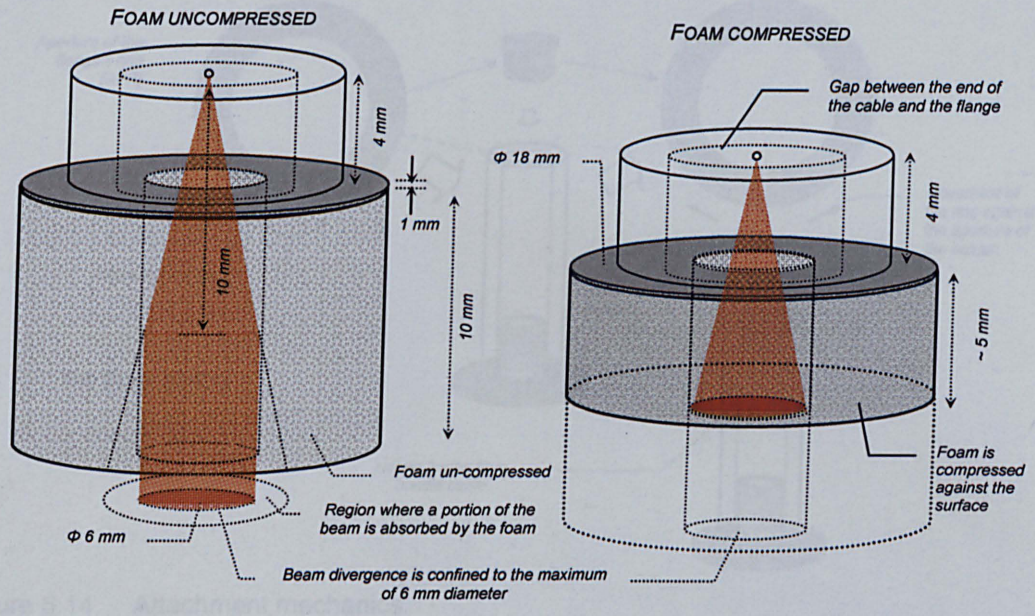

Figure 5.12 The effect of compression on the flange's foam and the divergence of the light beam: (a) the foam is not compressed – the distance source-detector to the surface is ~15 mm and part of the beam is absorbed by internal walls of the NIR absorbing foam, given a final area with a 6 mm diameter; (b) the foam is compressed – and compression reduces the thickness of the foam to about half, and the final area illuminated is about the same.

Another feature of the fibre holder is the utilization of a special ring to grip the bundle inside the holder. This ring: (a) avoid screws to grasp the fibre inside the bundle and (b) makes it easy to attach and de-attach the bundles to the helmet. The ring is translatable along the length of the bundle. Figure 5.13 shows the ring with its mechanical features.

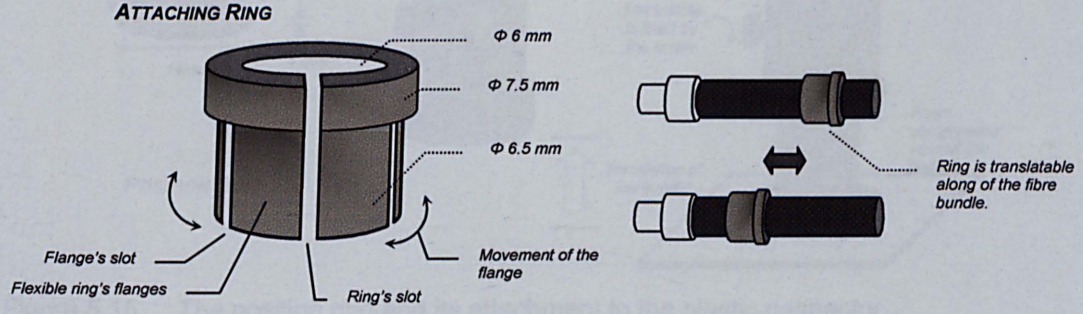

Figure 5.13 The ring attached to the cable.

The ring has a slot which enables it to be easily attached around the bundle and to be translated along the bundle. The ring also has flexible flanges with slots that allow the ring to be compressed and "click" securely into the end of the holder (figure 5.14).

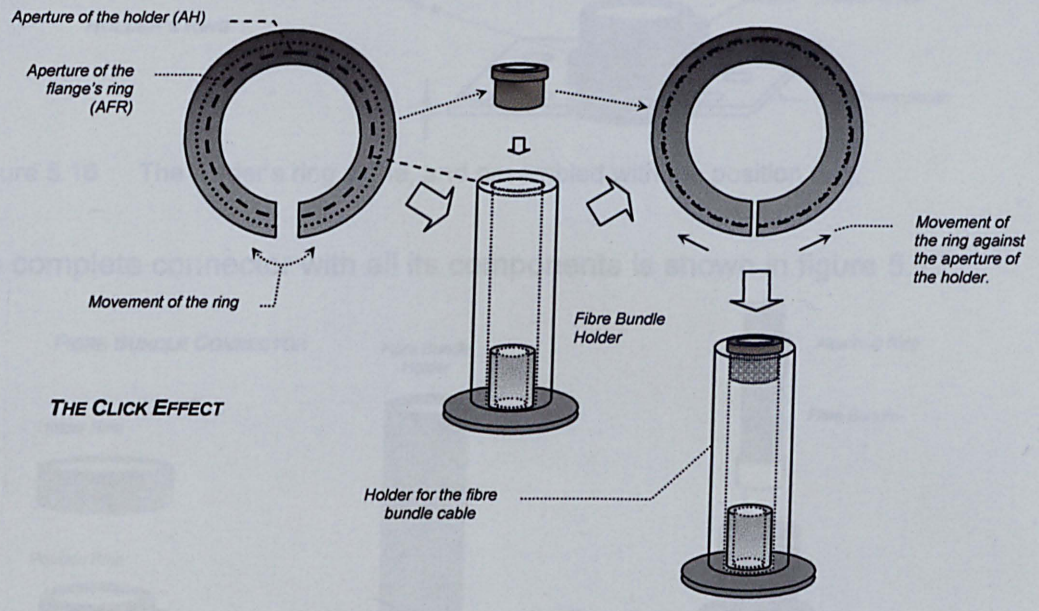

Figure 5.14 Attachment mechanics.

For accurate imaging the positions of the fibre bundles must remain stable (or unchanged) during the study and phantom reference measurement. A position ring is used with the fibre bundle holder, enabling the radial translation of the bundle inside the helmet (figure 5.15). When the flange's foam is in contact with the surface (without excessive pressure), the position screw is tightened, fixing its position.

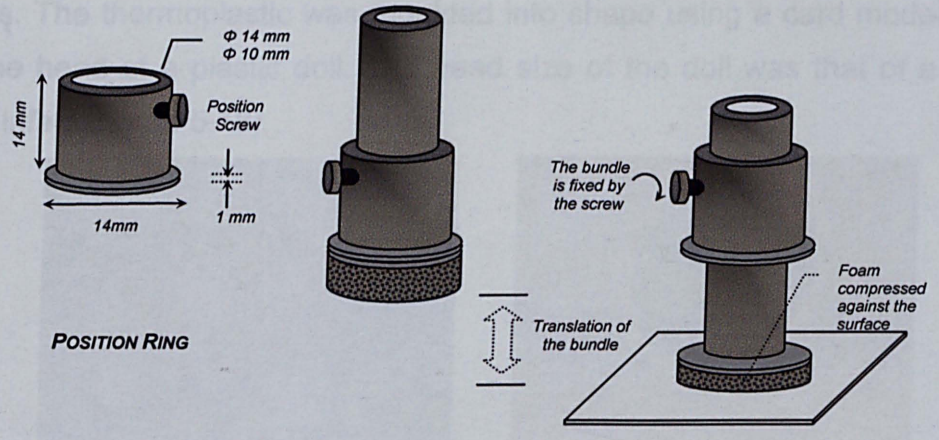

Figure 5.15 The position ring and its attachment to the plastic connector.

An additional ring attaches the connector the helmet's thermoplastic shell (figure 5.16) also giving stability for the position ring-bundle connector set.

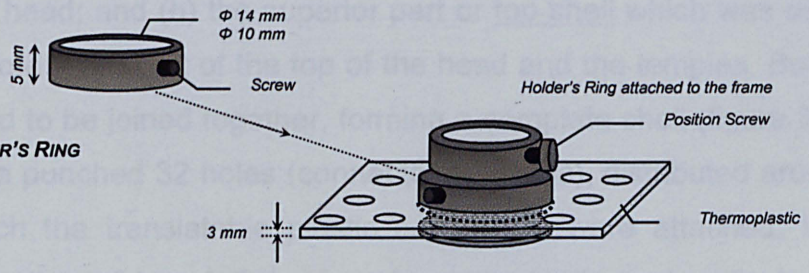

Figure 5.16 The holder's ring alone, and assembled with the position ring.

The complete connector with all its components is shown in figure 5.17.

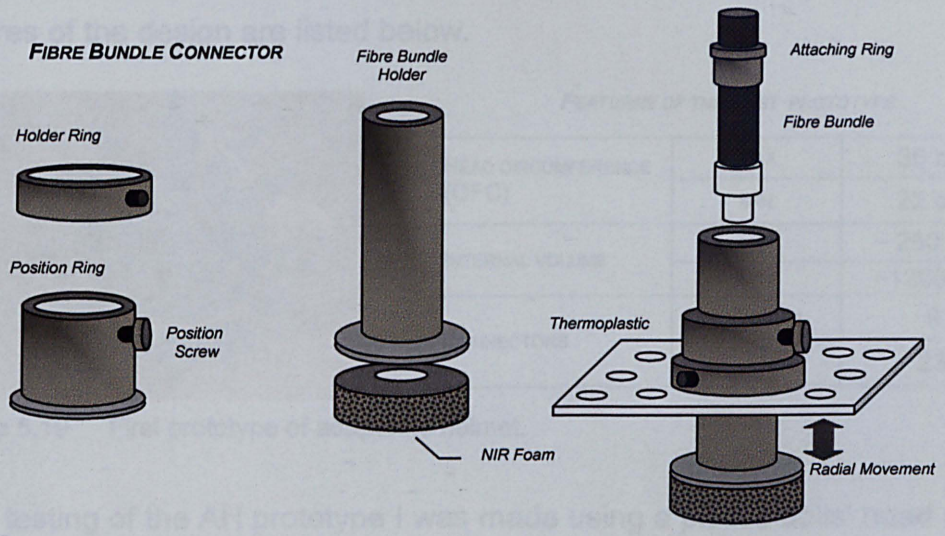

Figure 5.17 The complete fibre bundle connector and its parts.

The frame of the helmet was constructed using a similar process to that used for the custom-made helmets. The helmet was divided into two thermoplastic shells. The thermoplastic was moulded into shape using a card model based on the head of a plastic doll. The head size of the doll was that of a typical term infant (figure 5.18).

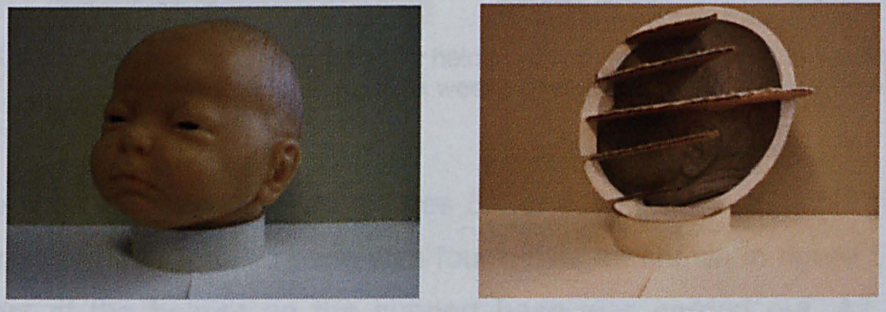

Figure 5.18 LEFT: The reference (term) baby with 35.2 cm of OFC and RIGHT: the card model to mould the warmed thermoplastic.

The two parts of the frame were: (a) the inferior part or bottom shell which supports the back of the infant's head and part of the neck and carries the weight of the head; and (b) the superior part or top shell which was designed to cover the forehead, part of the top of the head and the temples. Both parts were designed to be joined together, forming a complete shell (figure 5.19). In this shell were punched 32 holes (connector positions), distributed around the head, in which the translatable plastic connectors were attached. In each case, the direction of translation of each connector is perpendicular to the shell surface. A 10 mm-thick ring of soft foam (containing a 6 mm-diameter hole) is mounted on a plastic flange on the end of each connector. The features of the design are listed below.

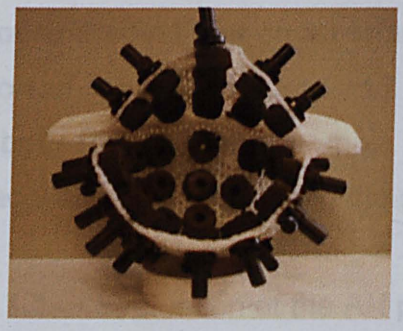

FEATURES OF THE FIRST PROTOTYPE

HEAD CIRCUMFERENCE (OFC)	MAX	36 cm
	MIN	22 cm
INTERNAL VOLUME	MIN	~ 250 cm^3
	MAX	~1200 cm^3
CONNECTORS	TOP SHELL	9
	CORONAL RING	23

Figure 5.19 First prototype of adaptable helmet.

Initial testing of the AH prototype I was made using a plastic dolls' head and is illustrated in figure 5.20.

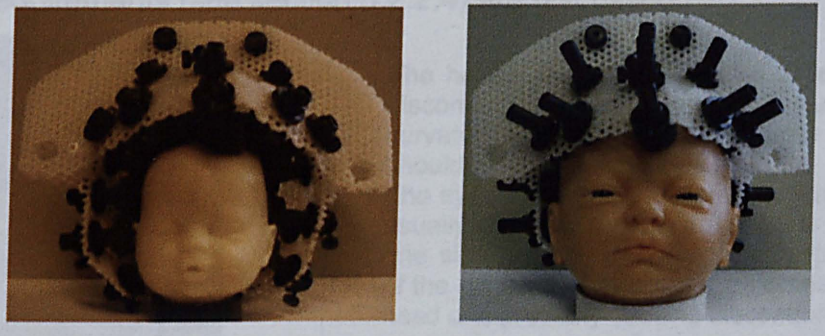

Figure 5.20 First prototype of adaptable helmet which was designed to accommodate head sizes of infants from 24 weeks gestational age (OFC = 22 cm) to term (OFC = 35.2 cm).

Like the custom-made helmets (figures 5.1 and 5.2), the adaptable helmet is also supported by a plastic base with four pillars as shown in figure 5. 21. An initial test of the helmet on the support base was carried out. All 32 fibre

bundles were attached to the respective plastic connectors and no deformation of the shell was observed due to the weight of the fibre bundles.

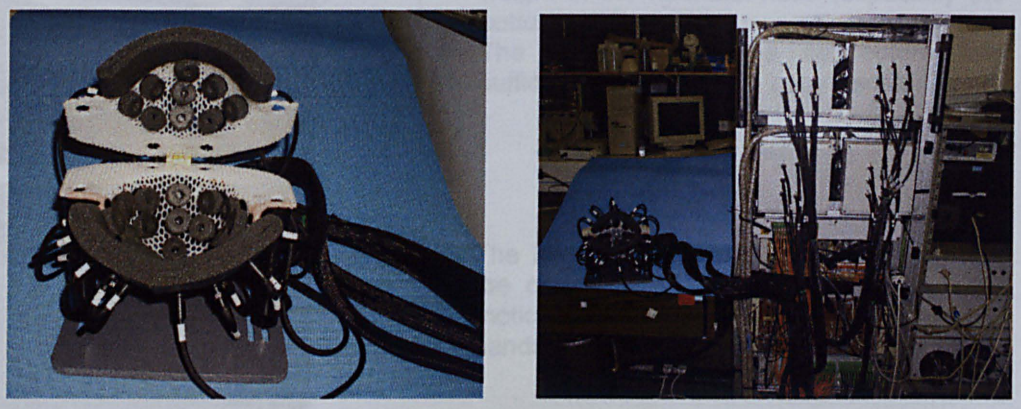

Figure 5.21 First prototype of adaptable helmet attached to the 32 MONSTIR fibre bundles.

Prior to the first test on an infant, it was important to clean the helmet, which involved wiping detergent and alcohol on the foam covering each connector on both shells. Then the whole frame was placed inside the cot and the infant head was positioned within the shells.

5.3.1.1 Evaluation of the AH prototype I design

The main observations resulting from the initial fitting of this prototype are summarized in figure 5.22, and the extent to which the helmet meets the general requirements (see section 5.2.2.4) are discussed.

2. The helmet appeared to cause a degree of discomfort to the baby, especially due to the curvature of neck and imbalance of the shoulders.
3. The eyes are partially covered, which babies usually do not like. Also the head is tilted to one side, indicating an irregular adjustment of the connectors over the back of the baby's head and probably causing discomfort.

1. The distribution of the weight of the baby's head was irregular, producing a noticeable pattern of red spots on the rear of the infant head.
2. The contact of the connectors on the bottom part with the head was poor and irregular (note the optode inside the region defined by the circumference).

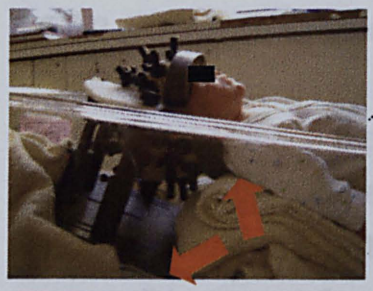

1. The frame was strong enough to support the weight of the neonatal head (especially the bottom shell).
2. The translation of the connectors was sufficient to fit the whole baby's scalp.

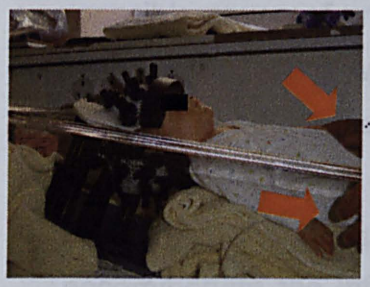

1. The helmet was tipped to compensate for the curvature of the bottom part; causing motion and discomfort to the baby (note the hands holding the baby).

Figure 5.22 Fitting the 1st prototype of adaptable helmet on a healthy baby of 35 weeks gestational age and head circumference of 34 cm.

The prototype was evaluated accordingly with the general recommendations established in section 5.2.2.4.

GR I	USEFUL DATA	REQUIREMENT STATUS	OUTCOME
	GR I	ESSENTIAL	NOT TESTED
FINAL STATUS	NOT TESTED		

GR II	OPTODE LOCATION	REQUIREMENT STATUS	OUTCOME
	GR II	ESSENTIAL	NOT TESTED
FINAL STATUS	NOT TESTED		

GR III	SAFETY	REQUIREMENT STATUS	OUTCOME
	GR III 1	DESIRABLE	PASSED
	GR III 2	DESIRABLE	PASSED
	GR III 3	ESSENTIAL	PASSED
	GR III 4	ESSENTIAL	FAILED
	GR III 5	ESSENTIAL	FAILED
	GR III 6	ESSENTIAL	FAILED
	GR III 7	DESIRABLE	NOT TESTED
FINAL STATUS	FAILED, THE DESIGN HAS FAILED IN THREE OF FOUR ESSENTIAL ITEMS RELATED WITH **SAFETY.**		

GR IV	SKIN ILLUMINATION	REQUIREMENT STATUS	OUTCOME
	GR IV 1	DESIRABLE	FAILED
	GR IV 2	ESSENTIAL	FAILED
FINAL STATUS	FAILED, THE DESIGN HAS FAILED IN 100% OF ITEMS RELATED WITH **ADEQUATE** EXPOSURE OF THE SKIN, ESPECIALLY DUE TO THE POOR AND UNEVEN CONTACT WITH THE BABY'S SCALP (SEE FIGURE 5.22).		

GR V	PROBE STRESS	REQUIREMENT STATUS	OUTCOME
	GR V	ESSENTIAL	PASSED
FINAL STATUS	PASSED (SEE FIGURE 5.21).		

GR VI	PROBE COVERAGE	REQUIREMENT STATUS	OUTCOME
	GR VI	ESSENTIAL	PARTIAL SUCCESS
FINAL STATUS	PARTIAL SUCCESS, THE EVALUATION OF THIS ITEM WAS ONLY PERFORMED ON PHANTOM HEAD, A REALISTIC DOLL HEAD, AND ONE BABY (SEE FIGURE 5.20).		

5.3.1.2 Additional recommendations for helmet designs

Following the fitting of the prototype on the infant, it was modified to eliminate gaps between the connectors and the head, to more evenly distribute the infant head weight over the connectors on the bottom part, and to eliminate any possible cause of uneven pressure on the infant head. Therefore, some new recommendations were added to the design of the adaptable helmet to overcome its early limitations and less successful outcomes. The following was added to GR III:

8. Design ergonomics parameters have to be taken in account to better accommodate the infant's head, such as the mean head width and the mean head length (see figure 5.23). For babies from 27 weeks to term, the range of head width is ~6.4 to 9.4 cm, and head length ~8.4 to 11.4 cm.

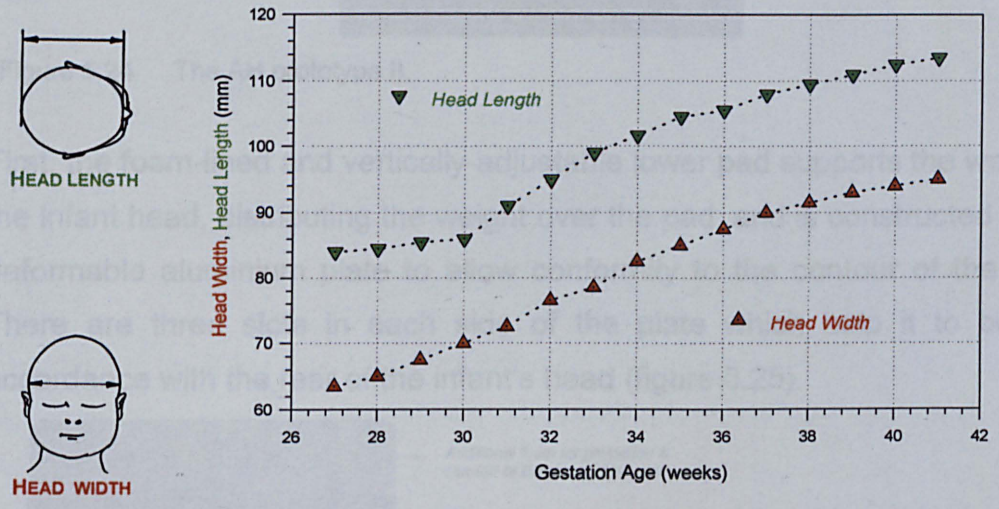

Figure 5.23 Averages of head width and head length, for both sexes, as a function of gestational age. Extracted from (Hall *et al*, 1989) (p105 &107).

Also, to GR IV was added:

3. To provide an even illumination and an even distribution of the weight of the infant's head in the bottom part of the helmet.

5.3.2 Adaptable helmet prototype II

A second design of adaptable helmet was manufactured and evaluated. It was again built of thermoplastic and consisted of three parts: a lower pad (which couples nine fibre bundles to the rear of the head), a fixed coronal

section supported by the base (attaching bundles to the top and sides of the head), and a top section (attaching bundles to the forehead) which was hinged at the back to facilitate rapid attachment and removal of the helmet - especially in emergency nursing care - (figure 5.24). The development of each part of the helmet is described in detail below.

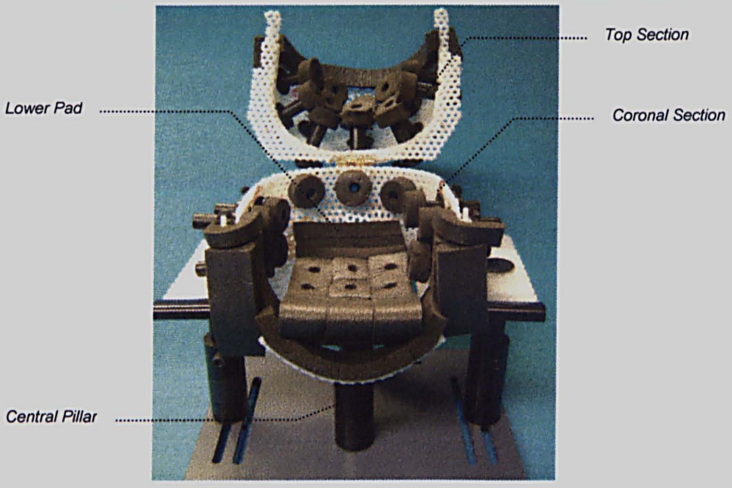

Figure 5.24 The AH prototype II.

First, the foam-lined and vertically-adjustable lower pad supports the weight of the infant head, distributing the weight over the pad, and is constructed from a deformable aluminium plate to allow conformity to the contour of the head. There are three slots in each side of the plate which help it to bend in accordance with the rear of the infant's head (figure 5.25).

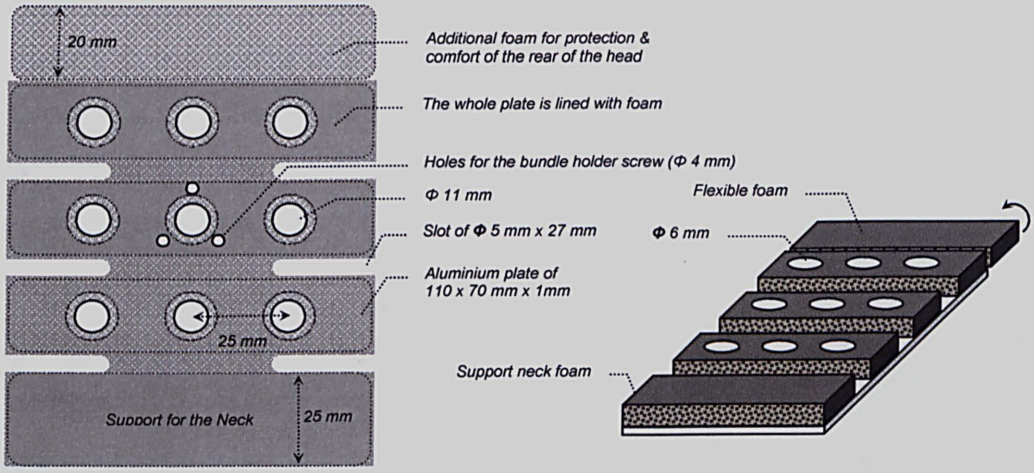

Figure 5.25 Aluminium plate used for the lower pad.

A non-translatable connector was designed for the lower pad which is fixed in the bottom plate using a holder ring (figure 5.26).

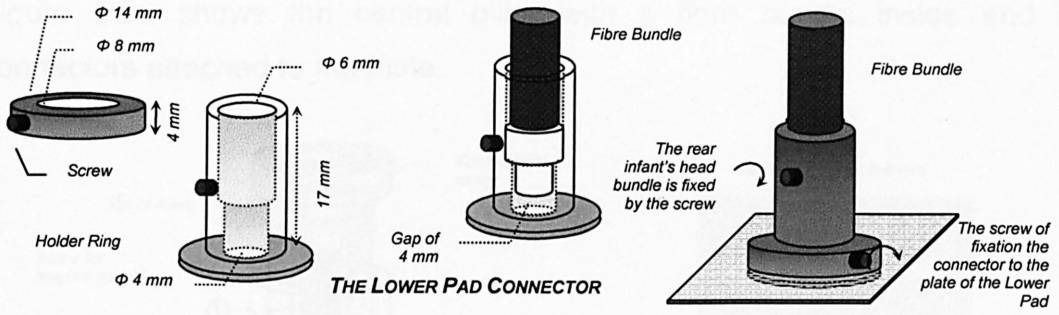

Figure 5.26 The connector for the Lower Pad.

The fibre bundles are attached to the connectors of the Lower Pad using screws, which prevent them falling out under gravity. A central pillar enables the height of pad to be adjusted and supports the weight of the infant's head (figure 5.27).

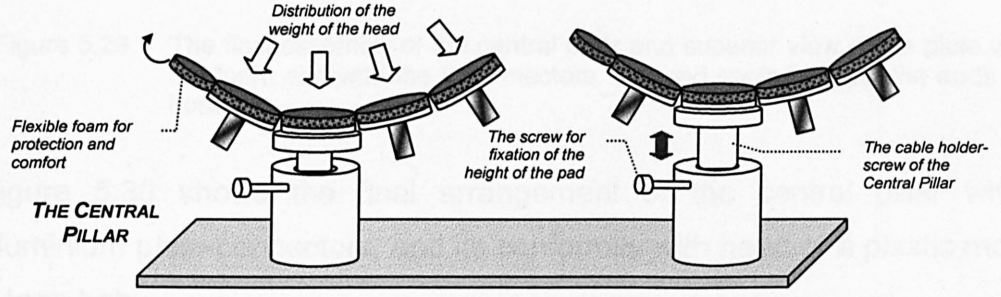

Figure 5.27 Lateral view of the lower pad showing the adjustment in height.

The central pillar is hollow and contains a large lateral opening, which enables an optical bundle to pass through and to be held by one fibre bundle connector in the centre of the lower pad. A holding screw enables the pillar to be fixed at a specific height (figure 5.28). Thus, the whole pad is translatable. A fibre bundle holder within the pillar is the same as those used in the rest of the helmet, except it is given a smaller flange.

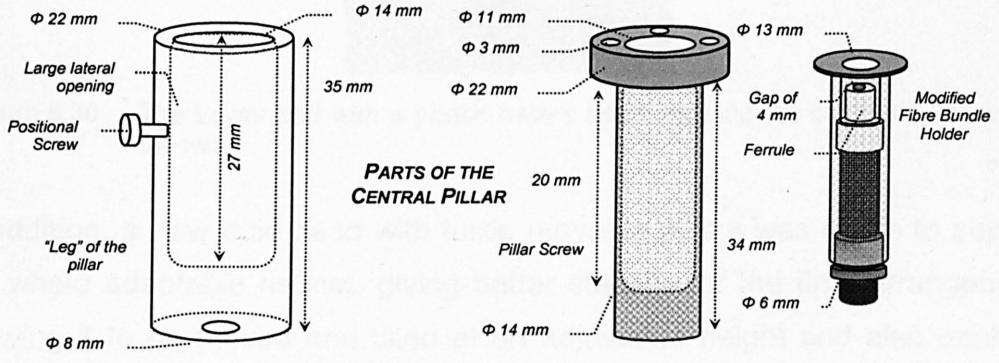

Figure 5.28 Parts of the central pillar.

Figure 5.29 shows the central pillar with a fibre bundle inside and all connectors attached to the plate.

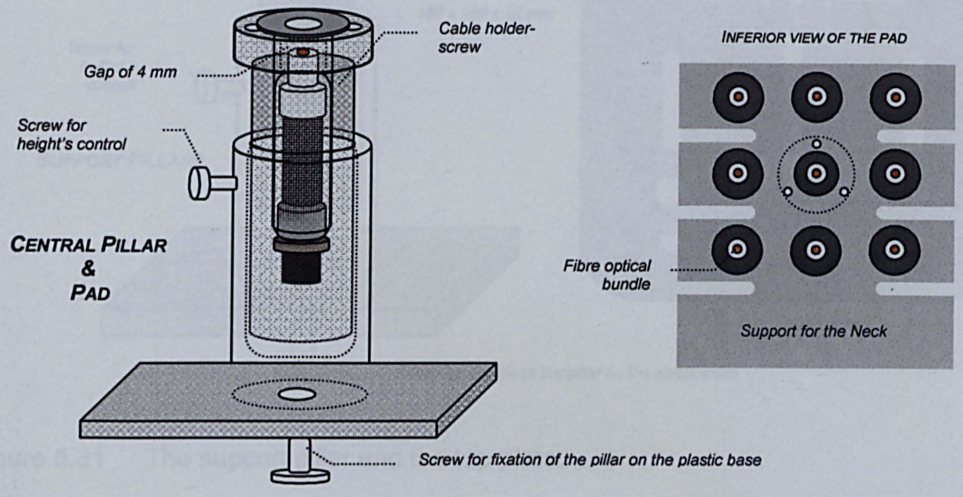

Figure 5.29 The final assembly of the central pillar and superior view of the plate without the foam and with the 9 connectors. The red spots indicate the ends of the bundles.

Figure 5.30 shows the final arrangement of the central pillar with the aluminium plate-connectors, and its conformity with head of a plastic model of a term baby.

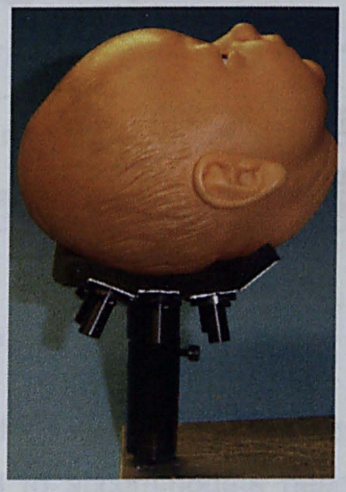

Figure 5.30 The Lower pad with a plastic baby's head showing the conformity between the two.

In addition, a new rigid base with three movable pillars was made to support the whole adaptable helmet, giving better stability for the final arrangement, allowing it to be moved and tilted at an adjustable height and also enabling access to attach the bundles to the connectors on the lower pad (figure 5.31).

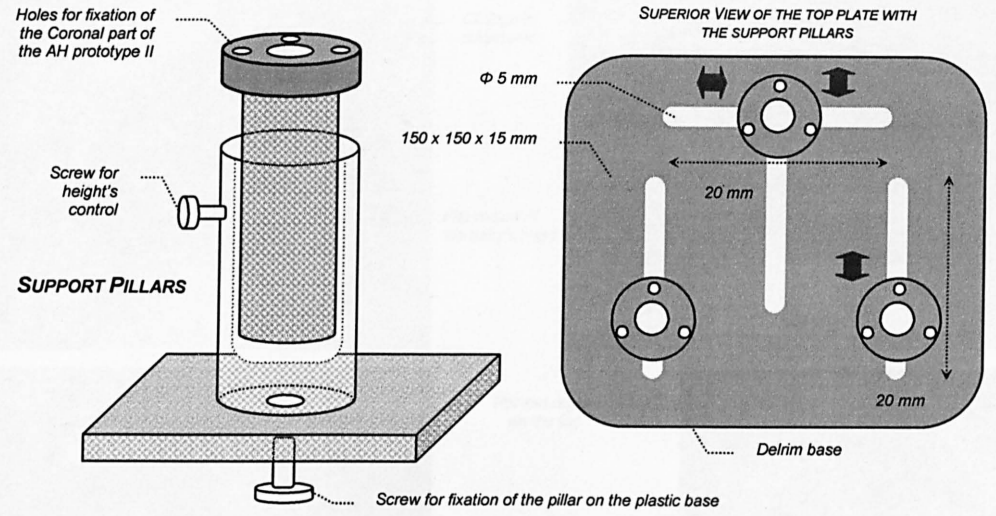

Figure 5.31 The support pillar and the top plate.

The base plate which the pillars is joined hinges to a lower plate, enabling the base to be rotated by 90° (figure 5.32). This mechanism is useful for reference measurements on phantoms (balloon or latex head) in imaging experiments as described later in section 5.3.2.1.

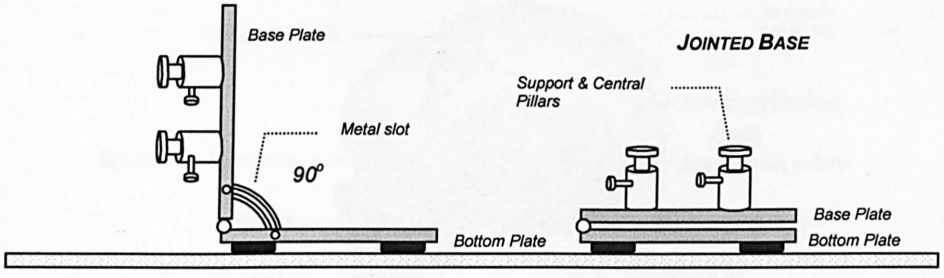

Figure 5.32 The jointed base.

The shapes and sizes of babies heads are very variable. Thus the AH prototype II was designed to accommodate head sizes of infants from 24 weeks gestational age to term. In addition, the design also took into account some general observations on infant heads (figure 5.33), such as: (a) the lateral parts of babies' heads are normally flat; (b) the rapid change in curvature of the rear in comparison with the top of the head; and (c) the top of the head is often somewhat pointed.

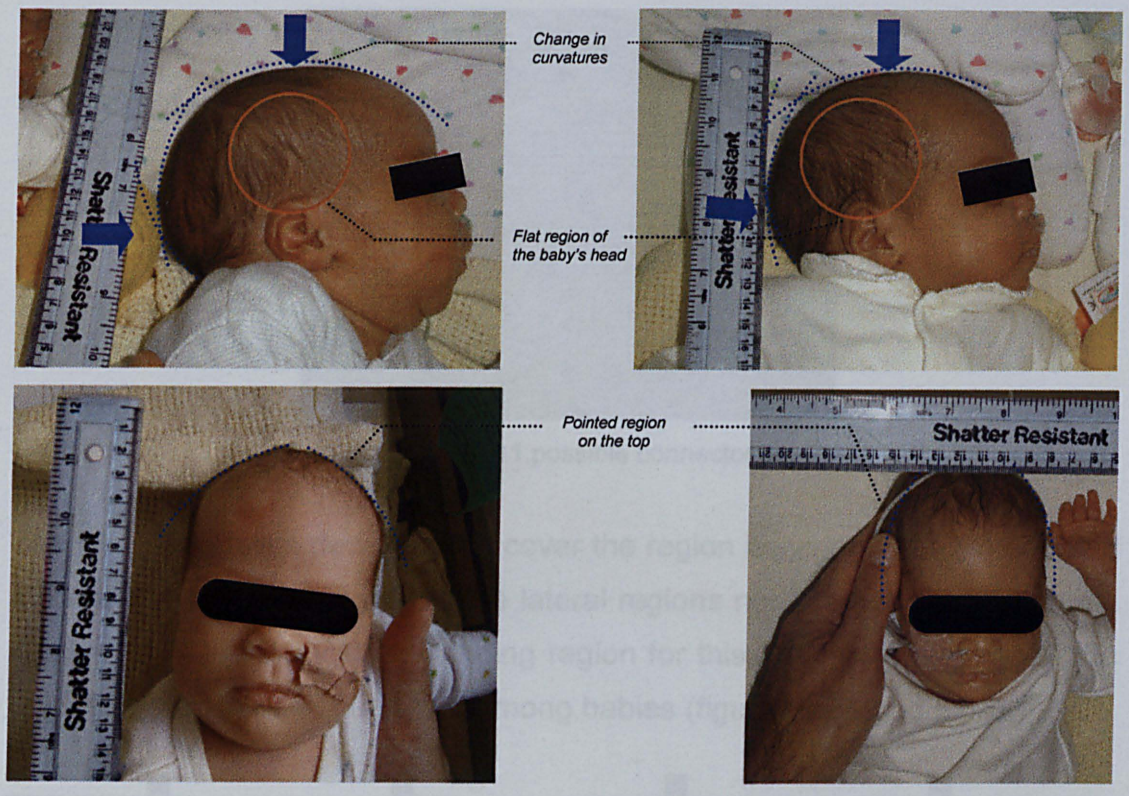

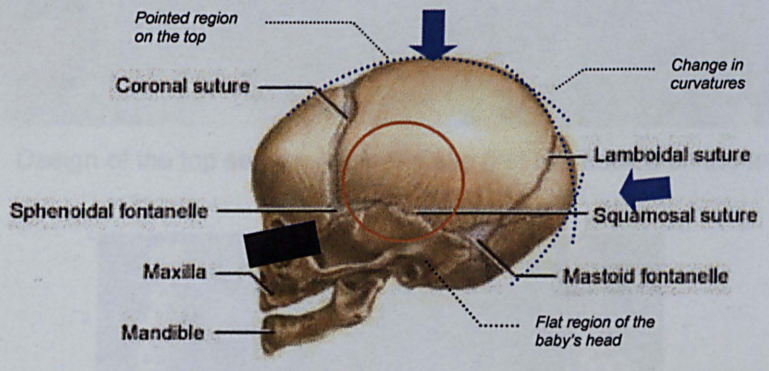

Figure 5.33 General observations about the flat region, the difference in curvature and the top region of the infant head. The babies above are healthy twins 36 weeks^{+2} old (baby at left has 36.5 cm of OFC and baby at right has 32.4 of OFC). The other two babies below are also healthy, the baby on the left is 37 weeks old and 36 cm of OFC, and on the right is 32 weeks old and 29.3 cm of OFC.

The difference in curvatures and the pointed top region were also considered during the design of the coronal section of the helmet (figure 5.34). The fibre bundles in the coronal section are coupled to the head using connectors which allow the bundles to be translated radially and then fixed in appropriate positions.

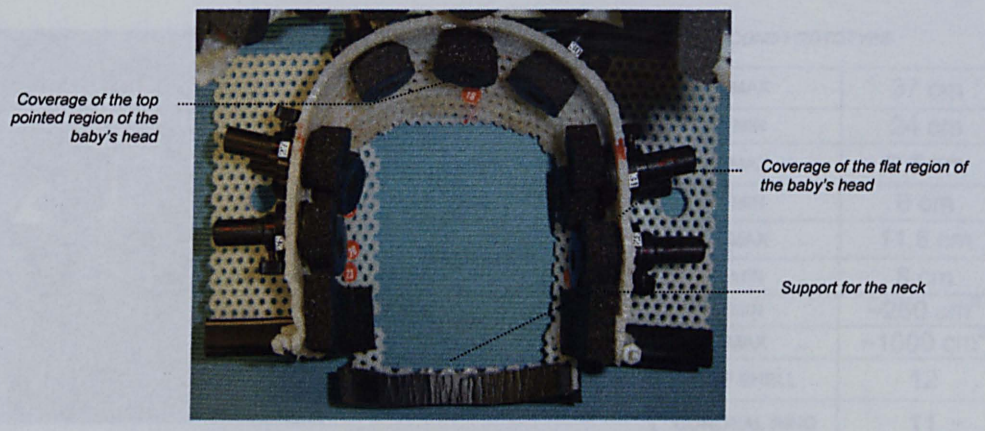

Figure 5.34 The coronal section with 11 possible connector positions.

The top section was developed to cover the region between the forehead and the top of the head and part of the lateral regions not covered by the coronal section. This is the most challenging region for this prototype because of the large variation in head curvature among babies (figures 5.35 and 5.36).

Figure 5.35 Design of the top section (Note the two first two babies on the left are twins).

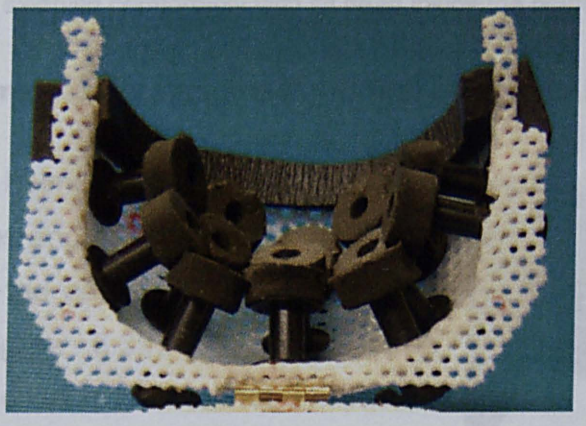

Figure 5.36 The top section with 12 possible connector positions.

The final assembly of the second prototype is shown in figure 5.37 and again is suitable for fitting babies from 24 weeks to term.

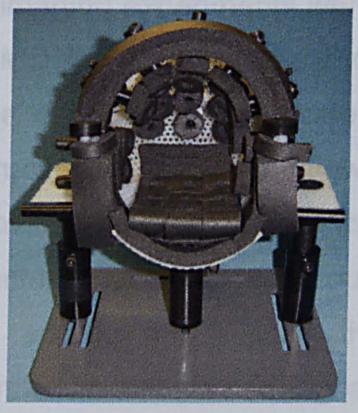

FEATURES OF THE SECOND PROTOTYPE

HEAD CIRCUMFERENCE (OFC)	MAX	37 cm
	MIN	24 cm
HEAD WIDTH	MAX	9.5 cm
	MIN	6 cm
HEAD LENGTH	MAX	11.5 cm
	MIN	8 cm
INTERNAL VOLUME	MIN	~250 cm^3
	MAX	~1000 cm^3
CONNECTORS	TOP SHELL	12
	CORONAL RING	11

Figure 5.37 Final arrangement: Adaptable helmet Prototype II.

Prior to performing an imaging study on an infant, the helmet was cleaned and taken to the Neonatal Unit (at UCL Hospital), and attached to a baby's head to check its fit. Careful attention was given to the connectors and to the lower pad, which was adjusted and bent to conform as closely as possible to the natural curvature of the rear of the head (figure 5.38).

Figure 5.38 LEFT: Adjustments before the optical scanning (fitting check) and RIGHT: the infant sleeping comfortably with its head inside the helmet.

5.3.2.1 Clinical measurements and Performance of the AH II

Before fitting the helmet, the cot was prepared with gel mattresses and covered with blankets to build the level of the cot up to the level of the helmet frame (figure 5.39). Also, all fibres bundles were attached to the helmet which was wrapped in a black zipped bag for protection against ambient light. The baby was then transferred to the cot by the physician, and placed in the helmet.

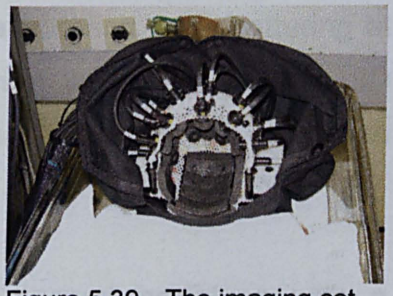

Figure 5.39 The imaging cot standing by the infant baby.

The imaging experiments were carried out at the cotside, in low ambient light with MONSTIR located next to the imaging cot. Some mechanical adjustment of the connectors was made to couple each to the scalp and to avoid the obstruction of the light pathway by the soft foam on the plastic flange. An automated procedure is performed to estimate the optimum positions of the (detector) VOAs for each source position. This process involves illuminating each source and finding the VOA positions for every detector which maximises the detected signal without exceeding the maximum count rate. The time necessary for this process is currently around 20 minutes and a file is generated called an acquisition definition file (ADF), which stores the VOA positions. The next step is the acquisition of image data, which is collected by illuminating at each source position sequentially for 10 seconds and detecting light transmitted through the head at all positions at the same time. It takes around 12 minutes to obtain a complete dataset. Also calibration data is obtained which involves recording light back-reflected from the scalp (absolute calibration, **AbsCal#_w.tps**). Normally, further data scans are taken over a period not longer than one and a half hours. After the infant scans, the baby is removed from the cot and returned to the nursery (the entire baby handling is performed by a physician or nurse). A reference phantom filled with a homogenous fluid is inserted into the helmet (Yusof *et al*, 2003), and a new acquisition of data from the reference phantom is performed. To conclude the experiment, the fibre bundles are removed from the helmet and MONSTIR is returned to the laser-laboratory. Later, measurements of the connector positions are acquired using a digitising arm. The data stored is then processed to generate the respective images of absorption and scattering at each of the two wavelengths (using TOAST) from which are derived 3D images of regional cerebral blood flow and regional tissue oxygen saturation (Hillman, 2002).

Eight preterm babies were scanned using the second prototype with a corrected median age of 38 weeks. Each was scanned immediately following a feed (to maximise the likelihood of the infant sleeping during the study). Ethical permission for the studies was granted by the local ethics committee,

and informed consent was obtained from one or both parents of each infant prior to the study. The details of each infant are shown in table 5.5.

Table 5.5 Details of 8 babies scanned with MONSTIR using the AH prototype II.

BABY DETAILS					
BABY STUDY #	BIRTH AGE [WEEKS^{+DAYS}]	AGE AT STUDY [DAYS]	CORRECTED AGE [WEEKS^{+DAYS}]	OFC [cm]	CLINICAL CONDITION
20	28^{+0}	63	37^{+0}	-	PRETERM IVH* (LEFT SIDE)
21	29^{+0}	50	36^{+1}	-	PRETERM HEALTHY
22	29^{+0}	50	36^{+1}	36.5	PRETERM HEALTHY
23	26^{+5}	105	41^{+5}	-	PRETERM HEALTHY
24	26^{+6}	78	38^{+0}	34.2	PRETERM HEALTHY
25	33^{+2}	21	36^{+2}	-	PRETERM HEALTHY
26	25^{+4}	114	41^{+6}	32.4	PRETERM HEALTHY
27	24^{+1}	135	43^{+3}	36	PRETERM IVH (LEFT SIDE)
*IVH: INTRAVENTRICULAR HAEMORRHAGE					

In terms of the safety and comfort of this prototype helmet, the design appears to be successful. All the babies were comfortably settled in the imaging cot with no evidence of uneven pressure over the infant head (figure 5.40). The maximum and minimum limits of the AH prototype II (figure 5.37) easily accommodated the range of infant head sizes, with a minimum of 32.4 cm (baby study 26) and a maximum of 36.5 cm (baby study 22).

Figure 5.40 Babies comfortably settled and sleeping in the imaging cot (baby study 21 and 22).

The baby study 20 using the adaptable helmet II was performed following the same procedure established for the customized helmets (see table 5.3). The evaluation of the experimentally measured TPSFs from the baby and from the reference balloon phantom, revealed an excessive poor contact of the connectors, leakage of light which produced pre-peaks, low counts on some detectors due to movement of the foam, obscuring the optode, and saturation of several detectors due to incorrect set of VOAs (ADF). Unfortunately, following the first study the positions were recorded incorrectly and image reconstruction was not attempted. After this first attempt, the procedures for

attaching the connectors were reviewed, leading to changes which we believed would substantially improve the data quality for subsequent scans.

The baby studies 21 and 22 were performed with the same ADF generated for the first imaging study. This procedure is reasonably justified when the arrangement of fibre bundles is the same, and the infant has approximately the same size and shape of head. However, it is particularly advantageous when the baby is restless, and therefore there is unlikely to be sufficient time to acquire a new ADF and perform an imaging scan. Each baby was scanned separately and we used the same sequence employed for the first study. The positions of the connectors were measured between scans. Reference data were recorded after each baby study scan, with the balloon phantom held inside the helmet (with the same connector positions), in a horizontal position, filled with intralipid solution. The previous adjustment of the connectors is kept the same.

Image reconstructions were attempted with unsuccessful results due to problems of the same nature as the first imaging study, with particular problems with the quality of the reference phantom data, which exhibited many pre-peak artifacts. This was caused by the tendency of the balloon not to deform sufficiently to the shape of the helmet when placed within it. Also, the horizontal position of the helmet made it difficult to couple the balloon to the optodes without excessive filling of the balloon (~1.5 litres), which increased the balloon's weight, causing it to slip out of the helmet. The risk of bursting of the balloon was increased due to the intralipid volume used (figure 5.41). The performance of the AH II is shown in table 5.6.

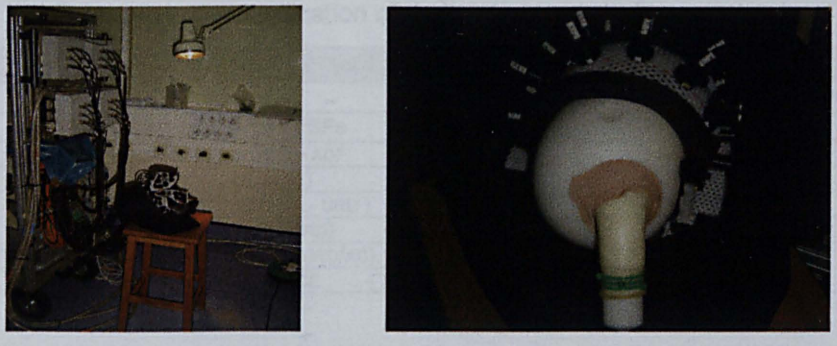

Figure 5.41 LEFT: The preparation to record the reference data with a balloon phantom, and RIGHT: The balloon inside the helmet.

Table 5.6 Performance of the adaptable helmet II for the experiments with babies studies 21 and 22.

PERFORMANCE OF AH II FOR BABIES STUDY 21 AND 22		
	BABY STUDY 21	BABY STUDY 22
THE TOTAL NUMBER OF TPSFS	960	960
CLOSED CHANNELS ("0") – ADF	142	142
ACTIVE CHANNELS (AC)	804	804
QM FILE (UN-REJECTED DATA - URD)	369	322
REJECTED DATA (=AC –URD)	449	482
PERFORMANCE OF EACH HELMET (= (URD/AC).100%)	45.9%	40.0%
AVERAGE PERFORMANCE	43%	

For the imaging baby studies 23 and 24, I developed the jointed base for the frame, which enabled the helmet to be rotated by 90° and made use of gravity to improve the contact between the bundles and the balloon (figure 5.42).

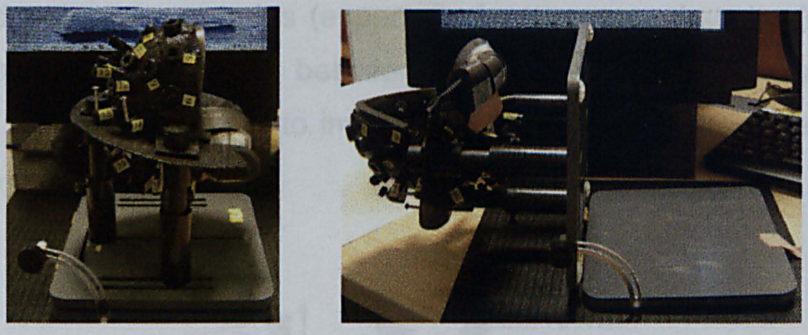

Figure 5.42 Helmet with the jointed base.

A comparison between the recorded reference data with that recorded for previous studies revealed an overall reduction of the pre-peaks in the set of measured TPSFs (Table 5.7). The optical fibre bundles in the helmet made sufficient contact with the surface of the balloon. However, the improvement was still not enough to produce reliable reconstructions due to the high number of rejected data. Table 5.8 shows the improvement with the overall reduction of the un-rejected data from the reference data due to the utilization of the jointed base.

Table 5.7 Evaluation of the utilization of the jointed base (reference data).

PERFORMANCE OF AH II FOR BABIES STUDIES 23 AND 24		
	BABY STUDY 23	BABY STUDY 24
THE TOTAL NUMBER OF TPSFS	960	960
CLOSED CHANNELS ("0") – ADF	143	140
ACTIVE CHANNELS (AC)	817	820
QM FILE (UN-REJECTED DATA - URD)	386	394
REJECTED DATA (=AC –URD)	431	426
PERFORMANCE OF EACH HELMET (= (URD/AC).100%)	47.2%	48%
AVERAGE PERFORMANCE	47.6 %	

Table 5.8 Comparison of the performance from baby study 21 to 24.

COMPARISON OF BABY STUDIES 21 TO 24				
	BABY STUDY 21	BABY STUDY 22	BABY STUDY 23	BABY STUDY 24
PERFORMANCE	45.9%	40.9%	47.2%	48%
PARTIAL AVERAGE	43% (WITHOUT JOINTED BASE)		47.6% (WITH JOINTED BASE)	
AVERAGE PERFORMANCE	45.3%			

Following further modifications in the helmet design, the imaging baby studies 25 and 26 were conducted and produced an overall improvement in quality and quantity of the recorded data from both babies and the reference balloon. This was due to a better conforming of the helmet with the head shapes and the use of the jointed-base for the phantom. I also made some *wedges rings* to be used with some optodes (especially for the coronal section). This ring slightly changes the angle between the thermoplastic frame and the connector, and in an attempt to improve the coupling between the head and the optode (figure 5.43).

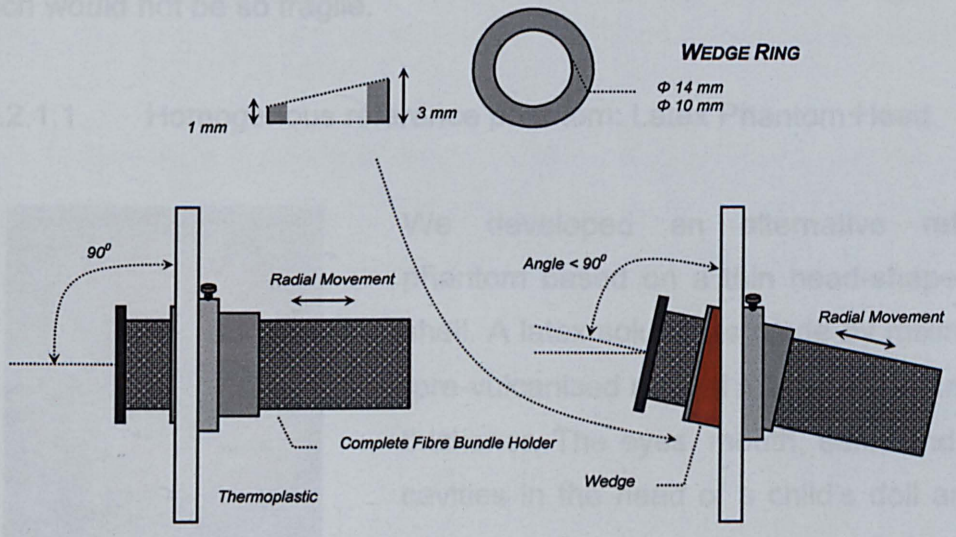

Figure 5.43 Features of the coronal ring and its utilization with the plastic connector.

In addition these babies had a smaller OFC, which helped to make the internal surface of the helmet (formed by the foam flanges) more compact and therefore providing better support (particular for the balloon). However, a significant percentage of data was rejected (less when compared with the previous studies using the adaptable helmet, but still greater when compared with studies using a custom-made helmet – tables 5.9 and 5.10).

Table 5.9 Performance of the adaptable helmet II for the experiments with baby studies 25 and 26.

PERFORMANCE OF AH II FOR BABIES STUDY 25 AND 26		
	BABY STUDY 25	BABY STUDY 26
THE TOTAL NUMBER OF TPSFS	960	1024
CLOSED CHANNELS ("0") – ADF	250	66
ACTIVE CHANNELS (AC)	710	958
QM FILE (UN-REJECTED DATA - URD)	342	470
REJECTED DATA (=AC –URD)	368	488
PERFORMANCE OF EACH HELMET (= (URD/AC).100%)	48.2%	49.1%
AVERAGE PERFORMANCE	48.7%	

Table 5.10 Comparison of the helmet performance from baby studies 21 to 25.

COMPARISON OF BABY STUDIES 21 TO 26						
BABY STUDY	21	22	23	24	25	26
PERFORMANCE	45.1%	40.9%	47.2%	48%	48.2%	49.1%
AVERAGE	46.4%					

When attempting to record the reference data for the seventh study, the reference balloon phantom burst, and intralipid solution poured inside the optode connectors. An alternative reference phantom was therefore sought which would not be so fragile.

5.3.2.1.1 Homogenous reference phantom: Latex Phantom Head

Figure 5.44 Head doll is prepared to be covered by liquid latex.

We developed an alternative reference phantom based on a thin head-shaped latex shell. A latex solution is made by mixing latex (pre-vulcanised natural rubber latex) and latex thickener. The eyes, mouth, ears, and others cavities in the head of a child's doll are filled with modeling clay to prevent holes in the latex or tearing when it is peeled off (figure 5.44).

With a small brush a shell is made by coating the doll's head with a thin layer of liquid latex, and left to dry for nearly 2h before adding the next layer. We used a minimum of 3 layers of the latex solution and then peeled it off when set (figure 5.45). The average thickness of the shell is around 0.6 mm. A series of shells of different sizes were generated using an assortment of dolls (figure 5.46).

Figure 5.45 Comparison between the original template with OFC = 21 cm and the Latex-head phantom.

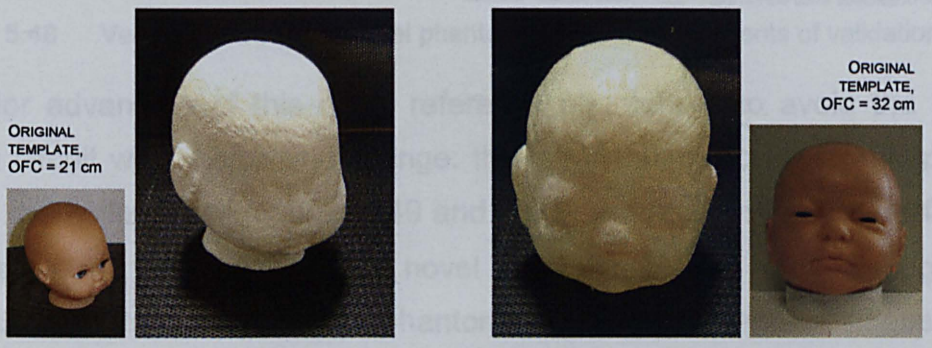

Figure 5.46 LEFT: Latex-head phantom with OFC = 21 cm and RIGHT: Latex-head phantom with OFC = 32 cm.

We note that after a period of a few weeks the latex shells change colour in some regions from almost transparent to orange-brown. This effect is probably related to the process of aging of the latex (figure 5.47).

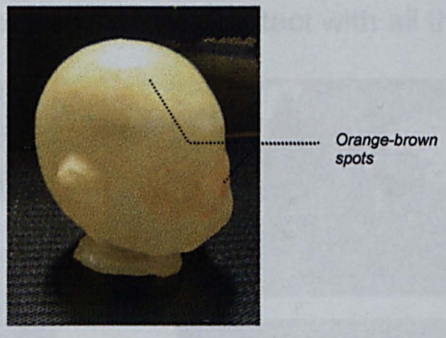

Figure 5.47 Aging of the latex heads.

For reference measurements a shell is chosen which best matches the size and shape of the infant being studied, and is filled with scattering fluid after being placed in the helmet. The helmet is carefully rotated by 90° for the reference measurement, so the fluid does not escape from the neck of the shell (figure 5.48).

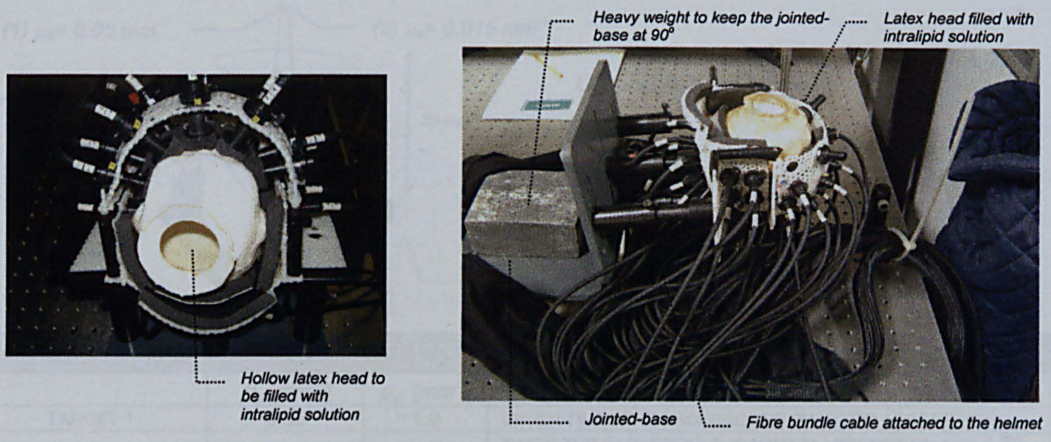

Figure 5.48 Versatility to use the novel phantom during its experiments of validation.

A major advantage of this novel reference phantom is to avoid the plastic tubing circuit with valves and syringe: the intralipid solution is simply poured inside the hollow shell (figures 5.49 and 5.50). An experiment was performed to assess the suitability of the novel latex head filled with homogenous intralipid solution as a reference phantom. In this experiment, small absorbing targets were introduced into the latex head phantom and it was filled with intralipid solution (figure 5.49 (a) and (b)). For a reference measurement, which is necessary for difference imaging, the same phantom was imaged without the targets (figure 5.49 (c)). The resulting reconstructed images should exhibit only the targets, at the expected geometric positions. Unlike the balloon phantom, the weight of the fluid tends to make the shell conform more closely to the helmet shape, providing good contact with all the fibre bundles.

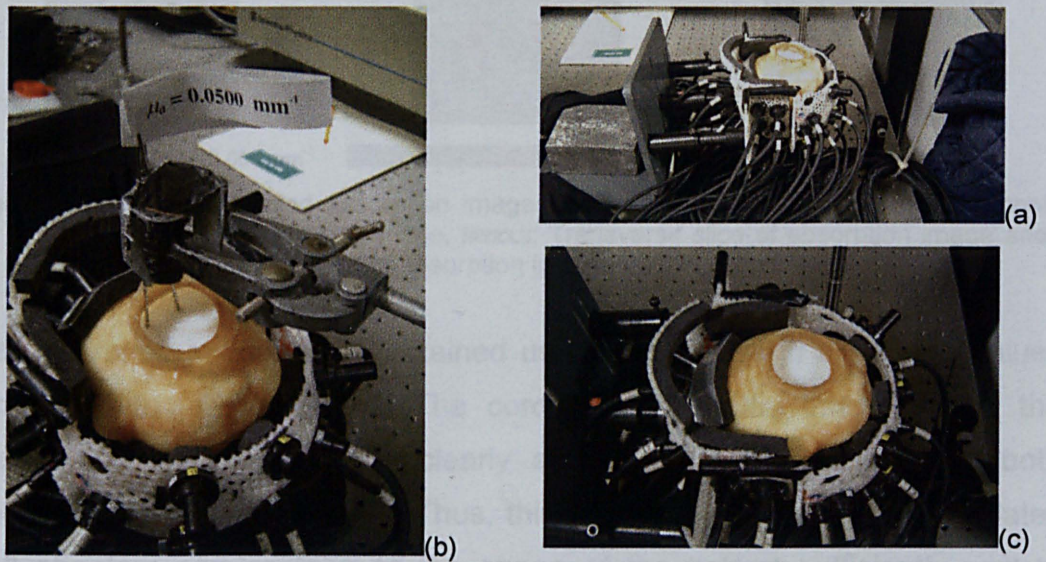

Figure 5.49 (a) Experimental set-up (b) Latex head with the targets and (c) Latex head without the targets.

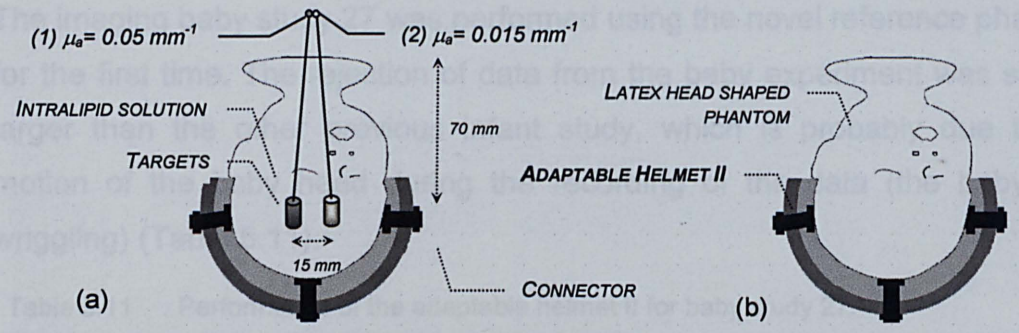

LATEX HEAD EXPERIMENT			
	μ_a [mm^{-1}]	$\mu_{s'}$ [mm^{-1}]	COMMENTS
TARGET 1	0.05	1.0	SEVEN TIMES THE BACKGROUND PHANTOM ABSORPTION.
TARGET 2	0.015	1.0	TWICE THE BACKGROUND PHANTOM ABSORPTION AND 3.33 TIMES THE ABSORPTION FROM THE TARGET 1.
INTRALIPID SOLUTION	0.007196	0.9972	TAKEN AS BACKGROUND PHANTOM VALUES.
TARGET'S DIMENSIONS	LENGTH = 10 mm WITH Ø = 10 mm		RESIN CYLINDERS.

Figure 5.50 (a) Latex head phantom filled with intralipid and targets and (b) latex head phantom reference filled with intralipid and without targets for reference measurements.

The intensity and meantime datatypes were extracted and evaluated from the experimental TPSF data (section 4.2.7.6). However, the images were reconstructed with TOAST using just meantime, since this is the only datatype used for most infant studies. The images show the range of μ_a values obtained from the reconstructed images (figure 5.51) (Gibson *et al*, 2003b).

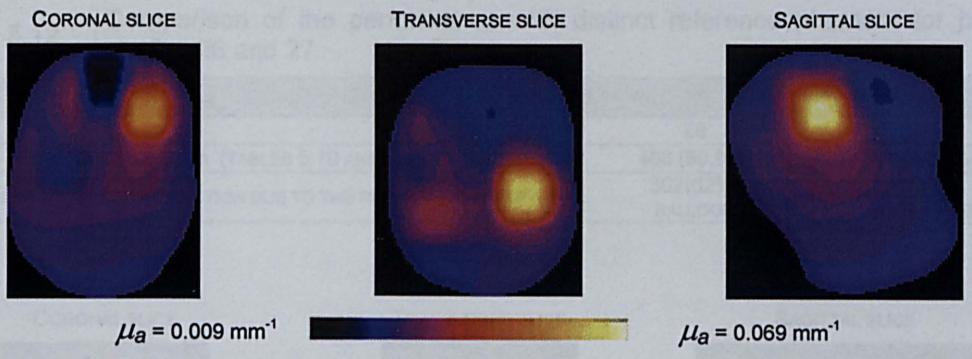

Figure 5.51 Reconstructed absorption images of latex shell with targets. LEFT: Coronal slice of absorption image, MIDDLE: Transverse slice of absorption image and RIGHT: Sagittal slice of absorption image.

The absorption images were obtained using differences in meantime values with and without the targets. The coronal and sagittal images show the presence of the targets very clearly at the expected locations for both absorption and scatter images. Thus, this experiment confirms that the latex shell phantom can conform to the shape of the helmet sufficiently well to provide data adequate for imaging.

The imaging baby study 27 was performed using the novel reference phantom for the first time. The rejection of data from the baby experiment was slightly larger than the other previous infant study, which is probably due to the motion of the baby head during the recording of the data (the baby was wriggling) (Table 5.11).

Table 5.11 Performance of the adaptable helmet II for baby study 27.

PERFORMANCE OF AH II FOR BABY STUDY 27	
	BABY STUDY 27
THE TOTAL NUMBER OF TPSFS	1024
CLOSED CHANNELS ("0") – ADF	73
ACTIVE CHANNELS (AC)	951
QM FILE (UN-REJECTED DATA - URD)	434
REJECTED DATA (=AC –URD)	517
PERFORMANCE OF HELMET (= (URD/AC).100%)	45.7%

The rejection of data due to the utilization of a new reference phantom was calculated and was found to be significantly smaller than for baby study 26. Thus, the utilization of the new latex head phantom has a better conformity with the shells of the helmet. However, the amount of data rejected was still unacceptably high (> 50%), and the resulting images exhibited significant artefacts, especially in the centre of the image (as shown in figure 5.52, in the internal regions of the dashed circles).

Table 5.12 Comparison of the performance with distinct reference phantom for baby studies 26 and 27.

COMPARISON OF BABY STUDIES 26 AND 27		
BABY STUDY	26	27
REJECTED DATA (TABLES 5.10 AND 5.11)	**488 (50.9%)**	**517 (54.3%)**
PERCENTAGE OF DATA REJECTION DUE TO THE REFERENCE PHANTOM	302(62%) BALLOON	191(37%) LATEX HEAD

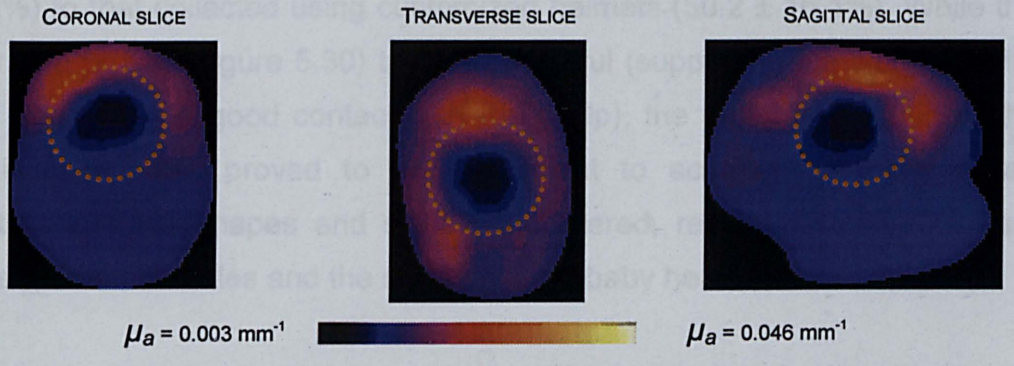

Figure 5.52 Reconstructed absorption images of baby study 27. LEFT: Coronal slice of absorption image, MIDDLE: Transverse slice of absorption image and RIGHT: Sagittal slice of absorption image.

Table 5.13 summarises the eight infant studies in terms of the problems encountered and the improvements introduced.

Table 5.13 Main events during imaging studies baby study 21 to 27.

ADAPTABLE HELMET PROTOTYPE II								
EVENTS	BABY STUDY							
	20	21	22	23	24	25	26	27
CONNECTOR POSITIONS MEASURED INACCURATELY	✓							
PROPERTIES OF INTRALIPID INADEQUATED (VALUES DIFFERENT FROM μ_a = 0.01 mm^{-1} and $\mu_{s'}$ = 1 mm^{-1}).	✓	✓	✓	✓	✓	✓	✓	
POOR COUPLING OF SOME OPTODES TO THE HEAD	✓	✓	✓	✓	✓	✓	✓	✓
POOR COUPLING OF SOME OPTODES TO THE REFERENCE PHANTOM	✓	✓	✓					
USE OF REFERENCE BALLOON PHANTOM	✓	✓	✓	✓	✓			
BURSTING OF PHANTOM							✓	
USE OF JOINTED-BASE				✓	✓	✓	✓	✓
USE OF WEDGE RINGS						✓	✓	✓
USE OF LATEX HEAD PHANTOM								✓
MOTION OF THE BABY (THE BABY WAS WRIGGLING*)	✓	✓	✓					✓
SOME DETECTORS ARE SATURATED DUE TO POOR FITTING	✓	✓	✓					

Table 5.14 shows the quantitative improvement after changes and modifications in the helmet given in table 5.13.

Table 5.14 Comparison of the performance from baby study 21 to 27

PARTIAL & TOTAL PERFORMANCE OF THE AH II							
BABY STUDY	21*	22*	23	24	25	26	27*
PARTIAL PERFORMANCE	45.1%	40.9%	47.2%	48%	48.2%	49.1%	45.7%
PARTIAL AVERAGE (21-23)		PARTIAL AVERAGE (21-24)			PARTIAL AVERAGE (21-27)		
43%		45.3 %			46.4%		
AVERAGE PERFORMANCE		46.3 ± 2.8%					
* EXCESSIVE HEAD MOVEMENT DURING THE DATA ACQUISITION.							

In conclusion, the eight infant imaging studies conducted using this second prototype provided an overall quality of data which was generally inferior (46.3 ± 2.8%) to that collected using customized helmets (50.2 ± 16.1%). While the lower pad proved (figure 5.30) to be successful (supporting the weight of the head and giving a good contact with the scalp), the radial translation of the remaining bundles proved to be insufficient to accommodate the broad variation in head shapes and sizes encountered, resulting in poor contact between some bundles and the surface of the baby head.

5.3.2.2 Evaluation of the AH prototype II design

The design of AH prototype II was also evaluated accordingly with the general recommendations established in sections 5.2.2.4 and 5.3.1.2.

GR I	USEFUL DATA	REQUIREMENT STATUS	OUTCOME
	GR I	ESSENTIAL	FAILED
FINAL STATUS	FAILED DUE TO THE AVERAGE PERFORMANCE IS UNDER THE MINIMUM VALUE OF 50% (SEE TABLE 5.14)		

GR II	OPTODE LOCATION	REQUIREMENT STATUS	OUTCOME
	GR II	ESSENTIAL	NOT TESTED
FINAL STATUS	NOT TESTED		

GR III	SAFETY	REQUIREMENT STATUS	OUTCOME
	GR III 1	DESIRABLE	PASSED
	GR III 2	DESIRABLE	PASSED
	GR III 3	ESSENTIAL	PASSED
	GR III 4	ESSENTIAL	PASSED
	GR III 5	ESSENTIAL	PASSED
	GR III 6	ESSENTIAL	PASSED
	GR III 7	DESIRABLE	NOT TESTED
	GR III 8	DESIRABLE	PASSED
FINAL STATUS	FOR THIS DESIGN, THE GR III WAS APPROVED, ALTHOUGH SOME MODIFICATIONS MAY BE PERFORMED TO ALLOW MEDICAL KITS.		

GR IV	SKIN ILLUMINATION	REQUIREMENT STATUS	OUTCOME
	GR IV 1	DESIRABLE	FAILED
	GR IV 2	ESSENTIAL	PASSED
	GR IV 3	ESSENTIAL	PASSED
FINAL STATUS	PARTIAL SUCCESS DUE TO BAD CONTACT OF THE OPTODES OF THE TOP SHELL AND CORONAL RING		

GR V	PROBE STRESS	REQUIREMENT STATUS	OUTCOME
	GR V	ESSENTIAL	PASSED
FINAL STATUS	APPROVED.		

GR VI	PROBE COVERAGE	REQUIREMENT STATUS	OUTCOME
	GR VI	ESSENTIAL	PASSED
FINAL STATUS	APPROVED, ALTHOUGH WITH PARTIAL CONTACT OF THE OPTODES WITH THE HEAD SURFACE		

The results of the GRs indicated that further improvements in the design were necessary, especially to improve the coupling of the optodes of the coronal and top sections with the scalp. Thus, a third prototype was developed.

5.3.3 Adaptable helmet prototype III

A third prototype of adaptable helmet was developed to significantly improve the contact of optodes with the top and sides of the infant head. First, the top

section was replaced with a slotted aluminium pad (figure 5.53), lined with soft NIR absorbing foam. This supports up to 13 fibre bundles and is suspended from above on a rod attached to a horizontal bar as shown in figure 5.54.

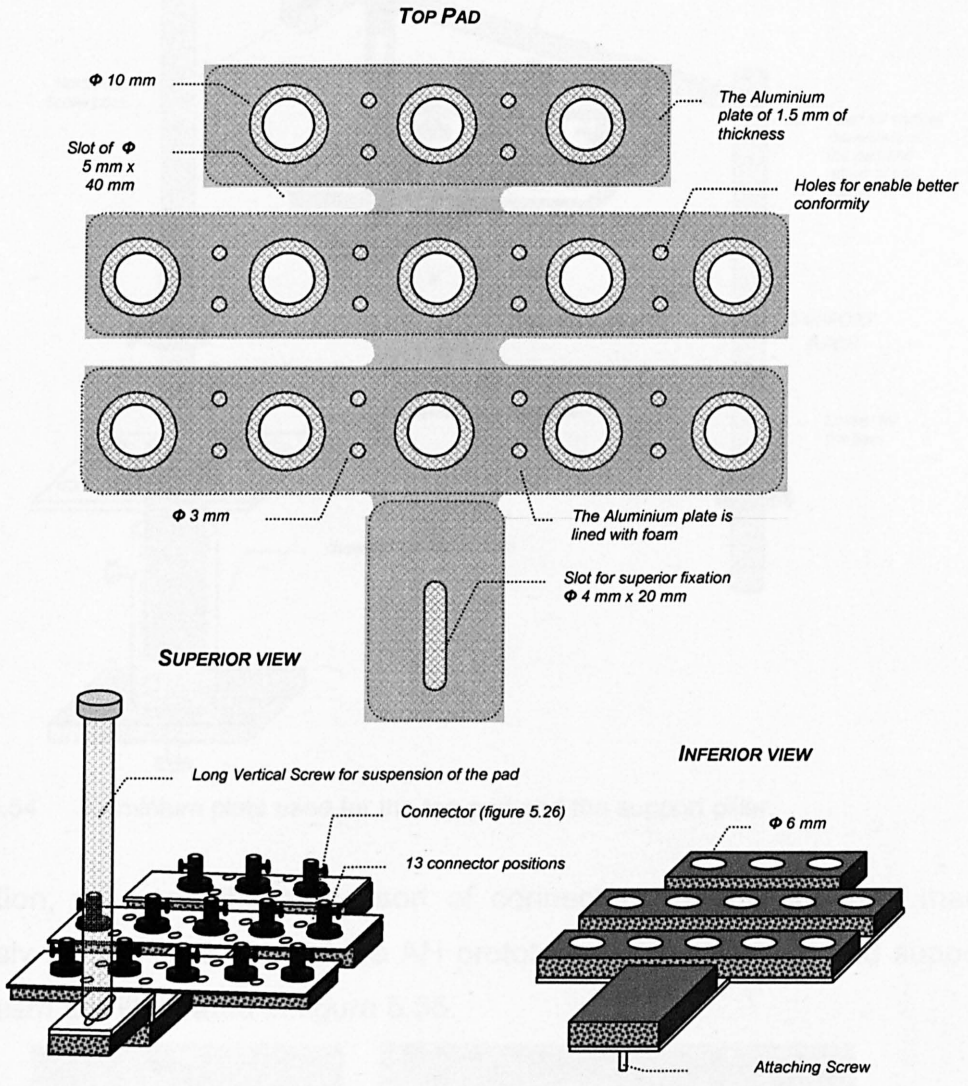

Figure 5.53 Aluminium plate used for the top pad.

The height of the pad can be adjusted by changing the height of the horizontal bar by altering the positions of its locking screws. However, this is a crude adjustment and is only made initially. Precise positioning of the top pad is made: (a) along the horizontal bar, where the top pad can be locked by a screw in a suitable position and (b) by translating the vertical rod. Both horizontal and vertical adjustments are made after a careful deformation of the aluminum plate around the front and top of the infant head (figures 5.54 and 5.55).

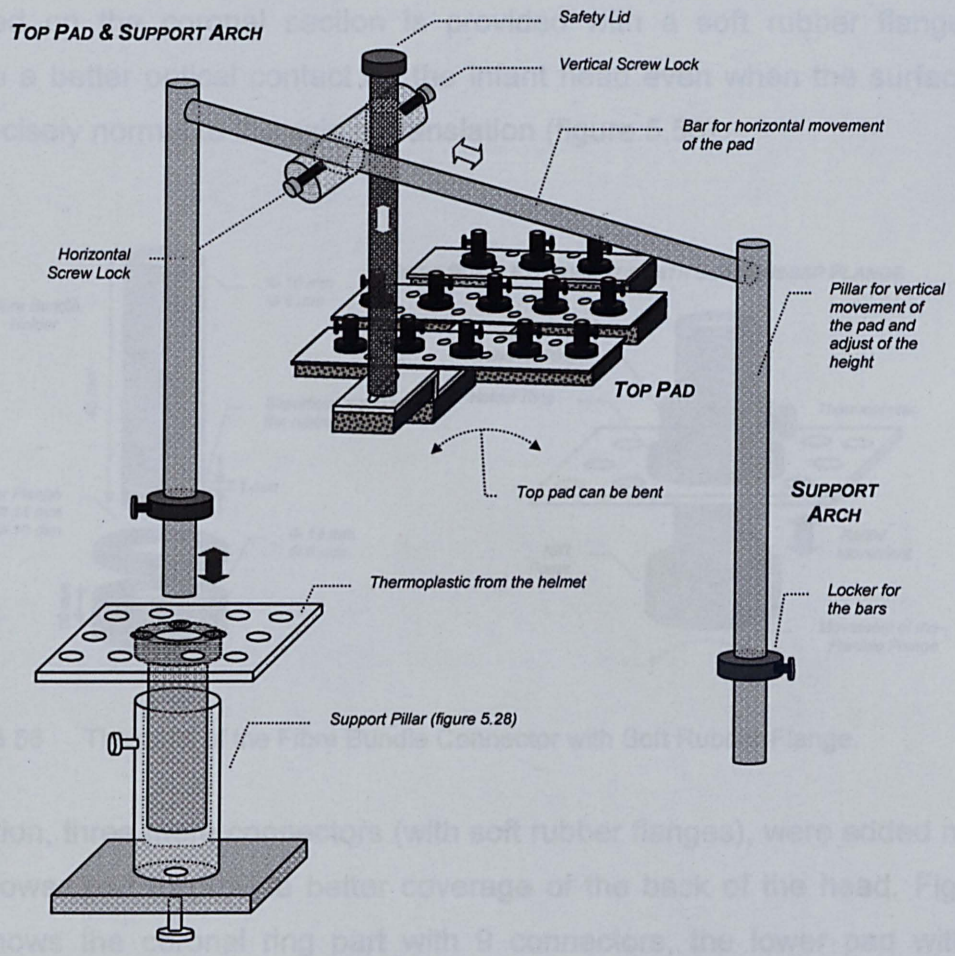

Figure 5.54 Aluminium plate used for the top pad and the support pillar.

In addition, we used the same sort of connectors for this top pad made previously for the lower pad of the AH prototype II. The top pad and support mechanism are illustrated in figure 5.55.

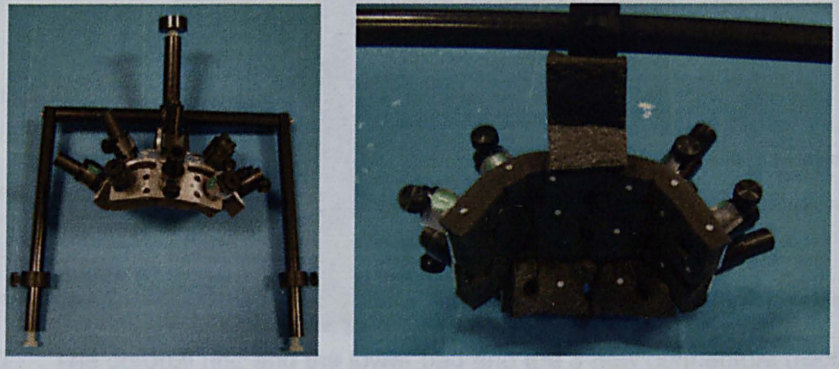

Figure 5.55 Top and back view of the top pad with the support arch.

The coronal section of the adaptable helmet II had a poor coupling between the optodes and the sides of the infant head, and therefore we developed an alternative connector in which the end of each radially translatable connector

attached on the coronal section is provided with a soft rubber flange to provide a better optical contact on the infant head even when the surface is not precisely normal to the axis of translation (figure 5.56).

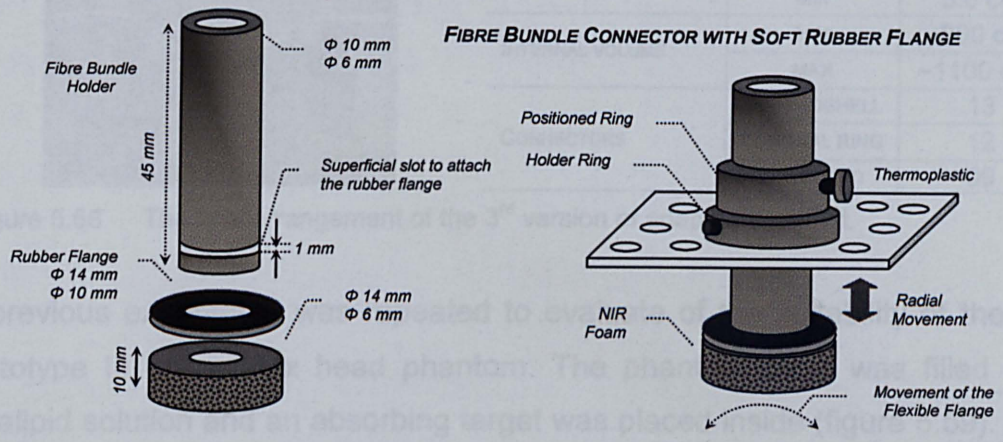

Figure 5.56 The parts of the Fibre Bundle Connector with Soft Rubber Flange.

In addition, three more connectors (with soft rubber flanges), were added near to the lower pad to provide better coverage of the back of the head. Figure 5.57 shows the coronal ring part with 9 connectors, the lower pad with 9 connectors and the 3 new connectors between the lower pad and the coronal section.

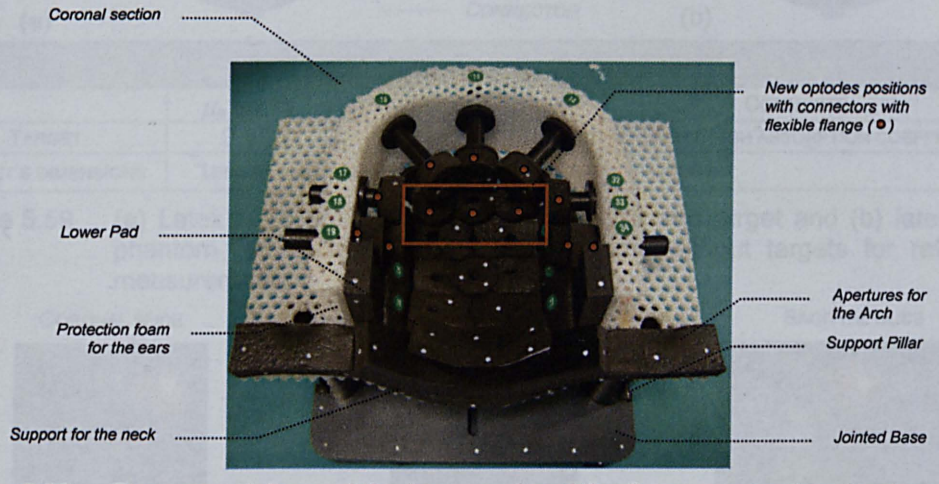

Figure 5.57 The coronal ring and the lower pad and the 3 new connectors (rectangle).

The final arrangement of the Adaptable Helmet Prototype III is shown in figure 5.58, including the coronal section & lower pad with the support arch & top pad and some of its features.

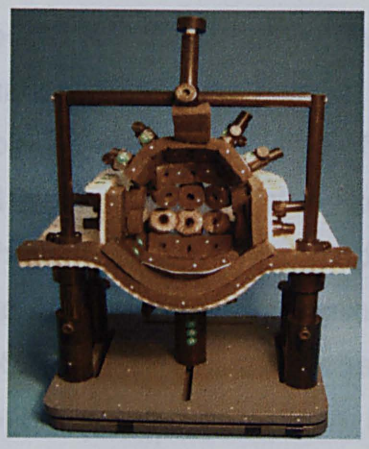

FEATURES OF THE THIRD PROTOTYPE		
HEAD CIRCUMFERENCE (OFC)	MAX	36 cm
	MIN	22 cm
HEAD WIDTH	MAX	11.5 cm
	MIN	5.5 cm
HEAD LENGTH	MAX	11.5 cm
	MIN	5.5 cm
INTERNAL VOLUME	MIN	~200 cm^3
	MAX	~1100 cm^3
CONNECTORS	TOP PADSHELL	13
	CORONAL RING	12
	LOWER PAD	09

Figure 5.58 The final arrangement of the 3rd version of adaptable helmet.

A previous experiment was repeated to evaluate of the suitability of the AH prototype III on a latex head phantom. The phantom head was filled with intralipid solution and an absorbing target was placed inside (figure 5.59). The absorption images reveal the presence of a target at the expected location (figure 5.60).

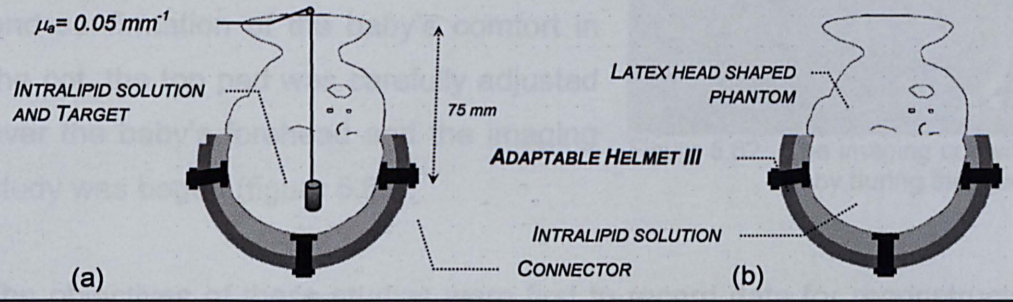

LATEX HEAD EXPERIMENT			
	μ_a [mm^{-1}]	$\mu_{s'}$ [mm^{-1}]	COMMENTS
TARGET	0.05	1.0	TARGET WITH A HIGH ABSORPTION COEFFICIENT.
TARGET'S DIMENSIONS	LENGTH = 10 mm WITH Ø = 10 mm		RESIN CYLINDER

Figure 5.59 (a) Latex head phantom filled with intralipid and target and (b) latex head phantom reference filled with intralipid and without targets for reference measurements.

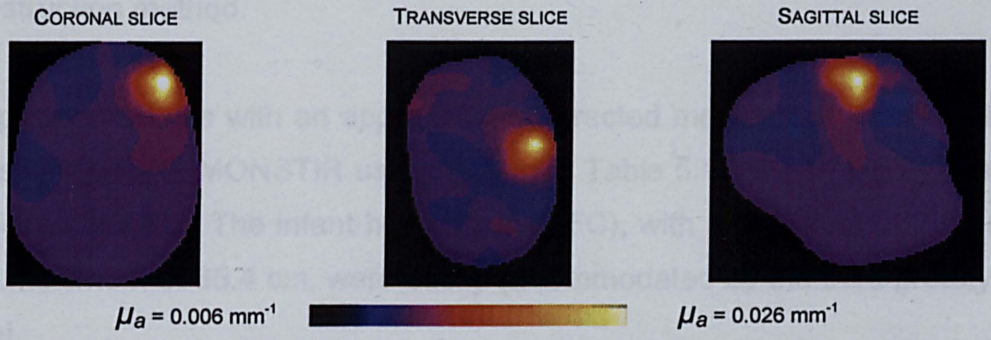

Figure 5.60 Reconstructed absorption images of the infant. LEFT: Coronal slice of absorption image, MIDDLE: Transverse slice of absorption image and RIGHT: Sagittal slice of absorption image.

A couple of days before the first clinical evaluation of the new helmet, it was cleaned and placed around the head of the consented infant baby to verify that it fitted adequately. For these studies we also made use of some wedge rings to improve coupling (figure 5.43). MONSTIR was then transferred to the clinic and prepared as before (figure 5.61).

Figure 5.61 The imaging cot prepared for the infant baby.

5.3.3.1 Clinical measurements and Performance of AH III

To evaluate the new head probe, we repeated the data acquisition sequence employed for the previous infants. Following appropriate safety precautions and confirmation of the baby's comfort in the cot, the top pad was carefully adjusted over the baby's forehead and the imaging study was begun (figure 5.62).

Figure 5.62 The imaging cot with the baby during the study.

The objectives of these studies were first to record data for reconstruction of static images, and second to acquire images to identify regions of the brain activated during evoked response. Both static and difference imaging reconstruction methods were attempted for the studies, the former using a non linear reconstruction package TOAST, and the latter employing a linear reconstruction method.

Nine preterm babies with an approximate corrected median age of 38 weeks were scanned with MONSTIR using the AHIII. Table 5.15 shows the details of each infant subject. The infant head sizes (OFC), with a minimum of 29.5 cm and a maximum of 35.4 cm, were easily accommodated by the third prototype helmet.

Table 5.15 Details of 9 babies scanned with MONSTIR using the AH prototype III.

BABY DETAILS					
BABY STUDY #	BIRTH AGE [WEEKS^{+DAYS}]	AGE AT STUDY [DAYS]	CORRECTED AGE [WEEKS^{+DAYS}]	OFC [cm]	CLINICAL CONDITION
28	36^{+0}	14	38^{+0}	31.5	PRETERM HEALTHY
29	31^{+5}	28	37^{+1}	33.5	PRETERM HEALTHY
30	26^{+5}	93	40^{+0}	35	PRETERM HEALTHY
31	27^{+5}	57	35^{+6}	34	PRETERM HEALTHY
32	39^{+5}	13	41^{+4}	35.4	PRETERM HEALTHY
33	32^{+2}	39	37^{+6}	34.5	PRETERM HEALTHY
34	26^{+0}	77	37^{+0}	32	PRETERM HEALTHY
35	25^{+0}	76	35^{+6}	29.5	PRETERM HEALTHY
36	23^{+3}	104	38^{+2}	32.2	PRETERM HEALTHY

As usual following the infant study, individual measurements contaminated by unwanted light resulting from poor contact were routinely identified and rejected from the set of data employed for image reconstruction.

The performance of the AH prototype III was again evaluated quantitatively by considering the percentage of *un-rejected data* (as shown earlier in tables 5.4 (CMH) and 5.14 (AH II)). This is shown in table 5.16.

Table 5.16 Performance of the adaptable helmet III for the babies studies 28 to 36.

PERFORMANCE OF AH III FOR BABY STUDIES									
BABY STUDY #	28	29	30	31	32[1]	33[2]	34	35	36
THE TOTAL NUMBER OF TPSFs	992	992	992	992	992	992	960	960	992
CLOSED CHANNELS ("0") – ADF	95	95	176	200	74	124	140	140	176
ACTIVE CHANNELS (AC)	897	897	816	792	908	868	820	820	816
QM FILE (UN-REJECTED DATA – URD)	598	549	416	448	262	386	473	595	408
REJECTED DATA (=AC –URD)	299	348	400	344	646	448	347	225	408
PERFORMANCE OF EACH HELMET (= (URD/AC).100%)	66.6	61.2	51.0	56.6	28.9	44.5	57.7	72.6	50.0
AVERAGE PERFORMANCE	**54.3 ±12.8%** (57.5 ± 9.2% WITHOUT BABY STUDY 32)[2]								
[1]	BABY STUDY 32: THE TOTAL NUMBER OF TPSF WAS REDUCED IN 10 DUE TO LASER SOURCE SATURATION								
[2]	AVERAGE PERFOMANCE WITHOUT CONSIDERING THE LOWEST PERFORMANCE OF THE STUDY.								

The fraction of un-rejected data for each study varies from 28.9% to 72.6%, with an average value of 54.3% for the 9 studies. The main causes of data rejection are: (a) the contamination of the data by ambient light and light leakage, (b) non-conformity of the helmet's sections with either the babies heads or the reference phantom, and (c) head movement by the infant. In addition, other occasional factors also contribute to reduced performance, such as: (a) fluctuation of the laser power during the data acquisition (e.g.

baby studies 32 and 33), which is sometimes due to an insufficient laser warm-up time (Hillman, 2002); (b) intermittent instability of the detectors, and (c) excessive head movement during data acquisition, which often required interruption of the study (e.g. baby study 33). Table 5.17 summarises specific features of the nine imaging studies.

Table 5.17 Specific features of baby studies 28 to 36.

ADAPTABLE HELMET PROTOTYPE III									
EVENTS	BABY STUDY								
	28	29	30	31	32	33	34	35	36
USE OF JOINTED-BASE	✓	✓	✓	✓	✓	✓	✓	✓	✓
USE OF WEDGE RINGS	✓	✓	✓	✓	✓	✓	✓	✓	✓
USE OF LATEX HEAD PHANTOM	✓	✓	✓	✓	✓	✓	✓	✓	✓
LEAKING OF LATEX HEAD PHANTOM			✓						
INTERMITTENT INSTABILITY OF THE SOURCES OR DETECTORS					✓	✓			
MOTION AND/OR WAKING OF THE BABY					✓	✓			

The higher performance achieved with the new helmet indicates that the modifications in the helmet design, such as the replacement of the top section with a slotted aluminium pad and the use of flexible rubber flanges on the optodes of the coronal section, are successful.

The improvement to the coupling of the optodes of the coronal and top sections with the scalp is evidenced by the average fraction of un-rejected data of 54.3%, which is above the average performance of the CMH. Figure 5.63 shows some pictures of the infant babies sleeping comfortably with their heads inside the helmet during the clinical studies.

Figure 5.63 Pictures of some babies scanned with MONSTIR and the AH III.

5.3.3.2 Image reconstruction and Evaluation of volume sampling

Image reconstruction was attempted for these infant studies, and the results for baby study 28 are shown in figure 5.64. The absorption images reconstructed with TOAST were obtained using differences in meantime. The range of μ_a values obtained is also shown.

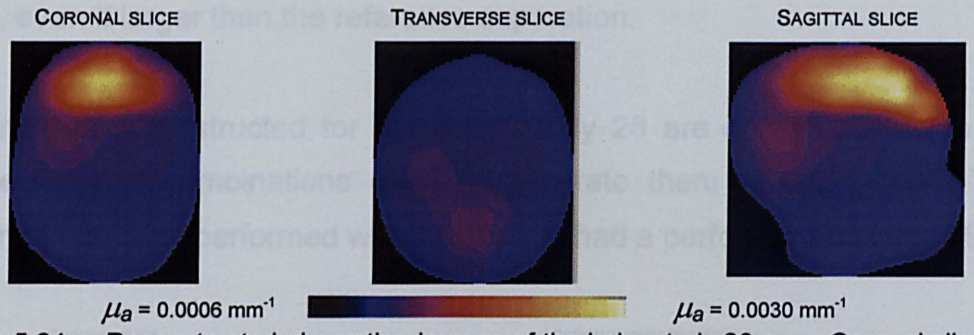

Figure 5.64 Reconstructed absorption images of the baby study 28. LEFT: Coronal slice of absorption image, MIDDLE: Transverse slice of absorption image and RIGHT: Sagittal slice of absorption image at 815 nm.

The resulting image reconstructions do not exhibit artefacts, especially in the centre of the image as observed earlier in figure 5.52. A common feature of images reconstructed with relatively poor data is a *hole* in the centre of the head where the optical properties are near or at their initial values (background values). This is due to a poor sampling of the centre, since the centre is only sampled by measurements at the largest source-detector separations, which are noisiest and therefore more likely to be rejected.

In order to analyze how effectively a given set of tomography data samples the central regions of an infant brain, a programme was developed (LINESOFSIGHT.m / **MATLAB**™), which displays the direct lines-of-sight across the head between sources and detectors for which measurable (and artefact-free) data were recorded. A low density of lines across the centre of the head may indicate that the sampling may be insufficient to reliably reconstruct the central regions. Results of this analysis can be correlated with the corresponding reconstructed images. The programme uses the mesh and QM file to identify the optode locations for each un-rejected measurement between the sources and detectors, and plots the lines, in the correct location in the coronal, transverse and sagittal mesh-projection. The largest lines-of-sight are

represented by black lines and smallest distances are represented in green (or clear) lines. The largest source-detector separations are those corresponding to distances larger than an arbitrary reference separation equal to the smallest distance between an optode in the top section and one in the lower pad of the AHs (and equivalent regions of the CMH). Source-detector separations which are between optodes in the same shell are labelled as small, even if larger than the reference separation.

The images reconstructed for the baby study 28 are shown alongside the source-detector combinations used to generate them in figure 5.65. This imaging study was performed with AH III, and had a performance of 66.6%

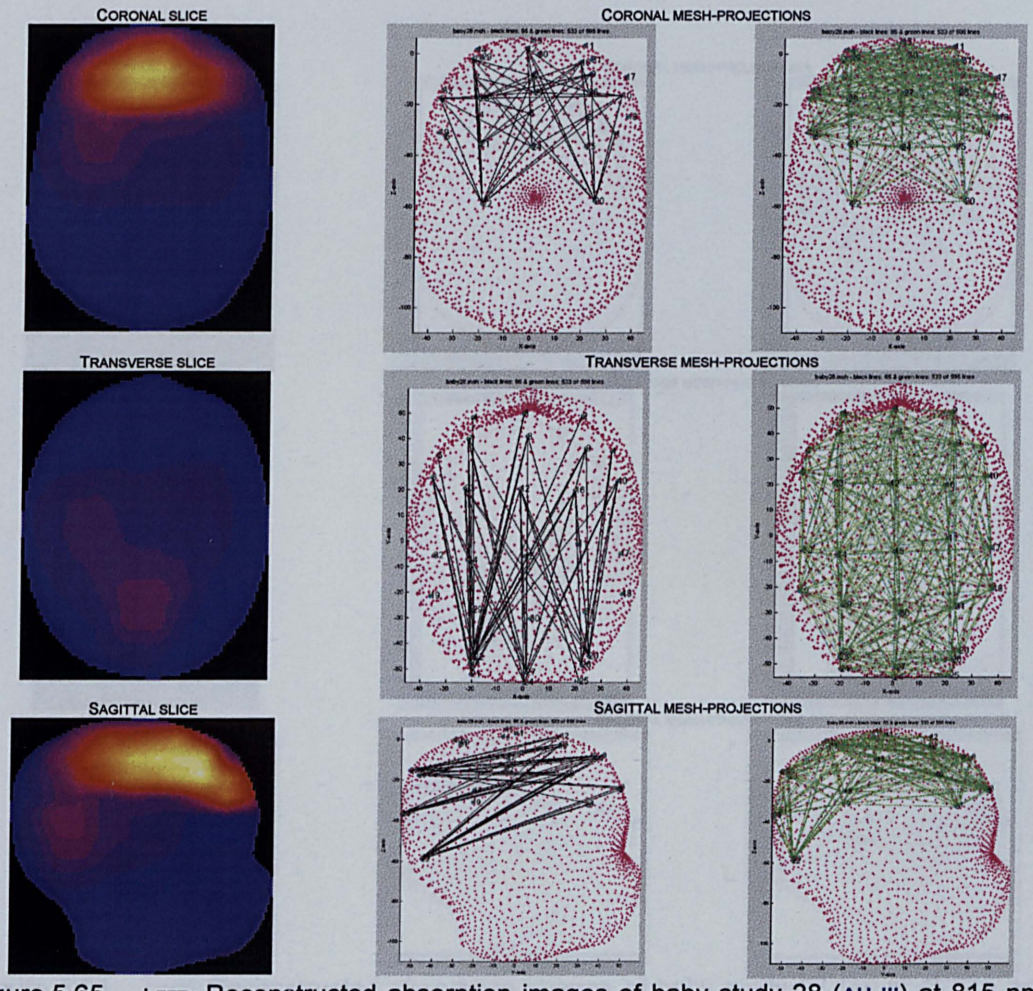

Figure 5.65 LEFT: Reconstructed absorption images of baby study 28 (AH III) at 815 nm. RIGHT: Coronal, transverse and sagittal projection with lines-of-sight, Black lines (largest s-d separation) and green lines (smallest s-d separation), for distance reference of 68.3 mm with a maximum s-d separation of 108.7 mm.

The plots in figure 5.65 confirm a reasonably good sampling across the centre of the head, and this agrees with the reconstructed images, which show that the absorption has been updated throughout the brain region. A decrease in the density of lines from the surface of the mesh toward the centre of the coronal mesh projections is noted, which also appears in the sagittal projections. In the transverse mesh projections a good coverage of the scalp surface is observed, with an approximately even spaced distribution of the source-detector positions.

The same analysis was performed on the data acquired for the baby study 27, and the results are shown in figure 5.66. This imaging study was performed with the AH II, and has a performance of 45.7%.

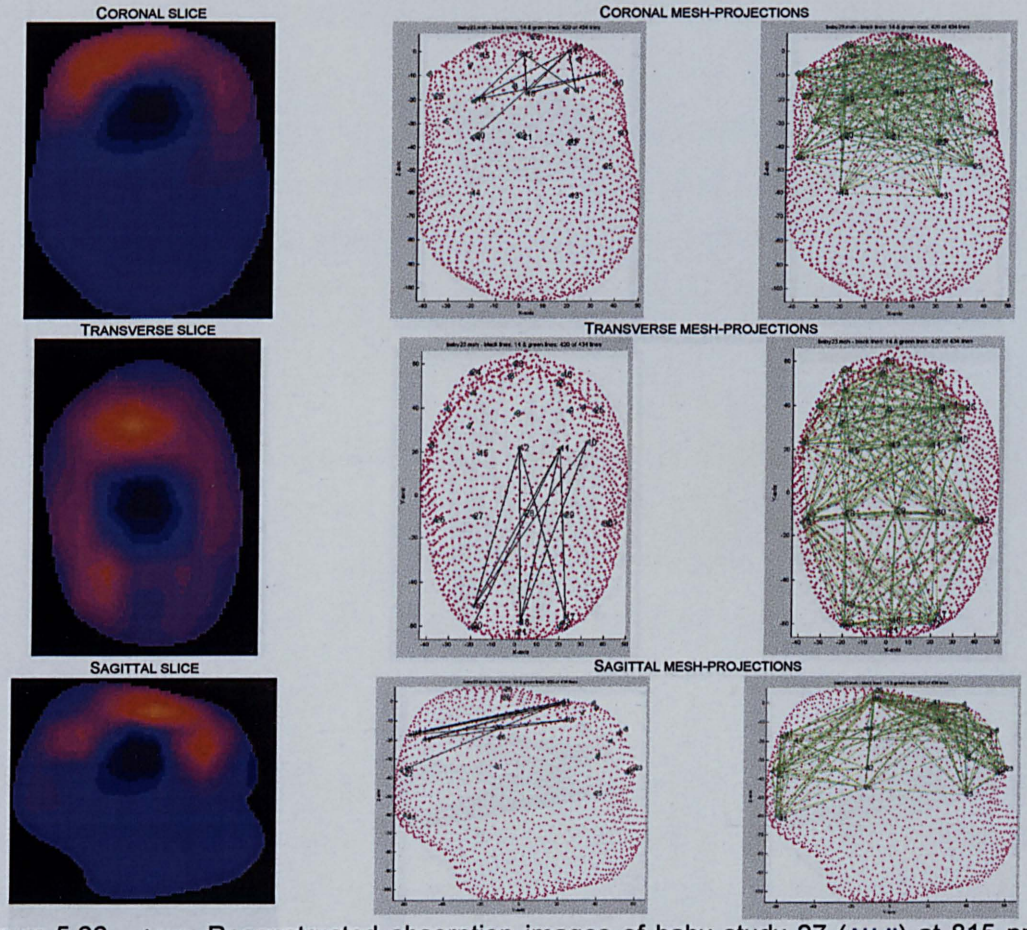

Figure 5.66 LEFT: Reconstructed absorption images of baby study 27 (AH II) at 815 nm. RIGHT: Coronal, transverse and sagittal projection with lines of sight. Black lines (largest s-d separation) and green lines (smallest s-d separation), for distance reference of 77.6 mm with a maximum s-d separation of 96.9 mm.

The image reconstructions clearly show the central region of the brain is poorly sampled, which agree with the low number of lines-of sight crossing the centre of the mesh-projections. In addition, the transverse mesh-projections show the poor coverage of the scalp surface, which also appears in the sagittal projection as a gap located in the rear of the projection. This sagittal mesh-projection also shows a higher concentration of optodes in the top region, but with a poor distribution around the scalp surface.

Finally, an evaluation was performed of the recorded data from baby study 17 and is shown in figure 5.67 with the respective image reconstructions. This imaging study was performed with a CMH, and had a performance of 73.2%.

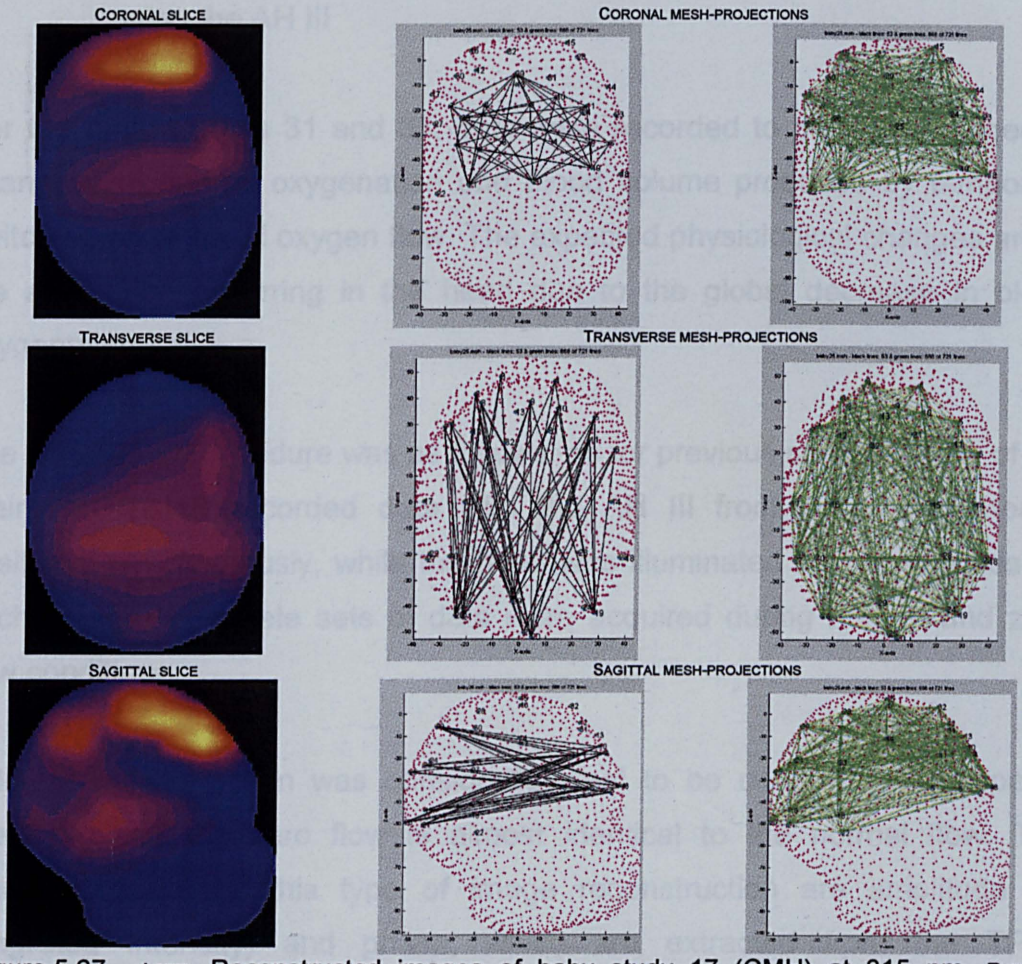

Figure 5.67 LEFT: Reconstructed images of baby study 17 (CMH) at 815 nm. RIGHT: Coronal, transverse and sagittal projection with lines of sight. Black lines (largest s-d separation) and green lines (smallest s-d separation), for distance reference of 63.3 mm with a maximum s-d separation of 98.0 mm.

The plots in figure 5.67 show a large number of lines-of sight crossing the central region of the mesh-projections in agreement with the set of reconstructed images. The transverse and sagittal mesh projections illustrate also a good coverage of the scalp surface (good distribution of the connectors).

Summarizing, as the performance of the study decreases, so does the fraction of lines crossing the central region of the brain. This implies that rejected data is more likely to correspond to larger source-detector separations. Thus, a higher performance of the study is likely to give a relatively higher density of lines in the central region, reducing the possibility of artefacts.

5.3.3.3 Whole-brain functional imaging of alterations in nasal oxygen flow using the AH III

For the baby studies 31 and 35, data were recorded to generate images of changes in cerebral oxygenation and blood volume produced by temporary switching-off of nasal oxygen flow. The expected physiological changes are in the absorption occurring in the head due to the global decrease in blood oxygenation.

The acquisition procedure was as follows: as for previous static imaging of the brain, MONSTIR recorded data with the AH III from all active detector positions simultaneously, while the head was illuminated for ten seconds for each source. Complete sets of data were acquired during normal and zero flow conditions.

A linear reconstruction was considered ideal to be used with this type of imaging since the zero flow is almost identical to the normal flow. The datatypes used for this type of image reconstruction are amplitude (or integrated intensity) and phase, which are extracted from the TPSF measurements at a given frequency (at 100 MHz). For more details see (Gibson et al, 2005a).

For the baby study 31, the change in oxygen saturation was constantly monitored using a pulse oximeter applied to the right foot of the infant. When the nasal oxygen flow was switched off the blood oxygenation gradually fell from 99% of oxygen saturation to 91% over a period of a minute or two. A decrease in blood oxygenation is expected to produce a decrease in absorption at 815 nm. Figure 5.68 shows preliminary images of absorption changes at 815 nm, in sagittal slices from the left (top left) to the right (bottom right) of the head.

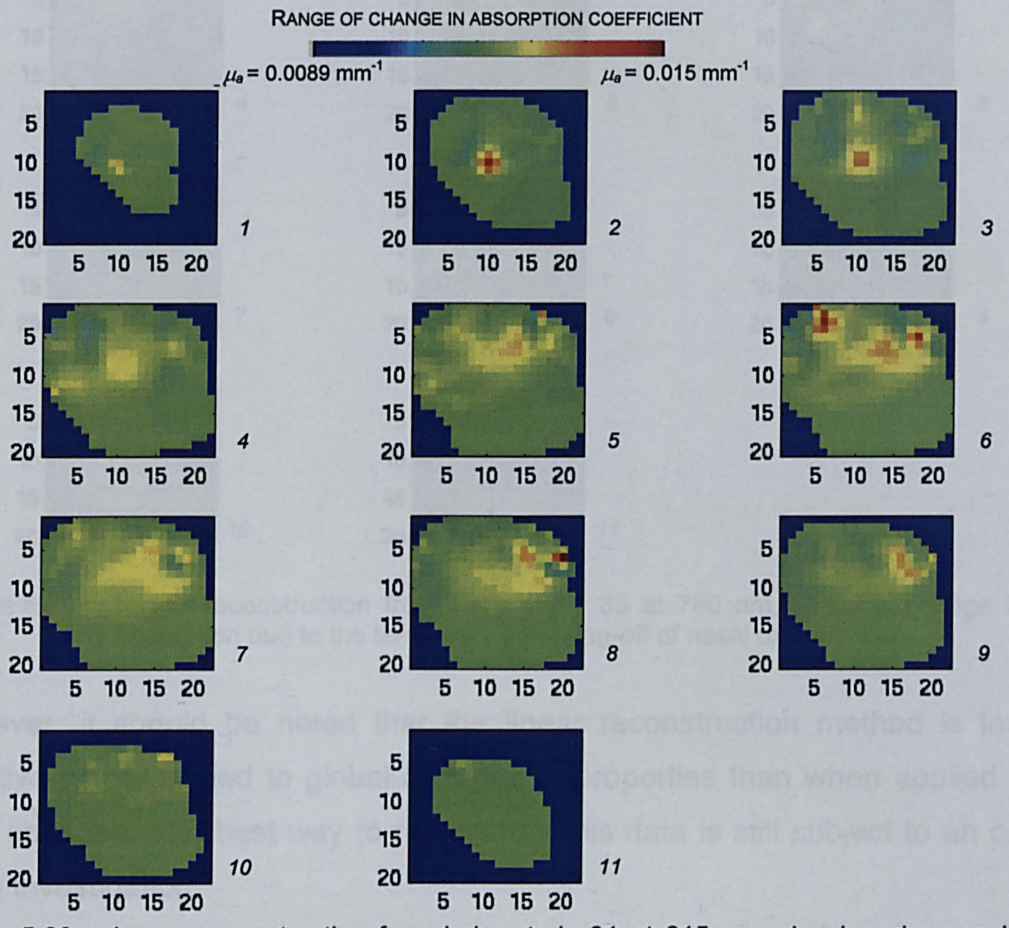

Figure 5.68 Image reconstruction from baby study 31 at 815 nm, showing changes in absorption due to the temporary switching-off of nasal oxygen flow.

Figure 5.68 also illustrates the slight decrease in absorption within localised regions in the brain of the infant.

For baby study 35, the respective change in oxygen saturation was from99 to 96%, following the switching-off of the nasal oxygen. Figure 5.69 shows the

images of changes in absorption at 780 nm, which it is expected to show an increase as oxygenation falls (the opposite effect to the images at 815 nm).

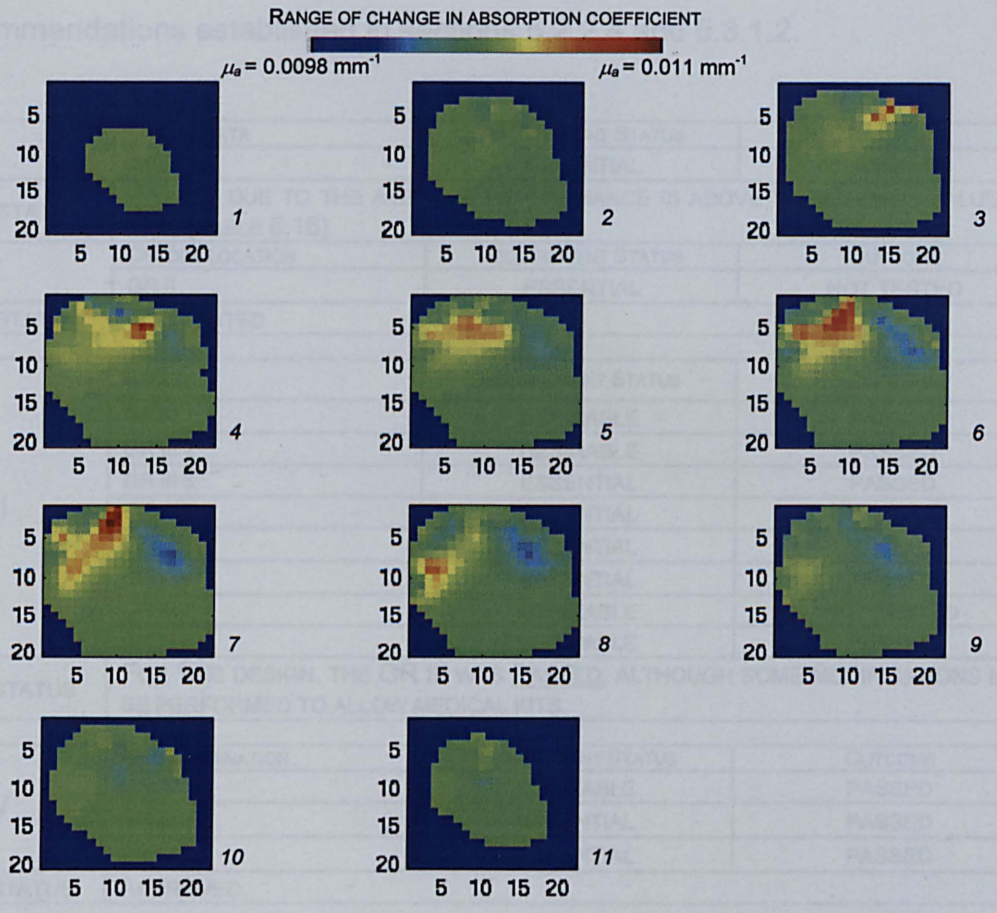

Figure 5.69 Image reconstruction from baby study 35 at 780 nm, showing change in absorption due to the temporary switching-off of nasal oxygen flow.

However, it should be noted that the linear reconstruction method is less effective when applied to global changes in properties than when applied to focal changes. The best way to reconstruct this data is still subject to an on-going investigation.

In conclusion, the AH III also has proved to be a suitable probe for imaging functional changes, even for the intensity (amplitude) datatype, which is more sensitive to any slight variation in the coupling of the sources and detectors.

5.3.3.4 Evaluation of the AH prototype III design

The design of AH prototype III was also evaluated in terms of the general recommendations established in sections 5.2.2.4 and 5.3.1.2.

GR I	USEFUL DATA	REQUIREMENT STATUS	OUTCOME
	GR I	ESSENTIAL	PASSED
FINAL STATUS	PASSED DUE TO THE AVERAGE PERFORMANCE IS ABOVE THE MINIMUM VALUE OF 50% (TABLE 5.16).		
GR II	OPTODE LOCATION	REQUIREMENT STATUS	OUTCOME
	GR II	ESSENTIAL	NOT TESTED
FINAL STATUS	NOT TESTED		

GR III	SAFETY	REQUIREMENT STATUS	OUTCOME
	GR III 1	DESIRABLE	PASSED
	GR III 2	DESIRABLE	PASSED
	GR III 3	ESSENTIAL	PASSED
	GR III 4	ESSENTIAL	PASSED
	GR III 5	ESSENTIAL	PASSED
	GR III 6	ESSENTIAL	PASSED
	GR III 7	DESIRABLE	NOT TESTED
	GR III 8	DESIRABLE	PASSED
FINAL STATUS	FOR THIS DESIGN, THE GR III WAS PASSED, ALTHOUGH SOME MODIFICATIONS MAY BE PERFORMED TO ALLOW MEDICAL KITS.		

GR IV	SKIN ILLUMINATION	REQUIREMENT STATUS	OUTCOME
	GR IV 1	DESIRABLE	PASSED
	GR IV 2	ESSENTIAL	PASSED
	GR IV 3	ESSENTIAL	PASSED
FINAL STATUS	APPROVED.		

GR V	PROBE STRESS	REQUIREMENT STATUS	OUTCOME
	GR V	ESSENTIAL	PASSED
FINAL STATUS	APPROVED.		

GR VI	PROBE COVERAGE	REQUIREMENT STATUS	OUTCOME
	GR VI	ESSENTIAL	PASSED
FINAL STATUS	APPROVED, ALTHOUGH A SPACED DISTRIBUTION OF THE OPTODES AROUND THE SCALP SURFACE MAY BE CONSIDERED TO IMPROVE THE SAMPLING OF THE CENTRAL REGION OF THE BRAIN.		

The result of the GRs indicates that 100% of the requirements were reached for this third prototype of adaptable helmet.

5.3.3.5 Discussion and Conclusions

The nine infant imaging studies scanned with MONSTIR using the third prototype provided an average performance which is *higher* than that for the AH II, and *slightly higher* than that for the CMH, as shown in table 5.18.

Table 5.18 Comparison of the performance between helmets prototypes.

COMPARISON OF PERFORMANCE		
ADAPTABLE HELMET PROTOTYPE III	CUSTOM MADE HELMET	ADAPTABLE HELMET PROTOTYPE II
54.3 ± 12.8%	50.2 ± 16.1%	46.3 ± 2.8%
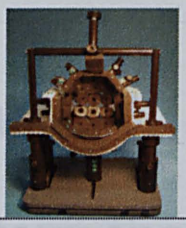	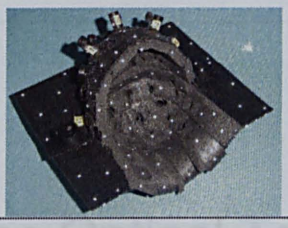	

Table 5.18 also shows a comparison between the average performance of the custom made and adaptable helmets. This shows that the third prototype is clearly effective an alternative to the CMHs, for imaging static optical properties and changes in properties.

Chapter 6

Performance of the Optical Topography Head Probes

6.1 Introduction

In this chapter, the probe designs and results of experimental studies involving the optical topography system are presented. The optical probes are designed to be used to investigate response within the cerebral cortex (figure 2.17). The general characteristics discussed in the chapter 5 will not be applied to the design of this sort of probe, although safety and comfort and the quality of the data are still principal goals in the design of the optical probes.

6.2 General Recommendations for topographic probes

The general requirements taken into account during the design of the topography probe are:

GR I. The optical arrangement must acquire useful data.

1. A minimum contamination of ambient light is essential and direct source-detector leakage must be avoided (good contact between the probe and the sampled region).
2. The probe must cover the sampled area with minimal sensitivity to hair and movement.

GR II. The probe design must consider:

1. The depth of the sampled region at which signals are most sensitive is generally assumed to be approximately equal to half the optode spacing (for typical spacing around 25-35 mm, the penetration depth is ~15mm (Gibson *et al*, 2005a).
2. The maximum useful source-detector separation is normally around 30-40 mm ((Blasi *et al*, 2006), (Gibson *et al*, 2005 a), (Koizumi *et al*, 2003), (Strangman *et al*, 2002), depending on the source intensity).

GR III. The probe must accommodate/sample a baby's head safely, and be quickly and easily removed for emergency nursing care.

6.3 The UCL optical topography probes

6.3.1 The optical connector

The optical probes developed for the UCL topography system have both sources and detectors coupled to the tissue under investigation via simple multimode PMMA optical fibres, of 1 mm diameter. These fibres are held within plastic ferrules inside the connectors, and a special plastic connector was made to accommodate both sources and detectors, depending on the respective ferrule (figure 6.1).

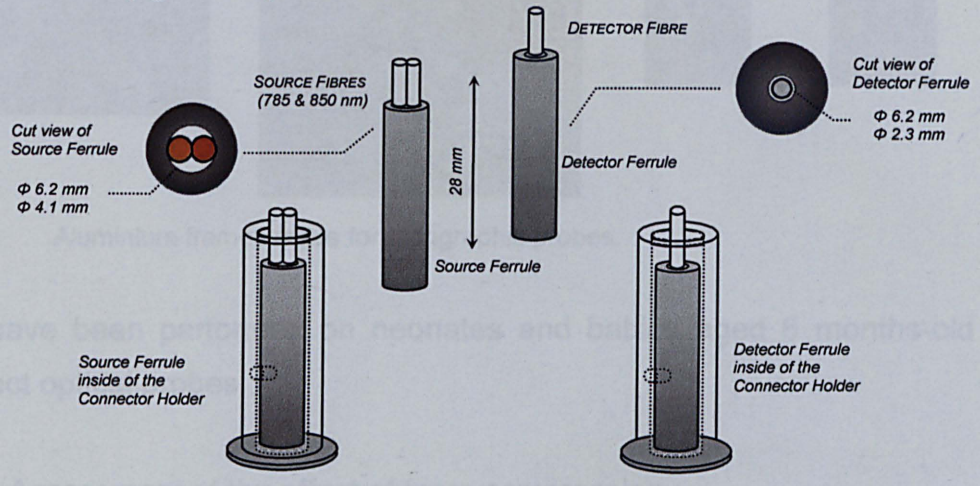

Figure 6.1 Plastic Connectors for UCL optical topography system.

The (source or detector) ferrule holder is attached to a support frame (or a plate) by a connector holder. The connectors maintain the ends of the fibers at a distance of ~10 mm above the scalp, illuminating a circular area of 6 mm diameter (see GR I2 from item 6.2). This reduces the sensitivity of the measurements to slight movement of the probe and to the presence of hair beneath the probe (figure 6.2).

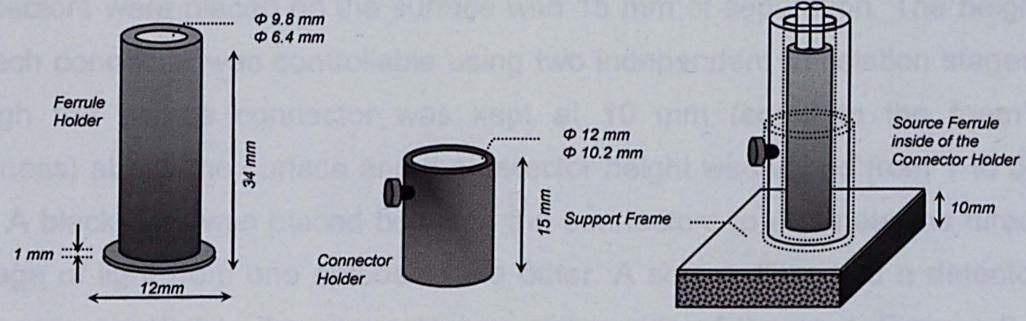

Figure 6.2 Plastic Connectors for UCL optical topography system.

The connectors are arranged in a specific geometry depending on the region to be investigated. To fix the geometry and to give support to the array, all the connectors are attached to a plate, which can be made from aluminium or flexible thermoplastic that can be moulded to the shape of the part of the body under investigation. Slots cut into the plate enable it to be easily deformed to accommodate the contour of an infant's head (figure 6.3).

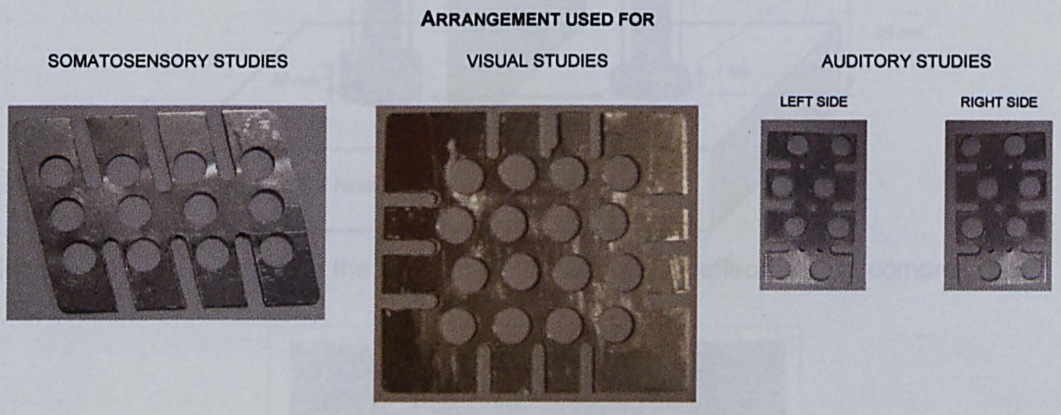

Figure 6.3 Aluminium frames made for topographic probes.

Studies have been performed on neonates and babies aged 6 months-old with distinct optical probes.

6.3.1.1 Assessment of the effect of foam compression

During clinical measurements some change in the compression of the foam could occur which may affect the data. Therefore, a series of experiments was performed to evaluate the effects on the detected intensity of compression of the protective foam of one of the connectors. A homogenous phantom was used consisting of a rectangular slab of 90x59x178 mm with uniform properties (μ_s' = 1 mm^{-1}, μ_a = 0.01 mm^{-1} @ 800 nm and refractive index of 1.56). Two connectors were placed on the surface with 15 mm of separation. The height of each connector was controllable using two independent translation stages, though the source connector was kept at 10 mm (equal to the foam's thickness) above the surface and the detector height was varied from 1 to 50 mm. A black card was placed between the connectors to eliminate the direct leakage of light from one optode to the other. A source fibre and a detector fibre were coupled to the connectors on either side of the card. Figures 6.4

and 6.5 show a schematic representation and a photo of the experimental set-up.

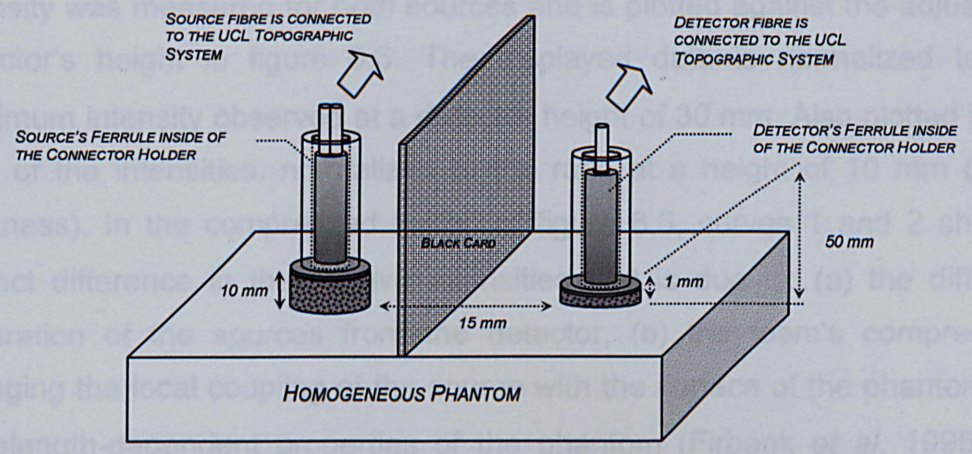

Figure 6.4 Schematic of the experiment to evaluate the effect of foam compression.

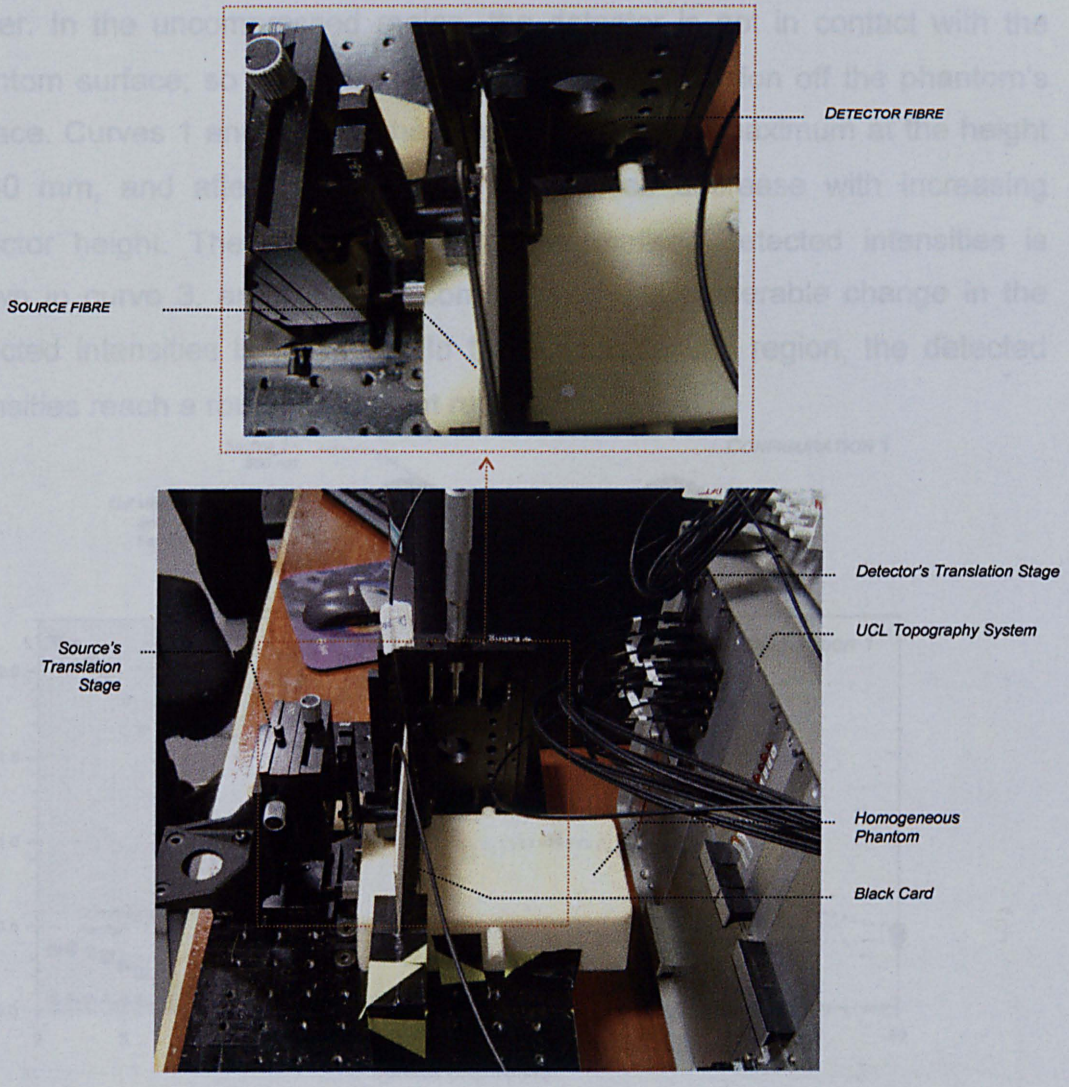

Figure 6.5 Photos of the experiment to evaluate the effect of foam compression.

In configuration 1, the source ferrule was rotated and fixed so that the 850 nm source was closest to the detector, as shown in figure 6.6. The detected intensity was measured for both sources and is plotted against the adjustable detector's height in figure 6.6. The displayed data is normalized to the maximum intensity observed at a detector height of 30 mm. Also plotted is the ratio of the intensities, normalized to the ratio at a height of 10 mm (foam thickness). In the compressed region of figure 6.6, curves 1 and 2 show a distinct difference in the relative intensities that is due to: (a) the different separation of the sources from the detector, (b) the foam's compression changing the local coupling of the source with the surface of the phantom, (c) wavelength-dependent properties of the phantom (Firbank *et al*, 1995 and Firbank and Delpy, 1993), and (d) slight fluctuations in laser diode source power. In the uncompressed region, the detector is not in contact with the phantom surface, so the detected light is due to reflection off the phantom's surface. Curves 1 and 2 show that intensities reach a maximum at the height of 30 mm, and after this point both intensities decrease with increasing detector height. The ratio between the normalised detected intensities is shown in curve 3, and for large compression a considerable change in the detected intensities is observed. In the uncompressed region, the detected intensities reach a roughly constant ratio.

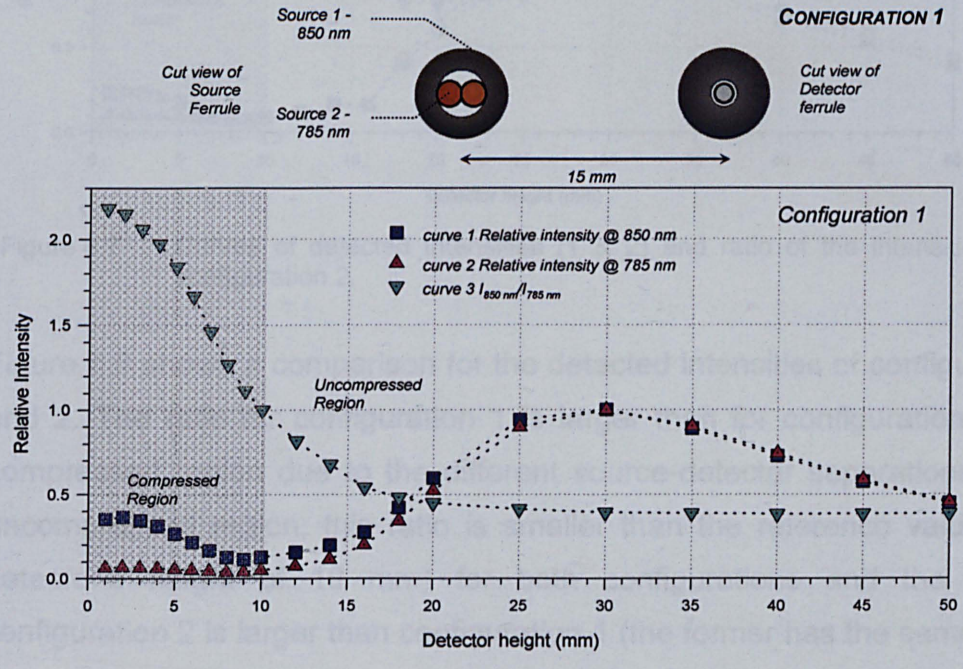

Figure 6.6 Curves of detected intensities (1 & 2) and ratio of the intensities (3) for configuration 1.

In configuration 2 of figure 6.7, the source ferrule was rotated until the distances between both sources and the detector were identical. The intensity from both sources was measured as before and plotted (curve 1 and 2). The ratio between both intensities was also calculated and plotted (curve 3). In figure 6.7, curves 1 and 2 are more similar than for configuration 1, which is due to the sources having the same separation from the detector. The losses are slightly less because of the increase in detected intensity from source 2 and an observed reduction of the obstruction of the light path due to the foam. However, in the compression region of curve 3, large compression of the foam still can cause a significant difference between the detected intensities. In the uncompressed region, the detected intensities again reach a roughly constant ratio.

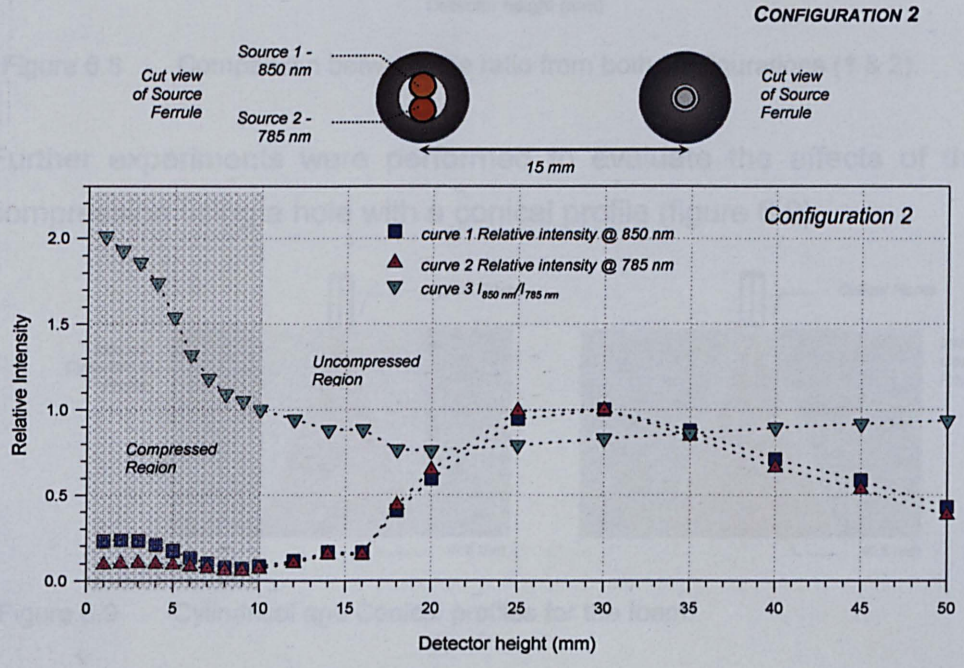

Figure 6.7 Curves of detected intensities (1 & 2) and ratio of the intensities (3) for configuration 2.

Figure 6.8 shows a comparison for the detected intensities of configurations 1 and 2. The ratio for configuration 1 is larger than for configuration 2 in the compressed region due to the different source-detector separations. In the uncompressed region, this ratio is smaller than the reference value (at the detector's height of 10 mm) for both configurations and the ratio for configuration 2 is larger than configuration 1 (the former has the same source-detector separation). However, even for configuration 2 a ratio of one is not

reached possibly due to: the small differences in the brightness of the each laser source, slight difference in source-detector separation, and wavelength-dependent properties of the phantom.

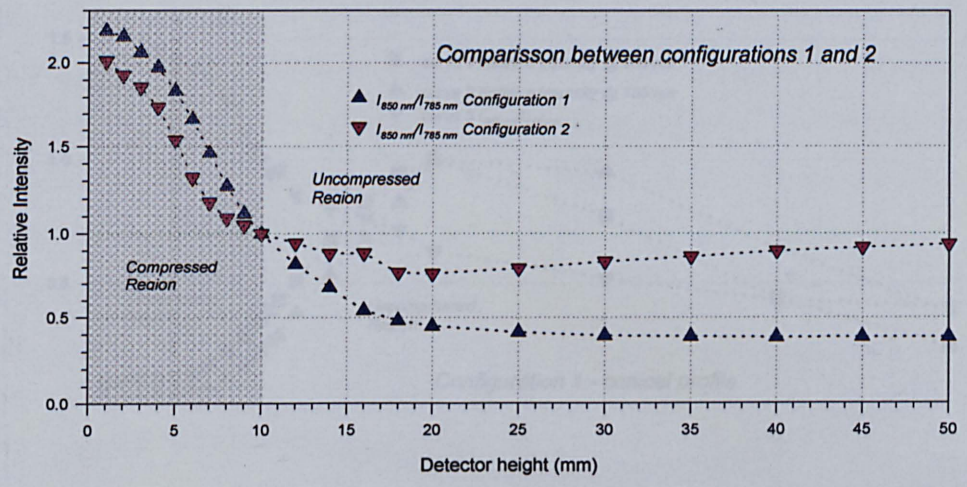

Figure 6.8 Comparison between the ratio from both configurations (1 & 2).

Further experiments were performed to evaluate the effects of the foam's compression using a hole with a conical profile (figure 6.9).

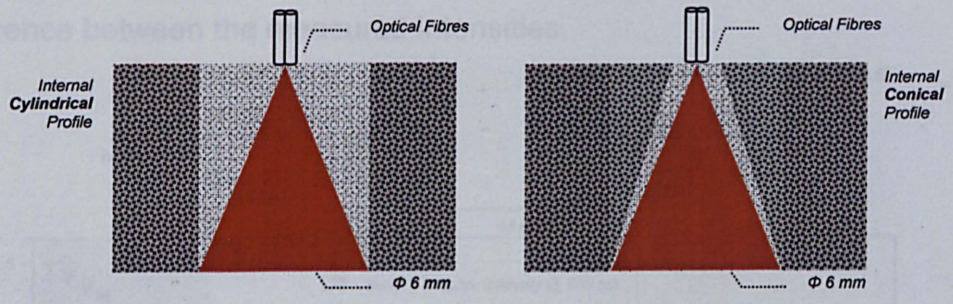

Figure 6.9 Cylindrical and Conical profiles for the foam.

The conical profile was designed to conform to the known divergence of the source beam. It is expected that it will produce less obstruction of the light pathway, resulting in a smaller difference in the ratio between the detected intensities. The ferrule configurations 1 and 2 (described above) were evaluated as before using the conical profile. The profile was made using a heated hole-punch with the approximate desirable conical shape. The results for configurations 1 and 2 are shown in the following figures 6.10 and 6.11 below. The displayed data is normalized to the maximum intensity observed at a detector height of 20 mm for the conical profile.

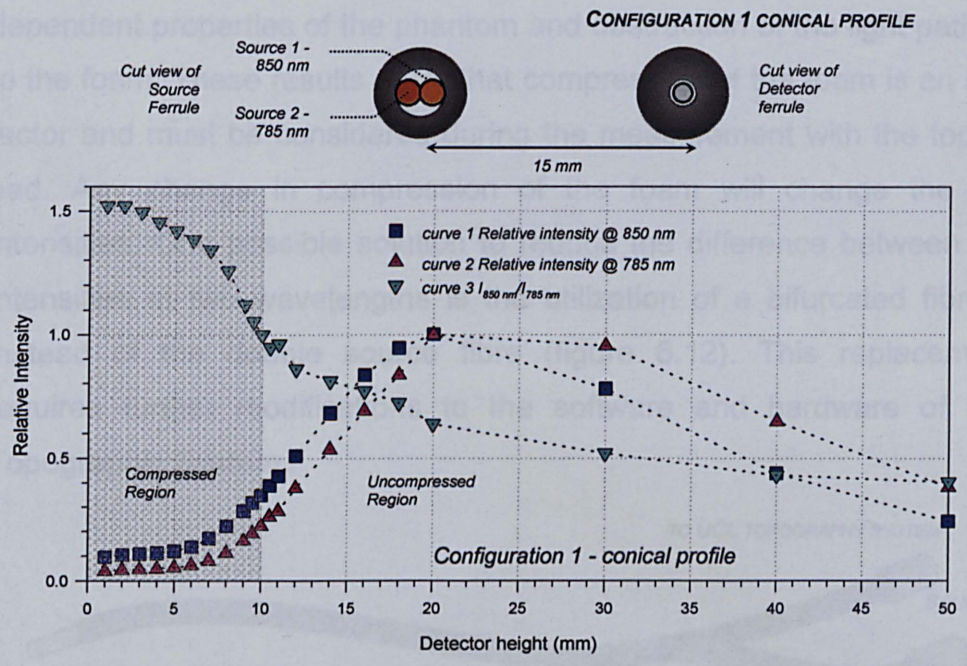

Figure 6.10 Curves of detected intensities (1 & 2) and ratio of the intensities (3) for configuration 1.

The advantage of the conical profile over the cylindrical is clearly shown in figure 6.11, particularly within the compressed region, where there is less difference between the measured intensities.

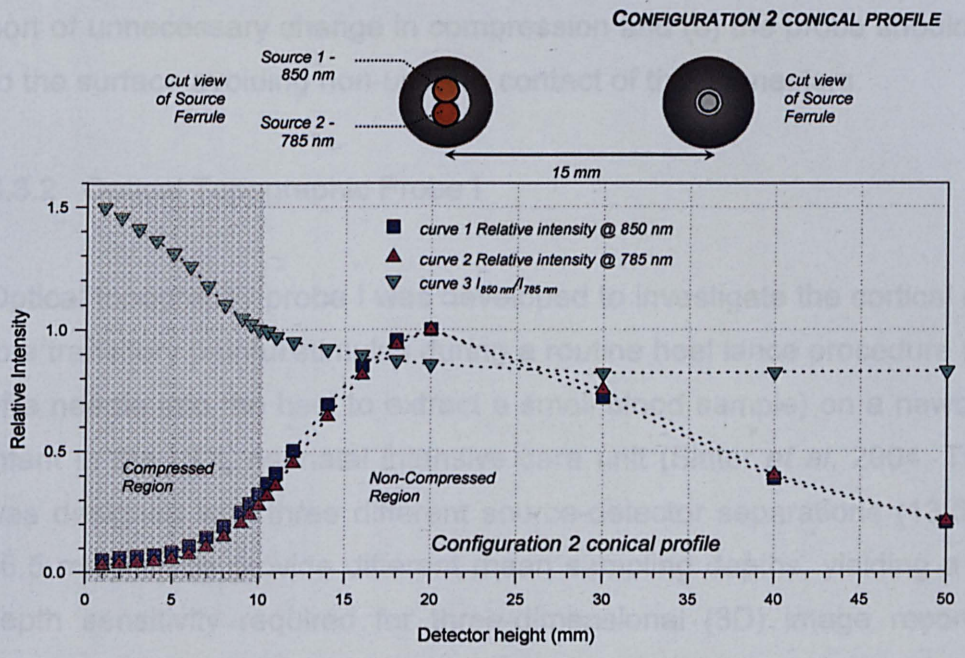

Figure 6.11 Curves of detected intensities (1 & 2) and ratio of the intensities (3) for configuration 2.

The conical profile exhibits less sensitivity to small compression. However, the differences in the detected intensities are still influenced by wavelength-

dependent properties of the phantom and obstruction of the light pathway due to the foam. These results show that compression of the foam is an important factor and must be considered during the measurement with the topographic pad. Any change in compression of the foam will change the detected intensities. One possible solution to reduce the difference between detected intensities at two wavelengths is the utilization of a bifurcated fibre bundle instead of the double source fibre (figure 6.12). This replacement also requires further modifications to the software and hardware of the UCL Topographic System.

Figure 6.12 Schematic picture of the bifurcated fibre bundle.

Some precautions should be considered prior to a measurement: (a) the probe should a have a good contact with the sampled surface avoiding any sort of unnecessary change in compression and (b) the probe should conform to the surface avoiding non-uniform contact of the connectors.

6.3.2 Optical Topographic Probe I

Optical topography probe I was developed to investigate the cortical response to a transitory painful stimulus during a routine heel lance procedure (insertion of a needle into the heel to extract a small blood sample) on a newborn term infant in the UCL neonatal intensive care unit (Slater *et al*, 2004. The probe was designed with three different source-detector separations (13.5, 21 and 26.5 mm) which provide different mean sampling depths, yielding a range in depth sensitivity required for three-dimensional (3D) image reconstruction (Everdell *et al*, 2005). The distribution of sources and detectors is shown in figure 6.13 and consists of 4 detectors and 8 source pairs coupled to the probe optical fibres.

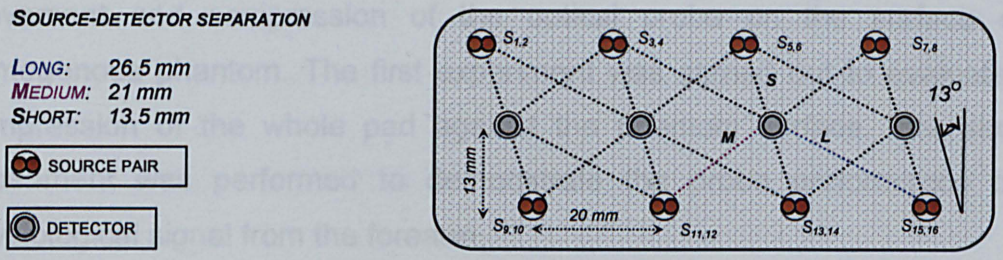

Figure 6.13 Distribution of the sources and detectors on the pad.

The support frame was made of an aluminium plate with 12 holes to attach the plastic connectors and slots to enable a controllable conformation of the probe (figure 6.14) to the infant head shape.

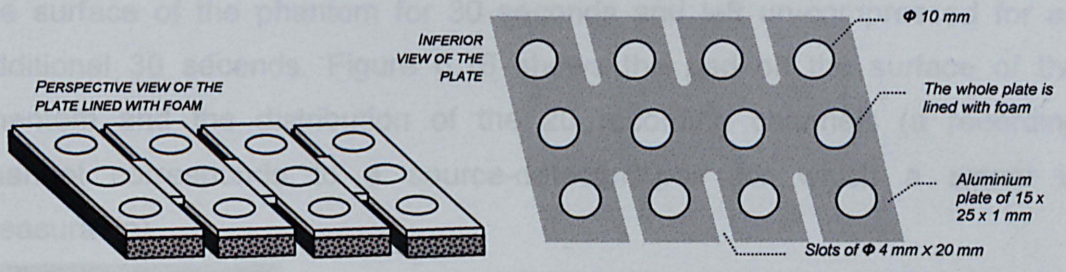

Figure 6.14 Aluminium frame plate.

The plate is also covered with a 10 mm thick layer of near-infrared absorbing foam (containing 6 mm – diameter holes) to provide a safe and comfortable optical contact with the head and prevent unwanted light reaching the detectors. The final arrangement is shown in figure 6.15 with the plastic connectors and also with the plastic fibre cables.

Figure 6.15 Views of the optical probe and an illustration of its utilization for measurements on an infant doll head.

Prior to the baby studies with the topographic pad to generate 2D maps of brain activation, some experiments were performed to evaluate the effects of

movement and compression of the optical probe on the surface of a homogenous phantom. The first experiment was carried out to evaluate the compression of the whole pad against the phantom surface. The second experiment was performed to demonstrate the probe performance on a physiological signal from the forearm.

6.3.2.1 Assessment of the Topographic Probe I: Compression of the Pad

A first series of experiments was performed using the rectangular slab phantom and the optical topographic pad. The pad was compressed against the surface of the phantom for 30 seconds and left un-compressed for an additional 30 seconds. Figure 6.16 shows the pad on the surface of the phantom and the distribution of the 20 recording channels (a recording channel corresponds to a source-detector pair for which a signal is measurable).

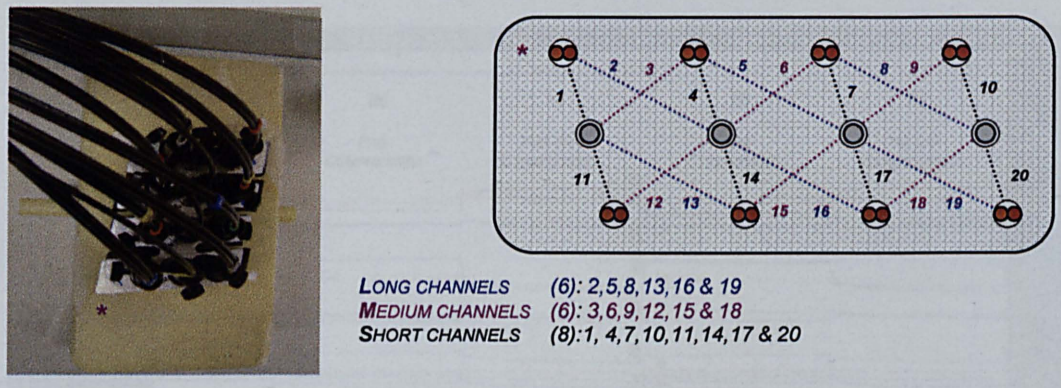

Figure 6.16 LEFT: Compression of the optical topographic pad against the phantom surface and RIGHT: Pad Channels (20 in total).

Figures 6.17 and 6.18 show the raw data recorded for the 20 channels for both wavelengths. The signals are plotted on an absolute scale with a different baseline for each channel. The protocol employed for the experiment was as follows: (a) the pad was placed uncompressed on the slab phantom (figure 6.16) and data were acquired for 20 seconds, (b) a first event mark is registered and, simultaneously, the whole pad was compressed against the phantom for 30 seconds, (c) the pad was released for 30 seconds, (d) the pad was compressed again for a further 30 seconds and simultaneously a second event mark is registered and (e) the pad was completely released. The

recorded data from figures 6.17 and 6.18 show that the signals are strongly affected by noise, especially the channels corresponding to large source-detector separations.

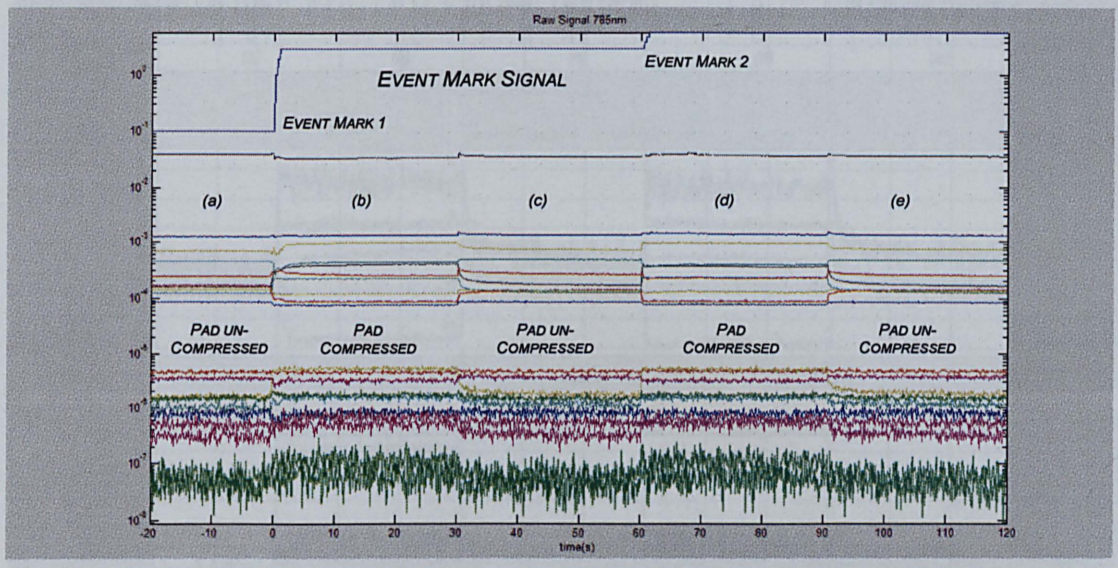

Figure 6.17 Detected intensities of the 20 channels with the *event mark* signal (on the top) at the wavelength of 785 nm.

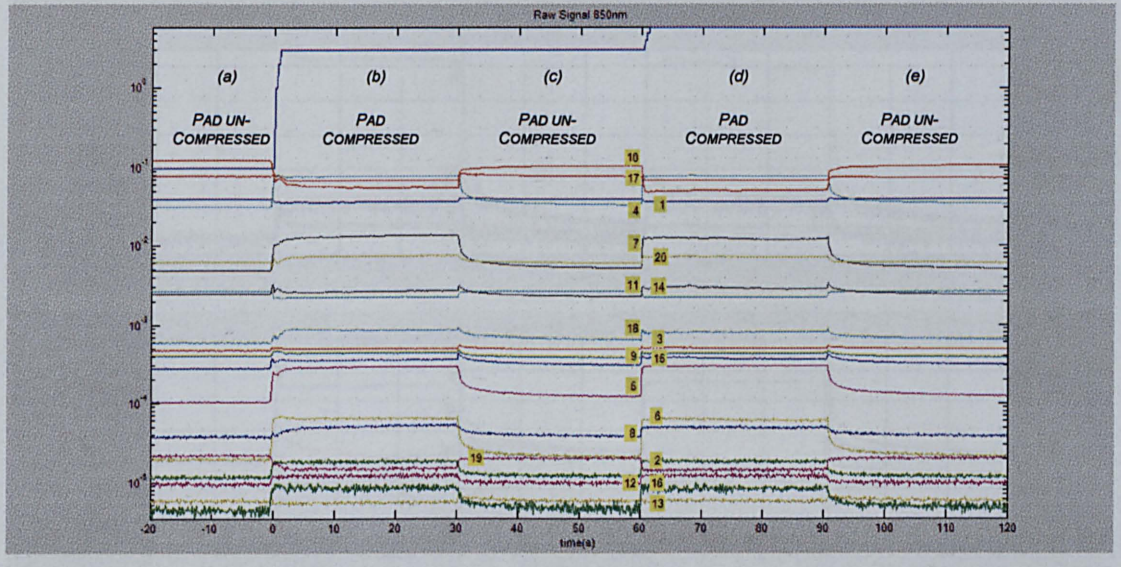

Figure 6.18 Detected intensities for the 20 channels with the *event mark* signal (on the top) at the wavelength of 850 nm.

During compression of the pad some signals change slowly due to the time it takes for the foam to redistribute when compressed. The different levels and variations in signals are due in part to changes in coupling and in part to movement of the foam in the path of the source beam. Following subtraction of the DC level of each signal, the data are re-plotted in figures (figure 6.19 (i), (ii) and (iii) for the three distinct separations of 26.5, 21 and 13.5 mm).

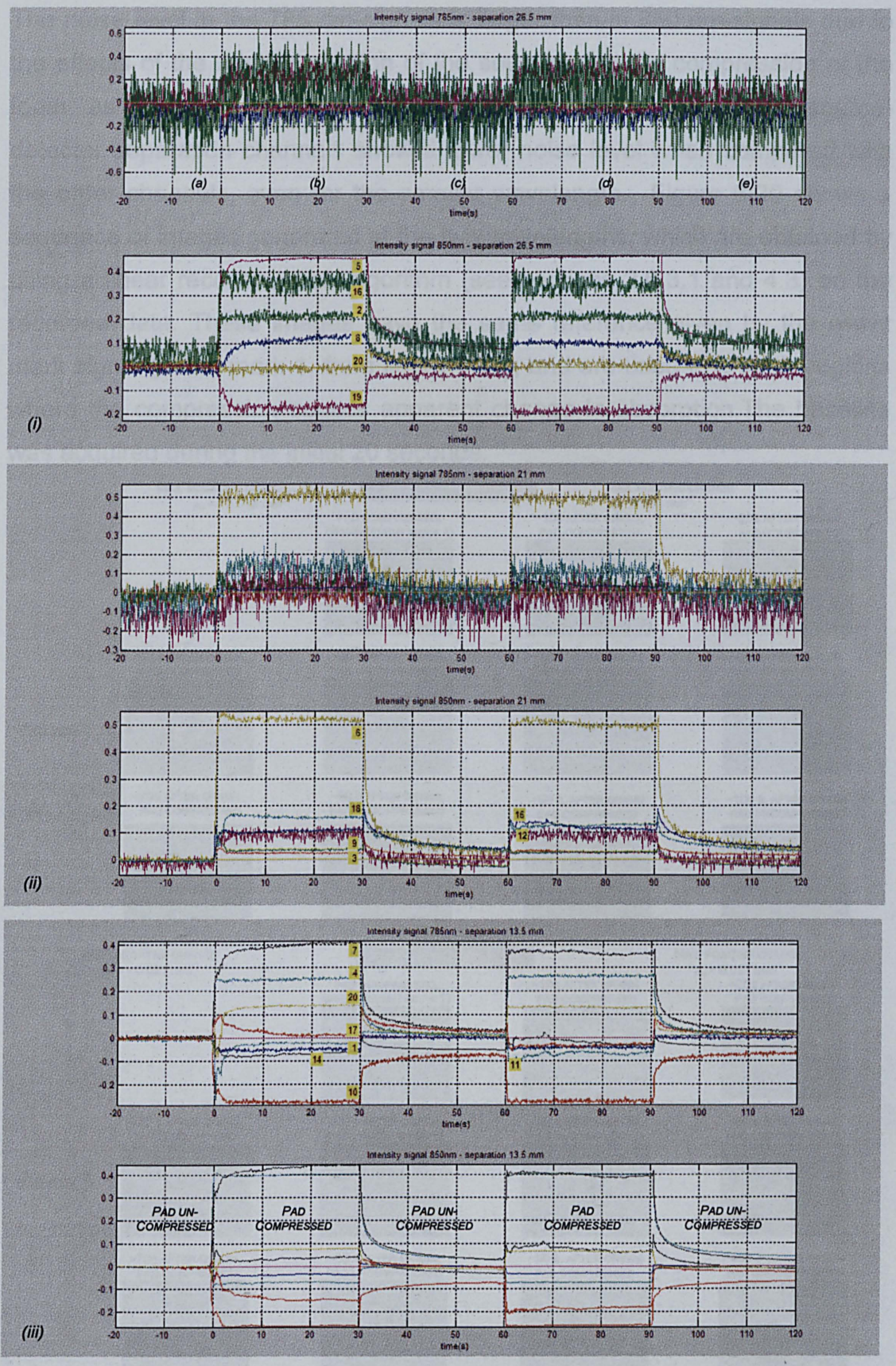

Figure 6.19 Detected Intensity signals for the three distinct separations during the pad compressed procedure, with a common baseline. The numbers represent the respective channels.

The noise level in the 785 nm-signals is larger than in 850 nm-signals due to the effects of the relative position of the sources and the compression of the foam, as described earlier in the section 6.3.1.1. Also, the short source-detector separation channels show a lower noise level when compared with the other channels, even for the smaller wavelength. Figure 6.20 shows a sequence of images generated at the two wavelengths, which are obtained by using a linear reconstruction algorithm (see sections 2.6.3.1 and 4.3) on the recorded data. These images have the same reference given by the event mark signal (event mark 1, from figure 6.17), and are used to identify regions where the compression causes apparent change in absorption.The baseline was acquired during the initial 20 seconds.

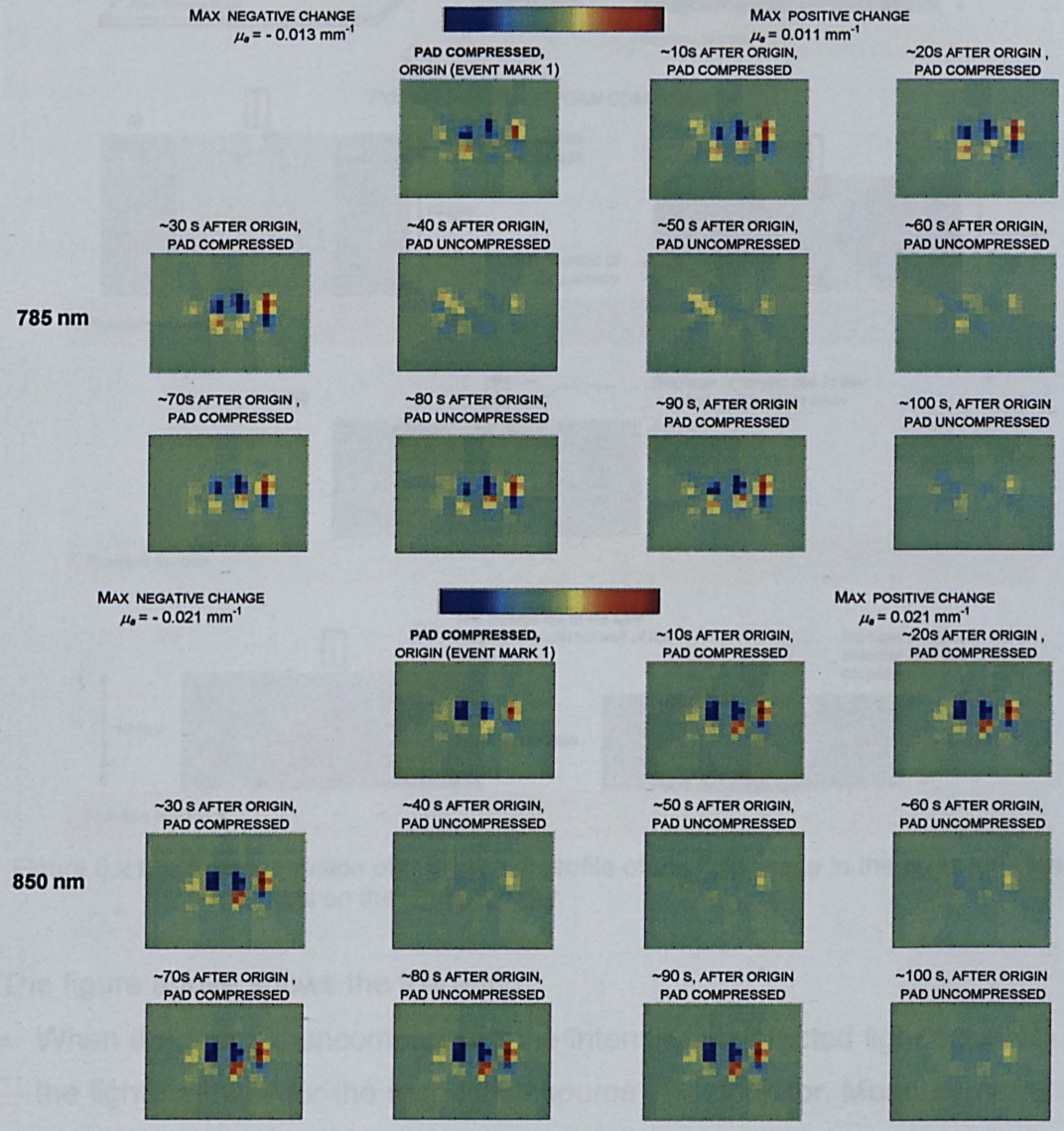

Figure 6.20 Sequence of absorption images at a 10 s time interval showing the change in signals due to the foam compression at 785 and 850 nm, respectively.

The sequence of images in figure 6.20 show the apparent changes in absorption resulting from the changes in the signal when the optode coupling varies and when (transverse and/or longitudinal) motion of the foam occurs in the light pathway. These changes are associated with the variation in the internal profile of the holes (mainly) and in the thickness of the foam, as summarised and schematically represented in figure 6.21.

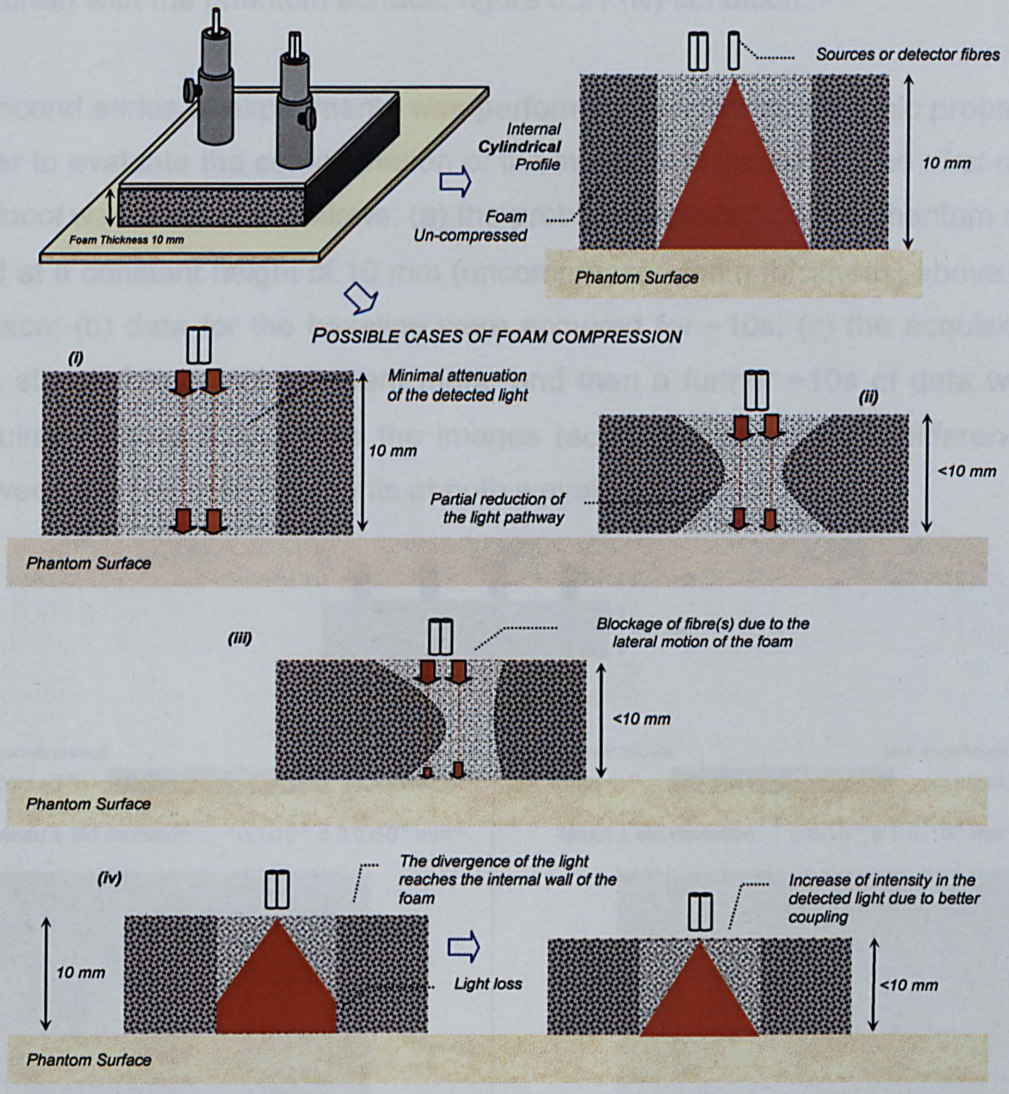

Figure 6.21 Representation of the internal profile of the hole made in the protective foam and effects on the light pathway.

The figure above shows the following:

- When the foam is uncompressed the intensity of detected light depends on the light pathway for the respective source and detector. Measurements for zero compression represent the baseline, figure 6.21 (i) condition.

- The red (bright) regions indicate an apparent increase in absorption caused by blockage of the light pathway (a reduction of the detected intensity below the baseline), figure 6.21 (ii) and (iii) conditions.
- The blue (or dark) regions represent an apparent decrease in absorption (due to an increase in detected intensity), which indicate the light pathway has been slightly improved and/or there is better coupling of the fibre (or fibres) with the phantom surface, figure 6.21 (iv) condition.

A second series of experiments was performed with the topographic probe, in order to evaluate the contamination of the image with artefacts. The *first data protocol* was defined as follows: (a) the probe was placed on the phantom and held at a constant height of 10 mm (uncompressed foam thickness) above the surface; (b) data for the baseline were acquired for ~10s; (c) the acquisition was stopped to select an event mark, and then a further ~10s of data were acquired. Figure 6.22 shows the images reconstructed from the differences between the two measurements at both wavelengths.

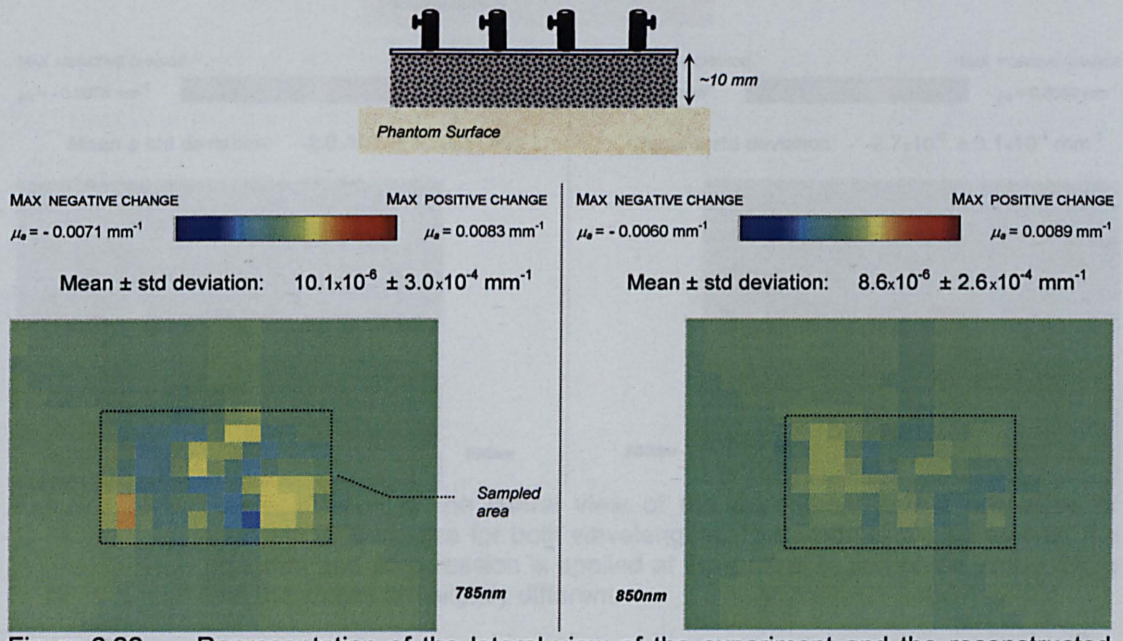

Figure 6.22 Representation of the lateral view of the experiment and the reconstructed images for both wavelengths. The probe is placed against the phantom without compression. Note that the scales are slightly different.

No changes to the position or compression of the probe was made between the two measurements, and as expected, the reconstructed images in figure 6.22 show no significant artefacts within the sampled region (the area directly

beneath the probe). Any small apparent changes in absorption must be due to small laser power fluctuations or other sources of random noise in the system. The average change in absorption and corresponding standard deviation are calculated for both images. The average values are very small with also small standard deviations, as expected.

The *second protocol* for data acquisition is described as follows: (a) the probe was held at the same position as for the first protocol; (b) a baseline measurement was acquired for 10 seconds; (c) the acquisition was stopped and the probe was compressed with a constant pressure on its central region (between the central optodes), and (d) data were acquired for a further 10 seconds during the compression. Figure 6.23 shows the reconstructed images generated using the differences between the baseline and the data acquired during compression for both wavelengths.

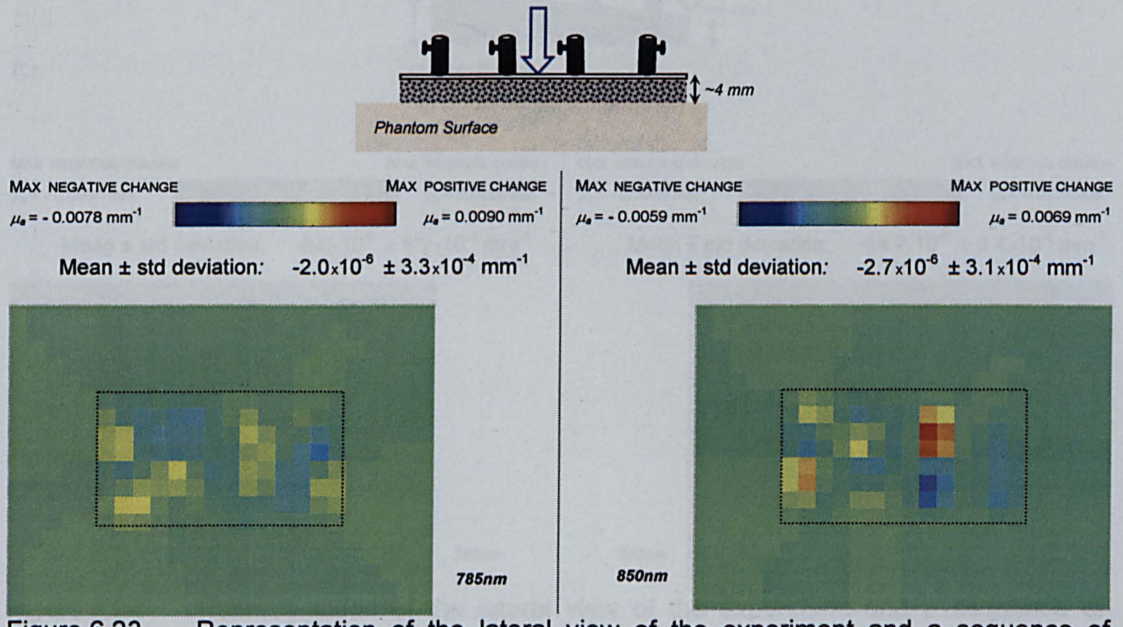

Figure 6.23 Representation of the lateral view of the experiment and a sequence of reconstructed images for both wavelengths. The probe is placed against the phantom and compression is applied at the central region of the probe. Note that the scales are slightly different.

The images show a random distribution of artefacts. The average change in absorption and standard deviation is again determined for both images. The average values are still relatively small with a small standard deviation. In comparison with the previous experiment, the calculated standard deviations show similar values, which indicates that an approximately even compression

of the pad (foam) produces only a small apparent change in the absorption coefficient, or a low level of artefacts.

The *third protocol* for data acquisition is described as follows: (a) the probe was held at the same location as for the first protocol; (b) a baseline measurement was acquired for ~10 s; (c) the acquisition was stopped and the probe was compressed with a constant pressure on its right edge, and (d) data were acquired for a further 10 s. The left edge of the probe was maintained at a constant height of 10 mm. The pressure was applied evenly over the length of the right side, and the degree of compression is expected to decrease over the longitudinal direction, from right to left. Figure 6.24 shows the reconstructed images generated from the compression-induced difference in measurements at both wavelengths.

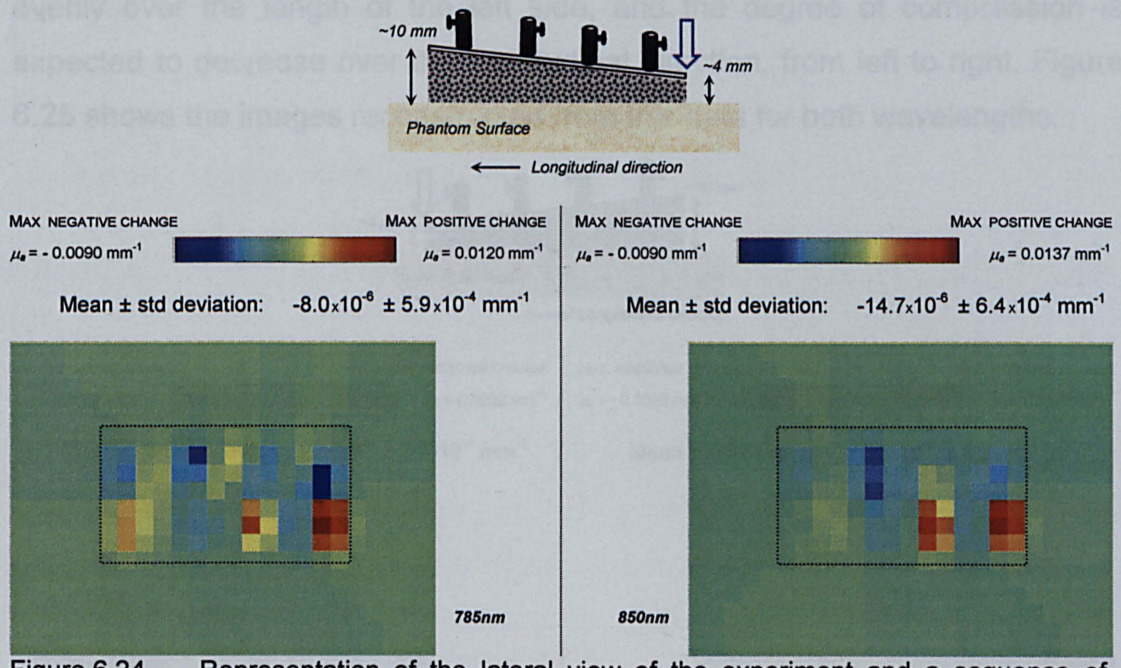

Figure 6.24 Representation of the lateral view of the experiment and a sequence of reconstructed images for both wavelengths. The probe is placed against the phantom and compression is applied along the right edge of the probe. Note that the scales are slightly different.

The reconstructed images show that the sampled area is filled with artefacts. The top half of both images show a fairly even distribution with a slight overall apparent decrease in absorption, which is likely due to better coupling as a result of movement of the foam, as shown in figure 6.21(iv). The bottom half shows some large apparent increases in absorption, suggesting that some

sources and detectors become blocked due to the longitudinal motion of the foam (particularly for the shorter s-d separations). There is some correlation between the (decreasing) change in the distribution of compression from right to left with the magnitude of the artefacts. Although the magnitude of the mean change in absorption is comparable to the first experiment (no compression), the standard deviation is roughly twice as large.

Finally, the *fourth protocol* for data acquisition is described as follows: (a) the probe was held at the same location as for the first protocol; (b) a baseline measurement was acquired for ~ 10 seconds; (c) the acquisition was stopped and the probe was compressed with a constant pressure on its left edge, and (d) data was acquired for a further 10 seconds. The right edge of the probe was maintained at a constant height of 10 mm. The pressure was applied evenly over the length of the left side, and the degree of compression is expected to decrease over the longitudinal direction, from left to right. Figure 6.25 shows the images reconstructed from this data for both wavelengths.

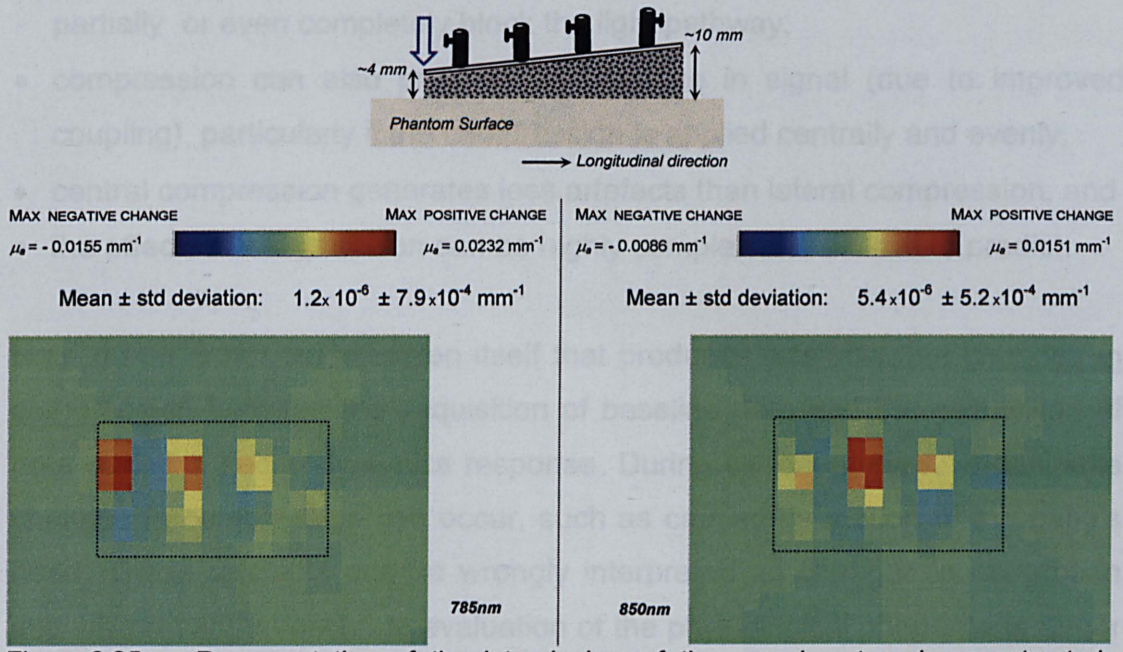

Figure 6.25 Representation of the lateral view of the experiment and reconstructed images for both wavelengths. The probe is placed against the phantom and compression is applied along the left edge of the probe. Note that the scales are slightly different.

The reconstructed images again show artefacts in the sampled area, although the distribution is somewhat different at the two wavelengths. The top of the

sampled area is more affected than the bottom, with artefacts clearly showing apparent increases in absorption. The lower half shows no overall change, probably because effects which cause an increase in intensity are cancelled by those which cause a decrease in intensity. The standard deviation in the change in absorption is similar to the last experiment.

From the results above we can deduce that compression in the centre of the pad generates less artefacts and less change in apparent absorption than compression on the extremes. This is due to the smaller changes to the obstruction of the light by the foam when compression is applied evenly downwards.

We can conclude the following from the experiments:

- even if the topographic probe is only slightly compressed against the phantom, artefacts are likely to occur;
- compression produces changes in the distribution of foam, which can partially or even completely block the light pathway;
- compression can also produce an increase in signal (due to improved coupling), particularly if the compression is applied centrally and evenly;
- central compression generates less artefacts than lateral compression, and
- the effects of compression can be highly complex and difficult to predict.

Note that it is not compression itself that produces artefacts, but changes in compression between the acquisition of baseline data and the acquisition of data during a haemodynamics response. During clinical studies, undesirable changes in compression can occur, such as caused by motion of the baby's head. These artefacts can be wrongly interpreted as changes in absorption and will prevent an accurate evaluation of the physiological phenomena under investigation. Since compression in the central region of the pad produces less artefacts than compression of the edges, this suggests that the probe should be mechanically supported via the centre of the probe when applied to the head or other part of the body.

6.3.2.2 Assessment of the Topographic Probe I: Pressure Cuff Measurements

In order to demonstrate the system performance on a physiological signal, an experiment was performed on the forearm of an adult volunteer, looking at the changes that occur in response to venous and arterial occlusions. The volunteer had the bendable topographic pad attached to the underside of the lower forearm and a blood pressure cuff was placed around the upper arm (figure 6.26).

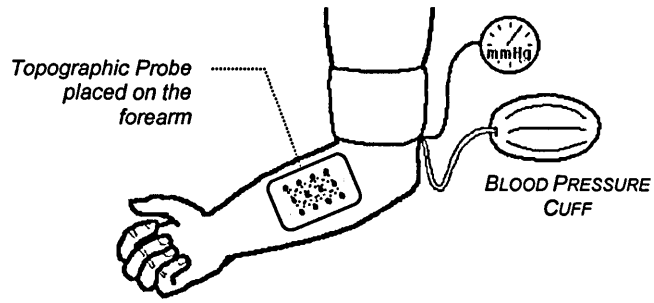

Figure 6.26 Schematic picture of the passive cuff experiments.

For the first experiment, the data protocol was defined as follows: (a) baseline recording for 60 s; (b) venous cuff occlusion at 40 mmHg, during 0 – 260 s; (c) venous cuff release at 260 s; (d) rest and recovery from 260 – 490 s. Figure 6.27 shows a plot of the HbO_2 and Hb changes, which were calculated using the equations [2.22] and [2.23]. It also shows the results for selected channels (i.e. those with the shortest source-detector separation and with less noise). The results match with the expected changes in both *[HbO_2]* and *[Hb]* during this manoeuvre: during venous occlusion, both *[HbO_2]* and *[Hb]* should rise as the normal venous flow is restricted while arterial blood continues to flow into the arm (Vaithianathan *et al*, 2004).

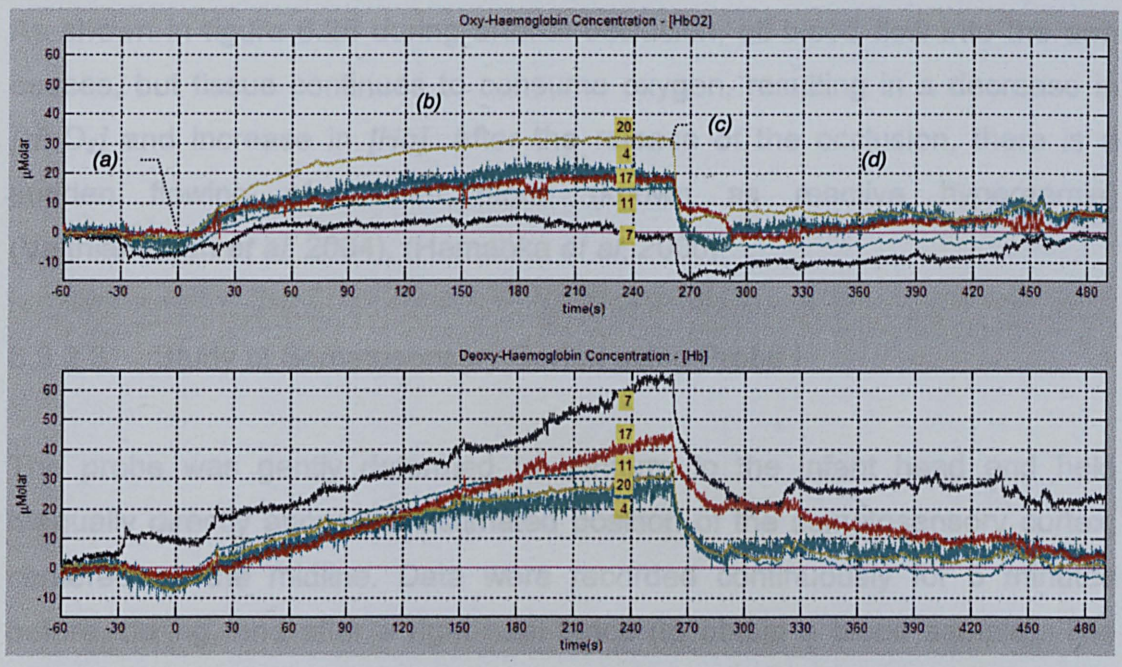

Figure 6.27 Detected signals (change in concentration) for the channels 4, 7, 11, 17 and 20 during venous occlusion.

For the second experiment, the volunteer was subjected to an arterial occlusion. With the pad and a pressure cuff placed at the same positions described above, the acquisition protocol was as follows: (a) baseline recording for 60 s; (b) arterial cuff occlusion at 200 mmHg, during 0 – 250 s; (c) arterial cuff release at 250 s; (d) rest and recovery from 250 – 490 s (figure 6.28).

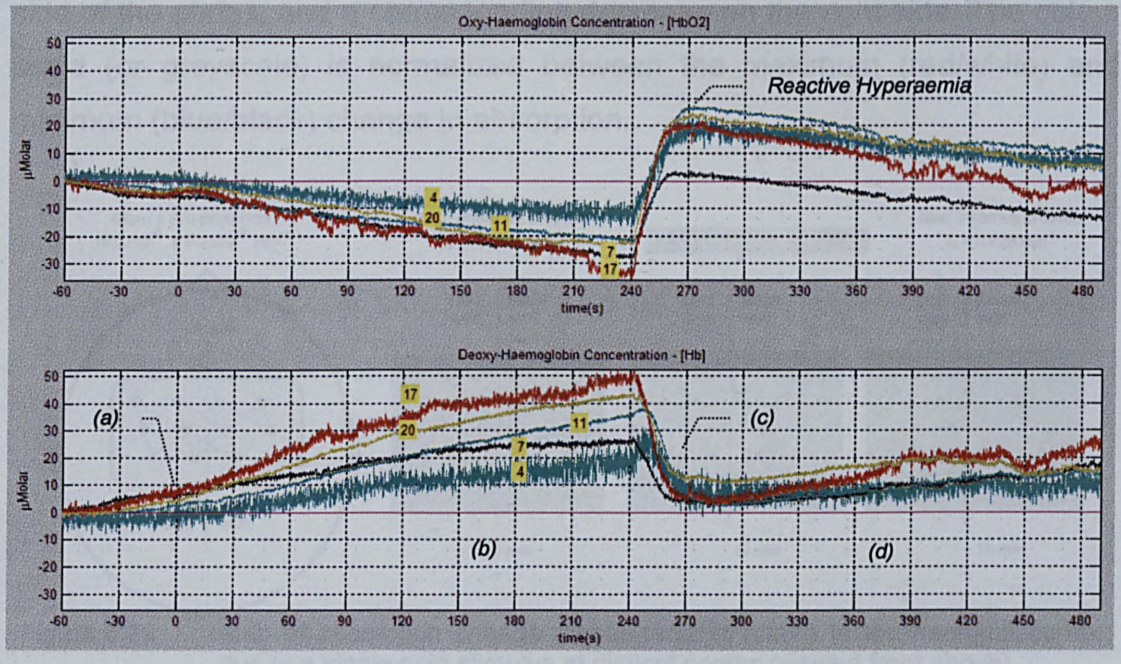

Figure 6.28 Detected signals (change in concentration) for the channels 4, 7, 11, 17 and 20 during arterial occlusion.

As shown in figure 6.28 during arterial occlusion, all blood flow into the arm ceases, but tissue continues to consume oxygen, resulting in a decrease in *[HbO_2]* and increase in *[Hb]*. After the release of the occlusion, there is a sudden flowing of arterial blood (known as reactive hyperaemia) (Vaithianathan *et al*, 2004), (Hamaoka *et al*, 2000).

6.3.2.3 Study of Somatosensory Cortex using Probe I

The probe was gently deformed to conform to the infant head and held manually directly above the estimated position of the somatosensory cortex, centered on the midline. Data were recorded continuously for 5 minutes before, during, and after a right heel lance (to obtain a blood sample). The recorded changes in intensity due to the stimulus were used to generate 3D images representing the change in absorption (in arbitrary units) occurring in the tissues beneath the probe. Due to the nature of the stimulus it is not possible to obtain data that can be subsequently block averaged to increase the signal to noise ratio. The images were obtained using a linear reconstruction algorithm. Figure 6.29 shows an image of the change in absorption at a 785 nm occurring at depths of 5, 10 and 15 mm below the surface. The image reveals an increase due to additional blood flow to the left side of the cortex, and a corresponding decrease on the right side. The colour scale (or greyscale) is normalized between the maximum (red/white) and minimum (blue/black) change in absorption.

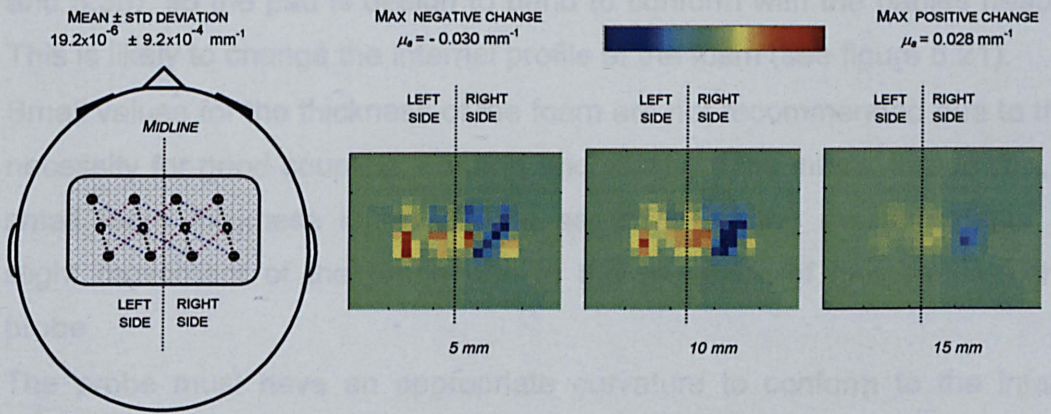

Figure 6.29 Map of absorption change (linear reconstruction) in the neonatal cortex due to a single pain stimulus at distinct depths (viewed from above).

Also, figure 6.30 shows a sequence of images which show the change in absorption in time intervals of 1 s at 785 nm occurring at a depth of 5 mm.

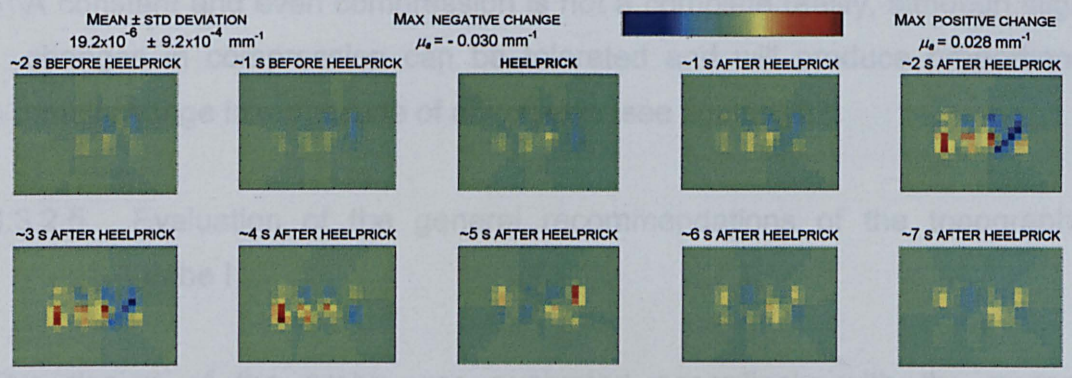

Figure 6.30 Sequence of images showing the change in absorption at 785 nm at a depth of 5 mm (right heel lance).

These findings agree with previous measurements obtained by (Slater *et al*, 2004), who used a two channel NIR spectrophotometer to investigate cortical pain processing in neonates using the haemodynamic response in the somatosensory cortex due to a right heel lance for blood sampling. An increase of concentration of total Haemoglobin (*[total Hb] = [Hb]+[HbO$_2$]*) was observed in the contralateral (on the opposite side of the stimulus) somatosensory cortex and a decrease in the ipsilateral (on the same side of the stimulus) somatosensory cortex.

6.3.2.4 General conclusions about the design of the topographic probe I

- The shapes and sizes of babies heads are very variable (see figures 5.33 and 5.35), so the pad is design to bend to conform with the babies heads. This is likely to change the internal profile of the foam (see figure 6.21).
- Small values for the thickness of the foam are not recommended due to the necessity for good coupling, comfort and safety of the infant. In addition, a small foam thickness increases the sensitivity of the measurements to slight movement of the probe and to the presence of hair beneath the probe.
- The probe must have an appropriate curvature to conform to the infant head to avoid gaps between the head and the probe and excessive stress

on the edges of the probe, which potentially can block the light pathway in the foam.

- A constant and even compression is not a complete reality, although slight changes in compression can be tolerated and will produce proportional small change in magnitude of absorption (see figure 6.23)

6.3.2.5 Evaluation of the general recommendations of the topographic probe I

The design of the probe was evaluated accordingly with the general recommendations described in section 6.2.

GR I	USEFUL DATA	REQUIREMENT STATUS	OUTCOME
	GR I 1	ESSENTIAL	PASSED
	GR I 2	ESSENTIAL	PASSED
FINAL STATUS	PASSED, THE DESIGN OF THE OPTODE HAS TAKEN IN ACCOUNT THE DIVERGENCE OF THE LIGHT BEAM (SEE FIGURES 5.10 AND 6.1).		

GR II		REQUIREMENT STATUS	OUTCOME
	GR II 1	ESSENTIAL	PASSED
	GR II 2	ESSENTIAL	PASSED
FINAL STATUS	PASSED, THE PROBE ENABLES DATA TO BE RECORDED AT 3 DIFFERENT SOURCE-DETECTOR SEPARATIONS, NEEDED FOR 3D IMAGE RECONSTRUCTION. PASSED, THE MAXIMUM SOURCE-DETECTOR DISTANCE WAS UNDER THE LIMITING RANGE		

GR III	SAFETY	REQUIREMENT STATUS	OUTCOME
	GR III	ESSENTIAL	PASSED
FINAL STATUS	PASSED, THE PROBE HAS NOT LEFT MARKS OVER THE SAMPLED REGION ON THE BABY'S HEAD.		

The design and manufacture of the probe under the recommendations has proved to be successful.

6.3.3 Optical Topographic Probe II

Another probe has been designed for optical topography studies of the visual cortex of babies aged 6-months-old, which are being investigated by Prof. Mark Johnson and colleagues at Birkbeck College in collaboration with our group at UCL. This probe has a different design from the previous topographic probe I, with a distribution of sources and detectors arranged to maximize the number of source-detector pairs with 3 different separations at 14.6 mm, 17.1 mm and 23.0 mm, and to cover a large portion of the surface visual cortex

with interrogation at different depths (Blasi *et al*, 2006). The distribution of sources and detectors is shown in figure 6.31 and consists of eight detectors and eight source pairs. The support pad was also made of an aluminium plate (1mm thickness) with 16 holes to attach the connectors, and with several slots to enable the plate to be easily conformed to the head surface (figure 6.31).

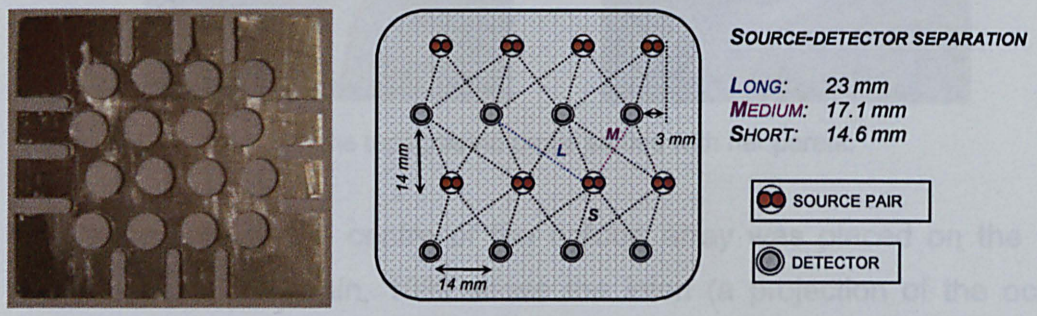

Figure 6.31 LEFT: Support for the optodes. RIGHT: Pad Channels (30 in total).

Some minor modifications were required to the control software of the UCL topography system for this probe configuration, which in general consists of a new source-detector pair list in a header file for those which are expected to provide a measurable signal. The final arrangement with the plastic connectors is shown in figure 6.32 below, and for these studies the probe incorporated some Velcro™ and Coban™ strips, enabling the pad to be comfortably held onto the baby's head.

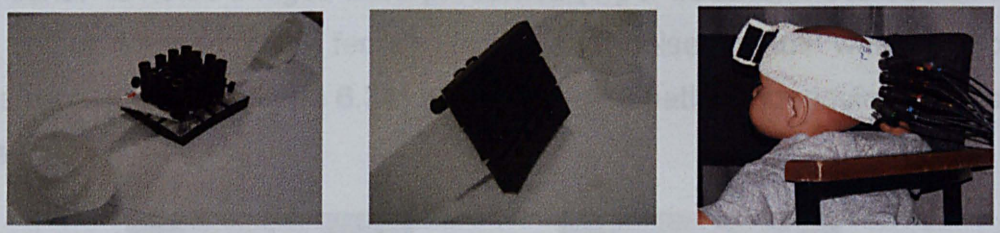

Figure 6.32 Views of the optical probe for visual cortex studies and an illustration of its utilization.

6.3.3.1 Study of the Visual Cortex using probe II

The study that was performed involved older infants, between 4 and 6 months of age. This was an attempt to repeat a study that had previously been performed with the NIRO 300 infrared spectroscopy system (Csibra *et al*, 2004). The objective of the experiment is to test whether the UCL topography system is able to detect subtle differences between evoked responses to two

complex visual stimuli in the babies. Figure 6.33 shows a subject settled with her parent during the experiment.

Figure 6.33 Baby with the topographic probe settled with her parent.

In this experiment the centre of the optode array was placed on the visual cortex area of the brain, 10% above the inion (a projection of the occipital bone that forms a slight lump at the back of the head just above the neck (Hall et al, 1989)) and across the midline, covering parts of both the temporal and parietal lobes. The baby was sat in front of a video screen and encouraged to watch the displayed images for as long as possible. The stimuli were presented in a cyclic loop and started with an animated cartoon to attract the baby's attention (during at least 10 s), 10 varying face images (1 per second) and more cartoons for 10 seconds. If it was considered that the baby's attention on the cartoons was kept for at least 4 continuous seconds, additional 10 noise images were presented (1 per second). Face stimuli were full colour images of 5 female faces and noise stimuli were artificially constructed images (figure 6.34) with the same spatial frequencies and as the faces.

Figure 6.34 LEFT: Face stimuli and RIGHT: Noise stimuli.

This time span allowed several cycles of data to be block-averaged together. The subject was filmed throughout the experiment so the video could be compared with the data with a view to identifying movement artefacts (Csibra

et al, 2004), (Blasi *et al*, 2006). Figure 6.35 shows the linear image reconstruction of the change in concentration of oxy-haemoglobin when the infant's attention is focussed on the face stimuli and noise stimuli.

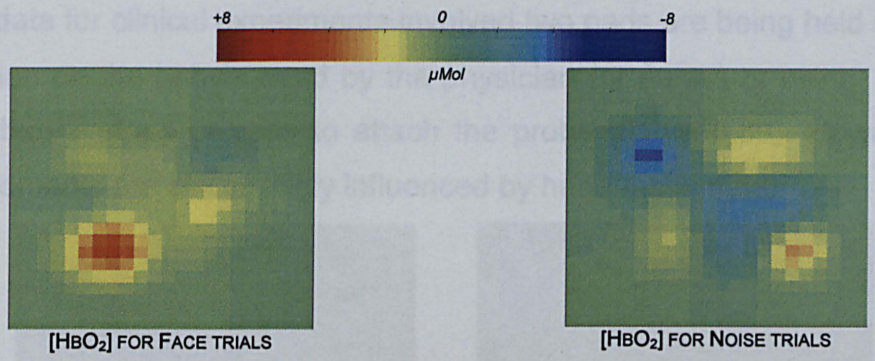

Figure 6.35 Image reconstructions for change in [HbO_2] for: LEFT- Face stimuli (elapsed time 10.2 s) and RIGHT- noise stimuli (elapsed time 6.5s).

6.3.3.2 Evaluation of the general recommendations of the topographic probe II

The design of the probe was evaluated accordingly with the general recommendations described in section 6.2.

	USEFUL DATA	REQUIREMENT STATUS	OUTCOME
GR I	GR I 1	ESSENTIAL	PASSED
	GR I 2	ESSENTIAL	PASSED
FINAL STATUS	PASSED.		

	DESIGN	REQUIREMENT STATUS	OUTCOME
GR II	GR II 1	ESSENTIAL	PASSED
	GR II 2	ESSENTIAL	PASSED
FINAL STATUS	PASSED.		

	SAFETY	REQUIREMENT STATUS	OUTCOME
GR III	GR III	ESSENTIAL	PASSED
FINAL STATUS	PASSED.		

The design and manufacture of the optical probe II under the recommendations has proved to be successful.

6.3.4 Optical Topographic Probe III

For auditory studies, another probe has been developed to be utilised for optical topography studies of the auditory cortex of babies up to 2 months-old,

which are being investigated by Professor Heather K J van der Lely and colleagues at Centre for Developmental Language Disorders & Cognitive Neuroscience-Dept Human Communication Science (UCL). Initial efforts to collect data for clinical experiments involved two pads are being held manually in position on the baby's head by the physician (or nurse) or using Velcro™ and Coban™ strips or caps to attach the probe (figure 6.36). However, the measurements are still strongly influenced by head movement.

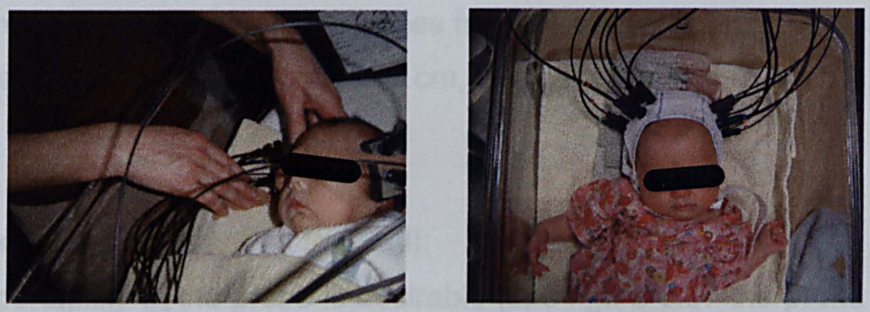

Figure 6.36 Attempts to stabilize the pad over the infant head, LEFT: with strips and RIGHT: with a cap.

We developed a prototype to be used, especially, for auditory studies on a baby in a cot (our own topographic imaging cot). The prototype holds the pair of pads in a desired location which can be varied accordingly to the size and shape of the infant head (figure 6.37).

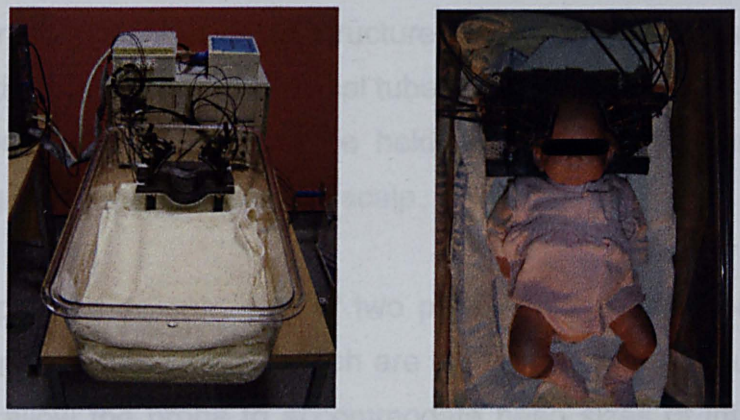

Figure 6.37 LEFT: Topographic imaging cot and RIGHT: An evaluation of the probe using a doll (size equivalent to a baby of 2 months-old).

During the development of this probe the general recommendations established in section 6.2 were observed and increased in some aspects compatible with the general recommendations for the design of the third prototype of adaptable helmet (section 5.2.2.4 and 5.3.1.2). Thus, for the design of this topographic probe the following are added to GR II:

3. The probe must support the weight of the baby's head and the attached fibre bundles without collapsing.
4. The optical array needs to be adaptable to a large range of sizes and shapes of babies heads (figure 5.10), including a mean head circumference from term to 6 months-old of ~35 to 43cm.
5. Ergonomic design parameters have to be taken in account to better accommodate the infant's head, such as the mean head width and the mean head length. For infant babies from 27 weeks to ~ 6 months age, the range of head width is ~6.4 to 11 cm, and head length ~8.4 to 15 cm (Hall *et al*, 1989).

Also, the following are added to GR III:

1. The portability of the probe is desirable (see figure 6.37 the probe is easily accommodated inside a cot).
2. It is desirable to easily and safely remove parts of the probe (support arm and pad) from the rest of the frame.
3. It must be possible to access the baby quickly for emergency nursing care.
4. The natural cavities (ears, nose and eyes) must be completely shielded from the incident NIR-light, especially the eyes.
5. It is desirable that the whole structure of the probe be compatible with other medical apparatus (e.g. nasal tubes, feeding lines).
6. The probe (or its pads) must be held on the sampled surface without producing pressure marks on the scalp.

The topographic probe consisted of two parts: a base to support the infant baby head and the pair of pads which are supported by two adjustable arms. These arms allow the probe to accommodate head sizes of infants from 24 weeks gestational age to 3 months-old. The base was made of thermoplastic™, which was moulded to make it suitable for the back of the infant heads. The template used for moulding was made in cardboard from photographs (3 orthogonal directions) of an appropriate doll. The base is supported by four pillars, which are attached to a plate (figure 6.38). The plate provides mechanical stability of the arrangement and also it gives flexibility to the arrangement to be used with a cot.

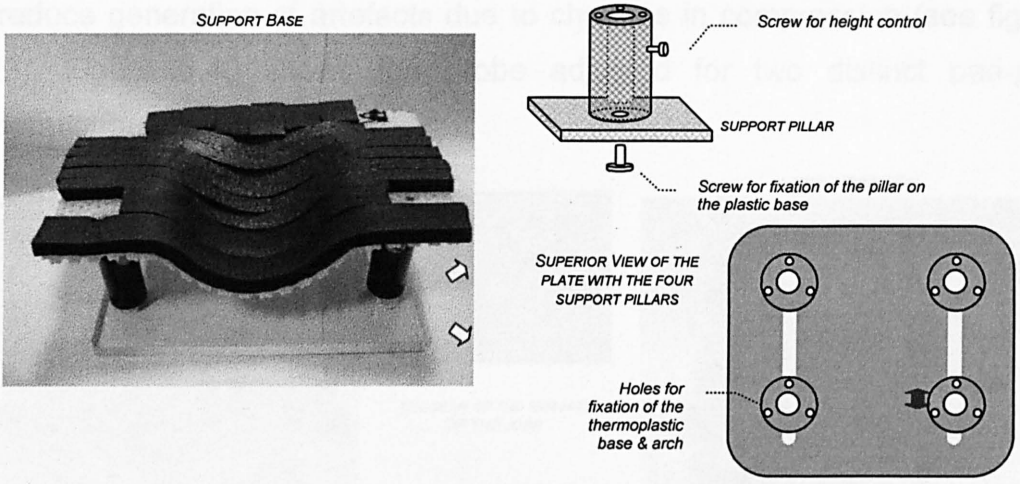

Figure 6.38 LEFT: Support base of the topographic probe III. RIGHT: Representations of support pillar and the plate with pillars.

The pillars are also hollow, which enables the support arch of the adaptable arms to be supported within them, as shown figure 6.39.

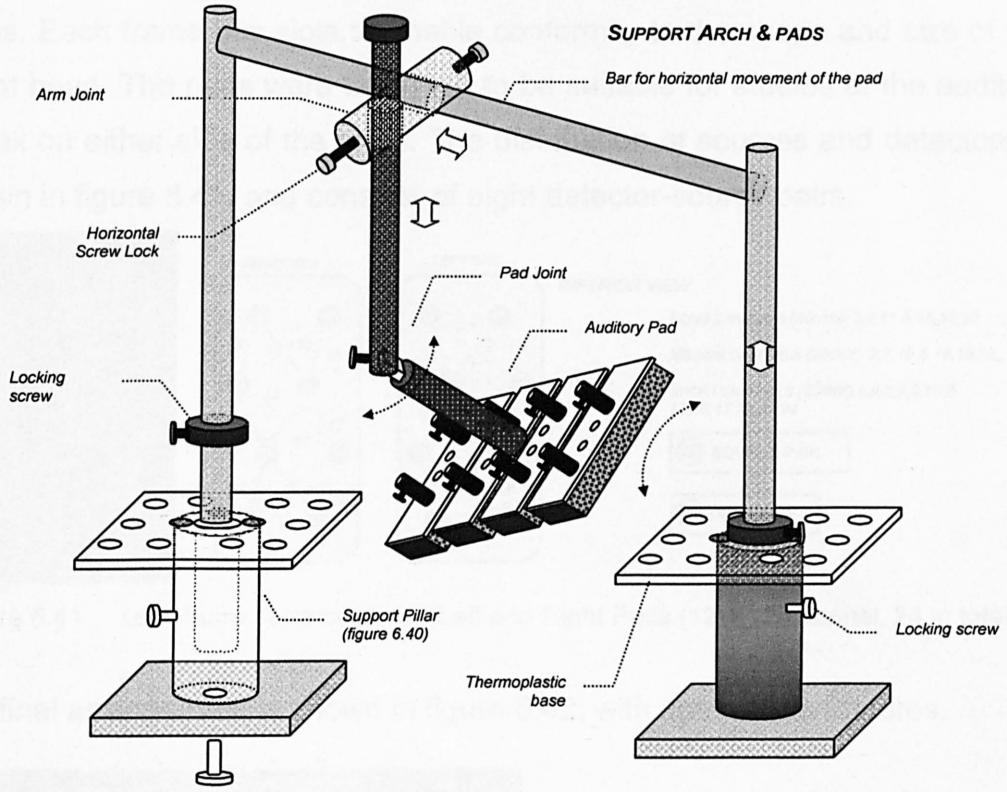

Figure 6.39 Representation of the support-arch with the auditory pad-arm for left side.

The pair of joints on each arm permits the arm to extend or contract. These movements also allow the distance between pads to be adjusted, which enables the probe to accommodate a large range of shapes and sizes of infant head. The support of each pad is attached approximately in the centre

to reduce generation of artefacts due to changes in compression (see figure 6.23). Figure 6.40 shows the probe adjusted for two distinct pad-pad separations.

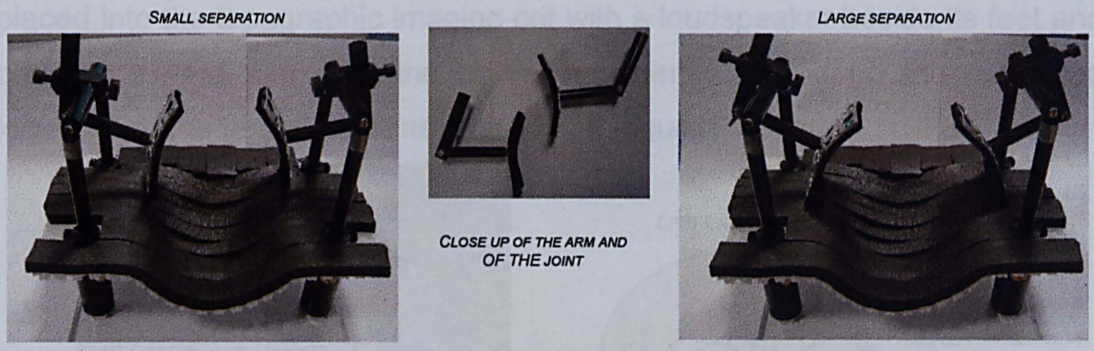

Figure 6.40 Topographic probe adjusted for two distinct head circumferences.

Each pad consists of an aluminium frame lined with protective, NIR- absorbing foam and plastic connectors, which are used to attach the source and detector fibres. Each frame has slots to enable conformity to the shape and size of the infant head. The pads were designed to be suitable for studies of the auditory cortex on either side of the brain. The distribution of sources and detectors is shown in figure 6.41, and consists of eight detector-source pairs.

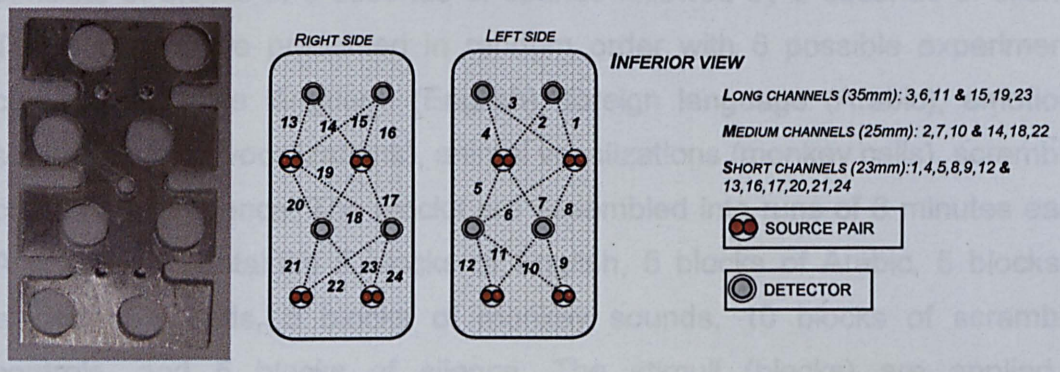

Figure 6.41 LEFT: Support frame. RIGHT: Left and Right Pads (12 + 12 channel, 24 in total).

The final arrangement is shown in figure 6.42, with some of its features.

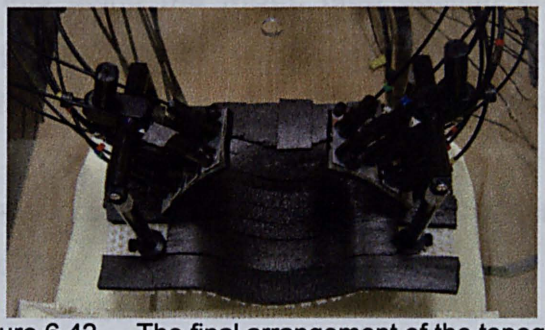

FEATURES OF THE PROTOTYPE		
HEAD CIRCUMFERENCE (OFC)	MAX	41 cm
	MIN	22 cm
HEAD WIDTH	MAX	13.5 cm
	MIN	6.5 cm
CONNECTORS	LEFT PAD	08
	RIGTH PAD	08

Figure 6.42 The final arrangement of the topographic probe III.

6.3.4.1 Study of the Auditory Cortex using topographic probe III

A study was performed on a male infant of 2 months^{+1week}-old. The infant was placed into the topographic imaging cot with a loudspeaker beside its feet and oriented toward him, and the probe was gently placed on the estimated locations of the temporal areas of the head (figure 6.43).

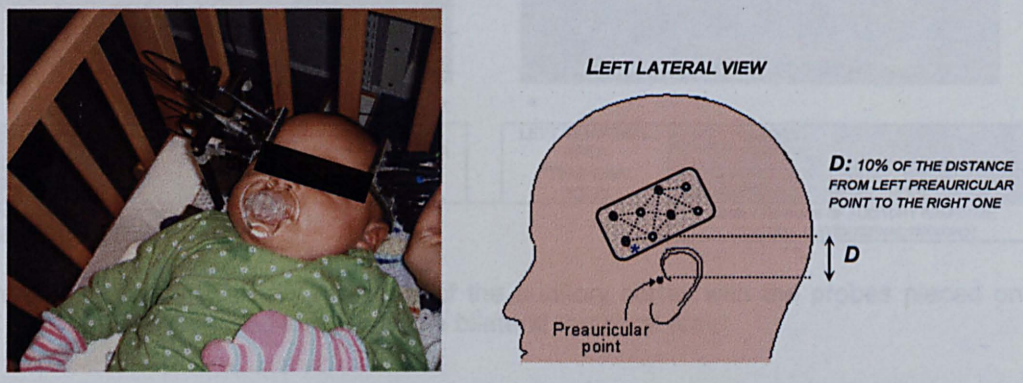

Figure 6.43 LEFT: The infant sleeping comfortably with its head inside the probe, and RIGHT: schematic representation of the location of the Left-probe on the baby's head

The stimuli used for optical topography studies of the auditory cortex of babies consists of blocks of 5 seconds of sounds followed by 5 seconds of silence. These blocks are presented in random order with 6 possible experimental conditions: native language (English), foreign language (Arabic), emotional sounds (human vocalizations), animal vocalizations (monkey calls), scrambled controls, and silence. The blocks are assembled into runs of 6 minutes each. A given run contained 5 blocks of English, 5 blocks of Arabic, 5 blocks of emotional sounds, 5 blocks of monkey sounds, 10 blocks of scrambled controls, and 5 blocks of silence. The stimuli (blocks) are applied in synchronization with the data acquisition. Later, the changes in *[HbO_2]*, *[Hb]* and *[total Hb]* within the bilateral temporal areas are determined from the raw signals using the MBLL (see section 2.6.1). As a response to the stimuli, simple images are generated using the difference between the mean values of *[total Hb]* during stimulation and baseline for each experimental condition.

Some preliminary results are shown in figure 6.44 of the response to emotional sounds versus silence.

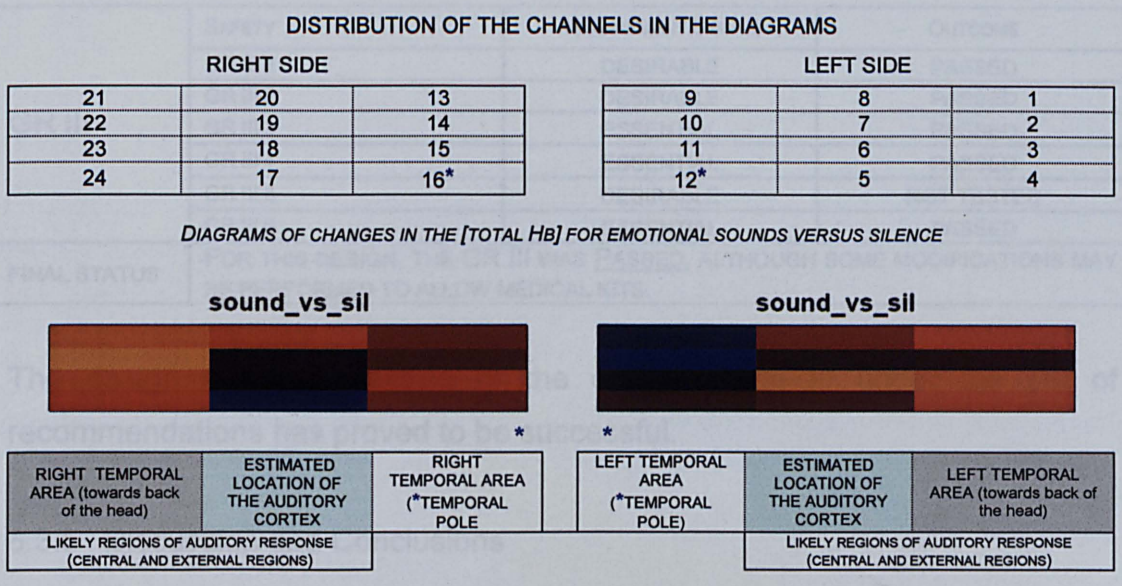

Figure 6.44 The preliminary response of the auditory cortex with the probes placed on the estimated location of the bilateral temporal area.

The images are generated using a programme developed by Professor van der Lely's group, and show the changes in total blood volume. The values are normalized for the maximum (yellow) and minimum (light blue) changes in the total blood volume, using a colour scale: yellow, orange, red, brown, black (no change), blue, light blue. The external regions of the images show an apparently larger activation than the internal regions.

6.3.4.2 Evaluation of the general recommendations of the topographic probe III

The design of prototype was evaluated accordingly with the general recommendations described in sections 6.2 and 6.3.4.

	USEFUL DATA	REQUIREMENT STATUS	OUTCOME
GR I	GR I 1	ESSENTIAL	PASSED
	GR I 2	ESSENTIAL	PASSED
FINAL STATUS	PASSED, THE DESIGN OF THE OPTODE HAS TAKEN IN ACCOUNT THE DIVERGENCE OF THE LIGHT BEAM (SEE FIGURES 5.10 AND 6.1).		

	DESIGN	REQUIREMENT STATUS	OUTCOME
GR II	GR II 1	ESSENTIAL	PASSED
	GR II 2	ESSENTIAL	PASSED
	GR II 3	ESSENTIAL	PASSED
	GR II 4	ESSENTIAL	PASSED
	GR II 5	ESSENTIAL	
FINAL STATUS	PASSED.		

	SAFETY	REQUIREMENT STATUS	OUTCOME
GR III	GR III 1	DESIRABLE	PASSED
	GR III 2	DESIRABLE	PASSED
	GR III 3	ESSENTIAL	PASSED
	GR III 4	ESSENTIAL	PASSED
	GR III 5	DESIRABLE	NOT TESTED
	GR III 6	ESSENTIAL	PASSED
FINAL STATUS	FOR THIS DESIGN, THE GR III WAS PASSED, ALTHOUGH SOME MODIFICATIONS MAY BE PERFORMED TO ALLOW MEDICAL KITS.		

The design and manufacture of the optical probe III under the set of recommendations has proved to be successful.

6.3.5 Discussion and Conclusions

Although the best way to reconstruct topographic data is still under investigation, the probes have been proved to be successful so far for data acquisition during clinical of studies of the somatosensory, visual and auditory cortices. Studies of the effects of changes in compression of the probe have shown that it is essential to minimise movement of the probe during studies, and emphasized the importance of probe robustness and stability when designing optical probes.

Chapter 7

Summary and Conclusions

7.1 Introduction

Diffuse optical imaging of the brain has been subject to considerable research interest at UCL and elsewhere for more than ten years. However, coupling a large number of optical fibre bundles to the head in order to perform imaging studies on patients and volunteers has remained a difficult and rather neglected problem. The work described in this thesis has focussed on the development of fibre optic probes for performing optical imaging of the brains of newborn infants. Specifically, the probes have been designed to perform measurements with the UCL 32-channel time resolved tomography system (MONSTIR) and the UCL frequency-multiplexed optical topography system.

7.2 Probe for optical tomography

In order to develop a probe suitable for performing optical tomography of the infant brain using MONSTIR, it was first determined that it must:
(a) accommodate a large range of sizes and shapes of babies' heads (from 24 weeks gestational age to term);
(b) provide full or partial coverage of the scalp to monitor the brain during functional stimulation;
(c) provide mechanical strength, comfort and safety for the baby and also to enable the measurement of the positions of the fibre bundles, and
(d) enable reliable, artefact-free data to be collected for optical image reconstruction.

Initially, custom-made helmets were manufactured for each individual infant, which yielded useful data and several studies involving such helmets were published. However, helmet manufacture was a time-consuming and highly skilled process, which caused less studies to be performed than otherwise would have been. Nevertheless, helmet construction provided a valuable insight into the necessary requirements for an interface between the 32 optical fibre bundles from MONSTIR and the fragile preterm infant baby head. This early period of the project enabled ideas to be developed which informed the

subsequent designs for an adaptable helmet suitable for a range of infant heads.

The first adaptable helmet consisted of two shells which supported an array of radially translatable connectors to which the fibre bundles were attached. Unfortunately this helmet was not successful, largely because of its tendency to leave pressure marks on the rear of the infants' heads. However, its design led to the specification of a series of general requirements (GRs) against which later designs were evaluated.

A second prototype was developed made of three sections, based again on radially translatable connectors but with a pad to support the weight of the head. This prototype was modified after each experiment in an attempt to improve its performance and the quality of the recorded data. During this period of the project an alternative and novel reference phantom was developed for infant tomographic studies, made of a thin head-shaped latex shell. This replaced the balloon phantom and avoided the constant risks of bursting of the balloon, and no longer required the tubing circuit with valves and syringe used to fill the balloon with the intralipid solution. Despite modifications to the second prototype, an evaluation of the quality of the data obtained with the helmet indicated that its average performance was still inferior to that of the average custom-made helmet. As a result, further improvements to the coupling of the optodes to the top and sides of the head were necessary. Some additional recommendations were included in the initial set of GRs.

A third prototype was developed using an upper pad section (a foam lined slotted aluminium pad), a lower pad to support the weight of the head, and a fixed coronal section with translatable connectors with flexible rubber flanges. The results have shown that the average performance of this third prototype is superior that of the customized helmets. This third prototype has been used successfully in all the most recent infant studies, including acquisition of static images of the brain and imaging of changes in cerebral blood oxygenation produced by temporary alterations in nasal oxygen flow.

Evaluation of the third prototype was assisted by analyzing the density of direct lines-of-sight across the head between sources and detectors which yielded measurable (and artefact-free) signals. A computer programme was developed which plotted the mesh-projection images which indicated the lines-of-sight, and these images were correlated with the corresponding reconstructed images. This revealed that a low density of lines across the centre of the head is more likely to be associated with a reduction in the largest source-detector separations (due to greater probability of noise contamination, and so to be rejected as useful data), and a lower fraction of un-rejected data (i.e. lower performance). This analysis may serve as a useful guide to data quality preliminary to performing 3D image reconstructions with the data.

Overall, the adaptable helmet development process has enabled the list of GRs to be refined, which now represent a valuable set of guidelines for any subsequent development of probes for optical tomography of the newborn infant brain.

7.2.1 Future work

The final prototype of helmet has been successfully used in the clinical environment with MONSTIR for recording data for static imaging studies and imaging changes in cerebral blood oxygenation produced by alteration in nasal oxygen flow. This probe continues to be used for further 3D tomography studies on newborn infants, such as on-going imaging studies of response to auditory, language, and somatosensory stimuli.

Further imaging static studies may also be carried out to perform a quantitative analysis of the relationship between the density of lines-of-sight within the mesh-projection and the reconstructed images.

Further work is also in progress to investigate the effectiveness of a reusable PVA gel-filled head-shaped reference phantom for infant tomography studies

(Hebden *et al*, 2006), as a possible replacement of the intralipid-filled latex head phantom (figure 7.1).

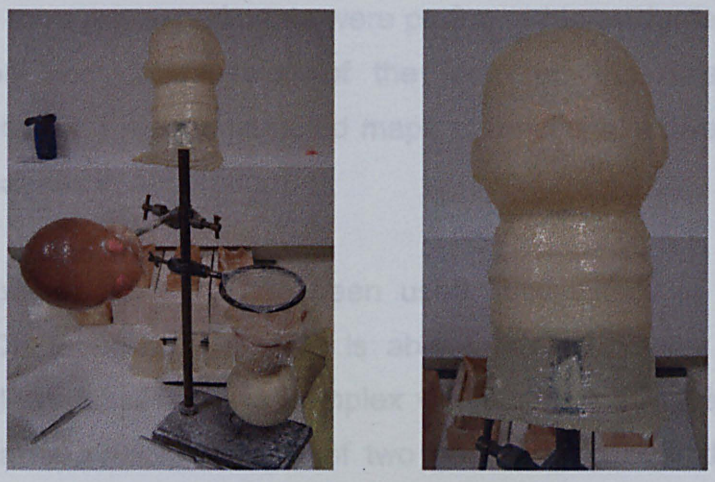

Figure 7.1 A PVA gel-filled head-shaped reference phantom.

Further mechanical modifications to the helmet design may be investigated, such as: a set of alternative top sections to provide optimum sampling of a greater range of infant head sizes, and especial supports for medical kits (e.g. pipes and tubes for infants under oscillating ventilators).

7.3 The topographic probes

Optical arrays or topographic probes were also made for use with the UCL frequency-multiplexed near-infrared topography system for imaging functional activation in the infant brain. Three distinct optical arrays were developed:
(a) the first probe was made to investigate the cortical response to a transitory painful stimulus during a routine heel lance procedure in preterm babies;
(b) a second probe was designed for optical topography studies of the visual cortex of babies aged 6-months-old, and
(c) a preliminary third prototype was developed for optical topography studies of the auditory cortex of babies aged 2-months-old.

The development of the first two probes was based on an initial set of general requirements which ensured the designs met a minimum set of conditions for safety, comfort, and data quality. The third probe designed for auditory studies was based on a revised set of general requirements, which incorporated some

of the important design criteria employed for the tomography probes. Because the topography probes were often to be used on older infants who have a strong tendency to move, experiments were performed to evaluate the effects of probe motion and compression of the foam on the data, and the subsequent effects on the reconstructed maps of functional activation (which represent the changes in absorption).

The second topographic array has been used successfully to investigate whether the UCL topography system is able to detect subtle differences between evoked responses to two complex visual stimuli in babies. Studies using the third array, which consists of two pads placed over the auditory cortex on each side of the head, are currently still in progress, although preliminary results are encouraging.

As for the adaptable helmet, the development process has also enabled a list of design guidelines to be compiled, which should be very useful for future topographic probe manufacture.

7.3.1 Future work

Studies of functional activation in the infant brain are currently in progress using the probes developed for this project, and similar studies of the adult brain are also being planned. Some re-design of the probe may be necessary for adult studies, to increase the mean source-detector separation to improve sensitivity to deeper tissues. Further work is required to investigate alternative arrangements of sources and detectors, and to determine what arrangement might give the optimum sampling (over a continuous range of depth) for 3D image reconstruction.

7.4 Publications

A paper on the development of optical probes for the UCL optical imaging systems was presented at a conference organised by the Optical Society of America (OSA) in Miami in March 2006:

Branco, G., Everdell, N.L., Gibson, A.P., Delpy, D.T., Hebden, J.C., Slater, R., Cantarella, A. and Meek, J.H. "Development of head probes for optical tomography and topography of the newborn infant brain." in *Biomedical Optics 2006 Technical Digest* (Optical Society of America, Washington, DC, 2006), SH41. ISBN: 1-55752-807-1

Another publication where I was among the authors:

Austin, T., Gibson, A.P., Branco, G., Yusof, R.Md., Arridge, S.R., Meek, J.H., Wyatt, J.S., Delpy, D.T., and Hebden, J.C. (2006) Three dimensional optical imaging of blood volume and oxygenation in the neonatal brain. *NeuroImage*, 31, 1426-1433.

References

1. (Arridge and Hebden, 1997) Arridge, S.R., and Hebden, J.C. (1997) Optical imaging in medicine: II. Modelling and reconstruction. *Physics in Medicine and Biology. Biol*, 42, 841-853.

2. (Arridge and Lionheart, 1998) Arridge, S.R., and Lionheart, W.R.B. (1998) Nonuniqueness in diffusion-based optical tomography. *Opt. Lett.*, 23, 882-884.

3. (Arridge and Schweiger, 1993) Arridge, S.R., and Schweiger, M. (1993) The use of multiple data types in time-resolved optical absorption and scattering tomography (TOAST). *Proc. SPIE*, 2035, 218-229.

4. (Arridge *et al*, 1992) Arridge, S.R., Cope, M., and Delpy, D.T. (1992) The theoretical basis forth determination of optical pathlengths in tissue: temporal and frequency analysis *Physics in Medicine and Biology. Biol*, 37, 1531-1560.

5. (Arridge *et al*, 1993) Arridge, S.R., Schweiger, M., Hiraoka, M., and Delpy, D.T. (1993) A finite element approach for modelling photon transport in tissue. *Med. Phys.*, 20(2), 299-309.

6. (Arridge, 1993) Arridge, S.R. (1993) The Forward and Inverse Problems in Time-Resolved Infrared Imaging, in Medical Optical Tomography: Functional Imaging and Monitoring. *SPIE Institute on Optical Tomography*, 35-64.

7. (Arridge, 1995) Arridge, S.R. (1995) Photon measurement density functions part1: analytic forms. *Applied Optics*, 34, 7395-7409.

8. (Arridge, 1999) Arridge, S.R. (1999) Optical tomography in medical imaging. *Inverse Problems*, 15, R41-R93.

9. (Austin *et al*, 2006) Austin, T., Gibson, A.P., Branco, G., Yusof, R.Md., Arridge, S.R., Meek, J.H., Wyatt, J.S., Delpy, D.T., and Hebden, J.C. Three dimensional optical imaging of blood volume and oxygenation in the neonatal brain. *NeuroImage*, 31, 1426-1433.

10. (Benaron *et al*, 2000) Benaron, D.A., Hintz, S.R., Villringer, A., Boas, D., Kleinschmidt, A., Frahm, J., Hirth, C., Obrig, H., van Houten, J.C., Kermit, E.L., Cheong, W.F., and Stevenson, E.L. (2000) Noninvasive functional imaging of human brain using light. *Journal Cereb. Blood Flow Metab.*, 20, 469–77.

11. (Binder *et al*, 1997) Binder, J.R., Frost, J.A., Hammeke, T.A., Cox, R.W., Rao, S.M., and Thomas, P. (1997) Human Brain Language Areas Identified by Functional Magnetic Resonance Imaging. *The Journal of Neuroscience*, 17(1), 353-362.

12. (Blasi *et al*, 2006) Blasi, A., Everdell, N., Hebden, J., Elwell, C., Fox, S., Tucker, L., Volein, A., Csibra, G., and Johnson, M. (2006) Near Infrared Topography with Depth Information for the Detection of Face Perception in Infants. in *Biomedical Optics 2006 Technical Digest* (Optical Society of America, Washington, DC, 2006), ME16. ISBN: 1-55752-807-1.

13. (Bluestone *et al*, 2001) Bluestone, A.Y., Abdoulaev, G., Schmitz, C.H., Barbour, R.L., and Hielscher, A.H. (2001) Three-dimensional optical tomography of hemodynamics in the human head. *Optics Express*, 9(6), 272-286.

14. (Boas *et al*, 2001) Boas, D., Gaudette, T., and Arridge, S.R. (2001) Simultaneous imaging and optode calibration with diffuse optical tomography. *Optics Express*, 8(5), 263.

15. (Bookheimer, 1996) Bookheimer, S.Y. (1996) Functional MRI Applications in Clinical Epilepsy. *NeuroImage*, 4, S139-S146.

16. (Branco *et al*, 2006) Branco, G., Everdell, N.L., Gibson, A.P., Delpy, D.T., Hebden, J.C., Slater, R., Cantarella, A. and Meek, J.H. (2006) Development of head probes for optical tomography and topography of the newborn infant brain. In *Biomedical Optics 2006 Technical Digest* (Optical Society of America, Washington, DC, 2006), SH41. ISBN: 1-55752-807-1.

17. (Cheong *et al*, 1990). Cheong, W., Prahl, S.A., and Welch, A.J. (1990) A review of the optical properties of Biological Tissues. *IEEE J. of Quantum Electronics*, 26(12), 563-568.

18. (Conway *et al*, 1984) Conway, J.M., Norris, K.H., and Bodwell, C.E. (1984) A new approach for the estimation of body composition: infrared interactance. *The American Journal Clinical Nutrition*, 40, 1123-1130.

19. (Cope and Delpy, 1988) Cope, M., and Delpy, D.T. (1988) System for long-term measurement of cerebral blood and tissue oxygenation on newborn infants by near infra-red transillumination. *Med. & Biol. Eng. & Comput.*, 26, 289-294.

20. (Cope, 1991) Cope, M. (1991) The application of near infrared spectroscopy to non invasive monitoring of cerebral oxygenation in the newborn infant. PhD thesis, University College London, Department of Medical Physics and Bioengineering, London.

21. (Csibra *et al*, 2004) Csibra, G., Henty, J., Volein, A., Elwell, C., Tucker, L., Meek, J., and Johnson, M.H. (2004) Near infrared spectroscopy reveals neural activation during face perception in infants and adults. *Journal of Paediatric Neurology*, 2(2), 85-89.

22. (Delpy and Cope, 1997) Delpy, D.T., and Cope, M. (1997) Quantification in tissue near-infrared spectroscopy. *Phil. Trans. R. Soc. Lond. B*, 352, 649-659.

23. (Delpy *et al*, 1988) Delpy, D.T., Cope, M., van der Zee, P., Arridge, S., Wray, S., and Wyatt, J.S. (1988) Estimation of optical pathlength through tissue from direct time of flight measurement. *Physics in Medicine and Biology. Biol*, 33(12), 1433-1442.

24. (Delpy, 1994) Delpy, D. (1994) Optical spectroscopy for diagnosis. *Physics World*, 14(8), 34-39.

25. (Duncan *et al*, 1995) Duncan, A., Meek J.H., Clemence, M., Elwell C.E., Tyszczuk, L., Cope, M., and Delpy, D.T. (1995) Optical Pathlength measurements on adult head, calf and forearm and the head of the newborn infant using a phase resolved optical spectroscopy. *Physics in Medicine and Biology. Biol*, 40, 295-304.

26. (Elwell, 1995) Elwell, C.E. (1995) A practical users guide to near infrared spectroscopy. UCL Reprographics, London, UK.

27. (Everdell *et al*, 2004) Everdell, N., Gibson, A.P., Tullis, I.D.C., Vaithianathan, T., Hebden, J., and Delpy, D.T. (2004) A frequency multiplexed near infra-red topography system for imaging functional activation in the brain. OSA Biomedical Topical Meetings, WF33, Miami.

28. (Everdell *et al*, 2005) Everdell, N.L., Gibson, A.P., Tullis, I.D.C., Vaithianathan, T., Hebden, J.C., and Delpy, D.T. (2005) A frequency multiplexed near-infrared topography system for imaging functional activity in the brain. *Review of Scientific Instruments*, 76, 72-76.

29. (Fantini *et al*, 2001) Fantini, S., Aggarwal, P., Chen, K., and Franceschini, M.A. (2001) Monitoring brain activity using near-infrared light. *American Laboratory*, 15-17.

30. (Fenwick, 1987) Fenwick, P. (1987) The inverse problem: a medical perspective. *IOP*, 32(1), 5-9.

31. (Firbank and Delpy, 1993) Firbank, M., and Delpy, D.T. (1993) A design for a stable and reproducible phantom for use in near-infrared imaging and spectroscopy. *Physics in Medicine and Biology. Biol.*, 38, 847-853.

32. (Firbank *et al*, 1993) Firbank, M., Hiraoka, M., Essenpreis, M., and Delpy, D.T. (1993) Measurement of the optical properties of the skull in the wavelength range 650–950 nm. *Physics in Medicine and Biology. Biol*, 38, 503–510.

33. (Firbank *et al*, 1995) Firbank, M., Oda, M., and Delpy, D.T. (1995) An improved design for a stable and reproducible phantom material for use in near-infrared spectroscopy and imaging. *Physics in Medicine and Biology. Biol.*, 40, 955-961.

34. (Franceschini *et al*, 2000) Franceschini, M.A., Toronov, V., Filiaci, M.E., Gratton, E., and Fantini, S. (2000) On-line optical imaging of the human brain with 160-ms temporal resolution. *Optics Express*, 6(3), 49-57.

35. (Franceschini *et al*, 2003) Franceschini, M.A., Fantini, S., Thompson, J.H., Culver, J.P., and Boas, D.A. (2003) Hemodynamic evoked response of the sensorimotor cortex measured noninvasively with near-infrared optical imaging. *Psychophysiology*, 40, 548–560.

36. (Francheschini and Boas, 2004) Francheschini, M.A., and Boas, D.A. (2004) Noninvasive measurement of neuronal activity with near-infrared optical imaging. *NeuroImage*, 21, 372-386.

37. (Fukui *et al*, 2003) Fukui, Y., Ajichi, Y., and Okada, E. (2003) Monte Carlo prediction of near-infrared light propagation in realistic adult and neonatal head models. *Applied Optics*, 42(16), 2881-2887.

38. (Gevins, 1998) Gevins, A. (1998) The future of electroencephalography in assessing neurocognitive functioning. *Electroencephalography and clinical Neurophysiology*, 106, 165-172.

39. (Gibson *et al*, 2003a) Gibson, A.P., Riley, J., Schweiger, M., Hebden, J.C., Arridge, S.R., and Delpy, D.T. (2003) A method for generating patient-specific finite element meshes for head modelling. *Physics in Medicine and Biology. Biol*, 48, 481-495.

40. (Gibson *et al*, 2003b) Gibson, A.P., Yusof, R.M.d., Dehghani, H., Riley, J., Everdell, N., Richards, R., Hebden, J.C., Schweiger, M., Arridge, S.R., and Delpy, D.T. (2003) Optical tomography of a realistic neonatal head phantom. *Applied Optics*, 42(16), 3109-3115.

41. (Gibson *et al*, 2005a) Gibson, A.P., Hebden, J.C. and Arridge S.R. (2005) Recent advances in diffuse optical imaging. *Physics in Medicine and Biology.* 50, R1 –R43.

42. (Gibson *et al*, 2005b) Gibson, A.P., Austin, T., Everdell, N.L., Schweiger, M., Arridge, S.R., Meek, J.H., Wyatt, J.S., Delpy, D.T., and Hebden, J.C. (2005) Three-dimensional whole-head optical tomography of passive motor evoked responses in the neonate. *NeuroImage.*

43. (Gibson, 2000) Gibson, A.P. (2000) Electrical Impedance Tomography of Human Brain Function. PhD thesis, University College London, Department of Physiology, London.

44. (Gowland *et al*, 2002) Gowland, P., Francis, S., Morris, P., and Bowtell, R. (2002) Watching the brain at work. *Physics World*, 31-35.

45. (Haddad *et al*, 2006) Haddad, N., Shihabuddin, B., Preissl, H., Holst, M., Lowery, C.L., and Eswaran, H. (2006) Magnetoencephalography in healthy neonates. *Clinical Neurophysiology*, 117, 289-294.

46. (Hall *et al*, 1989) Hall, J.G., Ursula, G., Froster, I., and Allanson, J.E. (1989) Handbook of normal physical measurements. Oxford University Press, 504p.

47. (Halliday *et al*, 1998) Halliday, H.L., McClure, B.G., and Reid, M. (1998) Handbook of Neonatal Intensive Care. 4th ed. W. B. Saunders. 270p.

48. (Hamaoka *et al*, 2000) Hamaoka, T., Katsumura, T., Murase, N., Nishio, S., Osada, T., Sako, T., Higuchi, H., Kurosawa, Y., Shimomitsu, T., Miwa, M., and Chance, B. (2000) Quantification of ischemic muscle deoxygenation by near infrared time-resolved spectroscopy. *Journal of Biomedical Optics*, 5(1), 102–105.

49. (Hebden *et al*, 1997) Hebden, J.C., Arridge, S.R., and Delpy, D.T. (1997) Optical imaging in medicine: I. Experimental techniques. *Physics in Medicine and Biology*, 42 (5), 825-840.

50. (Hebden *et al*, 2002) Hebden, J.C., Gibson, A., Yusof, R.Md., Everdell, N., Hillman, E.M.C., Delpy, D.T., Arridge, S.R., Austin, T., Meek, J.H., and Wyatt, J.S. (2002) Three-dimensional optical tomography of the premature infant brain. *Physics in Medicine and Biology*, 47, 4155-4166.

51. (Hebden *et al*, 2003) Hebden, J.C., Gonzalez, F.M., Gibson, A., Hillman, E.M.C., Yusof, R.Md., Everdell, N., and Delpy, D.T. (2003) Assessment of an *in situ* temporal calibration method for time-resolved optical tomography. *Journal of Biomedical Optics*, 8(1), 87-92.

52. (Hebden *et al*, 2004) Hebden, J.C., Gibson, A., Austin, T., Yusof, R.Md., Everdell, N., Delpy, D.T., Arridge, S.R., Meek, J.H., and Wyatt, J.S. (2004) Imaging changes in blood volume and oxygenation in the newborn infant brain using three-dimensional optical tomography. *Physics in Medicine and Biology*, 49, 1117-1130.

53. (Hebden, 2003) Hebden, J.C. (2003) Advances in optical imaging of the newborn infant brain. *Psychophysiology*, 40, 501-510.

54. (Hebden *et al*, 2006) Hebden, J.C., Price, B. D., Gibson, A. Royle, G. (2006) A soft deformable tissue-equivalent phantom for diffuse optical tomography. *Physics in Medicine and Biology*, 51, 5581-5590.

55. (Hielscher *et al*, 2002) Hielscher, A.H., Bleustone, A.Y., Abdoulaev, G.S., Klose, A.D., Lasker, J., and Stewart, M. (2002) Near-infrared diffuse optical tomography. *Disease Markets*, 18, 313-337.

56. (Hillman *et al*, 2000) Hillman, E.M.C., Hebden, J.C., Schmidt, F.E.W., Arridge, S.R., Schweiger, M., Dehghani, H., and Delpy, D.T. (2000) Calibration techniques and datatype extraction for time-resolved optical tomography. *Review Scientific Instruments*, 71(9), 3415-3427.

57. (Hillman, 2002) Hillman, E.M.C. (2002) Development of optical tomography techniques for functional imaging of the neonatal brain. PhD thesis, University College London, Department of Medical Physics and Bioengineering, London.

58. (Hintz *et al*, 1998) Hintz, S.R., Benaron, D.A., van Houten, J.P., Duckworth, J.L., Liu, F.W.H., Spilman, S.D., Stevenson, D.K., and Cheong, W.F. (1998) Stationary headband for clinical time-of-flight optical imaging at the bedside. *Photochem. Photobiol.*, 68, 361-369.

59. (Hintz *et al*, 2001) Hintz, S.R., Benaron, D.A., Siegel, A.M., Zourabian, A., Stevenson, D.K., and Boas, D.A. (2001) Bedside functional imaging of the premature infant brain during passive motor activation. *Journal Perinat. Med.*, 29, 335–43.

60. (Isobe *et al*, 2001) Isobe, K., Kusaka, T., Nagano, K., Okubo, K., Yasuda, S., Kondo, M., Itoh, S., and Onishi, S. (2001) Functional imaging of the brain in sedated newborn infants using near infrared topography during passive knee movement. *Neuroscience Letters*, 299, 221–224.

61. (Jennions *et al*, 2006) Jennions, D.K., Gibson, A.P., Everdell, N.L., Hebden, J.C., and Wolfgang, B. (2006) Fast Time-Resolved Optical Tomography for 3D Neonatal Functional Imaging. In *Biomedical Optics 2006 Technical Digest* (Optical Society of America, Washington, DC, 2006), SH45. ISBN: 1-55752-807-1.

62. (Jöbsis, 1977) Jöbsis, F.F. (1977) Noninvasive, infrared monitoring of cerebral and myocardial oxygen sufficiency and circulatory parameters. *Science*, 198, 1264-1267.

63. (Johnston, 1998) Johnston, P.G.B. (1998) The newborn child. 8th ed. New York: Churchill Livingstone.

64. (Kalender, 2006) Kalender, W.A. (2006) X-ray computed tomography. *Physics in Medicine and Biology. Biol*, 51, R29–R43.

65. (Kaltenbach and Kaschke, 1993) Kaltenbach, J.M., and Kaschke, M. (1993) Frequency and time-domain modelling of light transport in random media. Medical Optical Tomography: Functional Imaging and Monitoring. *SPIE*, 65–86.

66. (Kawaguchi *et al*, 2001) Kawaguchi, F., Ichikawa, N., Fujiwara, N., Yamashita, Y., and Kawasaki, S. (2001) Clinically available optical topography system. *Hitachi Review*, 50(1), 18-22.

67. (Koizumi *et al*, 2003) Koizumi, H., Yamamoto, T., Maki, A., Yamashita, Y., Sato, H., Kawaguchi, H., and Ichikawa, N. (2003) Optical topography: practical problems and new applications. *Applied Optics*, 42(16), 3054-3062.

68. (Law *et al*, 1991) Law, S.K., Nunez, P.L., Westdorp, A.F., Nelson, A.V., and Pilgreen, K.L. (1991) Topographical mapping of brain electrical activity. *IEEE*, 194-200.

69. (Malmivuo and Plonsey, 1995) Malmivuo, J., and Plonsey, R. (1995) *Bioelectromagnetism – Principles and Applications of Bioelectric and Biomagnetic Fields*, New York: Oxford University Press.

70. (Marieb and Hoehn, 2006) Marieb, E.N., and Hoehn, K. (2006) *Human Anatomy & Physiology*. Seventh edition. New York: Pearson International Edition.

71. (Martini *et al*, 1998) Martini, F., and Karleskint, G. (1998) *Foundations of anatomy and physiology*. London: Prentice Hall.

72. (Matcher *et al*, 1993) Matcher, S.J., Cope, M., and Delpy, D.T. (1993) Use of the water absorption spectrum to quantify tissue chromophores concentration changes in near-infrared spectroscopy. *Physics in Medicine and Biology. Biol*, 38, 177-196.

73. (Matthews *et al*, 1999) Matthews, P.M., Adcock, S.C., and Adcock, J. (1999) Functional magnetic resonance imaging: Clinical applications and potential. *Journal Inher. Metab. Dis.*, 22, 337-352.

74. (Mazziota, 2000) Mazziota, J.C. (2000) Imaging Window on the Brain. *Arch. Neurol.*, 57, 1413-1421.

75. (Meek *et al*, 1999a) Meek, J.H., Tyszczuk, L., Elwell, C., and Wyatt, J.S. (1999) Low cerebral blood flow is a risk factor for severe □Intraventricular haemorrhage. *Arch. Dis. Child Fetal Neonatal* Ed., 81, 15-18.

76. (Meek *et al*, 1999b) Meek, J.H., Elwell, C., McCormick, D.C., Edwards, A.D., Townsend, J.P., Stewart, A.L., and Wyatt, J.S. (1999) Abnormal cerebral haemodynamics in perinatally asphyxiated neonates related to outcome. *Arch. Dis. Child Fetal Neonatal* Ed., 81, 110-115.

77. (Meek, 2002) Meek, J.H. (2002) Basic principles of optical imaging and application to the study of infant development. *Developmental Science*, 5(3), 371-380.

78. (Mendelson, 1992) Mendelson, Y. (1992) Pulse Oximetry: Theory and Applications for Noninvasive Monitoring. *Clinical Chemistry*, 38/39, 1601-1607.

79. (Merenstein *et al*, 1998) Merenstein, G.B., and Gardner, S.L. (1998) *Handbook of Neonatal Intensive Care*. 4th ed. St. Louis, London: Mosby.

80. (Montandon and Zaidi, 2002) Montandon, M.L., and Zaidi, H. (2002) Functional Brain Imaging with Single Photon Emission Computed Tomography and Position Emission Tomography. *Business Briefing Global Healthcare.*

81. (Niemz, 1999) Niemz, M.H. (1996) *Laser-Tissue Interactions.* Springer-Verlag.

82. (Oda *et al*, 1997) Oda, M., Yamashita, Y., Kan, H., Miyajima, H., Sawaki, A., Nakano, T., Suzuki, S., Suzuki, A., Shimizu, K., Muramatsu, S., Sugiura, N., Ohta, K., and Tsuchiya, Y. (1997) Advanced Devices for Near-infrared Time-Resolved Spectroscopy and Optical Computed Tomography. *Proc. SPIE*, 2979, 765-773.

83. (Okada and Delpy, 2003) Okada, E., and Delpy, D.T. (2003) Near infrared light propagation in an adult head model I. Modeling of low-level scattering in the cerebrospinal fluid layer. *Applied Optics*, 42(16), 2906-2922.

84. (Okada *et al*, 1997) Okada, E., Firbank, M., Schweiger, M., Arridge, S.R., Cope, M., and Delpy, D.T. (1997) Theoretical and experimental investigation of near-infrared light propagation in a model of the adult head. *Applied Optics*, 36(1), 21-31.

85. (Ollinger and Fessler, 1997) Ollinger, J.M., and Fessler, J.A. (1997) Positron Emission Tomography. *IEEE Signal Proc. Maganize*, 14(1), 43-55.

86. (Oppenheim and Schafer, 1989) Oppenheim, A.V., and Schafer, R.W. (1989) Discrete-time signal processing. Englewood Cliffs, N.J. London: Prentice-Hall.

87. (Paetau, 2002) Paetau, R. (2002) Magnetoencephalography in pediatric neuroimaging. *Developmental Science*, 5(3), 361-370.

88. (Patterson *et al*, 1989) Patterson, M.S., Chance, B., and Wilson, B.C., (1989) Time resolved reflectance and transmittance for the non-invasive measurement of optical tissue properties. *Applied Optics*, 28(12), 2331-2336.

89. (Patterson *et al*, 1991) Patterson, M.S., Wilson, B.C., and Wyman, D.R. (1991) The propagation of optical radiation in tissue. I. Models of radiation transport and their application. *Lasers Med. Sci.*, 6,155-168.

90. (Rennie, 2005) Rennie, J.M. (2005) *Roberton's Textbook of Neonatology.* Fourth Edition. Elsevier.

91. (Riley *et al*, 2000) Riley, J., Dehghani, H., Schweiger, M., Arridge, S.R., Ripoll, J., and Nieto-Vesperinas, M. (2000) 3D optical tomography in the presence of void regions. *Optics Express*, 7(13), 462–467.

92. (Rolfe, 2000) Rolfe, P. (2000) In vivo near-infrared spectroscopy. *Annu. Rev. Biomed. Eng.*, 02, 715-54.

93. (Schmidt *et al*, 2000) Schmidt, E.W., Fry, M.E., Hillman, E.M.C., Hebden, J.C., and Delpy, D.T. (2000) A 32-channel time-resolved instrument for medical optical tomography. *Review of Scientific Instruments*, 71(1), 256-265.

94. (Schmidt, 1999) Schmidt, F.E.W. (1999) Development of a time-resolved optical tomography system for neonatal brain imaging. PhD Thesis, University College London, Department of Medical Physics and Bioengineering, London.

95. (Schmitz *et al*, 2002) Schmitz, C.H., Löcker, M., Lasker, J.M., Hielscher, A.H., and Barbour, R.L. (2002) Instrumentation for fast functional optical tomography. Review of Scientific instruments, 73(2).

96. (Schöberl, 1997) Schöberl, J. (1997) NETGEN - An advancing front 2D/3D-mesh generator based on abstract rules. *Computing and Visualization in Science*, 1, 41-52.

97. (Shalak and Perlman, 2004) Shalak, L., and Perlman, J.M. (2004) Hypoxic-ischemic brain injury in the term infant-current concepts. *Early Human Development 80*, 125-141.

98. (Simpson *et al*, 1998) Simpson, C.R., Kohl, M., Essenpreis, M., and Cope, M. (1998) Near infrared optical properties of ex-vivo human skin and subcutaneous tissues measured using the Monte-Carlo inversion technique. *Physics in Medicine and Biology*, 43, 2465-2478.

99. (Slater *et al*, 2004) Slater, R., Gallella, S., Boyd, S., Meek, J., and Fitzgerald, M. (2004) Noxious stimulation causes functional activation of the somatosensory cortex in newborn infants. *Early Human development*, 80, 169-192.

100. (Srinivasan, 1999) Srinivasan, R. (1999) Methods to improve the spatial resolution of EEG. *International Journal of Bioelectromagnetism*, 1(1), 102-110.

101. (Strangman *et al*, 2002) Strangman, G., Boas, D.A., and Sutton, J.P. (2002) Non-invasive neuroimaging using near-infrared light. *Biol. Psychiatry*, 52, 679-693.

102. (Suetens, 2001) Suetens, P. (2001) *Fundamentals of Medical Imaging*, 2nd edition, Cambridge University Press.

103. (Taga *et al*, 2000) Taga, G., Konishi, Y., Maki, A., Tachibana, T., Fujiwara, M., and Koizumi, H. (2000) Spontaneous oscillation of oxy- and deoxy-hemoglobin changes with a phase difference throughout the occipital cortex of newborn infants observed using non-invasive optical topography. *Neuroscience Letters*, 282,101-104.

104. (Teplan, 2002) Teplan, M. (2002) Fundamentals of EEG Measurement. Measurement Science Review, 2.

105. (Tidswell *et al*, 2001) Tidswell, T., Gibson, A., Bayford, R.H., and Holder, D.S. (2001) Three-Dimensional Electrical Impedance Tomography of Human Brain Activity. *NeuroImage*, 13, 283-294.

106. (Toronov *et al*, 2001) Toronov, V., Webb, A., Choi, J.H., Wolf, M., Michalos, A., Gratton, E., and Hueber, D. (2001) A Investigation of human brain hemodynamics by simultaneous near-infrared spectroscopy and functional magnetic resonance imaging. *Med. Phys.*, 28(4), 521–527.

107. (Vainthianathan *et al*, 2004) Vaithianathan, T., Tullis, I.D.C., Everdell, N., Leung, T., Gibson, A.P., and Delpy, D.T. (2004) The Design of a portable infrared mapping system for functional imaging on babies. *Review of Scientific Instruments*, 75(10), 3276-3283.

108. (van der Zee, 1992) van-der-Zee, P. (1992) Measurement and modelling of the optical properties of human tissue in the near infrared. PhD thesis, University College London, Department of Medical Physics and Bioengineering, London.

109. (van Veen *et al*, 2000) van Veen, R.L.P., Sterenborg, H.J.C.M., Pifferi, A., Torricelli, A., and Cubeddu, R. (2000) Determination of VIS-NIR absorption coefficients of mammalian fat, with time- and spatially resolved diffuse reflectance and transmission spectroscopy. *Optical Society of America.*

110. (Vo-Dinh, 2003) Vo-Dinh, T. (2003) Biomedical Photonics Handbook. USA: CRC Press.

111. (Volder, 2002) Volder, A.G. de (2002) Functional brain imaging of childhood clinical disorders with PET and SPECT. *Developmental Science*, 5(3), 344-360.

112. (Volpe, 2001) Volpe, J.J. (2001) Neurobiology of periventricular leukomalacia in the premature infant. *Pediatric Research*, 50(5), 553–562.

113. (Webb, 2000) Webb, S. (2000) The Physics of Medical Imaging. Great Britain: IOP.

114. (Webb, 2003) Webb, A. (2003) Introduction to Biomedical Imaging. New Jersey: IEEE Press.

115. (Webster, 1992) Webster, J.G. (1992) Medical Instrumentation: Application and Design. 2nd edition, Houghton Mifflin Co.

116. (Whitelaw, 2001) Whitelaw, A. (2001) Intraventricular haemorrhage and posthaemorrhagic hydrocephalus: pathogenesis, prevention and future interventions. *Semin. Neonatol*, 6, 135-146.

117. (Wickramasinghe *et al*, 1993) Wickramasinghe, Y.A.B.D., Palmer, K.S., Houston, R., Spencer, S.A., Rolfe, P., Thorniley, M.S., Oeseburg, B., and Colier, W. (1993). Effect of Fetal Hemoglobin on the Determination of Neonatal Cerebral Oxygenation by Near-Infrared Spectroscopy. *Pediatric Research*, 34(1).

118. (Woodard and White, 1986) Woodard, H.Q., and White, D.R. (1986) The composition of body tissues. *British Journal Radiol.*, 59, 1209–1219.

119. (Wyatt, 1993) Wyatt, J.S. (1993) Near-Infrared Spectroscopy in Asphyxial Brain Injury. *Perinatal Asphyxia*, 20(2), 369-378.

120. (Yaffe and Rowlands, 1996) Yaffe, M.J., and Rowlands, J.A. (1996) X-ray detectors for digital radiography. *Physics in Medicine and Biology. Biol.*, 42, 1-39.

121. (Yamashita *et al*, 1999) Yamashita, Y., Maki, A., and Koizumi, H. (1999) Measurement System for noninvasive dynamic optical topography. *Journal Biomedical Optics*, 4(4), 414-417.

122. (Yamashita *et al*, 2001) Yamashita, Y., Maki, A., and Koizumi, H. (2001) Wavelength dependence of the precision of noninvasive optical measurement of oxy-, deoxy, and total-hemoglobin concentration. *Med. Phys.*, 28(6), 1108-1114.

123. (Yusof *et al*, 2003) Yusof, R.Md., Hebden, J.C., Gibson, A., Everdell, N., Austin, T., Meek, J.H., Arridge, S.R., Wyatt, J.S., and Delpy, D.T. (2003) Validation of the use of homogenous reference phantoms for optical tomography of the neonatal brain. Proc. SPIE 4955, 6-11

124. (Zhao *et al*, 2005) Zhao, J., Ding, H.S., Hou, X.L., Zhou, C.L., and Chance, B. (2005) In vivo determination of the optical properties of infant brain using frequency-domain near-infrared spectroscopy. *Journal of Biomedical Optics*, 10(2).

125. (Zijlstra *et al*, 1991) Zijistra, W.G., Buursma, A., and W.P. Meeuwsen-van der Roest (1991) Absorption Spectra of Human Fetal and Adult Oxyhemoglobin, De-Oxyhemoglobin, Carboxyhemoglobin, and Methemoglobin. *Clinical Chemistry*, 37(9), 1633-1638.